

# Geothermometry by Raman spectroscopy of dispersed organic matter

Dissertation

zur Erlangung des mathematisch-naturwissenschaftlichen Doktorgrades  
“Doctor rerum naturalium”  
der Georg-August-Universität Göttingen

im Promotionsprogramm Geowissenschaften / Geographie  
der Georg-August University School of Science (GAUSS)

vorgelegt von

Nils Keno Lünsdorf

aus Weener (Ostfriesland)

Göttingen, 2015

Betreuungsausschuss:

Prof. Dr. Hilmar von Eynatten  
Abteilung für Sedimentologie und Umweltgeologie,  
Geowissenschaftliches Zentrum der Universität Göttingen  
Prof. Dr. Volker Thiel  
Abteilung für Geobiologie,  
Geowissenschaftliches Zentrum der Universität Göttingen

Mitglieder der Prüfungskommission:

Referent/in: Prof. Dr. Hilmar von Eynatten  
Abteilung für Sedimentologie und Umweltgeologie, Universität Göttingen  
Korreferent/in: Prof. Dr. Volker Thiel  
Abteilung für Geobiologie, Universität Göttingen  
2. Koerreferent/in: Prof. Dr. Ralf Littke  
Energy and Mineral Resources, RWTH Aachen

Weitere Mitglieder der Prüfungskommission:

Dr. István Dunkl  
Abteilung für Sedimentologie und Umweltgeologie, Universität Göttingen  
Dr. Burkhard Schmidt  
Abteilung für Experimentelle und Angewandte Mineralogie, Universität Göttingen  
Prof. Dr. Jonas Kley  
Abteilung für Strukturgeologie und Geodynamik, Universität Göttingen  
Prof. Dr. Gerd Rantitsch  
Abteilung für Angewandte Geowissenschaften und Geophysik, Montanuniversität Leoben  
Prof. Dr. Sharon Webb  
Abteilung für Experimentelle und Angewandte Mineralogie, Universität Göttingen

Tag der mündlichen Prüfung: 30.10.2015

**Composition of the thesis.** This cumulative thesis is composed of six chapters. Chapters 2 to 5 are manuscripts either already published or submitted. The thesis was financially supported by the Deutsche Forschungsgemeinschaft (DFG), grant number DU373/8-1. A short synopsis on each chapter follows.

**Chapter 1: Introduction.** This chapter presents the introduction to the thesis, laying out the motivation, approach and methodical framework.



**Chapter 2: Towards a higher comparability of geothermometric data obtained by Raman spectroscopy of carbonaceous material. Part 1: Evaluation of biasing factors.**

N. K. Lünsdorf, Dunkl I., Schmidt B. C., Rantitsch G., von Eynatten H.

This manuscript is published as: *Towards a Higher Comparability of Geothermometric Data obtained by Raman spectroscopy of Carbonaceous Material. Part 1: Evaluation of Biasing Factors*. Geostandards and Geoanalytical Research, 2014, 38(1), p. 73-94.

In this chapter the method of geothermometry based on Raman spectroscopy of carbonaceous material (RSCM) is tested for biasing sources. Experiments showed that the biasing sources can be sorted into three groups; (1) bias intrinsic to the spectral evaluation, (2) bias intrinsic to the experimental setup and (3) bias intrinsic to the carbonaceous matter. The manuscript provides conclusions to reduce the bias due to group one and two and is thus the basis for the following chapters.

The first author carried out the fieldwork, in which he was assisted by the second author. Additionally, the first author performed all experimental work and wrote a first version of the manuscript including all figures and tables. The second author provided sample material, participated in the operator bias test and helped to finalize the manuscript. The third author also participated in the operator bias test and was of great help in Raman analysis. The fourth author also participated in the operator bias test, provided access to the Raman spectrometer at the University of Leoben (Austria) and helped to finalize the manuscript. The fifth author helped to finalize the manuscript and as the second, third and fourth author he helped with discussing and interpreting the data.

**Chapter 3: IFORS - Iterative fitting of Raman spectra.**

N. K. Lünsdorf and J. O. Lünsdorf

This manuscript is published as: *Evaluating Raman spectra of carbonaceous matter by automated, iterative curve-fitting*. International Journal of Coal Geology, 2016, 160-161, p. 51 - 62

In this chapter a new approach to automated curve-fitting is presented that will decrease the bias due to spectral evaluation. The operating procedure of the algorithm is explained and the curve-fitting approach is tested on spectra of low anchizonal to epizonal carbonaceous matter. Two new RSCM parameters were derived which show a distinct correlation with random vitrinite reflectance and illite crystallinity.

The first author was responsible for the sample selection, carried out all sample preparation and performed the Raman spectroscopic analysis, the vitrinite reflectance measurements and designed the method to evaluate the data provided by the IFORS software. The first author also wrote most of the manuscript including all figures and tables. The second author wrote the core functionality of the IFORS algorithm and section 3.2.3 of the manuscript.

**Chapter 4: Raman spectroscopy of dispersed vitrinite - Methodical aspects and correlation with reflectance.**

N. K. Lünsdorf

This manuscript is published as: *Raman spectroscopy of dispersed vitrinite - Methodical aspects and correlation with reflectance*. International Journal of Coal Geology, 2016, 153, p. 75-86.

In this chapter methodical aspects of the correlation between vitrinite reflectance and RSCM parameters are investigated. To establish a methodical framework for the STA-RSCM method, the effect of polishing on the Raman spectrum of vitrinites had to be evaluated. Multi-wavelength Raman experiments revealed a two stage molecular evolution of vitrinites during coalification and graphitization.

**Chapter 5: Towards a higher comparability of geothermometric data obtained by Raman spectroscopy of carbonaceous material. Part 2: A revised geothermometer.**

N. K. Lünsdorf, Dunkl I., Schmidt B. C., von Eynatten H.

This manuscript is submitted to the journal of Metamorphic Geology.

In this chapter a first reference series with known peak metamorphic is introduced. The temperatures range from 160 °C to 600 °C. The methodical framework proposed in chapter 4 is extended to and modified for metamorphic samples and a revised geothermometer based on the STA-RSCM method is proposed and tested on the reference series.

The first and second author performed all fieldwork. The first author carried out all experimental work and wrote a first version of the manuscript including all figures and tables. The second, third and fourth author helped in discussing and interpreting the data and to finalize the manuscript.

**Chapter 6: Discussion and summary.** This last chapter summarizes the thesis, reflects on the main conclusions and provides an outlook for further research.

**Acknowledgements.** First of all I would like to thank all former and present members of the department of Sedimentology and Environmental Geology for the familiar atmosphere and positive attitude in the office.

Special thanks to Prof. Hilmar von Eynatten for his guidance during the four and a half years of my PhD thesis and for being a very patient doctoral adviser, who allowed me to work in my pace.

I would like to thank Dr. István Dunkl for being such a positive and welcoming person and his endless support throughout the years, be it in field, the laboratory or discussing new ideas. Thank you again for this great time, István.

Many thanks to Dr. Burkhard Schmidt for his support since the beginning of this project and his prudent advice in Raman spectroscopy and artificial maturation experiments.

I thank Prof. Gerd Rantitsch for his support during the fieldwork in Austria, his honest and most often constructive criticism in reviewing the manuscripts and for assistance during the analytical work at the University of Leoben.

I would like to thank Prof. Volker Thiel for his support in organic geochemistry related challenges, his advice on the analysis and preparation of the Kerogen samples and the discussions on many future topics that will keep me busy in the next years.

Programming was an integral part of this project and it wouldn't have been realized without the computer science expertise of my brother Ontje; thank you very much.

Of course, I couldn't have finished my thesis without preparing samples and thus, I thank Irina Ottenbacher, Judit Dunkl and Cornelia Friedrich for their helping hands. Also, chemical analysis was required and therefore, I thank Andreas Kronz for introducing me to the electron microprobe.

Further thanks to Lothar Laake and his team of the metal workshop for designing and building all the machinery that was needed.

I would like to thank Volker Karius, Reinhard Wolff, Anne Krippner, Aldo Alvan, Malte Schindler, Kersten Löwen, Ines Ringel and Guido Meinhold for being pleasant colleagues and more importantly for becoming friends over the years.

I am indebted to my parents, as I could always count on their support and understanding. Last but not least I thank Doro for her love and sharing her life with me.

ABSTRACT. Raman spectroscopy of carbonaceous material (RSCM) is frequently used to determine peak metamorphic temperature or to infer the coal rank as well as the degree of organic maturation. Several temperature calibrations exist, but methodical aspects limit the portability of these calibrations among laboratories and reduce overall comparability of the method. By identifying the subjectivity of spectral evaluation, experimental setup and sample heterogeneity as major sources of bias in the method, an outline to increase comparability could be established. To reduce the subjectivity during spectral evaluation the automated, user-input independent curve-fitting software 'IFORS' (Iterative Fitting Of Raman Spectra) has been written. To reduce the bias due to the experimental setup, a reference sample series has been collected that covers a temperature range of 160 °C to 600 °C. Multi-wavelength resonance Raman spectroscopy was performed during sample preparation on dispersed vitrinites that experienced diagenetic to epizonal pressure and temperature conditions to infer the analogy between the RSCM-method and reflectance of dispersed organic matter.

The IFORS software allowed to derive the scaled total area (STA) Raman parameter which accurately characterizes Raman spectra of carbonaceous matter. Based on the resonance Raman data it could be shown that STA-RSCM method can be used in analogue to vitrinite reflectance, that this method is robust to sample preparation, especially polishing, and that the resonance Raman spectra of vitrinite reflect a two-stage molecular evolution during coalification and graphitization. During the first stage, which ends approximately after the CM passed through the gas-window, linear polycyclic aromatic structure grow, while the second stage indicates growth of condensed polycyclic aromatic structures.

The STA-RSCM method has been extended to describe the Raman spectra of metamorphic CM and was successfully calibrated to the reference sample series. Thus, a revised RSCM-geothermometer valid from 160 °C to 600 °C is proposed. The sample series is available to the public and is supposed to be extended by the scientific community to further increase the quality of the reference series. When used in combination, the STA-RSCM method and the reference sample series will improve the overall comparability among laboratories and will advance the general applicability of this geothermometric method.

ZUSAMMENFASSUNG. Raman-Spektroskopie an kohligem Material (RSCM) ist eine häufig verwendete Methode, um die maximale Temperatur der Metamorphose oder die thermische Reife von Kohlen und organikreichen Sedimenten zu bestimmen. Für die Temperaturabschätzung wurden bereits mehrere Kalibrationskurven ermittelt, jedoch wird die Übertragbarkeit dieser Kalibrationen auf andere Labore durch methodische Aspekte eingeschränkt und die Vergleichbarkeit zwischen den Laboren dadurch reduziert. Die subjektive Auswertung von Spektren, das verwendete Messsystem und die Probenheterogenität bedingen die größte Streuung der Ergebnisswerte und ein Ansatz, mit dem Ziel die Vergleichbarkeit zu erhöhen, wurde formuliert. Um die Subjektivität der spektralen Auswertung zu verringern, wurde das 'IFORS' (Iterative Fitting Of Raman Spectra) Programm geschrieben, das die automatische, Benutzer-unabhängige Auswertung von Raman-Spektren ermöglicht. Um die Streuung aufgrund des verwendeten Messsystems zu reduzieren, wurde ein Referenzprobensatz zusammengestellt, der einen Temperaturbereich von 160 °C bis 600 °C abdeckt. Während der Probenaufbereitung wurde Resonanz-Raman-Spektroskopie mit mehreren Anregungswellenlängen an dispersen Vitriniten durchgeführt, die diagenetische bis epizonale Druck- und Temperaturbedingungen erfahren hatten, um die Gleichwertigkeit der RSCM-Methode und Vitrinitreflexion zu ermitteln.

Mit Hilfe des IFORS Programms wurde der 'scaled total area' (STA) Raman Parameter ermittelt, der das Raman Spektrum von kohligem Material präzise beschreibt. Auf Grundlage der Resonanz-Raman Daten konnte gezeigt werden, dass die Methodiken der STA-Raman Spektroskopie und Vitrinitreflexion analog zueinander sind, dass die STA-RSCM Methode gegenüber der Probenaufbereitung, insbesondere dem Polieren, robust ist, und dass die Resonanz-Raman Spektren der Vitrinite eine zweistufige molekulare Entwicklung während der Inkohlung und Graphitisierung aufzeichnen. Während der ersten Stufe, die kurz nach dem Durchschreiten des Gas-Fensters endet, wachsen vor allem lineare, polyzyklische, aromatische Kohlenwasserstoffe, während in der anschließenden zweiten Stufe kondensierte Formen von polyzyklischen, aromatischen Kohlenwasserstoffen wachsen.

Um die Raman Spektren von metamorphem, kohligem Material zu beschreiben, wurde die STA-RSCM Methodik erweitert und erfolgreich gegen die Temperaturinformation des Referenzprobensatzes kalibriert, so dass ein neues, überarbeitetes RSCM-Geothermometer vorgestellt werden konnte, das über einen Temperaturbereich von 160°C bis 600°C zulässig ist. Der Referenzprobensatz steht öffentlich zur Verfügung und es wird erwartet, dass der Probensatz verbessert werden kann, wenn er um Proben aus der wissenschaftlichen Gemeinschaft erweitert wird. Wenn beide Ansätze, die STA-RSCM Methodik und der Referenzprobensatz, miteinander kombiniert werden, erhöht sich die Vergleichbarkeit zwischen den Laboren und gleichzeitig steht diese geothermometrische Methode allen Laboren zur Verfügung.



# Contents

List of Figures	ix
List of Tables	xi
Chapter 1. Introduction	1
1.1. Motivation and approach	3
1.2. Methodical framework	3
Chapter 2. Towards a Higher Comparability of Geothermometric Data obtained by Raman spectroscopy of Carbonaceous Material. Part 1: Evaluation of Biasing Factors	11
2.1. Introduction	11
2.2. Methods and samples	12
2.3. Results and discussion	15
2.4. Conclusions and outlook	28
Chapter 3. IFORS - Iterative fitting of Raman spectra	31
3.1. Introduction	31
3.2. Approach and Algorithm	32
3.3. Case study	40
3.4. Conclusion	48
Chapter 4. Raman spectroscopy of dispersed vitrinite - Methodical aspects and correlation with reflectance	49
4.1. Introduction	49
4.2. Methods	52
4.3. Results and discussion	54
4.4. Conclusions	63
Chapter 5. Towards a higher comparability of geothermometric data obtained by Raman spectroscopy of carbonaceous material. Part 2: A revised geothermometer	65
5.1. Introduction	65
5.2. Samples	66
5.3. Methodical background	69
5.4. Results	72
5.5. Conclusions	84
Chapter 6. Discussion and summary	85
6.1. Discussion	85
6.2. Summary	87
Bibliography	89

Chapter 7. Appendix	101
7.1. Supplements to chapter 2	101
7.2. Supplements to chapter 3	104
Curriculum Vitae	120

## List of Figures

1.2.1	Energy levels and spectroscopic processes.	5
1.2.2	Selection rule for Raman active vibrations.	6
1.2.3	General setup of a Raman spectrometer.	6
1.2.4	The principle of confocality.	7
1.2.5	Setup of a Czerny-Turner spectrograph.	8
1.2.6	The relationship between dispersion and spectral coverage.	9
2.1.1	Definition of 'Crystallinity' levels for CM Raman spectra.	12
2.3.1	Results: Test 2 - Influence of baseline correction.	18
2.3.2	Results: Test 3 - Reproducibility.	19
2.3.3	Results: Test 4 - Influence of spectral evaluation software on parameter ratios.	21
2.3.4	Results: Test 5 - Influence of operator's personal fitting strategy on parameter ratios.	23
2.3.5	Results: Test 5 - continued.	24
2.3.6	Results: Test 6 - Influence of sample preparation on parameter ratios.	24
2.3.7	Particulate and disperse carbonaceous matter.	25
2.3.8	Results: Test 7 - Influence of sample heterogeneity on parameter ratios.	26
2.3.9	Results: Test 8 - Influence of structural anisotropy on parameter ratios.	27
2.3.10	Results: Test 9 - Influence of Raman systems on parameter ratios.	28
2.3.11	Results: Test 9 - continued.	29
3.2.1	Correction of a Raman spectrum for dispersion.	33
3.2.2	Simplified flow chart of the IFORS algorithm.	34
3.2.3	IFORS software - The 'peak indexing' function.	35
3.2.4	Carbonaceous matter Raman spectra from the lower anchizone to epizone.	37
3.2.5	The 'Raman Area Ratio' (RAR) and 'Scaled Total Area' (STA) parameters.	39
3.3.1	IFORS software - Determination of optimum HWHM value.	41
3.3.2	STA of different organoclast groups.	42
3.3.3	Random vitrinite reflectance compared to STA and RAR.	44
3.3.4	The influence of the excitation wavelength on D_STA and the RAR parameter.	46
3.3.5	D_STA compared to the RA1-ratio.	47
4.2.1	Determination of the D/G-ratio.	54
4.2.2	Spectral processing according to the STA-RSCM method.	55

4.3.1	Evolution of surface roughness during polishing.	55
4.3.2	Raman spectra of graphitic CM contaminated by polish slurry.	56
4.3.3	Changes in Raman parameters during polishing.	58
4.3.4	The effect of polishing on the D/G-ratio.	59
4.3.5	The correlation of the STA-RSCM method with vitrinite reflectance.	60
4.3.6	The wavelength dependent shift of the central D-band value during maturation.	62
5.1.1	Simplified geological overview map of the Central and Western Alps.	66
5.2.1	Simplified tectonic overview map of the Central Alps.	67
5.2.2	Simplified geological overview map of the Schistes Lustrés complex.	68
5.3.1	Nomenclature of CM Raman spectra.	71
5.4.1	Raman parameters of the Glarus Alps and Pyrophyllite-In samples.	73
5.4.2	Raman parameters of the Schistes Lustrés samples.	75
5.4.3	MgCO <sub>3</sub> -content of calcites from the Bündnerschiefer samples.	76
5.4.4	Raman parameters of the Bündnerschiefer and Lepontine Alps samples.	77
5.4.5	Raman parameters of the complete reference series.	79
5.4.6	Intensity distribution in the G-band-region during metamorphism.	80
5.4.7	The revised STA-RSCM-geothermometer.	81
5.4.8	Spectral evolution of CM examined by different lasers.	81
5.4.9	Comparison of the R2- and RA1-ratio with the STA parameter.	82

## List of Tables

2.2.1	Sample list - chapter 2.	13
2.2.2	Summary of the test strategies.	16
2.3.1	Results: Test 1 - Influence of curve-fitting strategy on parameter ratios.	17
2.3.2	Results: Test 2 - Influence of baseline correction.	19
2.3.3	Results: Test 3 - Reproducibility.	20
2.3.4	Results: Test 5 - Influence of operator's personal fitting strategy on parameter ratios.	22
2.3.5	Results: Test 7 - Influence of sample heterogeneity on parameter ratios.	25
3.3.1	Sample list - chapter 3.	40
3.3.2	RAR and STA values of CM from low anchizonal to epizonal conditions.	43
4.2.1	Sample list - chapter 4	53
5.2.1	Sample list - chapter 5.	69
5.3.1	Mineral Raman band intervals.	72



## Introduction

With the advent of lasers and the development of multi-channel, charged coupled device detectors, Raman spectroscopy experienced a resurgence and became a very popular method in chemistry, physics and related fields of science. This non-destructive, non-contacting, spectroscopic method rapidly provides information on the molecular structure of the analyte and is frequently used in geosciences for mineral identification (Bartholomew, 2013; Bishop et al., 2004; Das and Hendry, 2011; Groppo et al., 2006; Haskin et al., 1997; Hope et al., 2001; Jehlička et al., 2009; White, 2009), fluid inclusion studies (Burke, 2001; Frezzotti et al., 2012; Guillaume et al., 2003; Pasteris et al., 1988; Rosso and Bodnar, 1995; Rosasco and Roedder, 1979; van den Kerkhof and Olsen, 1990), studies concerning pressure and temperature related phase transitions (Auzende et al., 2004; Daniel et al., 1995; Gillet, 1996; Gunasekaran and Anbalagan, 2007; Lin, 2003; Palmer et al., 1994; Salje et al., 1993), estimation of metamorphic pressures (Enami et al., 2007) and temperatures (Aoya et al., 2010; Beyssac et al., 2002a; Kouketsu et al., 2014; Lahfid et al., 2010).

First systematic studies on the Raman spectrum of graphite and assignment of vibrational modes to the observed Raman bands were carried out by Tuinstra and Koenig (1970). In pure graphite, measured perpendicular to the basal plane, only the  $E_{2g}$  mode at  $1582\text{ cm}^{-1}$  is observed and has been termed as the G-band. In micro-crystalline graphite an additional band appears at ca.  $1350\text{ cm}^{-1}$ , which was attributed to the  $A_{1g}$  mode, which becomes Raman active, according to Tuinstra and Koenig (1970), due to the finite dimensions of the crystallites. Because this Raman band is always observed in disordered carbon materials it has been termed D-band. Vidano et al. (1981) showed that the position of the D-band shifts with the used excitation wavelength which was studied in more detail by Wang et al. (1990). Ferrari and Robertson (2001) showed that not only the D-band position is dependent on the excitation wavelength, but also the width of the G-band and the D/G-intensity ratio, which implies that the general shape of the CM Raman spectrum is dictated by the used laser wavelength.

Regardless of the mentioned band dispersion effects, already Beny-Bassez and Rouzaud (1985) proofed that Raman spectroscopy can infer the degree of crystallinity of graphite. However, the basis for future RSCM studies was given by Pasteris and Wopenka (1991) and later Wopenka and Pasteris (1993) who provided a systematic study on the graphitization of CM in metapelites and could show that the Raman spectrum of carbonaceous material progressively changes with increasing metamorphic degree. Later, Yui et al. (1996) extended this concept to low-grade metamorphic rocks. Beyssac et al. (2002a) could show that the progressive changes in the CM Raman spectra with increasing metamorphism are related to the metamorphic temperature. Because the reactions to form graphite are irreversible, the structure of metamorphic CM is most likely unaffected by retrograde pressure and temperature decrease during exhumation. Therefore, Beyssac et al. (2002a) could introduce an empirical geothermometer based on the structural evolution of CM during metamorphism. This geothermometer records the peak metamorphic temperature and is valid over a temperature range of  $330\text{ }^{\circ}\text{C}$  to  $650\text{ }^{\circ}\text{C}$ . Usually curve-fitting is used to characterize the

shape of a CM Raman spectrum by a numerical value. Common curve-fitting approaches involve baseline subtraction prior to fitting, which applies residual minimization by variation of function parameters. Commonly used functions in curve-fitting are Voigt, Lorentz, Gauss or pseudo-Voigt functions (Beysac et al., 2002a; Sadezky et al., 2005; Lahfid et al., 2010). In the case of the initial RSCM-geothermometer, Beysac et al. (2002a) used four Voigt functions during fitting to calculate the so called R2-ratio, which is based on the area values of the used Voigt functions.

The proposed RSCM-geothermometer is frequently used in geological studies (Beysac et al., 2007; Forer et al., 2009; Wiederkehr et al., 2011; Scharf et al., 2013), because carbonaceous matter is ubiquitous in meta-sedimentary rocks. Thus, the next step was to extend the RSCM-geothermometer to lower temperatures. Already Rahl et al. (2005) increased the temperature range of the RSCM-geothermometer down to values as low as 100 °C based on apatite (U-Th)/He dating and apatite and zircon fission track data by combining the R2 ratio after Beysac et al. (2002a) with the D/G intensity ratio. Later, Lahfid et al. (2010) provided two new Raman parameter ratios which were calibrated for low temperature metamorphic conditions over a temperature range of 180 °C to 320 °C. However, the approach of Lahfid et al. (2010) can not be applied to higher metamorphic temperatures. Recently, Kouketsu et al. (2014) published a calibration over 165 °C to 655 °C based on multiple curve-fitting strategies and the user has to decide when to apply which fitting strategy. Despite its ease of applicability, several methodical aspects need to be considered when the RSCM-geothermometer is to be used. Already Wopenka and Pasteris (1993) realized that the laser power has to be attenuated during measurement to avoid thermal alteration or degradation of the CM due to its high absorption coefficient. Because of the anisotropic structure of graphite, the Raman spectrum changes with respect to the polarization direction of the laser beam and the orientation of the crystallographic axis of graphite (Katagiri et al., 1988; Compagnini et al., 1997) and therefore Beysac et al. (2002a) suggested to measure perpendicular to the graphite c-axis, i.e. parallel to the orientation of the graphene sheets. Additionally, graphite and graphitic CM is very sensitive to mechanical preparation and polishing leads to severe alteration of the CM Raman spectrum and thus graphitic CM has to be measured beneath a translucent phase, if the sample surface needs polishing (Wopenka and Pasteris, 1993; Beysac et al., 2003; Ammar and Rouzaud, 2012). Furthermore, the mentioned wavelength dependency of the CM Raman spectrum prevents the usage of this plethora of calibration lines, if the same wavelength is not available.

Although the RSCM-geothermometer is still not appropriately calibrated to diagenetic temperatures, i.e. below 150 °C, the Raman spectra of Kerogen type 3 and coal can be used to gain information on the maturity stage of the organic matter (Kelemen and Fang, 2001; Liu et al., 2013; Hinrichs et al., 2014). In coals and in the dispersed organic matter (DOM) of sedimentary rocks the progressive increase in reflectance of the maceral collotelinite, which belongs to the vitrinite maceral group, is measured to infer the coal rank or organic maturity (ICCP, 1998). This increase in reflectance is related to the increasing carbon content and degree of aromatization (Taylor et al., 1998). Thus, the structural reorganization on molecular scale during coalification explains the correlation of Raman data with reflectance values. However, coal is a very heterogeneous substance and depending on its rank, different macerals provide different Raman spectra and reflectance values (Guedes et al., 2010). Therefore, identification of the correct maceral group is of prime importance and more easily done in coals than in DOM of sediments, because the textural relationship between the macerals is preserved in the coal. Especially in DOM studies the misidentification of vitrinite leads to severe difference in results among laboratories (Borrego et al., 2006).



Furthermore, methodical aspects like small particle size, the presence of high reflecting phases (e.g. pyrite) in the organic matter and the quality of polishing influence the reflectance measurement (Borrego et al., 2006). Due to the indicated correlation between the RSCM method and vitrinite reflectance it is worthwhile to investigate if the Raman spectrum of vitrinite and dispersed organic matter is also influenced by the above mentioned methodical aspects and if it could provide a more accurate measure for maturity.

### 1.1. Motivation and approach

From the outline given above it is apparent that there are many different calibrations for the RSCM-geothermometer. These calibrations were generated by applying different curve-fitting strategies on Raman spectra collected with different Raman spectrometers, resulting in calibrations that are specific to the laboratories they were generated in and the portability of the calibrations to other laboratories is questionable. Thus, it is one aim of this thesis to increase the comparability and general applicability of the RSCM-geothermometer by providing a more standardized procedure. This will be achieved by identifying the most severe sources of bias in the method, introduction of an automated, user-input independent curve-fitting software and the compilation of a reference sample series with known peak metamorphic temperatures. After the methodical framework has been established and tested on the reference series, the revised RSCM-geothermometer and the reference series can be distributed to other laboratories.

Because Raman spectroscopic data of vitrinites correlates with their reflectance values, it is another aim of the thesis to investigate if both methods can be used in analogue and if Raman spectroscopy of dispersed vitrinites could provide a new maturity index. As stated above, reflectance measurements on vitrinite are affected by methodical aspects (see chapter 1). Thus, it is investigated which methodical aspects affect have an impact on the acquired Raman data, focusing on the effect of polishing on the Raman spectrum of vitrinites, by analyzing dispersed vitrinites during sample preparation. Because the used sample set covers diagenetic to epizonal pressure and temperature conditions, the progressive maturation of dispersed organic matter was analyzed by both, Raman spectroscopy and reflectivity, which allowed a detailed comparison the methods.

### 1.2. Methodical framework

In the following sections an overview about Raman spectroscopy is provided. First, an introduction to the Raman effect is given, followed by a description of the general components of a Raman micro-spectroscopic system.

**1.2.1. The Raman effect.** Raman scattering is a type of inelastic scattering of an electromagnetic wave by matter and was first proven by C. V. Raman in 1928 (Raman and Krishnan, 1928). A qualitative description of the interaction of an oscillating electromagnetic field with a molecular system is given in (Dietzek et al., 2011) who state that the electronic field of the incident radiation will distort the charge distribution of a molecule and therefore will induce a dipole moment, which is the source of a secondary electronic field irradiating from the molecule. This secondary field represents the scattered light (Dietzek et al., 2011). In the following, Raman scattering is explained on the basis of a diatomic linear molecule as discussed in Ferraro et al. (2003).

In Raman spectroscopy the incident electromagnetic field is given by a laser light source and the electric field strength of the laser light oscillates according to equation 1.2.1

$$(1.2.1) \quad E = E_0 \cos 2\pi\nu_0 t$$

with  $E_0$  being the amplitude and  $\nu_0$  is the frequency of the laser. The oscillating electric field then induces an electric dipole moment in the molecule. This dipole moment  $P$  depends on the molecular polarizability  $\alpha$  and the applied electric field  $E$  (eq. 1.2.2), where  $\alpha$  determines the extend of distortion of the electric charge distribution around the molecule with respect to the equilibrium distribution. The polarizability of a molecule is usually anisotropic as the electric charge distribution is more readily shifted along a chemical bond than perpendicular to it.

$$(1.2.2) \quad P = \alpha E = \alpha E_0 \cos 2\pi\nu_0 t$$

As the molecule vibrates along its long-axis with a frequency of  $\nu_m$  and an amplitude  $q_0$  the atomic nuclei move out of their equilibrium geometry and this nuclear displacement  $q$  can be expressed by equation 1.2.3.

$$(1.2.3) \quad q = q_0 \cos 2\pi\nu_m t$$

Because the vibration represents a periodic shifting of positive charge, it will have an effect on the negative, electric charge distribution around the nuclei. Thus, the polarizability is not static, but is modified by the nuclear motion (Dietzek et al., 2011). That is, the polarizability at a non-equilibrium geometry is given by equation 1.2.4

$$(1.2.4) \quad \alpha = \alpha_0 + \left( \frac{\partial\alpha}{\partial q} \right)_0 q_0$$

where  $\alpha_0$  is the molecular polarizability at the equilibrium geometry,  $q_0$  relates to the nuclear displacement and refers to a distance away from the equilibrium geometry and  $(\partial\alpha/\partial q)_0$  is the change in polarizability with change in position, evaluated at the equilibrium geometry. Therefore, the electronic dipole moment can be expressed as:

$$\begin{aligned} P &= \alpha E_0 \cos 2\pi\nu_0 t \\ &= \alpha_0 E_0 \cos 2\pi\nu_0 t + \left( \frac{\partial\alpha}{\partial q} \right)_0 q_0 E_0 \cos 2\pi\nu_0 t \\ &= \alpha_0 E_0 \cos 2\pi\nu_0 t + \left( \frac{\partial\alpha}{\partial q} \right)_0 q_0 E_0 \cos 2\pi\nu_0 t \cos 2\pi\nu_m t \\ (1.2.5) \quad &= \alpha_0 E_0 \cos 2\pi\nu_0 t + \\ &\quad \frac{1}{2} \left( \frac{\partial\alpha}{\partial q} \right)_0 q_0 E_0 [\cos \{2\pi(\nu_0 + \nu_m)t\} + \cos \{2\pi(\nu_0 - \nu_m)t\}] \end{aligned}$$

Here, the first term represents an oscillating dipole that emits light at the same frequency as the incident laser light (Ferraro et al., 2003), which corresponds to the Rayleigh scattered light (Fig. 1.2.1). The second term contains two dipole moments with frequencies different to the laser frequency. In the case of Stokes-Raman scattering the frequency of the emitted light is reduced by the molecular vibration frequency  $\nu_m$  and Anti-Stokes-Raman scattering occurs when the frequency of the emitted light is increased by  $\nu_m$  (Fig. 1.2.1). Thus, molecular structural information can be gained from a Raman spectrum, because the observed Raman bands relate to molecular vibrations. Figure 1.2.1 shows a summary of the different scattering processes in terms of energy levels.

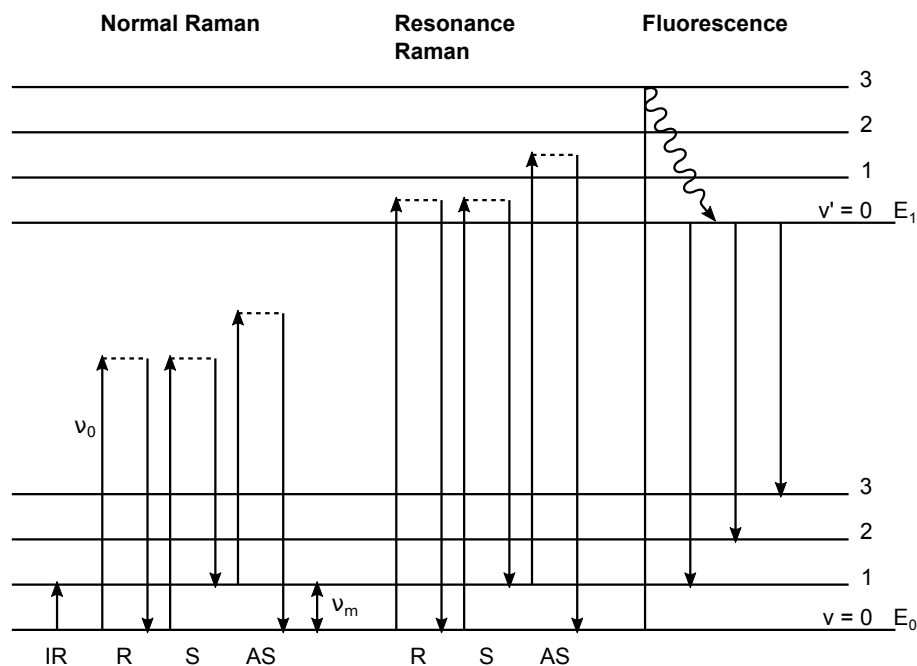


**Figure 1.2.1.** This figure shows the schematic distribution of energy levels (without rotational energy levels) of a diatomic molecule and the processes of infrared absorption, Raman scattering and fluorescence (after Ferraro et al., 2003). IR: Infrared; R: Rayleigh scattering; S: Stokes scattering; AS: Anti-Stokes scattering; E: Electronic state;  $v$ : vibrational state;  $\nu_0$ : laser frequency;  $\nu_m$ : vibrational frequency

From equation 1.2.5 it is evident that no Raman scattered light will be emitted from the sample if the term  $(\partial\alpha/\partial q)_0$  is zero. Thus, the polarizability must change during vibration for it to be Raman active. In Figure 1.2.2 the selection rule for Raman active vibrations is explained by a linear, triatomic molecule. During the symmetric stretching vibration (Fig. 1.2.2a) the polarizability increases when the vibration amplitude decreases to its minimum  $-q$  and decreases with increasing vibration amplitude and is at its minimum at  $+q$ . Hence, the electronic polarizability increases monotonously along the vibration coordinate  $q$  which means that the derivative of the electronic polarizability  $(\partial\alpha/\partial q)_0$  is not zero at the equilibrium position and the vibration is thus, Raman active. In the case of antisymmetric stretching and bending vibrations (Fig. 1.2.2b) the polarizability changes symmetrically along  $q$  and the derivative of the polarizability becomes zero at the equilibrium geometry, rendering these vibrations Raman inactive.

**1.2.2. The Raman spectrometer.** Figure (1.2.3) shows the general setup of a Raman spectrometer with its main components. These consist of an excitation source, focusing and collecting optics, a spectral analyzer unit and a detection unit.

**Excitation source.** Usually lasers are used for excitation as they provide monochromatic light with a high energy density. The high energy density is required, because the fraction of Stokes-Raman scattered light is low with about every  $10^6$ th to  $10^8$ th photon being Stokes-Raman scattered. General requirements to the laser system are (Hollricher, 2011; Dubessy et al., 2012):

- Gaussian beam shape
- linear polarization, to record polarization properties of the sample
- the laser lineshape needs to be far below  $1 \text{ cm}^{-1}$  to avoid broadening of Raman bands
- the laser light needs to be frequency and power stabilized

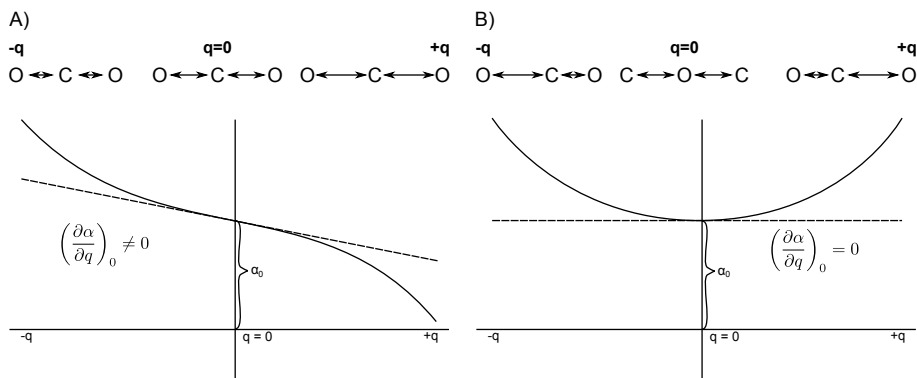


**Figure 1.2.2.** A) The symmetric stretching vibration. The equilibrium configuration of the vibration is given at  $q_0$  and the polarizability increases with bond shortening ( $-q$ ) and decreases with bond elongation ( $+q$ ), thus the change in polarizability at  $q_0$  is not zero and the vibration is Raman active. B) The antisymmetric stretching vibration. The polarizability is symmetric on both sides of  $q_0$  and therefore the change in polarizability at  $q_0$  is zero and the vibration is not Raman active. (after Ferraro et al., 2003)

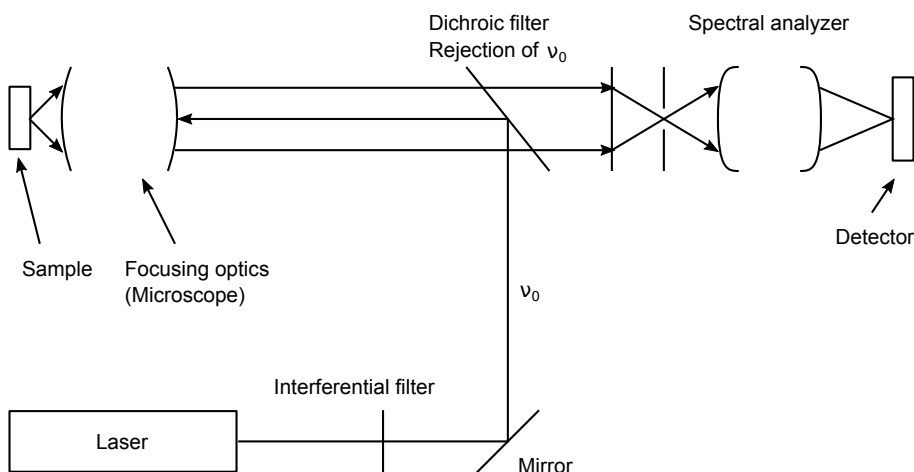


**Figure 1.2.3.** The general setup of Raman spectrometer (after Dubessy et al., 2012).

The intensity of the Raman signal can further be increased by increasing the laser frequency and its power. Because the Raman scattering intensity is proportional to fourth power of the frequency, excitation with 400 nm results in Raman signal 16 times higher than excitation at 800 nm (Hollricher, 2011). However, many substances, especially organic substances, fluoresce when irradiated with UV or blue light, while less or no fluorescence is observed when the sample is excited with red or near infrared light. Thus, choice of the excitation wavelength also depends on sample properties.

Commonly used lasers are continuous wave, ionized gas lasers, gas lasers and diode or semiconductor lasers. The first group uses either  $\text{Ar}^+$ ,  $\text{Kr}^+$  or a mixture of both for laser light generation. The characteristics of these lasers are well known, i.e. wavelengths are determined with an accuracy of 1 pm, the linewidth is less than ca.  $0.1 \text{ cm}^{-1}$  and the long-term stability of the output power is within 1 % of the laser output (Dubessy et al., 2012). These lasers generate multiple excitation lines. According to Bridges (1964) an  $\text{Ar}^+$  laser generates following lines: 454.5 nm, 457.9 nm, 465.8 nm, 472.7 nm, 476.5 nm, 488 nm, 496.5 nm, 501.7 nm, 514.5 nm and 528.7 nm, while  $\text{Kr}^+$  gives, among other, following lines: 350.7 nm, 356.4 nm, 406.7 nm, 647.1 nm and 676.4 nm (Bridges and Chester, 1965).

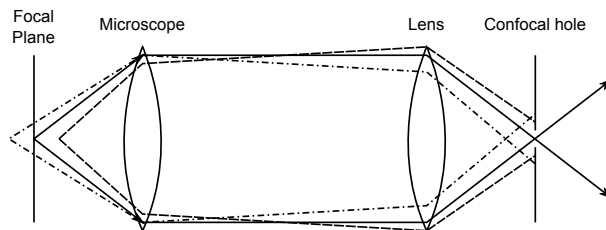


**Figure 1.2.4.** *The principle of confocality. Rays that do not originate from the focal plane are rejected at the confocal hole (after Dubessy et al., 2012).*

The most frequently installed gas laser is the He-Ne laser, where the strong Ne emission line at 632.8 nm (White and Gordon, 1963) is used for excitation. Major advantages of diode lasers are, among other, their small size, low cost, efficiency and they are often tunable. However, the diode laser frequency depends not on well defined atomic lines, as in gas lasers, but on operation temperature and diode design (McCreery, 2000). Thus, frequency stabilization is of major importance when diode lasers should be used in Raman spectroscopy. The stabilization is achieved by precise temperature control and by using so called external cavity diode lasers in which a diffraction grating operates the frequency selection (McCreery, 2000).

Before the laser light is introduced to the focusing and collection optics by a dichroic filter, an interferential filter is used to select the laser line of interest and to reject all other potential lines to avoid multiple Raman signals of the same sample (Fig. 1.2.3).

**Focusing and collection optics.** Confocal Raman microscopes are often used in the 180° backscattering geometry. In this setup the same objective is used to focus the laser light onto the sample and to collect the scattered light. It is thus important to use an objective with a high numerical aperture to increase the spatial resolution ( $d_{xy}$ ) and collection efficiency. The spatial resolution of a confocal microscope is approximated by equation 1.2.6 (Dubessy et al., 2012). The confocality of the microscopical system ensures that the collected scattered light stems to a great proportion from the focal point. The axial resolution ( $d_z$ ) is controlled by the diameter of the confocal hole, which rejects out of focus beams (Fig. 1.2.4), by the wavelength and the numerical aperture (eq. 1.2.7, Dubessy et al., 2012)

$$(1.2.6) \quad d_{xy} = \frac{0.46\lambda}{N.A.}$$

$$(1.2.7) \quad d_z = \frac{1.4\lambda}{(N.A.)^2}$$

Because the light passes through the objective and microscope twice, both should have a transmission as high as possible in the wavelength range of the scattered light. Before the collected light is passed through to the spectral analyzer unit, the intense Rayleigh scattered light needs to be rejected. This is achieved by the same dichroic filter that introduced the light to the microscope and only the Stokes scattered light can pass.

**Spectral analyzer and detection unit.** There are several spectral analyzer, or spectrograph designs of which the Czerny-Turner setup is very common. It consists of an entrance slit, a collimating mirror, the diffraction grating, a focusing mirror and an exit slit (Fig. 1.2.5). The Raman scattered light is focused through the entrance slit on the collimating mirror which reflects the light across the complete length of the grating. From the grating the dispersed light is reflected

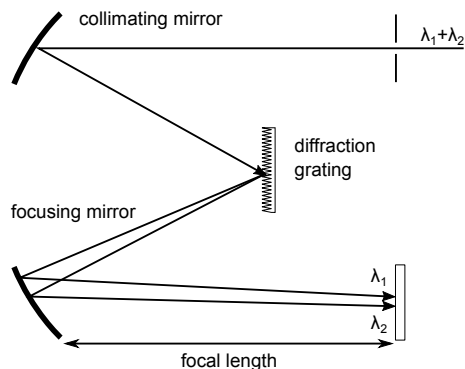


**Figure 1.2.5.** A schematic representation of a Czerny-Turner spectrograph (after McCreery, 2000).

to the second mirror which focuses the light on the exit slit (Fig. 1.2.5). The later can be directly replaced by a charged coupled device (CCD).

The most important component of the spectrograph, is the diffraction grating. It is used to disperse the polychromatic, Raman scattered light. From the fundamental grating equation (eq. 1.2.8)

$$(1.2.8) \quad d \sin \Theta = m \lambda$$

where  $d$  is the distance between the lines on the grating,  $\Theta$  is the angle of diffraction,  $m$  corresponds to the diffraction order and  $\lambda$  is the wavelength, it follows that the angle of diffraction changes with the wavelength of the incident light. This dispersion is often expressed as the reciprocal linear dispersion  $d\lambda/dl$  [nm/mm], which describes how much of the spectrum is dispersed over a unit on the detector or focal plane and is nearly constant for small  $\Theta$  (McCreery, 2000). For a single grating spectrograph, like the Czerny-Turner spectrograph, the reciprocal liner dispersion is given by (eq. 1.2.9)

$$(1.2.9) \quad \frac{d\lambda}{dl} = \frac{d \cos \Theta}{mF}$$

where  $d$ ,  $m$  and  $\Theta$  are as above and  $F$  is the focal length of the focusing mirror. The wavelength difference of the Raman scattered light and the incident light (Raman shift) is conventionally given in wavenumbers  $\nu$ , which is the reciprocal of the wavelength, with units of  $\text{cm}^{-1}$ . Following McCreery (2000) the change in Raman shift with wavenumber is not constant (eq. 1.2.10)

$$(1.2.10) \quad d\nu = \frac{1}{\lambda^2} d\lambda$$

and the dispersion in terms of Raman shift becomes:

$$(1.2.11) \quad \frac{d\nu}{dl} = \frac{d \cos \Theta (\nu_0 - \nu_j)^2}{mF}$$

with  $\nu_0$  being the absolute wavenumber of the laser and  $\nu_j$  is the Raman shift. It is evident that smaller  $d$ -values, i.e. denser gratings, and a larger focal distance will decrease the linear dispersion. This increases the spectral resolution, because a smaller part of the spectrum is spread over a detector unit, or pixel in the case of a CCD. Since the dimensions of the CCD chip are fixed to commonly 256 x 1024 pixels at a pixel width of 25  $\mu\text{m}$ , the increased resolution comes at the cost of spectral coverage. Figure 1.2.6 summarizes the relations between dispersion, resolution, spectral coverage and wavelength for several spectrograph compositions.

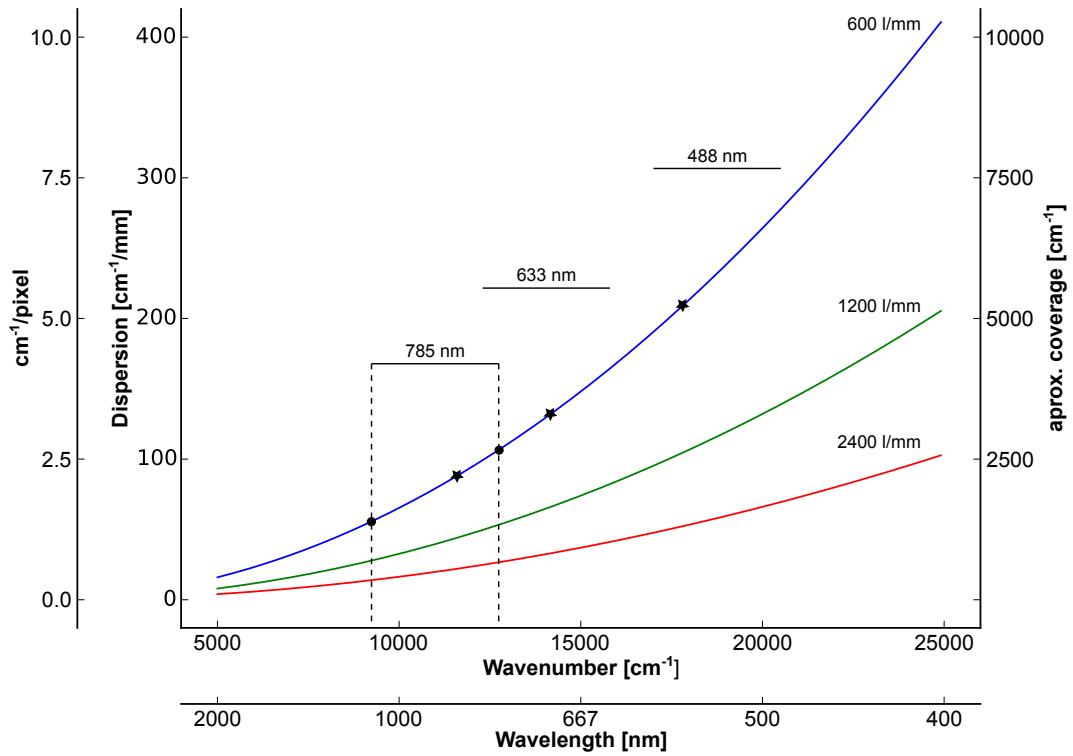


**Figure 1.2.6.** The relationship between dispersion, spectral coverage, grating and spectral resolution. The dispersion of a spectrometer with a focal length of 250 mm and a pixel width of 25  $\mu\text{m}$  is shown for three different gratings. As expected, the spectral coverage, indicated by the stars, and the dispersion increase with increasing line spacing. The relative position of a Stokes Raman spectrum from 0 to 3400  $\text{cm}^{-1}$  is indicated by the horizontal lines. The black dots on the 600 l/mm curve mark the spectral resolution for the 785 nm laser at a Raman shift of 0  $\text{cm}^{-1}$  and 3400  $\text{cm}^{-1}$ , which are ca. 2.5  $\text{cm}^{-1}/\text{px}$  and ca. 1  $\text{cm}^{-1}/\text{px}$  respectively. (after McCreery, 2000).





# Towards a Higher Comparability of Geothermometric Data obtained by Raman spectroscopy of Carbonaceous Material.

## Part 1: Evaluation of Biasing Factors

Authored by N.K. Lünsdorf, I. Dunkl, B. C. Schmidt, G. Rantitsch, H. v. Eynatten and  
published as: *Towards a Higher Comparability of Geothermometric Data obtained by Raman  
spectroscopy of Carbonaceous Material. Part 1: Evaluation of Biasing Factors*. Geostandards and  
Geoanalytical Research, 2014, 38(1), p. 73-94.

### 2.1. Introduction

Geothermometry by Raman spectroscopy of carbonaceous material (RSCM; Beyssac et al., 2002a) becomes more and more popular due to its ease of applicability and non-destructiveness (e.g. Rantitsch et al., 2004; Guedes et al., 2005; Forer et al., 2009; Huang et al., 2010; Wiederkehr et al., 2011; Endo et al., 2012). The Raman spectrum of carbonaceous material (CM) enclosed in metasediments changes systematically with increasing degree of metamorphism (e.g. Pasteris and Wopenka, 1991; Jehlička and Bény, 1992; Wopenka and Pasteris, 1993). Beyssac et al. (2002a) showed that those changes are mainly controlled by temperature and calibrated a geothermometer based on CM Raman spectra. This geothermometer is based on parameters calculated by spectral curve-fitting of the Raman bands (Fig. 2.1.1). However, there are multitude of different curve-fitting strategies using variable numbers (2 – 5) of model components (Lorentzian-, Voigt-, Gaussian- or Breit-Wigner-Fano-functions), fitting the acquired spectrum (e.g. Beyssac et al., 2002a; Quirico et al., 2003; Sadezky et al., 2005; Lahfid et al., 2010). Important function parameters (position, height, full width at half maximum FWHM, and area), reflecting the thermal transformation of CM, are derived from the extracted components. This allows the calibration of different parameter-ratios against metamorphic temperature (Beyssac et al., 2002a; Rantitsch et al., 2004; Rahl et al., 2005; Baziotis et al., 2006; Aoya et al., 2010; Lahfid et al., 2010).

As the parameter-ratios are the condensates of many steps (e.g. sample preparation, Raman measurement, and spectrum evaluation) they accumulate several biasing factors. The sources of bias can be grouped into three categories: (1) bias intrinsic to spectral curve-fitting, (2) bias intrinsic to the CM and (3) bias intrinsic to the experimental design and the specific Raman system used.

Factors of the first category are different baseline corrections, different mathematical functions (Gaussian, Lorentzian, Voigt, etc.) used for peak-fitting, and the different number of components used to model the Raman spectra. Examples for the second category are structural anisotropy, sample preparation, and sample-heterogeneity. Factors of the third category include used excitation wavelength, spectral grating and light detection device, among others.

In this paper, many of the above mentioned potential sources of bias are evaluated by a suite of simple experiments in which, at best, only one parameter influences the experimental results.

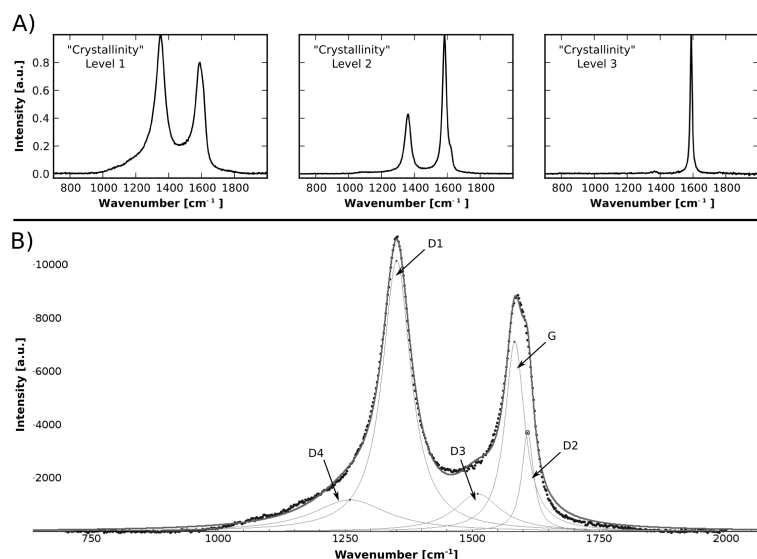


**Figure 2.1.1.** A) Representative Raman spectra of the three 'crystallinity levels'. B) An example for the decomposition of a 'crystallinity level 1' Raman spectrum by five components according to Lahfid et al. (2010). The two bands of the first-order region are described by D1, D2, D3, D4 and G components. D4 widens the low wavenumber side of the D1 band while D2 appears only as a weak shoulder on the high wavenumber side of the G band.

## 2.2. Methods and samples

**2.2.1. Samples.** The sample set (Table 2.2.1) covers a wide structural range from low to high 'crystallinity' degree of CM. The studied samples derive from the Triassic flysch of the Tethyan Himalayan sequence of SE Tibet (Dunkl et al., 2011), from the Eastern Alps (Rantitsch et al., 2004), and from the Thuringian Forest (Germany) (Kunert, 1999).

In order to enrich CM every sample has been treated chemically. The samples were crushed to particles smaller than 5 to 10 millimeters. The rock-chips were initially placed in a 1:1 solution of 37 % hydrochloric acid to dissolve carbonates and after decantation mixed with 1:1 diluted 48 % hydrofluoric acid to dissolve silicates. After hydrofluoric acid treatment the sample suspensions were decanted and diluted with de-ionized water until a pH-value of 5 to 6 was reached. Remaining fluids were evaporated in a drying oven at 50 °C. About 10 to 20 mg of the dried CM were mixed with 1 - 2 ml de-ionized water in a small glass vial and placed into an ultrasonic bath for about 60 seconds in order to disperse the carbonaceous material. This suspension was deposited on a glass slide.

**2.2.2. Raman spectroscopy.** All Raman measurements were performed with a Horiba Jobin Yvon HR800-UV spectrometer, with attached Olympus BX41 microscope, if not stated otherwise. The general measurement configuration used a 488 nm Ar<sup>+</sup>- laser for excitation, a spectral grating with 600 l/mm, a long working distance 100x objective with a numerical aperture of 0.8 and the diameter of the confocal hole was set to 100 μm. If not stated otherwise the laser light was circular polarized, a spectral range of 700 – 2000 cm<sup>-1</sup> was recorded in one spectral window in 3-5 accumulations of 10 - 30 seconds. The laser power on the sample surface was controlled by density filters to 0.3 – 0.5 mW to exclude thermal alteration of the sample. Per sample 15 measurements were conducted on different sample spots. The Raman system was calibrated against the 520.4 cm<sup>-1</sup> line of a Si-waver.

**Table 2.2.1.** List of samples. Long: longitude; Lat: latitude; s: standard deviation; n: number of measurements; ND: not determined.

Sample	Long	Lat	Region	R1	std	R2	std	RA1	std	RA2	std	n
L29	87.1829	28.6685	SE Tibet	n.d.	n.d.	n.d.	n.d.	0,61	0,01	1,56	0,05	15
DB45	91.1048	29.0483	SE Tibet	n.d.	n.d.	n.d.	n.d.	0,58	0,02	1,40	0,10	15
DB21	91.6362	28.9271	SE Tibet	n.d.	n.d.	n.d.	n.d.	0,59	0,02	1,47	0,12	15
DB26	92.1574	29.1036	SE Tibet	0,73	0,06	0,49	0,01	n.d.	n.d.	n.d.	n.d.	15
DB28	92.0433	29.1454	SE Tibet	0,65	0,06	0,45	0,02	n.d.	n.d.	n.d.	n.d.	15
DB36	91.6764	28.9881	SE Tibet	0,63	0,03	0,46	0,02	n.d.	n.d.	n.d.	n.d.	15
L1	ca. 87.332	ca. 29.040	SE Tibet	0,40	0,05	0,37	0,02	n.d.	n.d.	n.d.	n.d.	15
DB16	91.1906	28.7015	SE Tibet	0,38	0,03	0,36	0,01	n.d.	n.d.	n.d.	n.d.	15
TU2	92.2606	28,8136	SE Tibet	0,32	0,04	0,33	0,02	n.d.	n.d.	n.d.	n.d.	15
L45	88.0787	28.8651	SE Tibet	0,27	0,03	0,30	0,02	n.d.	n.d.	n.d.	n.d.	15
L57	88.1518	28.8372	SE Tibet	0,15	0,02	0,22	0,02	n.d.	n.d.	n.d.	n.d.	15
Kohl1	47.6617	15.6575	Austria	n.d.	n.d.	n.d.	n.d.	0,63	0,01	1,74	0,07	15
MAU	47.0451	13.2452	Austria	0,44	0,03	0,40	0,02	n.d.	n.d.	n.d.	n.d.	15
KL2-2	50.3944	11.4014	Thuringian Forest	n.d.	n.d.	n.d.	n.d.	0,61	0,00	1,54	0,02	30
KL2-3	50.4009	11.3529	Thuringian Forest	n.d.	n.d.	n.d.	n.d.	0,60	0,00	1,47	0,02	30
KL2-4	50.362	11.4057	Thuringian Forest	n.d.	n.d.	n.d.	n.d.	0,60	0,01	1,50	0,04	30
KL2-11	50.2632	11.5218	Thuringian Forest	n.d.	n.d.	n.d.	n.d.	0,63	0,00	1,67	0,02	30
KL2-17	50.3549	11.5109	Thuringian Forest	n.d.	n.d.	n.d.	n.d.	0,63	0,00	1,73	0,01	30
KL2-18	50.3268	11.3777	Thuringian Forest	n.d.	n.d.	n.d.	n.d.	0,57	0,01	1,32	0,03	30

**2.2.3. Evolution of the first-order Raman spectrum of CM.** After deposition and early diagenesis, the organic content of sedimentary rocks constitutes a heterogeneous mixture of organic compounds. During organic maturation mainly O, H, N and to a lesser degree C are expelled from the organic material, changing the chemical composition and structure of the residual organic material. This process leads to an enrichment of aromatic species (for a review see Vandenbroucke and Largeau, 2007).

The aromatic species form so called 'basic structural units' (BSU) of polyaromatic (4-10 cycles) layers, isolated or piled up by 2 – 3 units (Oberlin, 1989). The nanometer sized BSU is described by the mean stacking height ( $L_c$ ) and the mean basal plane diameter ( $L_a$ ). During the early stages of diagenesis and catagenesis the BSUs are randomly oriented, but start to synchronize their orientation to form molecular orientation domains (Bustin et al., 1995; Vandenbroucke and Largeau, 2007). During graphitization  $L_c$  and  $L_a$  progressively increase while at the same time the number of defects and the interplaner spacing between the graphene layers is reduced (Buseck and Huang, 1985; Wopenka and Pasteris, 1993). Thus, graphitic material of high 'crystallinity' has few structural defects, large  $L_a$  and  $L_c$  values and a low interplanar spacing.

In the Raman spectra of CM, the above outlined transformation process is reflected by the change in shape (Fig. 2.1.1a) of the most prominent Raman bands in the first order spectrum (ca. 700 – 2000  $\text{cm}^{-1}$ ). Overall there are at least five Raman bands in the first order spectrum of CM (Fig. 2.1.1b). Following Sadezky et al. (2005) and Marshall et al. (2010) these bands are denominated as D1 (ca. 1350  $\text{cm}^{-1}$ ), D2 (ca. 1620  $\text{cm}^{-1}$ ), D3 (ca. 1500  $\text{cm}^{-1}$ ), D4 (ca. 1250  $\text{cm}^{-1}$ ) and G (ca. 1580  $\text{cm}^{-1}$ ). The G-band is assigned to the Raman active  $E_{2g}$  optical phonon in graphite (Tuinstra and Koenig, 1970; Reich and Thomsen, 2004). The D1- and D2-bands are defect-induced (Pimenta et al., 2007) and depend on the excitation energy due to double-resonant Raman scattering (Reich and Thomsen, 2004). For more information see Pócsik et al. (1998), Matthews et al. (1999), Thomsen and Reich (2000), Saito et al. (2001), Reich and Thomsen (2004)

and Pimenta et al. (2007). The D3-band supposedly originates from amorphous carbons and D4-band is attributed to  $sp^2$ - $sp^3$  bonds or C-C and C=C stretching vibrations of polyene-like structures (Sadezky et al. (2005) and references therein).

Generally, the number of Raman bands decrease from low to high metamorphic conditions (Wopenka and Pasteris (1993); Yui et al. (1996); Beyssac et al. (2002b), see Fig. 2.1.1a). As the performed mode of spectral curve-fitting changes with 'crystallinity level', the recorded spectrum is first evaluated 'by eye' by a rough qualitative classification (Fig. 2.1.1):

'Crystallinity level 1': This level describes poorly crystalline CM that exhibits a rather complex spectrum in which two broad, overlapping Raman bands at ca.  $1350\text{ cm}^{-1}$  (D1) and ca.  $1580$  to  $1600\text{ cm}^{-1}$  (G + D2) and a third band at ca.  $1250\text{ cm}^{-1}$  (D4) as shoulder on the  $1350\text{ cm}^{-1}$  band are present.

'Crystallinity level 2': This level describes moderately to well crystalline CM. Here the spectra are less complex, as the band at ca.  $1250\text{ cm}^{-1}$  (D4) is absent. The intensities of the  $1350\text{ cm}^{-1}$  band (D1) and the overlapping region between  $1350\text{ cm}^{-1}$  and  $1580\text{ cm}^{-1}$  are decreasing while the  $1580$ - $1600\text{ cm}^{-1}$  band (G) gets more intense and narrow. Moreover, a new band at ca.  $1620\text{ cm}^{-1}$  (D2) appears as a clear shoulder.

'Crystallinity level 3': This level describes well crystalline CM and graphite. The spectra are simple with only the  $1350\text{ cm}^{-1}$  and  $1580\text{ cm}^{-1}$  bands present. The  $1350\text{ cm}^{-1}$  band is broad and of low intensity while the  $1580\text{ cm}^{-1}$  band is intense and sharp (low FWHM). In case of pure graphite, only the G-band appears (Tuinstra and Koenig, 1970).

**2.2.4. Spectral Evaluation.** Before fitting the first order Raman spectrum of CM a background correction is essential. The background is usually modeled as a linear, polynomial or spline function. The mode of such baseline is crucial for spectral curve-fitting, as all peak parameters are influenced by the baseline function. As manual baseline correction is very susceptible to subjectivity, a linear baseline with two control points is proposed to yield the most reproducible results. To increase the reproducibility of manual baseline correction, the control points, which define the slope of the linear baseline function, are placed in the spectral region of  $800$  to  $900\text{ cm}^{-1}$  and  $1800$  to  $1900\text{ cm}^{-1}$  for all 'crystallinity levels'.

In this study the peak- and curve-fitting software Fityk (Wojdyr (2010); <http://fityk.nieto.pl>) is used for deconvolution of the Raman spectrum of CM into the different components (D and G bands). However, any other peak fitting software can be used for this purpose. In our approach, the position and shape of the components are detected automatically by the software. If this is not successful, the components are located manually. Because Voigt- and Lorentzian-functions are most commonly used in RSCM-thermometry, all components are modeled here as Voigt- or Lorentzian-functions with unfixed peak parameters (FWHM, height, position, area and shape). For 'crystallinity level 1', five components (D1, D2, D3, D4, G) result in a good fit (e.g. Sadezky et al. (2005); Lahfid et al. (2010), see Fig. 2.1.1b). For 'crystallinity level 2', a good solution is obtained with 3 to 4 components (D1, D2, G, [D3]; see Beyssac et al., 2002a) and for 'crystallinity level 3' only two components (D1, G) are needed. The components are assigned sequentially to the model, which is also sequentially fitted to the data with by the Levenberg-Marquardt-method (Moré, 1978). If components are displaced during fitting, take unlikely shapes or are in any other way inconsistent, the solution is rejected. Subsequently, the component parameters have to be changed and the model has to be solved again. This procedure is repeated until a satisfying fit is obtained. The complete fitting protocol is available in Appendix S1.

Once the parameters of all components are obtained, different ratios can be calculated which correlate to the maximum metamorphic temperature (Beysac et al., 2002a; Rantitsch et al., 2004; Rahl et al., 2005; Baziotis et al., 2006; Aoya et al., 2010; Lahfid et al., 2010). The most common are the R1- and R2-ratio (Beysac et al. (2002a); Eq. 2.2.1 and Eq. 2.2.2) and the RA1- and RA2-ratio (Lahfid et al. (2010); Eq. 2.2.3 and Eq. 2.2.4). The R1-ratio corresponds to the height of the D1-component divided by the height of the G-component. The integrated area of the D1-component divided by the sum of the integrated areas of the D1-, D2- and G-component gives the R2-ratio. The sum of the integrated areas of the D1- and D4-component divided by the sum of the integrated areas of the D1-, D2-, D3-, D4- and G-components forms the RA1-ratio and the sum of the integrated areas of the D1- and D4-component divided by the sum of the integrated areas of the D2-, D3- and G-component is the RA2-ratio.

$$(2.2.1) \quad R1 = \left( \frac{D1}{G} \right)_{Intensity}$$

$$(2.2.2) \quad R2 = \left( \frac{D1}{(D1 + D2 + D3)} \right)_{Area}$$

$$(2.2.3) \quad RA1 = \left( \frac{(D1 + D4)}{(D1 + D2 + D3 + D4 + G)} \right)_{Area}$$

$$(2.2.4) \quad RA2 = \left( \frac{(D1 + D4)}{(D2 + D3 + G)} \right)_{Area}$$

**2.2.5. Systematic tests of the biasing factors.** In order to estimate the impact of different biasing factors, a series of experiments was designed. All experiments focus on selected factors while other factors are kept constant (see Table 2.2.2).

To compare the accuracy of the measurements of the different samples the percental fraction of the standard deviation of the mean, i.e. the relative standard deviations are used as a comparative index. According to the calibration range of the calibration curves of Beysac et al. (2002a) and Lahfid et al. (2010) it is calculated that an increment of 0.01 in the commonly used parameter-ratios R2, RA1 and RA2 (Beysac et al., 2002a; Lahfid et al., 2010) is equivalent to 4 °C, 12 °C, and 2 °C, respectively. These values estimate the significance of each experiment with respect to the initial calibration uncertainty which is  $\pm 50$  °C for Beysac et al. (2002a).

## 2.3. Results and discussion

### 2.3.1. Spectral processing bias.

Test 1 - Influence of curve-fitting strategy on parameter ratios. The factors that influence the fitting are the signal to noise ratio, the position and slope of the baseline, type of function used (Voigt, Lorentzian, Gaussian, etc.) and the start position and shape of the inserted peak. Lahfid et al. (2010) suggested that CM spectra of low-grade metamorphic rocks ('crystallinity level 1' of this study) should be fitted by Lorentzian functions and not by non-converging Voigt functions. When 'crystallinity level 2 and 3' samples are fitted, Voigt functions should be used according to Beysac et al. (2002a).

In this experiment, the amount of scatter in the parameter-ratios due to the fitting procedure is quantified. From the different 'crystallinity levels', single spectra with a high signal to noise

**Table 2.2.2.** Summary of the different tests. The influencing factors are listed in columns and the single experiments are shown in rows. The tested factors are emphasized by gray color and empty fields indicate irrelevant factors in the given test. 1 = single; M = multiple

Test	Influence of ...	Person	Sample (per cryst. level)	Spot	Measurement (per spot)	Type (function) of components	Baseline correction	Software	Sample prep. (chemically enriched CM vs. rock chips)	Orientation	Spectrometer
1	spectral fitting strategy	1	1	1	1	M	1				
2	baseline correction	1	1	1	1	1	M				
3	empirical scatter	1	1	1	M	1	1				
4	evaluation software	1	M	M	1	1	1	M			
5	personal fitting strategy	M	M	M	1	1	1	1			
6	sample preparation	1	M	M	1	1	1	1	M	1	1
7	sample heterogeneity	1	M	M	M	1	1	1	1	1	1
8	anisotropy	1	1	M	1	1	1	1	1	M	1
9	Raman system	M	1	M	1	1	1	1	1	1	M

ratio, are repeatedly (20 times) evaluated, using the above outlined fitting strategy. To exclude a variation due to the baseline correction, baseline-corrected spectra were used for each repetition. As the system often does not converge with automatically positioned Voigt functions, a strict fitting protocol has been used in which the functions are added manually (see Appendix S1). The same procedure has been performed with Lorentzian functions. Since the signal to noise ratio and slope of baseline is constant, the only variable is given by the initial conditions (i.e. position and shape of the components).

This experiment shows that in the 'crystallinity level 1', the fitting strategy has a significant influence on the parameter ratios. The repeated evaluation of the same spectrum, results in different RA1 and RA2-ratios when Lorentzian- and Voigt-functions are used (Table 2.3.1). Additionally, the variation in RA1- and RA2-ratios of the 20 evaluations of the same spectrum is greater when only Voigt-functions are used (Table 2.3.1).

In the 'crystallinity levels 2 and 3', the choice of the function does not influence the results (Table 2.3.1). This is in line with previous results by Lahfid et al. (2010). However, the Lorentzian and Voigt-fits of 'crystallinity level 2 and 3' samples result in basically the same R1 and R2 ratios. Thus, there seems to be no justification for changing from Lorentzian- to Voigt-functions for better crystalline samples. Instead, for the sake of linearity, we suggest to use the same function for processing samples of all 'crystallinity levels'. As the fits with Lorentzian functions perform well for low and high crystalline samples, this is the function type to be used for all the fits.

**Table 2.3.1.** Results of test 1: comparison of R1, R2, RA1 and RA2 of the three 'crystallinity levels' fitted with Lorentzian and with Voigt functions. r.s.d.: relative standard deviation.

	'Crystallinity level 1' - Lorentzian				'Crystallinity level 1' - Voigt			
Sample	R1	R2	RA1	RA2	R1	R2	RA1	RA2
L29	1,701	0,671	0,615	1.599	1.374	0,748	0,643	1,803
r.s.d. [%]	<b>0,1</b>	<b>0,0</b>	<b>0,0</b>	<b>0,0</b>	<b>10,2</b>	<b>3,4</b>	<b>1,7</b>	<b>4,6</b>
DB45	1,281	0,641	0,586	1.414	1.200	0,679	0,618	1,619
r.s.d. [%]	<b>0,0</b>	<b>0,0</b>	<b>0,0</b>	<b>0,0</b>	<b>2,3</b>	<b>0,8</b>	<b>0,2</b>	<b>0,6</b>
DB21	1,423	0,612	0,603	1.521	1.391	0,638	0,633	1,721
r.s.d. [%]	<b>0,0</b>	<b>0,0</b>	<b>0,0</b>	<b>0,0</b>	<b>1,1</b>	<b>0,5</b>	<b>0,2</b>	<b>0,6</b>
	'Crystallinity level 2' - Lorentzian				'Crystallinity level 2' - Voigt			
DB36	0,673	0,477	—	—	0,668	0,477	—	—
r.s.d. [%]	<b>0,0</b>	<b>0,0</b>	—	—	<b>0,0</b>	<b>0,0</b>	—	—
DB28	0,675	0,455	—	—	0,668	0,453	—	—
r.s.d. [%]	<b>0,0</b>	<b>0,0</b>	—	—	<b>0,0</b>	<b>0,0</b>	—	—
L1	0,391	0,371	—	—	0,39	0,371	—	—
r.s.d. [%]	<b>0,0</b>	<b>0,0</b>	—	—	<b>0,0</b>	<b>0,0</b>	—	—
	'Crystallinity level 3' - Lorentzian				'Crystallinity level 3' - Voigt			
DB16	0,016	0,048	—	—	0,016	0,049	—	—
r.s.d. [%]	<b>0,0</b>	<b>0,0</b>	—	—	<b>0,0</b>	<b>0,1</b>	—	—
DB28	0,019	0,064	—	—	0,019	0,065	—	—
r.s.d. [%]	<b>0,0</b>	<b>0,0</b>	—	—	<b>0,0</b>	<b>0,0</b>	—	—
TU2	0,025	0,073	—	—	0,025	0,073	—	—
r.s.d. [%]	<b>0,0</b>	<b>0,0</b>	—	—	<b>0,0</b>	<b>0,0</b>	—	—

Test 2 - Influence of baseline correction. The baseline correction significantly influences the results. As stated above, a linear baseline is more reproducible because only two control points are needed to define the line slope. It is tested here to what extent the varying position of the baseline points will influence the results. Three scenarios were tested by a Python (Pilgrim, 2004) script using the extensions Numpy and Scipy (Ascher et al., 2001; Oliphant, 2007): (1) the low wavenumber control point is fixed while the high wavenumber control point is moved. (2) Is the inversion of (1), (3) both control points are moved towards each other with the same increment. Every 10th data point was chosen as a new control point for baseline correction. Obviously, this procedure is only valid if the background can be approximated by a linear baseline. If the background is curved by fluorescence, the background cannot be described by a linear function and this procedure fails.

In every experiment, ten baselines were calculated. As the spectral resolution is ca.  $2 \text{ cm}^{-1}$ , the moving control point was varied in a range of about 200 wavenumbers (Fig. 2.3.1a-c).

Another frequently used type of baseline correction is represented by polynomial and spline functions, both result in curved baselines. To account for this, another script was used in which the first and last  $n$  data points, choosing  $n = \{10, 20, \dots, 100\}$ , were selected for 10 different spline interpolations (Fig. 2.3.1d). To compensate for noise effects the spectra were smoothed by using a penalized least squares approach (Eilers, 2003). For reasons given above (see Test 1), all fits were performed using Lorentzian functions. For 'crystallinity level 1 and 2', the experiments demonstrate that the model uncertainty of a linear baseline results in a ratio scatter below 1 % r.s.d. (relative standard deviation, Table 2.3.2).

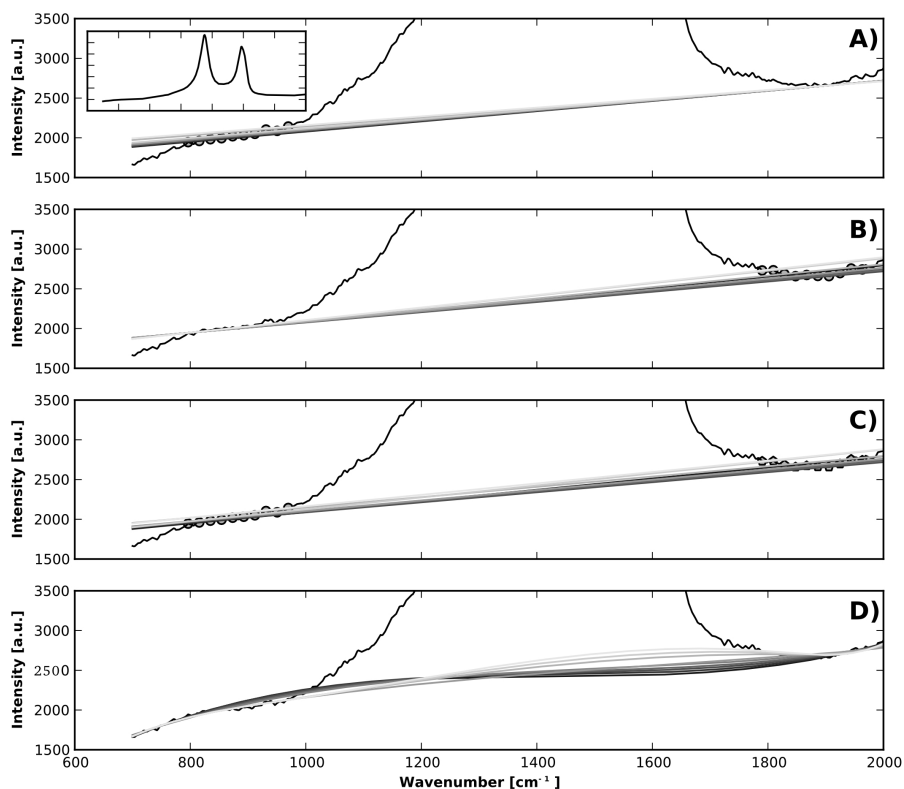


**Figure 2.3.1.** Results of test 2; the baseline correction is tested by varying the baseline slope and baseline type for a 'crystallinity level 1' spectrum. A) The low wavenumber side control point (circle) is variable. B) The high wavenumber side control point is variable. C) Both control points are variable. D) The same spectrum as in A, B and C but with curved baselines derived from spline interpolation. a.u. = arbitrary units. The inset in A) shows the complete spectrum, which has been used in A, B, C and D.

Only R2 of 'crystallinity level 3' shows a greater scatter. The curved baseline leads to an increased variation in RA1 and RA2 for 'crystallinity level 1' samples. For 'crystallinity level 2' the variation is negligible, and for 'crystallinity level 3' the r.s.d. of R2 is again high (Table 2.3.2).

Consequently, the reproducibility of the RA1 and RA2 ratios in 'crystallinity level 1' is higher when a linear baseline is used. Also, the positioning of control points within the same wavenumber intervals is of high importance.

Translating the R2 and RA1 ratios of the curved baseline corrected spectra into a metamorphic temperature using the equations given in Beyssac et al. (2002a) and Lahfid et al. (2010), the resulting temperature variation is about 5 – 10 °C for level 3 samples and about 20 – 30 °C for level 1 samples. For linear baseline corrected samples the temperature variation of R2 of level 3 samples is less than 5 °C and for RA1 of level 1 samples ca. 10 °C.

Test 3 - Reproducibility (repeated analysis of the same spot). In this test series, the total empirical scatter generated by the Raman system (i.e. minor variations in beam intensity, dispersion effects in the optical path, etc.) is examined. 10 spectra, each representing the mean of two acquisitions of thirty seconds, were recorded successively on the same spots and the evaluations were made strictly in the same way (using linear baseline and applying the evaluation protocol, see sections Test 1 - Influence of curve-fitting strategy on parameter ratios and Test 2 - Influence of baseline correction).

From Figure 2.3.2 it is obvious that the behavior of 'crystallinity level 1' differs from the more ordered material. The Raman parameters of the less ordered organic material are highly



**Table 2.3.2.** Results of test 2: influence of baseline correction. R1, R2, RA1 and RA2 ratios for the three 'crystallinity levels' with varying linear baselines and spline interpolated, curved baselines. Cryst. Lvl: 'Crystallinity level', r.s.d.: relative standard deviation.

	Cryst. Lvl 1				Cryst. Lvl 2		Cryst. Lvl 3	
	R1	R2	RA1	RA2	R1	R2	R1	R2
Low wavenumber side control point variable								
Average	1,432	0,614	0,602	1,512	0,597	0,437	0,016	0,034
r.s.d. [%]	<b>0,2</b>	<b>0,1</b>	<b>0,4</b>	<b>1,0</b>	<b>0,1</b>	<b>0,1</b>	<b>0,6</b>	<b>6,3</b>
High wavenumber side control point variable								
Average	1,440	0,616	0,607	1,542	0,596	0,437	0,016	0,038
r.s.d. [%]	<b>0,6</b>	<b>0,5</b>	<b>0,3</b>	<b>0,8</b>	<b>0,1</b>	<b>0,2</b>	<b>0,4</b>	<b>8,8</b>
Both control points variable								
Average	1,441	0,617	0,605	1,530	0,597	0,437	0,016	0,036
r.s.d. [%]	<b>0,6</b>	<b>0,5</b>	<b>0,3</b>	<b>0,7</b>	<b>0,1</b>	<b>0,2</b>	<b>0,6</b>	<b>12,1</b>
Curved baseline – Spline interpolation								
Average	1,435	0,613	0,595	1,469	0,595	0,435	0,016	0,045
r.s.d. [%]	<b>0,9</b>	<b>1,0</b>	<b>2,1</b>	<b>5,2</b>	<b>0,0</b>	<b>0,2</b>	<b>0,7</b>	<b>14,4</b>

sensitive to the absorbed laser energy. The RA1 and RA2 ratios of 'crystallinity level 1' decrease during the first three measurements; after those, the data scatter randomly. This phenomenon was already detected by Quirico et al. (2005) who suggested that most likely photo-oxidation of the sample controls the fluorescence and Raman signal of the sample, even if very low energy is applied. Additionally, they demonstrated that the signal (fluorescence + Raman) stabilizes faster when measured in an inert (Argon) atmosphere. However, the changing fluorescence cannot be ruled out completely (Quirico et al., 2005).

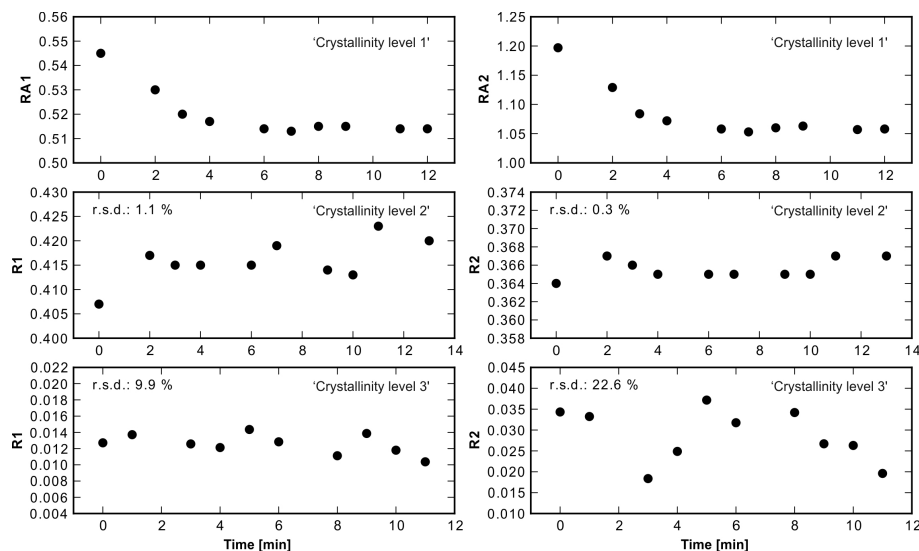


**Figure 2.3.2.** Results of test 3; the reproducibility by repeated analysis. The subplots show time series of the RA1, RA2, R1 and R2 ratios (according to Beyssac et al., 2002a; Lahfid et al., 2010) for samples of the three 'crystallinity levels'. All measurements were performed consecutively at the same spot. The first 3 measurements of 'crystallinity level 1' are influenced by luminescence that changes strongly with time, but afterwards the detected ratios are basically stable.

The time-dependent change in RA1- and RA2-ratio of 'crystallinity level 1' samples demonstrates that the Raman analysis of such organic material needs special care. Even in case of low laser energy, the possible transformation of the organic material or the declining fluorescence

**Table 2.3.3.** *Results of test 3: Empirical scatter of repeated measurements.*

	Scatter generated by spectral decomposition with linear baseline (see Test 2)		Scatter generated by repeated analysis of the same spot (with linear baseline correction)	
	Cryst. Lvl. 2	Cryst. Lvl. 3	Cryst. Lvl. 2	Cryst. Lvl. 3
R1 r.s.d. [%]	0,1	0,6	1,1	9,9
R2 r.s.d. [%]	0,2	12,1	0,3	22,6

change the signal by time, resulting in highly affected results by repeated measurements on the same spot. Therefore, the empirical scatter of 'crystallinity level 1' material cannot be determined by repeated analyses on the same spot.

In level 2 and 3 samples, the parameter ratios (R1, R2) do not change significantly with time (Fig. 2.3.2). Thus, the variability of the fitting results is a reliable measure of the reproducibility by repeated analysis. However, the scatter generated by the spectral decomposition (incl. baseline correction) is included and forms an indistinguishable part of the total scatter. Thus, the left panel of Table 2.3.3 shows the scatter of spectral decomposition (Test 1 and 2), while the right panel shows the total empirical scatter. The lesson of this experiment is that the evaluation of level 3 is extremely sensitive to minor modifications in the fitting procedure (for instance baseline correction).

This artificial uncertainty, which is introduced by spectral processing, is in the range of ca. 20 % r.s.d. of R2. Translating the calculated R2-ratios into temperature (Beysac et al., 2002a) results in a spread of ca. 10 °C for the same measuring spot and adds to the calibration uncertainty of the RSCM geothermometer.

Test 4 - Influence of spectral evaluation software on parameter ratios. In this experiment, thirteen samples from low to high 'crystallinity' were measured at five random spots holding the measuring conditions and the background correction constant. The spectra were evaluated by three different computer programs: Fityk (Wojdyr, 2010), Labspec 5 (Horiba Scientific, Edison, New Jersey 08820, USA) and Peakfit (SeaSolve Software, Inc, Framingham, Massachusetts 01702, USA). Thus, differences in R1, R2, RA1 and RA2 ratios are generated exclusively by the used evaluation software and applied fitting strategy. The contribution to the scatter from sample heterogeneity can be neglected, because identical spectra were evaluated.

From Figure 2.3.3 it is evident that there are essentially no differences in R1 and R2 for the whole sample set. In case of RA1 and RA2, Fityk generates systematically higher ratios than Labspec and Peakfit; however, the differences are well within one standard deviation (except for sample L29).

Test 5 - Influence of operator's personal fitting strategy on parameter ratios. In this test the personal bias in curve-fitting is analyzed. Therefore, the same five spectra per sample obtained from DB21, DB36 and L45 were handed to four different operators. Spectral processing was first conducted by the operators without any recommendation and afterwards the same spectra were processed by the operators according to the recommended fitting protocol (see Appendix S1). The spectral processing was performed once with Lorentzian functions only and once with Voigt functions only. That is for each sample five Lorentzian and five Voigt R1, R2, RA1 and RA2 values were derived by each operator. The five values of a given ratio were summed and then the absolute difference of the sums of two operators for a given sample was used for comparison. This approach is valid since identical spectra were evaluated and if the operators produced the same ratios the

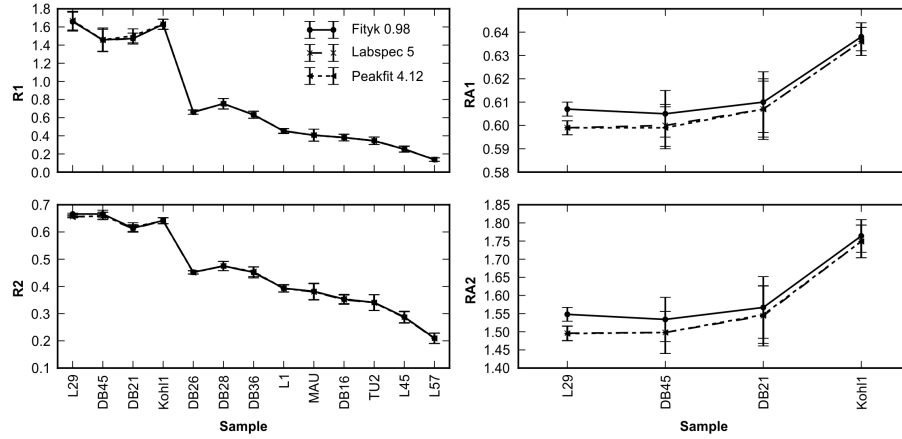


**Figure 2.3.3.** Results of test 4; the influence of spectral evaluation software. Comparison of the  $R1$ ,  $R2$ ,  $RA1$  and  $RA2$  ratios (Beysac et al., 2002a; Lahfid et al., 2010) determined with different programs. The sample 'crystallinity' increases from left to right. The error bars indicate one standard deviation of five measurements.

absolute difference between these operators must be zero. It can be deduced from Table 2.3.4 that there are variable and sometimes significant differences between the operators. The summed absolute differences are reduced by the spectral processing protocol when only Voigt functions are used (Table 2.3.4). If only Lorentzian functions are used a slight increase in the differences can be observed. This is most likely due to differences in the baseline correction performed by the operators, because if the type of function is the only variable, no change in the parameter ratios is observed in the case of Lorentzian functions, which is shown in section Test 1 - Influence of curve-fitting strategy on parameter ratios.

Especially Figure 2.3.4 shows that the differences between the operators can be significant (see insert A in Fig. 2.3.4). That is for a given spectrum the difference in  $RA1$  can be as high as 0.05 (Fig. 2.3.5) which would translate to ca. 60 °C. The differences in  $R2$  of 'crystallinity level 2' samples between the operators are in the range of about 0.01 to 0.03 (Fig. 2.3.4) which corresponds to a temperature range of ca. 4 °C to 12 °C.

These observations imply that the way of spectral processing is a key feature in the achievement of parameter-ratios and should be defined very precisely. At the same time it is obvious that the used protocol needs refinement which is documented, for instance by the increase in the differences for Lorentzian functions.

### 2.3.2. Sources of biasing factors intrinsic to the carbonaceous material.

Test 6 - Influence of sample preparation on parameter ratios. The goal of this test is to check if there are deviations in the parameter ratios due to sample preparation. Untreated rock fragments and HCl-HF-digestion enriched CM were compared. The sample set of the Thuringian Forest (Table 2.2.1) was selected for this test. These black shales experienced sub-greenschist facies metamorphism (Kunert, 1999). Therefore, the curve-fitting method after Lahfid et al. (2010) with five Lorentzian components was used.

Each sample was measured directly as rock fragment with a laser orientation perpendicular to the schistosity. This was done because it is assumed that the typically planar CM-particles settle parallel to the glass slide surface, resulting in a laser orientation more or less perpendicular to the CM.

**Table 2.3.4.** The sub-tables A and B show the sums of the absolute differences for the R1, R2, RA1 and RA2 ratios between the four operators. In each row the ratios of two operators are compared. If the sum of an operator is not available, the values (printed in italics) of the compared operator are not used in the total sum. n.a.: not available

A)	Sum of differences - 'crystallinity' level 1 – Voigt before protocol		Sum of differences - 'crystallinity' level 1 – Voigt after protocol		Sum of differences - 'crystallinity' level 1 – Lorentz before protocol		Sum of differences - 'crystallinity' level 1 – Lorentz after protocol	
	Compared operators	RA1	RA2	RA1	RA2	RA1	RA2	RA1
1 – 2	n.a.	n.a.	<i>0,124</i>	<i>0,994</i>	n.a.	n.a.	<i>0,021</i>	<i>0,142</i>
1 – 3	0,056	0,402	0,005	0,019	0,041	0,257	0,041	0,275
1 – 4	0,090	0,610	0,021	0,153	0,030	0,190	0,018	0,116
2 – 3	n.a.	n.a.	<i>0,129</i>	<i>0,975</i>	n.a.	n.a.	<i>0,020</i>	<i>0,133</i>
2 – 4	n.a.	n.a.	<i>0,145</i>	<i>1,148</i>	n.a.	n.a.	<i>0,039</i>	<i>0,258</i>
3 – 4	0,033	0,208	0,016	0,172	0,012	0,080	0,059	0,391
Sum (excluding n.a. and italics)	<b>0,180</b>	<b>1,220</b>	<b>0,042</b>	<b>0,344</b>	<b>0,083</b>	<b>0,527</b>	<b>0,119</b>	<b>0,782</b>
B)	Sum of differences - 'crystallinity' level 2 – Voigt before protocol		Sum of differences - 'crystallinity' level 2 – Voigt after protocol		Sum of differences - 'crystallinity' level 2 – Lorentz before protocol		Sum of differences - 'crystallinity' level 2 – Lorentz after protocol	
	Compared operators	R1	R2	R1	R2	R1	R2	R1
1 – 2	0,047	0,185	0,002	0,001	n.a.	n.a.	0,025	0,064
1 – 3	0,075	0,007	0,033	0,101	0,031	0,061	0,072	0,080
1 – 4	0,064	0,024	0,036	0,006	0,024	0,064	0,041	0,033
2 – 3	<i>0,028</i>	<i>0,192</i>	<i>0,036</i>	<i>0,101</i>	n.a.	n.a.	<i>0,047</i>	<i>0,016</i>
2 – 4	<i>0,017</i>	<i>0,161</i>	<i>0,034</i>	<i>0,007</i>	n.a.	n.a.	<i>0,066</i>	<i>0,031</i>
3 – 4	0,011	0,031	0,070	0,094	0,008	0,003	0,114	0,047
Sum (excluding n.a. and italics)	<b>0,243</b>	<b>0,600</b>	<b>0,211</b>	<b>0,310</b>	<b>0,062</b>	<b>0,129</b>	<b>0,227</b>	<b>0,159</b>

From Figure 2.3.6 it is evident that HF-samples produce higher RA ratios, i.e. RA1 is about 0.01 and RA2 is about 0.1 higher, which translates to temperature differences of ca. 13 °C and 22 °C, respectively. Furthermore, the standard deviations of the HF-samples are slightly smaller. Even if the surface of the rock fragments follows the schistosity it still has a given roughness which might affect the orientation of the CM particles to the laser beam and thus explain a larger spread of parameter ratios. Furthermore, it is speculated that the systematically higher, less scattered RA ratios of the HF-samples might be due to reduction of functional groups or lower clay mineral content due to hydrofluoric acid treatment. It has been shown by Villanueva et al. (2008) that 'clay' introduces a strong Raman background and Ahn et al. (1999) showed that carbonaceous material can be interstratified within illite. Thus, HF-treatment is thought to minimize strong Raman background from CM interconnected with clay minerals.

Test 7 - Influence of sample heterogeneity on parameter ratios. Sample heterogeneity in terms of RSCM is reflected in the variability of a given parameter ratio. Supposedly the different chemical composition of the precursor organic materials yields different Raman spectra (Kribek et al., 1994; Valentim et al., 2004; Guedes et al., 2010). Considering that the organic content of a given sedimentary rock is a mixture of two or more maceral groups (Hutton et al., 1994), a spread of parameter ratios will result. This has a greater impact on parameter ratios of CM dispersed in low-grade metamorphic rocks. Furthermore, recycled detrital organic grains can carry signals of a higher degree of organic maturation from the sediment source areas. Therefore, sample heterogeneity is combining various factors and has to be considered.

As shown in Test 1, the scatter due to spectral evaluation is basically excluded if the fitting is performed with Lorentzian functions only and scatter due to variation of the linear baseline is low (Tables 2.3.1 and 2.3.2) for 'crystallinity levels 1 and 2'. Thus, the scatter resulting from

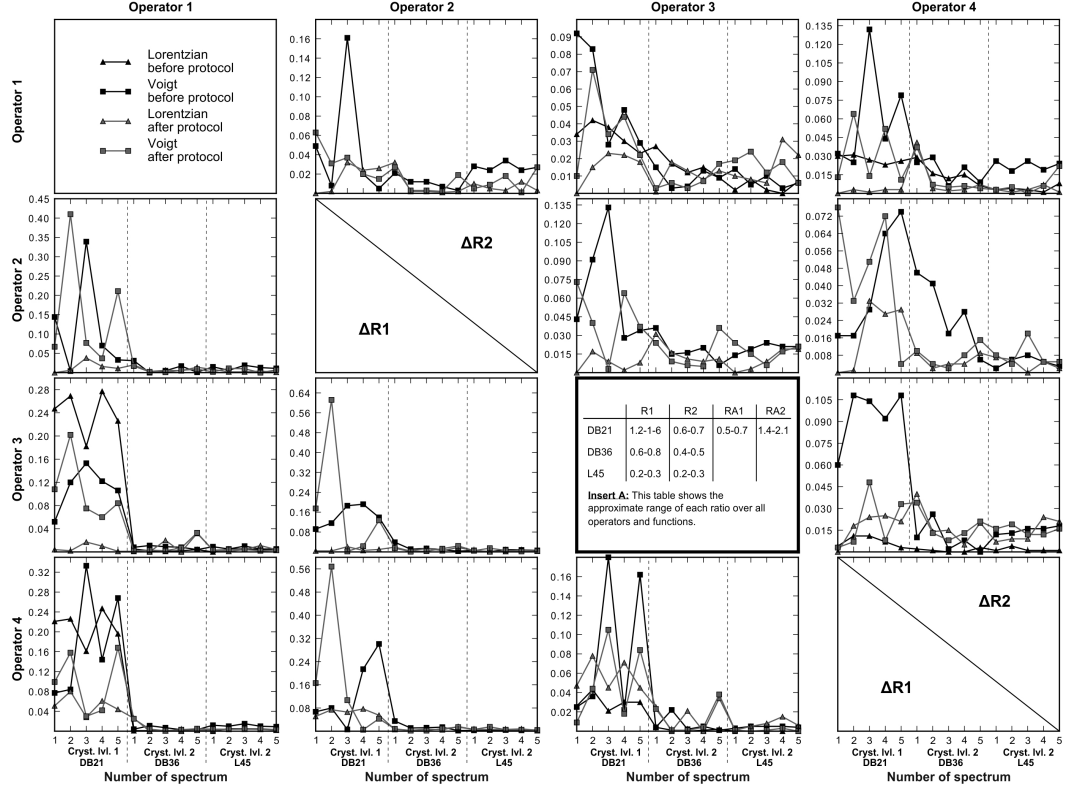


**Figure 2.3.4.** Results of test 5; this matrix plot shows the influence of operator's personal fitting strategy. The lower left triangle of the matrix shows the absolute differences in R1 (termed  $\Delta R1$ ) and the upper right triangle shows the absolute differences in R2 (termed  $\Delta R2$ ) between the operators (e.g. column one gives  $\Delta R1$  between operator 1 and the others, while row one gives  $\Delta R2$  between operator 1 and the others). Each plot in the matrix represents the absolute differences between two operators for the given 15 spectra, which are listed along each x-axis. In most cases, especially for 'crystallinity level 1', the differences are reduced by the protocol. Insert A shows the range of the ratios in order to the estimation of the impact of the personal bias.

multi grain analysis is mainly inherited by the sample heterogeneity itself. To estimate the sample heterogeneity 30 randomly chosen sample spots were analyzed in four HF-HCl treated CM samples of 'crystallinity level 2'. For each sample spot five successive spectra (each the average of five accumulations with a duration of ten seconds) were recorded to estimate the total empirical scatter.

The mean square of weighted deviates (MSWD) is used to quantify sample heterogeneity. The MSWD is widely used in geochronology to determine if the observed scatter in a data set is consistent with the calculated analytical uncertainty of the individual measurements (Powell et al., 2002). It is a measure of the ratio of the observed scatter of the data points ( $t_i$ ) around the mean value ( $t_m$ ) to the expected scatter from the assigned errors ( $\sigma_i$ ) (Vermeesch, 2010). If the assigned errors are the only cause of scatter, the MSWD will tend towards unity and '*MSWD values much greater than unity generally indicate either underestimated analytical errors, or the presence of non-analytical scatter*' (Ludwig, 2003).

$$(2.3.1) \quad MSWD = \frac{1}{n-1} \sum_{i=1}^n \frac{(t_i - t_m)^2}{\sigma_i^2}$$

By solving equation 2.3.1 where  $t_i$  is the arithmetic mean of the repeated measurements in one grain,  $t_m$  is the mean of all grains and  $\sigma_i$  is the standard deviation of the data obtained in

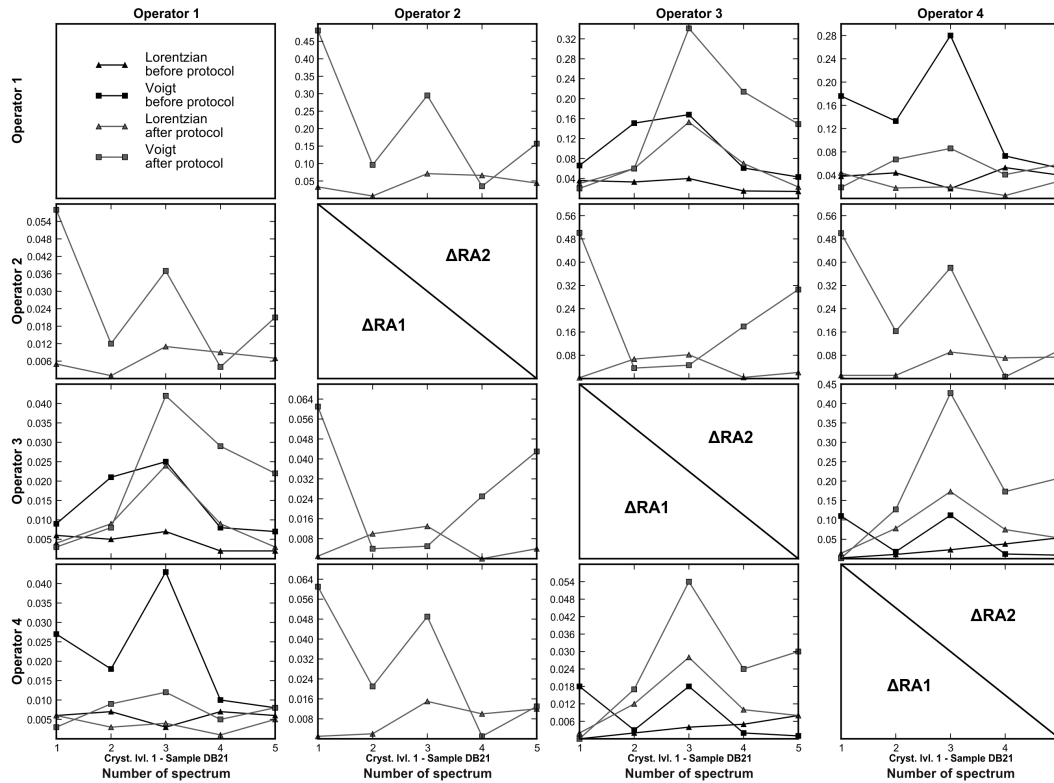


**Figure 2.3.5.** Results of test 5; this matrix plot shows the influence of operator's personal fitting strategy. The lower left triangle of the matrix shows the absolute differences in RA1 (termed  $\Delta RA1$ ) and the upper right triangle shows the absolute differences in RA2 (termed  $\Delta RA2$ ) between the operators (e.g. column one gives  $\Delta RA1$  between operator 1 and the others, while row one gives  $\Delta RA2$  between operator 1 and the others). Each plot in the matrix represents the absolute differences between two operators for the given 5 spectra of a 'crystallinity' level 1 sample. The results are ambiguous as in some cases the differences are reduced and in other cases increased by the use of the protocol. The range of the ratios is given in insert A in figure 5.

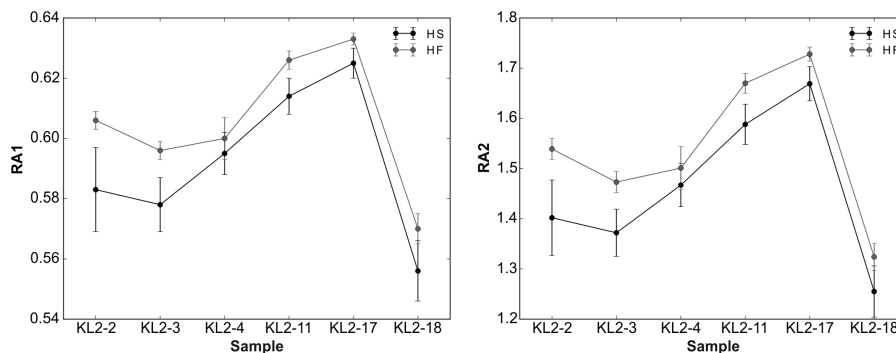


**Figure 2.3.6.** Results of test 6; the influence of sample preparation. The RA1 and RA2 ratios of the hydrofluoric acid treated samples (HF) are systematically higher and have a lower standard deviation than the ratios of the hand specimen (HS).

one grain, it is estimated to which extend the overall scatter is influenced by the empirical scatter. Figure 2.3.8 shows the R1 and R2 ratios plotted in measuring order and their associated MSWD. MSWD values are remarkably high (MSWD = 47 – 318, Figure 2.3.8), indicating the presence of non-analytical scatter in all samples, that is thought to be mainly caused by sample heterogeneity.

**Table 2.3.5.** Comparison of R1 and R2 ratios of disperse and large particulate CM. (5 measurements per sample). r.s.d.: relative standard deviation.

Sample	large particulate CM				disperse CM			
	R1	r.s.d. [%]	R2	r.s.d. [%]	R1	r.s.d. [%]	R2	r.s.d. [%]
L29	—	—	—	—	0,96	<b>7</b>	0,60	<b>16</b>
DB45	0,01	<b>137</b>	0,06	<b>143</b>	1,22	<b>7</b>	0,66	<b>9</b>
DB21	0,34	<b>104</b>	0,42	<b>48</b>	1,30	<b>5</b>	0,64	<b>3</b>
Kohl1	1,42	<b>3</b>	0,63	<b>0</b>	1,67	<b>8</b>	0,68	<b>3</b>
DB26	0,18	<b>63</b>	0,25	<b>49</b>	0,78	<b>4</b>	0,50	<b>3</b>
DB28	0,19	<b>62</b>	0,26	<b>58</b>	0,61	<b>26</b>	0,44	<b>14</b>
DB36	0,01	<b>100</b>	0,02	<b>106</b>	0,62	<b>8</b>	0,45	<b>4</b>
MAU	0,22	<b>33</b>	0,26	<b>17</b>	0,36	<b>19</b>	0,34	<b>11</b>
L1	0,35	<b>18</b>	0,34	<b>8</b>	0,46	<b>53</b>	0,39	<b>24</b>
DB16	0,15	<b>51</b>	0,20	<b>46</b>	0,35	<b>14</b>	0,33	<b>8</b>
TU2	0,15	<b>115</b>	0,18	<b>79</b>	0,27	<b>8</b>	0,29	<b>6</b>
L45	0,08	<b>94</b>	0,14	<b>59</b>	0,21	<b>13</b>	0,25	<b>8</b>
L57	0,03	<b>79</b>	0,08	<b>50</b>	0,12	<b>13</b>	0,18	<b>11</b>

In several acid treated CM samples the heterogeneity is already well detectable by reflected light microscopy. Frequently two particle types of CM are present. 'Large particulate CM' is formed by particles with a grain size range of ca. 20 to 100  $\mu\text{m}$  and is a bright grey to white reflective light appearance (Fig. 2.3.7). In contrast, 'disperse CM' has a grain size of less than 10  $\mu\text{m}$  and is of dark grey colour in reflected light (Fig. 2.3.7).

Table 2.3.5 shows the R1 and R2 ratios with associated relative standard deviation of large particulate and disperse CM for the entire sample set. It is obvious that the Raman parameter ratios of the large particulate CM differ strongly from the disperse CM of the same sample and the scatter in R1 and R2 of large particulate CM is much higher. A similar observation is made in the rock fragments of the Thuringian black shales comparing coarse organoclasts and dispersed CM; however the differences of the parameter ratios are minor (ca. 0.01 in RA1).

These observations imply that one has to be aware that already matured, detrital CM populations may be present in a sample, which is also an important issue in vitrinite reflectance measurements (e.g. Nzoussi-Mbassani et al., 2005). Because of the irreversibility of the thermal maturation of CM, the population of lowest maturity is usually chosen (Nzoussi-Mbassani et al., 2005). In this case, a proper number of observations (Raman spectra) is necessary to identify the different populations. Aoya et al. (2010) proposed a minimum of ca. 25 measurements per samples to reflect sample heterogeneity.

Test 8 - Influence of structural anisotropy on parameter ratios. Due to its strong structural anisotropy, Raman spectra of graphite and very well crystalline CM depend on the orientation of

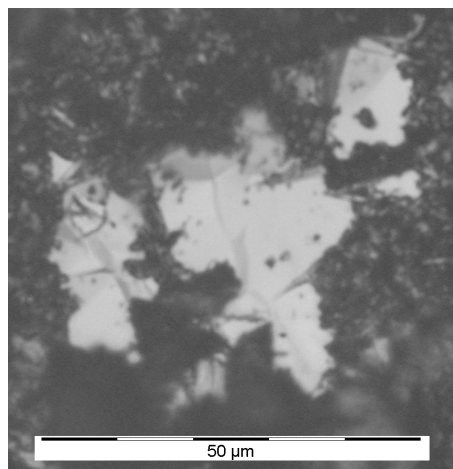


**Figure 2.3.7.** Photomicrograph showing large particulate CM (light grey) surrounded by fine-grained disperse CM (dark grey) in HCl-HF concentrated organic material deposited on a glass slide.

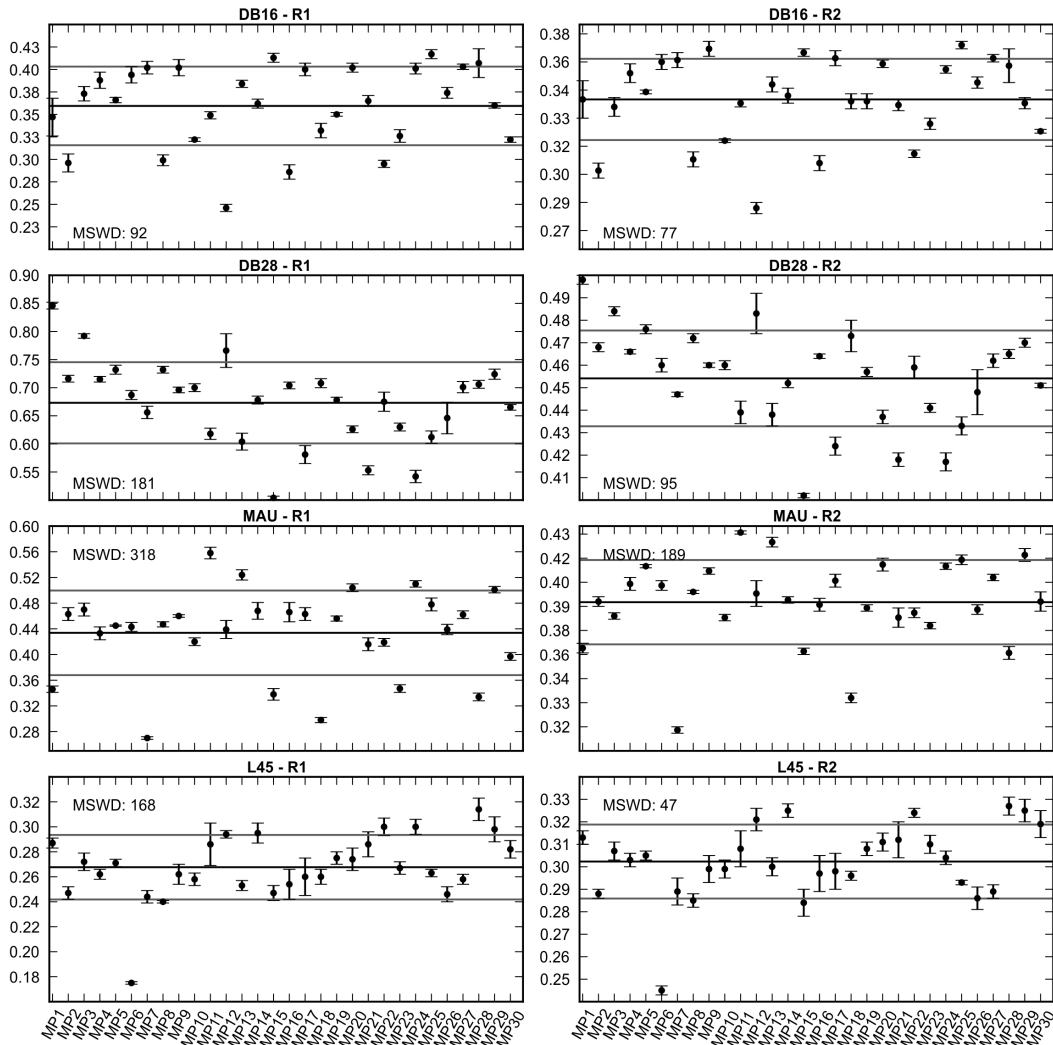


**Figure 2.3.8.** Results of test 7; the influence of sample heterogeneity. The mean square weighted deviation (MSWD, according to Vermeesch, 2010) has been calculated for four samples in the 'crystallinity level 2'. Five spectra were recorded at each of the 30 randomly chosen measuring points (MP). If the value of the MSWD is high then the overall scatter of the points is dominated by the sample heterogeneity. If the MSWD-value is low then uncertainty of the individual measuring points represents well the overall scatter of the population. The solid black line represents the average of all measurements of one sample and the solid grey lines are the associated positive and negative standard deviation. Error bars represent the standard deviation of individual measuring points.

the laser beam to the crystallographic c-axis (Katagiri et al., 1988; Wang et al., 1989; Compagnini et al., 1997). Katagiri et al. (1988) showed that the intensity ratio of the D1- and G-band is minimal when the incident laser beam is parallel to the c-axis of the graphitic material and the ratio is at its maximum when the laser beam is perpendicular to the c-axis.

Natural graphite occurs usually as microcrystallites of a few 100 nm length (Beyssac and Lazzeri, 2012). The optical c-axis of micro-crystallites enclosed in rocks is generally orientated perpendicular to the main fabric (Beyssac and Lazzeri, 2012). To quantify the effect of coherent microcrystallite orientation on the R1 and R2 ratios in natural samples, a sample was rotated directly under the laser beam.

To check if there are systematic deviations due to polarization effects a spectrum with linear and a spectrum with circular polarized laser light was recorded at each measuring point. From



a sample (DB26) with well-developed schistosity a rock cylinder of 6 mm diameter was drilled parallel to the schistosity. The cylinder was then mounted into a sample holder and rotated by an increment of  $20^\circ$  underneath the laser beam. Thus, the orientation of the CM with respect to the laser beam is varied and the change in R1 and R2 ratios is observed as a function of schistosity orientation.

In this experiment, the generation of structural defects in the CM by the drilling of the rock core has to be considered. However, Crespo et al. (2006) showed that the graphitic structure is insignificantly changed by short grinding periods ( $<10$  min). We therefore assume that the water-cooled, gentle drilling process applied here has generated insignificant modification of CM on the cylinder surface of the drilled rock core.

Measurements were performed across five sections along the sample cylinder and the mean of R1 and R2 of the five measurements for each  $20^\circ$ -step was calculated (Fig. 2.3.9). It is obvious that the R1 and R2 ratios increase when the CM is rotated from  $0^\circ$  to  $90^\circ$  (i.e. from a perpendicular orientation to a parallel orientation). This indicates a virtual decrease in 'crystallinity'. The expected increase from 0 to  $90^\circ$  is followed by a decrease in R1 and R2 from about  $100$  to  $180^\circ$  which implies a better virtual 'crystallinity' which is again the result of a perpendicular orientation of the CM to the laser beam. Also, the polarization of the laser light does not lead to systematic differences in the R1 and R2 ratios (Fig. 2.3.9). However, due to a high standard deviation (Fig. 2.3.9) the significance of this preliminary test is low.

Consequently, it is deduced that sample anisotropy varies the R1 ratio by ca. 0.1 and the R2 ratio by ca. 0.04 (ca.  $15^\circ\text{C}$ ). Of course, this is only valid for the sample tested here. Nevertheless, this test points out that sample orientation should be kept in mind when performing Raman measurements on higher crystalline carbonaceous materials.

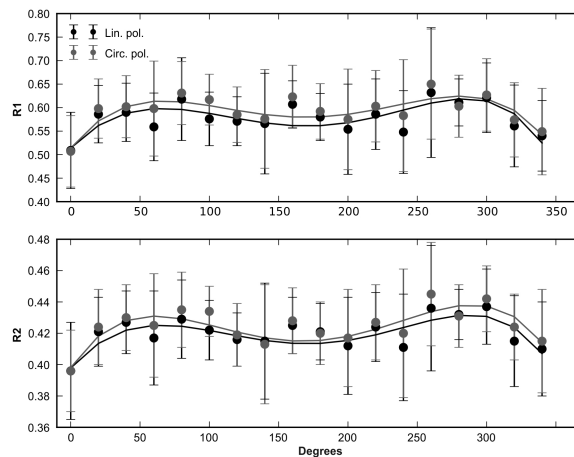


**Figure 2.3.9.** Results of test 8; the influence of sample preparation. At  $0^\circ$  and  $180^\circ$  the laser beam is perpendicular to the schistosity and at  $90^\circ$  and  $270^\circ$  the orientation is parallel. The solid lines are weighted polynomial regressions which represent the trend in the data better. Lin. pol. = linear polarized laser light; circ. pol. = circular polarized laser light.

### 2.3.3. Sources of variation intrinsic to the experimental design and Raman system.

Test 9 - Influence of Raman systems on parameter ratios (interlaboratory comparison). As many different configurations of Raman systems exist, a small scale interlaboratory comparison

was performed to elucidate the variation in results (i.e. R1, R2) with respect to the Raman instruments and their major components, for instance the spectral grating.

The effect of different gratings of the Horiba Jobin Yvon LabRAM HR800-UV spectrometer in Göttingen on the Raman spectrum of sample DB26 is shown in Figure 2.3.10. For comparison the intensities are normalized to the height of G band. It is demonstrated that a finer grating generates a more intense D1-band, which leads to differences in the R1 and R2 ratios. Spectrum a) in Figure 2.3.10 gives 0.52 and 0.39 while spectrum b) gives 0.66 and 0.44 R1 and R2 ratios, respectively. This indicates, if a linear relation between parameter ratio and grating is assumed, that finer gratings produce higher ratios and that a difference in grating of 1800 1/mm generates a shift in R1 and R2 of 0.14 and 0.05, corresponding to a temperature range of up to 20 °C.

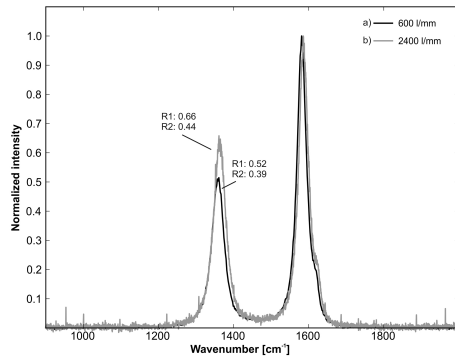


**Figure 2.3.10.** Results of test 9; Raman spectra of the same measuring spot acquired by different gratings. The R1-ratios of spectrum a) and b) are 0.52 and 0.66 and the R2-ratios are 0.39 and 0.44.

Hannover, Germany) also equipped with a 532 nm laser, a spectral grating of 1200 1/mm and a 50x objective with a NA of 0.75 and a Horiba Jobin Yvon LabRAM HR800 UV (Dept. of Mineralogy, Eötvös Loránd University, Budapest) also with a 532 nm laser, a spectral grating of 600 1/mm and a 100x objective with a NA of 0.9.

To obtain a rough estimation of the sample heterogeneity, five spots were measured per sample with each system. As the difference in grating is 600 and 1200 1/mm for the three spectrometers tested, a difference of about 0.046 (R1) and 0.017 (R2) is expected for 600 1/mm and 0.093 (R1) and 0.033 (R2) for 1200 1/mm. Comparing the R1 and R2 ratios of the three samples, a far greater difference between the three spectrometers is evident, especially for the R1 ratio (Fig. 2.3.11). Although some sample heterogeneity must also be considered here, the dominant reason for the observed variation must be the different spectrometer compounds like gratings or CCD cameras. Consequently, this test demonstrates that some deviation in the Raman spectroscopic results of CM between different Raman systems cannot be avoided because of the large diversity of different components in the spectrometers that influence the spectral resolution, the signal intensity and peak positions.

## 2.4. Conclusions and outlook

The most important information derived from our study of Raman spectroscopy of carbonaceous material can be summarized as follows:

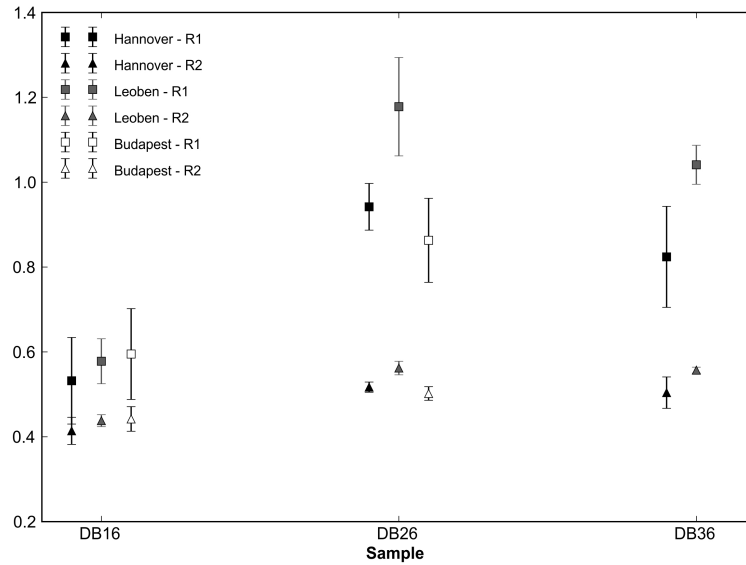


**Figure 2.3.11.** Results of test 9; the spread of the R values obtained by the interlaboratory comparison. The same excitation wavelength (532 nm), but different Raman systems were used in the laboratories. Depending on the sample, significant differences are observed between the laboratories, especially in the R1 ratio.

- (1) Spectral curve-fitting induces significant variation. The amount of variation depends on the degree of 'crystallinity' (i.e. structural order) of the CM sample and is highest in low crystalline material. The software used for curve-fitting does not influence the results.
- (2) Personal bias has a significant impact on the results. Thus, a standardized fitting procedure is proposed (see supporting information) for studies involving RSCM.
- (3) In very low-grade, organic rich metasediments the separation of CM by hydrochloric and hydrofluoric acid treatments generates a systematic shift in peak ratios when compared to measurements performed on untreated rock samples.
- (4) Sample heterogeneity appears in a high proportion of samples; the scatter of the Raman parameters in CM grain populations is much higher than the variation of measurements within a grain. This represents a significant source of error in RSCM geothermometry and can be controlled only by enhanced number of measurements and by avoiding the detrital grains that carry inherited, high maturation signal.
- (5) Spectra of the same sample recorded with different Raman systems show distinct contrasts, due to differences in Raman system components.
- (6) When measuring higher grade crystalline samples (level 2 and level 3), the structural anisotropy of CM needs to be considered.

The presented results of nine experiments prove a rather high empirical deviation between RSCM geothermometrical data generated by different Raman instruments and data processing procedures. Different laser excitation wavelength generate even more deviation (Vidano et al., 1981; Wang et al., 1990; Matthews et al., 1999; Sato et al., 2006).

The total error due to the listed biasing factors is difficult to assess, but from the conducted experiments it can be estimated that the error, especially for higher 'crystalline' samples, is in the range of 10 – 30 °C if the temperature is derived from the R2-ratio. For the RA1- and RA2-ratio, the error range is even larger. For the R2-ratio this error range is below the given error of  $\pm 50$  °C of the RSCM-thermometer (Beysac et al., 2002a). However, if the same calibration is used by

different laboratories, the above stated biasing factors will influence the R2-ratios and thus the temperature estimates may differ approximately by the above-stated error range.

More consistent results can be expected if samples, measurements and thermometer calibrations are performed with the same instrumental setup and data processing procedure. Therefore, we suggest to improve the RSCM method by developing and distributing a natural sample series that can be used to calibrate a laboratory. When the calibration is based on measurements of reference materials any instrumentation related bias or drift can be corrected and even different excitation wavelengths could be used. In this case every laboratory can generate its own calibration equation before and after a measuring session. Such a calibration system is used and widely accepted for stable isotope studies (V-SMOW, Gonfiantini, 1978), for fission-track and in-situ U/Pb geochronology (Hurford and Green, 1983; Compston et al., 1984; Frei and Gerdes, 2009) or for the determination of 'illite crystallinity' (Kisch et al., 2004). A reference material series is under preparation. The criteria used for selection of the reference materials are (1) independent and well constrained maximum temperature, (2) fresh character, (3) homogeneity of the CM particles, and (4) availability of the sample locality. This will be reported in detail in a coming communication (part 2).

## IFORS - Iterative fitting of Raman spectra

Authored by N. K. Lünsdorf and J. O. Lünsdorf and published as: *Evaluating Raman spectra of carbonaceous matter by automated, iterative curve-fitting*. International Journal of Coal Geology, 2016, 160-161, p. 51 - 62

### 3.1. Introduction

Raman spectroscopy is a widespread analytic method in geosciences. It is, for instance, used for mineral identification (Bartholomew, 2013; Bishop et al., 2004; Das and Hendry, 2011; Groppo et al., 2006; Haskin et al., 1997; Hope et al., 2001; Jehlička et al., 2009; White, 2009), analysis of fluid inclusions (Burke, 2001; Frezzotti et al., 2012; Guillaume et al., 2003; Pasteris et al., 1988; Rosso and Bodnar, 1995; Rosasco and Roedder, 1979; van den Kerkhof and Olsen, 1990), analysis of phase transitions in relation to pressure and temperature (Auzende et al., 2004; Daniel et al., 1995; Gillet, 1996; Gunasekaran and Anbalagan, 2007; Lin, 2003; Palmer et al., 1994; Salje et al., 1993), to estimate coal rank (Hinrichs et al., 2014), examination and characterization of coal macerals (Guedes et al., 2010; Morga, 2011) and coke (Morga et al., 2015; Rantitsch et al., 2014) or to derive the maximum metamorphic temperature (Aoya et al., 2010; Beyssac et al., 2002a; Kouketsu et al., 2014; Lahfid et al., 2010). If Raman bands are characterized, spectral curve fitting is often applied. However, the process of curve-fitting is commonly biased by subjectivity, because many programs require manual intervention, especially when baseline manipulation is required (Lünsdorf et al., 2014). Here, the 'Iterative Fitting of Raman Spectra' (IFORS) software is presented, which arose out of the necessity to evaluate Raman spectra multiple times without user guidance and was initially designed for studies concerning geothermometric information obtained by RSCM.

RSCM is based on the transformation of CM to graphite. The structural reorganization in relation to the degree of metamorphism can be analyzed by Raman spectroscopy (Wopenka and Pasteris, 1993; Yui et al., 1996; Beyssac et al., 2002b; Lahfid et al., 2010; Aoya et al., 2010; Beyssac and Lazzeri, 2012; Kouketsu et al., 2014). In the case of metasedimentary rocks, Beyssac et al. (2002a) showed that the CM transformation mainly depends on the metamorphic temperature and that the structural state of the CM is not influenced by retrograde processes. Thus, the maximum metamorphic temperature can be derived by RSCM. This is achieved by describing the Raman spectrum with a user defined series of functions (Gauss, Lorentz, Voigt, etc.) and by forming a function parameter ratio that is linked to the metamorphic temperature. The average function parameter ratio of a given sample is influenced by several biasing factors that can be sorted in three groups, i.e. bias due to the CM (heterogeneity, anisotropy, etc.), bias due to the Raman system (e.g. laser wavelength) and bias due to the curve-fitting strategy (Lünsdorf et al., 2014). Bias due to the curve-fitting strategy is induced by the operator himself, who introduces subjectivity by manual intervention and thereby reduces the general comparability of RSCM results (Lünsdorf et al., 2014). To overcome the operator driven biasing factor, Lünsdorf et al. (2014) concluded that an automated curve-fitting routine is needed.

Here we present an iterative algorithm that is based on the randomized mutation of function parameters. The approach follows the idea that the recorded spectrum consists of high-frequency signal components and low-frequency baseline components with added normal distributed noise (Schulze et al., 2005). The signal components are described by pseudo-Voigt (PV) functions and the baseline component by a polynomial, which are modeled simultaneously.

The main purpose of the algorithm is the batch fitting of CM spectra. To test if the IFORS software is able to describe the transformation of CM, a sample set of very low grade metamorphic conditions has been collected. These conditions are defined through illite crystallinity and vitrinite reflectance data after Kunert (1999), see Table 3.3.1 for details. Very low grade metamorphism is used here in the sense of Frey (1987a). It describes the pressure and temperature conditions after early diagenesis to the onset of greenschist facies, which covers a temperature field of approximately 100 to 300 °C. This metamorphic range is, on the basis of illite crystallinity (IC), subdivided in the diagenetic zone, anchizone and epizone (Frey (1987a) and references therein). In IC the full width at half maximum (FWHM) of the diffractometric basal X-ray reflection of illite is measured and the zone boundaries are 0.42 between diagenesis and anchizone and 0.25 for the transition from the anchizone in the epizone (Kisch, 1990; Kisch et al., 2004).

Because IFORS generates results with variable numbers of PV functions, two new Raman parameters are introduced that are independent of the number of functions. The Raman Area Ratio (RAR) uses a ratio of PV function area parameters and the Scaled Total Area (STA) utilizes the Scaled Total Area of all PV functions of the curve-fitted spectrum. Both parameters describe the transformation of CM during very low grade metamorphism.

### 3.2. Approach and Algorithm

During evaluation of Raman or other spectral data the baseline is often estimated by a linear, a polynomial or a spline function (Baek et al., 2011; Bradley, 2007; Cao et al., 2007; de Rooi and Eilers, 2012; Rowlands and Elliott, 2011) and these function's values are usually subtracted from the spectrum before the signal functions are modeled (Bradley, 2007). This approach requires the discrimination of baseline and signal data points. However, it is often difficult to separate baseline data points from signal data points, especially when many Raman bands are overlapping. In addition, linear functions are often not able to describe the inherent curvature of the baseline and polynomials need to be constrained properly to avoid fluctuation of the polynomial, which is especially important at the endpoints of the spectrum and when high degree (>6) polynomials are used.

In our approach the signal and baseline components of the spectrum are modeled iteratively at the same time. The theoretical intensity of a Raman band is described by a Lorentz function (Rull, 2012). However, impurities, defects and the instrument profile function add a normally distributed component to the Lorentzian shape of a Raman band (Vácz, 2014). Therefore, the pseudo-Voigt (PV) profile (eq. 3.2.1) given in Sánchez-Bajo and Cumbreira (1997) was chosen, because it is a linear combination of the Gauss and Lorentz profile and describes the shape of the recorded Raman bands more appropriately.

$$(3.2.1) \quad PV(x) = I_0 \cdot \left( \eta \cdot \frac{1}{1 + (x - x_0)^2 / w^2} + (1 - \eta) \cdot \exp \left( -\ln(2) \cdot (x - x_0)^2 / w^2 \right) \right)$$

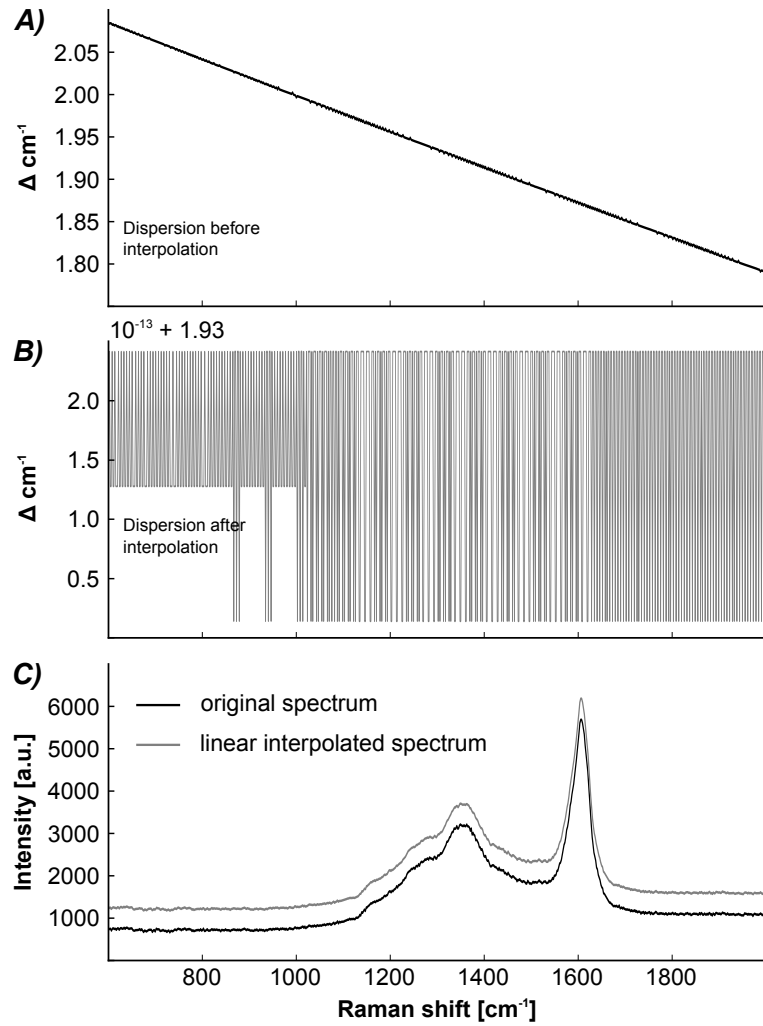


**Figure 3.2.1.** Data point distance equalization for a spectrum acquired with the 488 nm laser. A) The dispersion in the spectrum shown in C) across the spectral range from 600 to 2000  $\text{cm}^{-1}$  is presented. With increasing wavenumbers the distance ( $\Delta \text{cm}^{-1}$ ) between two data points decreases from ca. 2.11 to 1.8. B) A magnification on the wavenumber distance ( $\Delta \text{cm}^{-1}$ ) after equalization. The distance is virtually constant at  $1.93 \Delta \text{cm}^{-1}$ . The minor differences can be as high as  $2 \cdot 10^{-13}$  are probably due the quantization error. C) A spectrum before (black line) and after (gray line) distance equalization and linear interpolation.

$I_0$  is the height,  $x_0$  the central position,  $\eta$  the shape factor which controls the fractions of the Lorentz and Gauss components and  $2w$  is the FWHM of the PV function.

**3.2.1. Preprocessing.** A Raman spectrum represents the accumulation of dispersed light over the fixed distance of the detector width, i.e. usually  $1024 \times 256$  equidistant pixels. As the dispersion depends on the wavelength the data point distance decreases from short wavelengths to longer wavelengths (Fig. 3.2.1a). Therefore, the data point distance needs to be equalized. This is done by generating a new x-axis with the same number of data points as the original spectrum equally distributed from the lowest wavenumber to the highest wavenumber (Fig. 3.2.1b). The intensity values at the generated wavenumbers are derived by linear interpolation from the original data (Fig. 3.2.1c).

As the wavenumber and intensity ranges, as well as the number of data points in a given spectrum depend on the experimental setup, the data has to be normalized prior to decomposition.

Therefore, the intensity vector is scaled to its maximum value and multiplied by 100, the wavenumber vector is normalized to scale from 0 to 100. This is necessary to ascertain that later changes in the PV function parameters affect the intensity and wavenumber vector on the same scale. To generate meaningful results the PV functions need to be constrained during the fitting process. The minimum signal width is set to the distance between two data points and the maximum signal width is fixed to a given wavenumber value (see section 3.3.2). The minimum signal intensity is initially set to an arbitrary value of 2, which is automatically changed during the fitting process based on the noise estimation. Negative height parameters are rejected during the fitting process. The last constraint is the minimum signal distance. It is set to five times the distance between two data points and is required to avoid redundant PV functions. The initial baseline is set to zero. All constraints can be modified by the user to create user-defined curve-fitting routines. However, any changes applied to the constraints need to be reported.

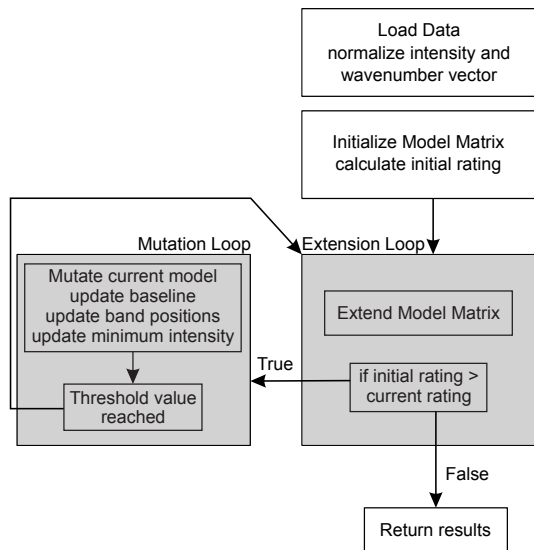


**Figure 3.2.2.** A simplified flow chart showing the algorithm's general sequence of operations.

the current residuals and then modified in the mutation loop (see section 3.2.4). In the for-loop the parameters of the latest PV function (e.g. the row of ones, see above) are replaced by the current constraint values and the current peak position. Whenever a value in the MM is changed it is validated if the applied change is in accord with the constraints. If a new, validated rating is less than the former rating, the validated and extended MM is passed to the ML.

**3.2.3. Mutation loop.** In the mutation loop the pseudo-Voigt function parameters stored in the model matrix are optimized by employing a random search heuristic. The algorithm randomly selects a peak parameter from the MM and modifies this parameter by a value 'delta' which is also drawn randomly from a normal distribution. The validated, modified MM is discarded, if its rating is higher in comparison to the original MM. These steps constantly repeat until a stop-criterion is reached.

The basis for the mutation is the so called sigma matrix (SM), which is of the same shape as the MM. It is initialized with a fixed value sigma (2 was chosen here). The SM is used both to select a parameter from the MM and to scale 'delta'. This is done by converting the SM into a



probability density function, which is used to look up the index of a MM value to modify. Thereby, MM values with an associated high sigma value are preferentially selected for modification. The same sigma value is used as the standard deviation of the normal distribution from which 'delta' is chosen. Thus, high sigma values lead to higher delta values and therefore to larger peak parameter changes. In return 'delta' is also used to heuristically adapt the selected sigma value. That is, if a delta value improved the rating, it is assumed that modification with similar delta values leads to further rating improvements. To ensure a delta value of similar magnitude gets drawn in a following step, sigma gets exponentially smoothed by absolute 'delta' and a smoothing factor 'alpha' which is fixed to 0.985 (eq. 3.2.2).

$$(3.2.2) \quad \sigma_{i+1} = \alpha \cdot \sigma_i + (1 - \alpha) \cdot |\delta|$$

If 'delta' did not improve the rating, it is assumed that smaller delta values need to be examined. In this case, the sigma value is also exponentially smoothed, but with zero (eq. 3.2.3).

$$(3.2.3) \quad \sigma_{i+1} = \alpha \cdot \sigma_i + (1 - \alpha) \cdot 0$$

After mutation, the sum of the SM is calculated and if it is above a fixed threshold ('sigma-threshold'), the process repeats itself by selecting a new value from the MM. Otherwise, the optimization terminates.

Speaking figuratively, the sigma matrix allows the optimization to adapt dynamically. If a value of the MM has been successfully modified with a large delta value (relative to its sigma value), sigma and thereby also the probability to select this MM value in the next iteration increases. This allows the optimization to quickly converge to the local optimum of a MM value. If the MM value nears its local optimum, the probability of finding improvements decreases which is reflected in a decreasing sigma value. This, in turn, increases the probability to select values in other parts of the MM for modification. However, a low sigma is not fixed. The modification in other parts of the MM may change the local optimum of said MM value, causing sigma to increase and decrease again eventually.

### 3.2.4. Updating the baseline, band positions and minimum intensity.

Each time an improving delta has been found, the baseline, as well as the minimum signal intensity is approximated and a list of the possible peak positions is generated. The baseline is given by a fifth degree polynomial that is interpolated

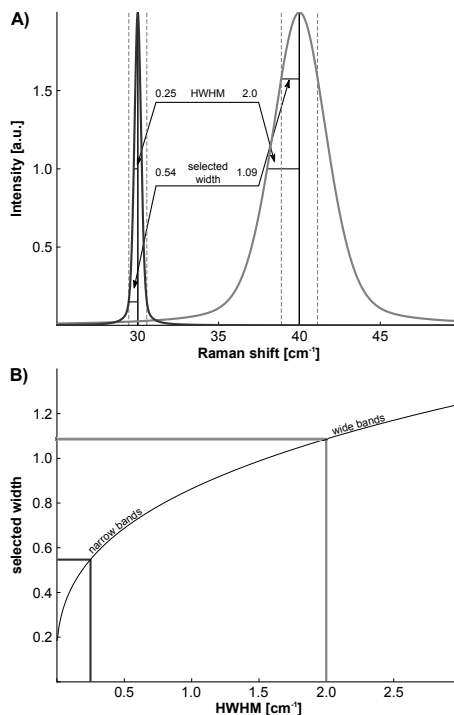


**Figure 3.2.3.** The 'peak indexing' function. The purpose of this function is to select a large proportion of data points of narrow Raman bands and only the apex region of wide Raman bands. A) The rejection interval for a narrow and a wide band is indicated by the vertical dashed lines. B) The function values of eq. 3.2.4 for a given HWHM range is shown.

through the difference vector, which is the difference between the intensity vector and the sum of all PV function values. With progressing optimization the PV functions approximate the Raman bands and the resulting difference vector has been stripped of the signal components, leaving a 'signal-free' representation of the spectrum. Thereby, the baseline approximation is indirectly controlled by the optimization of the PV functions.

The calculation of the minimum signal intensity and the list of peak positions are coupled. The peak positions are first estimated by the 'possible peak position' list which contains indices of data points of the current residuals that have a higher intensity value than the current minimum signal intensity. Because noise can manifest as a single data point above the current minimum signal intensity value, the list is filtered for single data points. Only data points that have direct neighbors remain in the list. If a Raman band is insufficiently described by a PV function, high local residuals result, giving peak positions that are already covered by a PV function. This occurs when strong noise is present or in the case of an incomplete fitting of the Raman band apex. Thus, the residual values of already described Raman bands are excluded from the 'possible peak position' list. Based on the PV functions width, the apex region of a Raman band is selected. The selection region of a narrow Raman bands needs to be wide, to select the complete band (Fig. 3.2.3a). The selection region of a wide Raman band, on the other hand, must be small (Fig. 3.2.3a) because otherwise real peak positions might be masked, which would be the case when Raman bands overlap. The function which transfers a narrow width to a wider one depending on the current width and vice versa is given by equation 3.2.4 and has been deduced empirically.

$$(3.2.4) \quad selectedwidth = width \cdot \left( width + \frac{width}{4} \right)^{-\frac{2}{3}}$$

The example in Figure 3.2.3a shows that the selection region covers most of the narrow PV function, while the selection region of the wide PV function only spans the apex region. The indices of the 'possible peak positions' list are compared to the indices of the selection regions to remove indices of data points that are already described by a PV function.

The minimum signal intensity marks the boundary between noise and signal and is given by 2.5 times the standard deviation of the noise. When the signal and baseline components are subtracted from the spectrum only the noise remains. Therefore, the residuals will approach the noise with proceeding iterations. Due to the iterative nature of the algorithm the early residuals will contain part of the signal. To compensate for this, the first derivative of the residuals is used. Of course, the absolute values of the derivative at signal positions will be high, which will lead to artificially high standard deviation of the derivative vector. Therefore, the derivative values at the apex region of a Raman band need to be replaced. As these regions are known from the 'peak position' list, they are substituted by values drawn from a normal distribution with the mean and standard deviation of the current derivative vector.

The baseline, minimum signal intensity and the peak position list are constantly updated during the mutation loop and when the ML terminates, their optimized values are forwarded to the extension loop in which the MM is further extended by PV function. The algorithm repeats itself until there are no more possibilities to add a new function. This occurs when the fit sufficiently describes the signal and baseline parts of the spectrum. At this stage the residuals approximate the noise of the spectrum and the minimum signal intensity constraint will be greater than any value in the residuals, which leaves no option to introduce a new signal function and the algorithm stops.

The software is written in the Python programming language (Pilgrim, 2004) using Numpy and Scipy (Ascher et al., 2001; Oliphant, 2007) and was tested on Linux and Windows operating systems. It is available upon request, together with user instructions and test spectra.

**3.2.5. Alternative RSCM parameters.** Figure 3.2.4 shows a progression of CM Raman spectra from the low anchizone to epizone. The main features are the so called G-band (after graphite) and D-band (defect band). In graphite the G-band is the  $E_{2g}$  vibrational mode of the aromatic plane and is centered at  $1582 \pm 1 \text{ cm}^{-1}$  (Reich and Thomsen, 2004) while the D-band becomes active when there is disorder in the graphite lattice (Pimenta et al., 2007). Depending on the laser wavelength used in the Raman experiment, the center values of the D-band range from about 1300 to 1400  $\text{cm}^{-1}$  (Vidano et al., 1981; Wang et al., 1990; Pócsik et al., 1998; Matthews et al., 1999; Saito et al., 2001). This behavior is explained either by a double resonant Raman scattering process (Thomsen and Reich, 2000; Reich and Thomsen, 2004) or by selective resonance Raman scattering of differently sized and structured polycyclic aromatic hydrocarbon subgroups in the CM (Castiglioni et al., 2004; Di Donato et al., 2004; Negri et al., 2002, 2004). Therefore, the laser wavelength should not be changed during RSCM-thermometry studies. Under very low grade metamorphic conditions however, the G-band position shifts to 1600 – 1610  $\text{cm}^{-1}$  and in the D-band region (1000 – 1500  $\text{cm}^{-1}$ ) a composite band forms which is often described by 3 (Sadezky et al., 2005; Lahfid et al., 2010) and for diagenetic conditions by 7 functions (Li et al., 2006).

The CM Raman spectrum changes significantly from the low anchizone to the epizone. While the G-band position is fixed, its width decreases. Major changes also occur in the D-band region. In this region, the central D-band, described by function 1 in Figure 3.2.4, increases in intensity while the other bands, described by

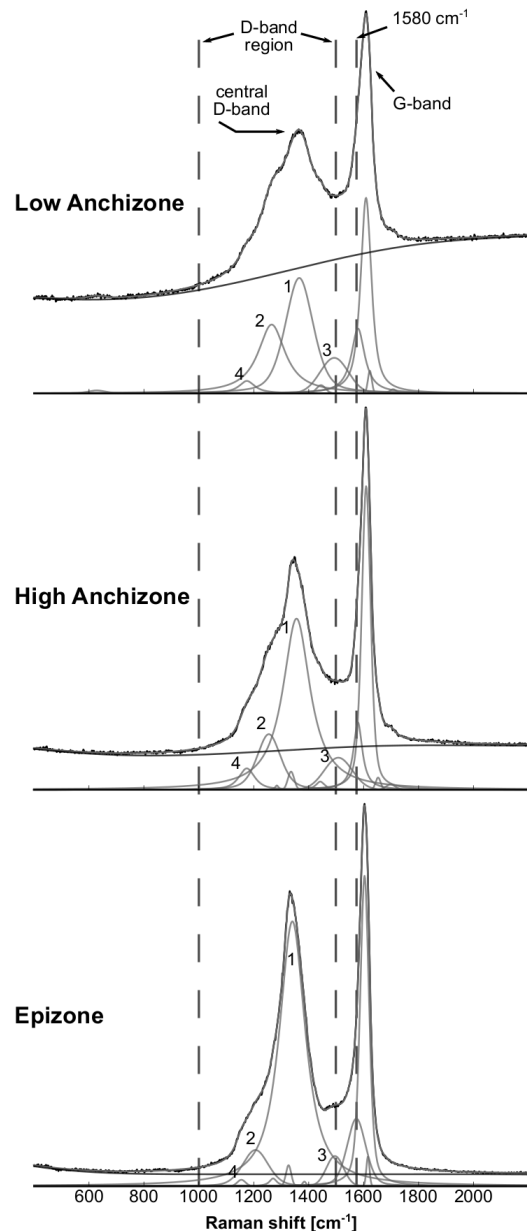


**Figure 3.2.4.** Changes in the CM-Raman spectrum (488 nm) from the low anchizone via high anchizone to the epizone. The G-band position is shifted to 1600 – 1610  $\text{cm}^{-1}$  and its width decreases from anchi- to epizone. In the D-band region the central D-band increases while all other bands decrease in intensity. This is reflected by the numbered PV functions (1 to 4) of the fit. Function 1 increases in intensity and functions 2 to 4 decrease.

functions 2 to 4 in Figure 3.2.4, decrease in intensity and area. These changes must be described by a numerical value.

The ‘classic’ approach is to curve-fit the spectrum and to produce a ratio of function parameters; most frequently the height or area values are used (Beysac et al., 2002a; Sadezky et al., 2005; Quirico et al., 2009; Lahfid et al., 2010). These procedures often require an a priori approximation of the baseline and adhere to a given recipe, i.e. which functions to use and how many. Furthermore, the used recipes might work for a certain range of CM spectra but might fail for other ranges. For instance the R2-ratio after Beysac et al. (2002a) describes the metamorphic transformation path of CM very well. Because the R2-ratio is quasi constant below temperatures of 330 °C (Beysac et al., 2002a) it fails for anchizonal to epizonal samples. The latter can be described by the RA1 and RA2 ratios after Lahfid et al. (2010), which in turn are not temperature calibrated for metamorphic samples and also, no values of RA1 or RA2 have been reported for metamorphic samples. As the exact number of Raman bands, i.e. the number of Raman active vibrations, in spectra of diagenetic to epizonal CM is unknown, the solution to a curve-fit should not be restricted to a given number of functions. This often results in large spectral residue, especially when only few functions are allowed. Instead, the result of a curve-fit should minimize the residuals, which can only be achieved if the number of used functions is unrestrained. Furthermore, Lünsdorf et al. (2014) showed that especially baseline correction but also the initial function parameters introduce variation in the curve-fit results when the same spectrum is evaluated several times. This ‘evaluation uncertainty’ increases when the shapes of the Raman bands are poorly defined, i.e. when broad bands overlap. The evaluation uncertainty is often not recognized during manual evaluation, as usually one solution per spectrum is generated. Because of the randomized and iterative workflow the ‘IFORS’ software does not follow a strict recipe. The number of used PV functions can vary from curve-fit to curve-fit depending on the shape of the spectrum (Fig. 3.2.5). If the Raman bands show intensive overlapping, the number of PV functions and their parameters can differ when the same spectrum is evaluated several times (Fig. 3.2.5a, c) and thus the evaluation uncertainty can be assessed.

A new ratio is introduced here that is able to handle a variable number of functions. Following the ‘classic’ approach, this ratio is also a function parameter ratio and formed by selecting the highest PV function in the D-band region (Dmax) and by adding up the area parameters of all PV functions (Fig. 3.2.5a, c). From this total sum the area of Dmax is subtracted and the obtained sum is divided by the Dmax area (3.2.5).

$$(3.2.5) \quad RAR = \frac{\sum Area_{all\ functions} - Area_{Dmax}}{Area_{Dmax}}$$

Because only the area parameters of the PV functions are used, the ratio is named ‘Raman Area Ratio’ (RAR). However, in diagenetic samples the variability in function parameters of multiple evaluations of the same spectrum can be substantial, with coefficients of variation (CV) as high as 10.2 % in RAR. To overcome this source of scatter, more stable numerical value is used. This value is given by the Scaled Total Area (STA) of the curve-fit (Fig. 3.2.5). Because the IFORS software extracts the signal functions, a noise-free and baseline corrected representation of the spectrum is obtained by the sum-curve of the signal functions. This sum-curve is cut to the spectral range of 1000 to 1800 cm<sup>-1</sup> (Fig. 3.2.5a, c) and scaled to the maximum value in the D-band region (Fig. 3.2.5b, d). The STA method provides the D\_STA parameter which represents the sum of the scaled sum-curve values of the Raman shift interval from 1000 – 1800 cm<sup>-1</sup>. From Figure 3.2.5a

and c it is evident that the function parameters of the curve-fits scatter, i.e. there are multiple function parameter combinations that describe the same spectrum. The sum-curves of these curve-fits are very similar (Fig. 3.2.5b, d) which results in a reduction of evaluation scatter indicated by a CV of 0.9 % for D\_STA compared to a CV of 10.2 % for RAR. In epizonal samples the variability in function parameters of multiple evaluations decreases, which is indicated by a CV of 4.2 % in RAR. However, D\_STA is still less variable, shown by the nearly identical sum-curves in (Fig. 3.2.5d) and a CV of 0.2 %.

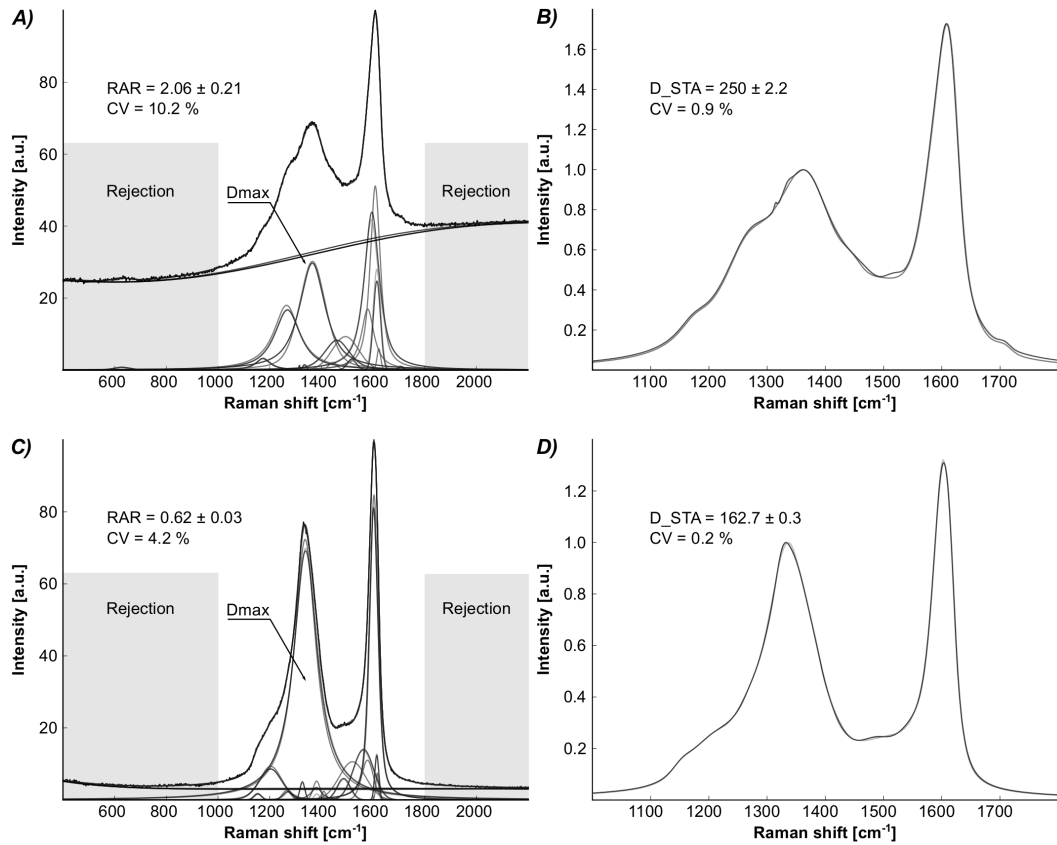


**Figure 3.2.5.** The 'Raman Area Ratio' and 'Scaled Total Area' parameter. The same spectra are evaluated three times and the different evaluations are coded by decreasing gray values. A) The spectrum shows intensive overlapping in the D-band region, resulting in three models with different PV functions which gives a coefficient of variation (CV) of 10.2 % for RAR of these models. B) The STA of the same three models; the CV is reduced to 0.9 %. C) and D) The evaluated spectrum shows less overlap and both methods yield consistent results.

For the STA method to work it is very important to fit the same spectral region. It is recommended here to use the spectral range from 400 to 2200 cm<sup>-1</sup> because in this range the CM signal is centered with plenty of baseline signal to its sides which allows proper baseline modeling. Also, the number of data points in the sum-curve needs to stay the same. Because the number of data points in the spectrum depends on the number of channels on the CCD-detector of the Raman system (typically CCDs with 1024 channels are used, but CCDs with more channels are also employed) the value of STA would scale with the CCD channel number. To produce comparable D\_STA values the number of data points in the sum-curve is fixed to 512 by linear interpolation.

**Table 3.3.1.** The sample locations with according illite crystallinity and vitrinite reflectance values. (\*) indicates that the  $R_r$  value is calculated as  $(2R_{max} + R_{min})/3$  (Taylor et al., 1998). std = standard deviation,  $R_r$  = random reflectance,  $n$  = number.

Sample Code		Coordinates		Illite crystallinity		Vitrinite Reflectance [%]		
Kunert (1999)	This study	Lat (N)	Long (E)	$\Delta^2\Theta$	std	Rr	std	n
FR129	KL2-11	50°15'47.66"	11°31'18.53"	0.318	0.013	(*)4.62	0.21	40
FR105	KL2-12	50°17'19.22"	11°33'29.31"	0.354	0.016	(*)4.43	0.28	40
	KL2-13C	50°17'50.38"	11°35'21.64"			(*)4.31	0.30	40
FR109	KL2-17	50°21'17.61"	11°30'39.25"	0.292	0.000	(*)4.58	0.27	40
FR128	KL2-18	50°19'36.3"	11°22'39.61"	0.392	0.007	2.28	0.19	40
FR126	KL2-19	50°18'22.67"	11°21'23.60"	0.349	0.013	2.48	0.29	40
FR125	KL2-20	50°19'34.81"	11°21'7.6"	0.344	0.003	1.73	0.18	50
FR118	KL2-21	50°19'35.30"	11°22'36.18"	0.213	0.005	(*)5.61	0.23	36
FR117	KL2-22	50°28'48.51"	11°23'34.44"	0.192	0.007	(*)6.37	0.44	40
FR122	KL2-3	50°24'3.23"	11°21'10.49"	0.386	0.012	3.14	0.28	40
FR127	KL2-4	50°21'43.33"	11°24'20.45"	0.341	0.014	3.90	0.33	30
FR112	KL2-5	50°23'42.67"	11°29'23.64"	0.235	0.008	(*)4.89	0.27	40
FR111	KL2-7	50°22'20.8"	11°31'4.37"	0.237	0.004	(*)4.77	0.32	40
FR111	KL2-8	50°22'13.22"	11°31'10.41"	0.237	0.004	(*)5.14	0.32	40
FR142	KL5-12	50°17'12.3"	11°21'44.86"	0.301	0.008	(*)3.71	0.22	40
FR141	KL5-13	50°18'49.21"	11°23'42.44"	0.367	0.000	2.87	0.19	40
FR139	KL5-14	50°20'3.90"	11°24'39.33"	0.306	0.003	2.44	0.21	40
	KL5-4	50°23'15.80"	11°18'51.77"			2.43	0.25	40
FR185	KL5-5	50°24'2.0"	11°18'49.49"	0.374	0.004	(*)3.22	0.17	40
	KL5-6	50°23'49.17"	11°18'53.67"			2.21	0.24	40
FR195	KL5-10A	50°20'43.93"	11°18'0.35"	0.516	0.005	2.08	0.18	40
FR193	KL5-7	50°23'8.76"	11°19'12.2"	0.449	0.011	2.52	0.24	26
FR197	KL5-11	50°18'31.38"	11°19'14.92"	0.433	0.018	2.23	0.16	30

### 3.3. Case study

**3.3.1. Samples and methods.** To test the automatic evaluation method, a sample set which covers the very low grade metamorphic conditions from high diagenesis to the epizone is used. The Lower Carboniferous flysch series of the Teuschnitz syncline, located in southern Thuringia, provides a good study area as this series has already been probed in detail by Kunert (1999) and analyzed for illite crystallinity and vitrinite reflectance (Table 3.3.1). Only the organic rich shales and slates of the flysch series have been probed, following the sampling plan of Kunert (1999).

All Raman spectra were recorded with a Horiba Jobin Yvon HR800-UV with an attached Olympus BX-41 microscope. The measurements were performed with a 488 nm diode, a 633 nm HeNe- and a 785 nm diode-laser in 180° backscattering geometry and the Raman scattered light was collected through a 100x, 0.8 NA long working distance objective. The laser light was circular polarized. The diameter of the confocal hole was set to 100  $\mu\text{m}$  and a holographic grating with 600 l/mm dispersed the light on a 1024x256 Peltier-cooled CCD chip. The on-surface laser power was regulated by density filters to 0.3 to 0.5 mW. Spectra were recorded from 10 to 60 s and consist of 3 – 5 accumulations. During measurement sessions the system is calibrated to the 520.4  $\text{cm}^{-1}$  band of silicon.

Ten randomly selected organoclasts were measured with each laser in each sample. The spectra were acquired at the untreated sample surface to avoid any alteration of the CM due to polishing which has a strong impact on the Raman spectrum of micro-crystalline graphite and graphite (Ammar and Rouzaud, 2012; Beyssac et al., 2003).

For vitrinite reflectance measurements the samples have been cut perpendicular to foliation and whole rock samples have been mounted in epoxy resin. All reflectance values, except for samples KL5-7 and KL5-11, have been obtained through a Leica DMRX microscope with attached TIDAS PMT IV photometer (J&M Analytics). Samples KL5-7 and KL5-11 were analyzed by a SpectraVision PMT system (A.S. & Co.). For samples without apparent bireflectance the random vitrinite reflectance ( $R_r$ ) was determined with unpolarized light (546 nm) and for bireflecting samples the maximum and minimum reflectance values were recorded using polarized light (see Taylor et al., 1998).

During spectral evaluation, following constraints were used for the curve-fits:

- the maximum width constraint is set to  $60 \text{ cm}^{-1}$  (see below).
- the smoothing parameter alpha is fixed at 0.985 (3.2.3)
- The 'sigma-threshold' (3.2.3) is fixed at 0.01.

The values for alpha and the ML termination threshold were empirically deduced and result in reasonable models for all tested spectra.

**3.3.2. Results and Discussion.** The maximum width constraint is of major importance for the outcome of the curve-fit, because it directly controls the number of PV functions used during decomposition. This will especially affect the spread of RAR values and to a lesser extend the spread of D\_STA values. Therefore, a reasonable width value needs to be determined for

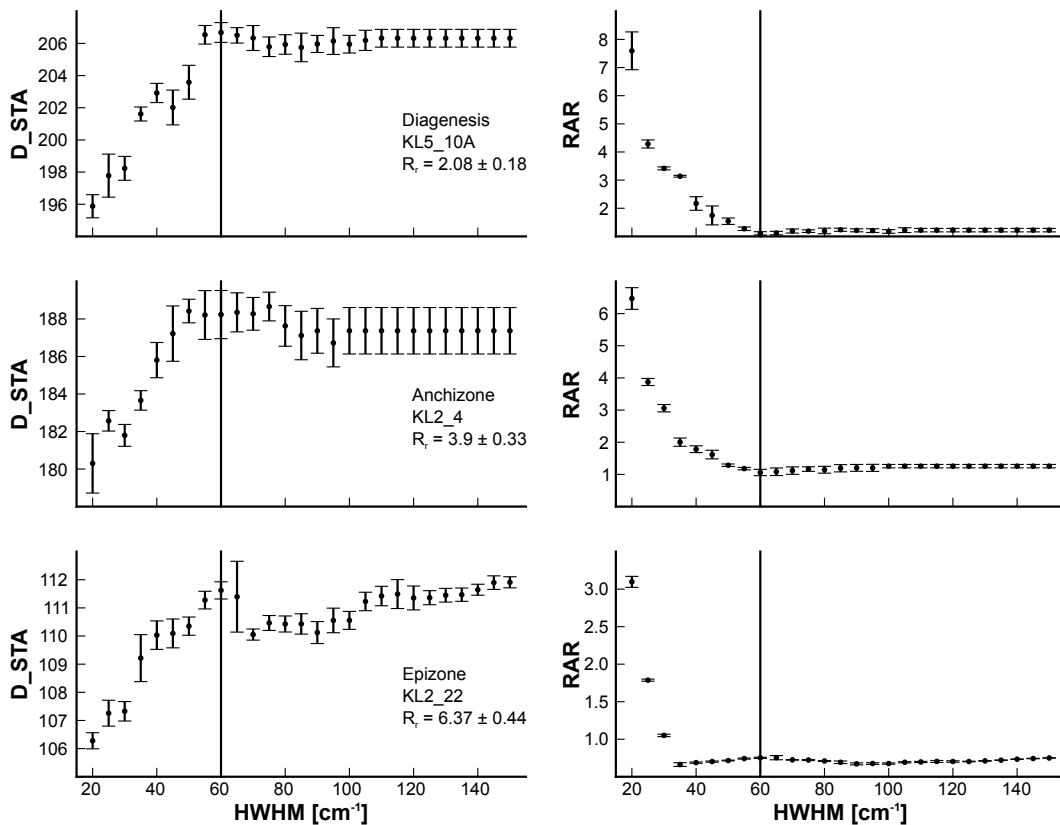


**Figure 3.3.1.** Changes in the STA and RAR parameters with increasing PV function HWHM. Both parameters show consistent values after PV function HWHM reached  $60 \text{ cm}^{-1}$ , irrespective of the low temperature metamorphic stage.

the decomposition of CM Raman spectra. To this end three spectra were evaluated 10 times

with the width parameter ranging from 20 to 150 wavenumbers in 5 wavenumber steps. In terms of very low grade metamorphism the samples reflect the diagenetic zone, the anchizone and the epizone and were selected to investigate if a general width value can be deduced. From Figure 3.3.1 it is evident that RAR decreases with increasing PV width. Using a small width value leads to decompositions with many PV functions with low area values. Thus, the decrease in RAR is related to the increasing area value of the Dmax PV function. For diagenetic and anchizonal samples RAR stabilizes after a HWHM value of 60  $\text{cm}^{-1}$  is reached and for epizonal samples RAR stabilizes already at a HWHM of 35  $\text{cm}^{-1}$ . The D\_STA parameter also stabilizes after a HWHM of 60  $\text{cm}^{-1}$ . This test clearly shows that a HWHM of 60  $\text{cm}^{-1}$  gives consistent D\_STA and RAR values for CM spectra, independent of very low grade metamorphic degree. Table 3.3.2 shows RAR and D\_STA values obtained with a HWHM of 60  $\text{cm}^{-1}$  of the sample set with their respective CV. In the case of the 488 nm series the  $CV_{D\_STA}$  ranges from ca. 1 % to ca. 5 % while  $CV_{RAR}$  ranges from ca. 3 % to ca. 18 %. Thus, the STA method gives more consistent results and because the evaluation uncertainty in D\_STA is ca. 1 % CV, it can be deduced that D\_STA better represents the sample heterogeneity compared to the RAR approach.

3.3.2.1. *Evaluating the Raman Area Ratio and the Scaled Total Area.* It was noted that in some samples, especially low anchizonal samples, multiple groups of organoclasts are present that show similar D\_STA values and spectral shapes (Fig. 3.3.2). Because D\_STA correlates to  $R_r$  (see below), it is more likely that the organoclasts with lower D\_STA values belong either to recycled vitrinites or inertinites. Therefore, the group with lower D\_STA values has been excluded from the sample average (Table 3.3.2).

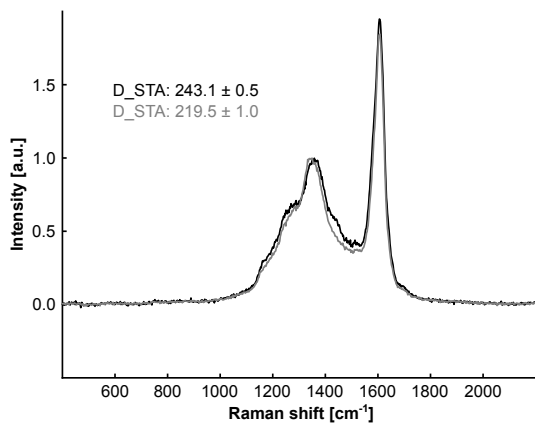


**Figure 3.3.2.** STA of different organoclast groups. Representative spectra (488 nm) of two organoclast groups in sample KL2\_19 based on their D\_STA values and spectral shape. The D\_STA values of the representative spectra are shown together with their evaluation uncertainty. It is evident that the shape and D\_STA value of the gray spectrum are significantly different from the black spectrum. As lower D\_STA values indicate a higher  $R_r$ -value, the gray spectrum likely belongs to recycled vitrinite or to the inertinite group in this sample. The black spectrum probably belongs to the vitrinite group.

Figures 3.3.3a and b show the relationship between  $R_r$  and the RSCM parameters. A linear model describes the relationship with significant coefficients of determination. Comparison of the standard deviations of the RSCM parameters and vitrinite reflectance shows that the standard deviations of D\_STA and  $R_r$  are similar in low anchizonal samples. In anchizonal to epizonal samples the standard deviations of  $R_r$  values increase, likely due to increasing bi-reflectance, while the standard deviations of the corresponding D\_STA values do not increase (Fig. 3.3.3b). The same is true for RAR, but for low anchizonal samples the standard deviation is higher than the standard deviation in the  $R_r$  data. The coefficients of determination indicate that D\_STA is better correlated to random vitrinite reflectance than RAR which is likely caused by the higher evaluation uncertainty in the RAR parameter. Thus, the D\_STA correlation is considered to reflect the data trend more appropriately. Due

to the more consistent results, D\_STA should be chosen over RAR in RSCM studies.



**Table 3.3.2.** *RAR, D\_STA and CV values of the sample set obtained with the PV maximum width constrained to 60 cm<sup>-1</sup> for the 488, 633 and 785 nm laser. It is evident that the coefficient of variation of the D\_STA data is always lower than of the respective RAR data. Avg = average, std = standard deviation, CV = coefficient of variation, n = number.*

Sample	RAR - 488 nm			RAR - 633 nm			RAR - 785 nm			D_STA - 488 nm			D_STA - 633 nm			D_STA - 785 nm			n		
	Avg	Std	CV	Avg	Std	CV	Avg	Std	CV	Avg	Std	CV	Avg	Std	CV	Avg	Std	CV	488	633	785
KL2-11	0.933	0.166	17.80	0.783	0.129	16.41	0.749	0.071	9.48	173.30	5.29	3.05	158.60	4.17	2.63	153.56	6.26	4.08	10	10	10
KL2-12	0.968	0.137	14.17	0.701	0.140	19.99	0.690	0.065	9.45	174.48	3.31	1.90	162.57	6.87	4.23	159.59	3.96	2.48	10	10	10
KL2-13C	0.834	0.071	8.56	0.735	0.072	9.77	0.641	0.064	9.92	173.74	3.32	1.91	164.49	4.91	2.99	159.85	6.70	4.19	10	10	10
KL2-17	0.796	0.107	13.40	0.759	0.120	15.81	0.628	0.058	9.25	165.24	3.95	2.39	152.57	4.53	2.97	147.26	5.48	3.72	10	10	10
KL2-18	1.433	0.106	7.38	1.348	0.120	8.91	1.253	0.184	14.71	238.69	3.25	1.36	217.69	3.86	1.77	211.50	8.92	4.22	10	7	8
KL2-19	1.430	0.150	10.47	1.420	0.152	10.72	1.401	0.169	12.07	239.31	5.41	2.26	225.29	8.88	3.94	220.25	6.58	2.99	4	9	8
KL2-20	1.951	0.264	13.51	1.518	0.267	17.59	1.283	0.185	14.38	247.14	4.45	1.80	227.60	8.66	3.81	212.73	7.05	3.31	5	9	8
KL2-21	0.583	0.029	4.93	0.473	0.031	6.51	0.430	0.029	6.69	161.75	1.87	1.16	150.50	4.93	3.28	137.54	5.83	4.24	10	10	10
KL2-22	0.642	0.053	8.32	0.515	0.048	9.37	0.407	0.027	6.52	111.17	5.04	4.53	112.50	8.46	7.52	124.87	5.91	4.73	10	10	10
KL2-3	0.974	0.073	7.45	0.894	0.106	11.82	1.120	0.316	28.19	193.17	4.33	2.24	186.86	4.81	2.58	190.75	5.04	2.64	10	10	9
KL2-4	0.953	0.028	2.96	0.939	0.102	10.87	0.901	0.096	10.65	196.54	5.11	2.60	188.85	9.99	5.29	179.57	7.89	4.39	9	9	10
KL2-5	0.662	0.057	8.67	0.465	0.023	4.89	0.423	0.028	6.57	135.68	3.32	2.45	141.09	6.98	4.94	131.31	5.36	4.08	10	10	10
KL2-7	0.632	0.055	8.66	0.475	0.016	3.33	0.428	0.021	4.83	152.63	3.20	2.10	143.81	5.04	3.51	132.18	7.07	5.35	10	10	10
KL2-8	0.596	0.044	7.32	0.599	0.057	9.53	0.493	0.042	8.47	150.96	5.90	3.91	133.49	9.77	7.32	133.83	6.35	4.74	10	10	10
KL5-12	0.929	0.091	9.80	0.885	0.082	9.21	0.820	0.085	10.42	189.20	6.98	3.69	183.06	5.54	3.03	177.96	7.58	4.26	10	10	10
KL5-13	1.014	0.092	9.07	1.014	0.128	12.67	1.120	0.221	19.69	207.17	8.70	4.20	198.42	7.74	3.90	198.14	6.23	3.15	9	10	10
KL5-14	1.270	0.103	8.13	1.160	0.077	6.60	1.277	0.351	27.50	225.05	7.06	3.14	211.89	5.91	2.79	210.30	9.15	4.35	10	9	7
KL5-4	1.229	0.094	7.62	1.338	0.145	10.86	1.192	0.109	9.15	222.00	4.36	1.96	216.69	6.19	2.86	206.43	3.87	1.88	9	10	10
KL5-5	1.038	0.050	4.80	1.176	0.140	11.90	na	na	na	203.74	6.67	3.28	199.72	7.86	3.94	na	na	na	10	10	na
KL5-6	1.204	0.157	13.03	1.185	0.144	12.13	1.143	0.139	12.20	219.23	6.83	3.11	209.78	7.26	3.46	205.07	5.56	2.71	9	6	7
KL5-10A	1.335	0.086	6.42	1.379	0.125	9.03	1.254	0.145	11.55	234.74	5.30	2.26	220.15	5.08	2.31	220.25	8.65	3.93	8	10	7
KL5-7	1.262	0.084	6.67	1.187	0.191	16.08	1.107	0.176	15.93	223.68	4.89	2.19	206.26	12.30	5.96	206.51	7.91	3.83	9	9	10
KL5-11	1.393	0.100	7.21	1.096	0.075	6.88	1.033	0.206	19.95	228.00	2.45	1.07	208.74	4.72	2.26	197.67	9.76	4.94	10	10	10

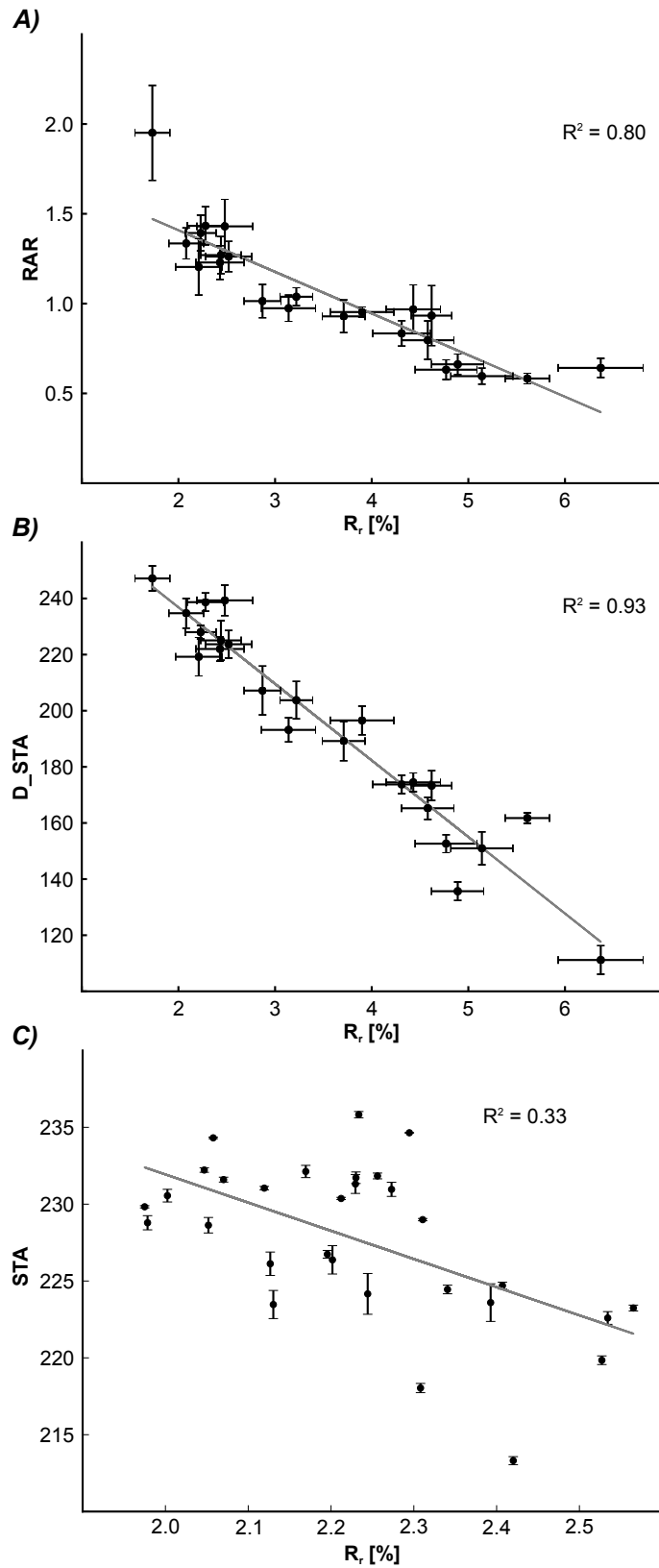


**Figure 3.3.3.** A), B) The correlation of random vitrinite reflectance with the RSCM parameters RAR and STA of the 488 nm series. C) The correlation of STA (488 nm) and  $R_r$  on a finer scale. Each data point is a vitrinite grain and shows its reflectance and associated STA value.

Because the trend lines in Figures 3.3.3a and b only show the correlation of sample averages, it was tested if  $R_r$  and  $D\_STA$  also correlate on a finer scale (Fig. 3.3.3c). To this end the same vitrinites in the polished mount of sample KL5-11 have been analyzed by both methods. This was achieved by coordinate transformation and optical verification. The effect of polishing on the vitrinite Raman spectrum was recently evaluated by Lünsdorf (2016). Following Lünsdorf (2016),  $D\_STA$  is systematically decreased by the polishing process. Due to this and because vitrinites of the same sample are compared with each other, the  $D\_STA$  values in Figure 3.3.3c are comparable. Figure 3.3.3c proposes a relatively low coefficient of determination (0.33) and a correlation coefficient of  $-0.57$ . This implies a statistical significance at the 5 % level of the negative correlation between  $D\_STA$  and  $R_r$  at the single sample level which indicates that  $D\_STA$  is able to distinguish minor changes in reflectivity. Due to the demonstrated correlation it should be possible to separate differently reflecting populations of organoclasts in dispersed organic matter analysis on the basis of their  $D\_STA$  values, which is also supported by the grouped  $D\_STA$  values in some samples (see above).

3.3.2.2. *The effect of different excitation wavelengths.* The complete sample set has been measured by the 488, 633 and 785 nm lasers to test the influence of the wavelength on the  $D\_STA$  and RAR parameter. Sample KL5\_5 is missing in the 785 nm series (Table 3.3.2), because no analyzable spectra could be obtained from this sample. Despite the differences in spectral shape and amount of luminescence (Fig. 3.3.4a), both parameters show linear and inverse correlations with vitrinite reflectance (Fig. 3.3.4b, c). This test clearly demonstrates that the STA approach is able to describe the structural evolution of CM during very low grade metamorphism, irrespective of the used excitation wavelength. However, the absolute RAR and  $D\_STA$  values of the different lasers are offset, i.e. the general progression is  $D\_STA_{488nm} > D\_STA_{633nm} > D\_STA_{785nm}$ . The same applies to the RAR values. The maximum absolute difference between  $D\_STA_{488nm}$  and  $D\_STA_{633nm}$  is 21 while the maximum difference between  $D\_STA_{488nm}$  and  $D\_STA_{785nm}$  is 34 which evaluates to 0.14  $D\_STA/nm$  and 0.12  $D\_STA/nm$ , respectively. This implies that minor differences in the excitation wavelength, for instance between the 488 nm and 514.5 nm lasers, would result in an offset in  $D\_STA$  of about 2 to 4 for a given sample. This hypothetical offset is well within one standard deviation of the STA method (Table 3.3.2). Consequently, deviation in STA due to such minor wavelength differences can probably be neglected.

3.3.2.3. *Comparing STA-RSCM to an established RSCM-method.* Common parameters used to describe Raman spectra of very low grade metamorphic samples are the RA1 (3.3.1) or RA2 (3.3.2) ratios of Lahfid et al. (2010) who decompose the spectrum with 5 Lorentz functions after baseline subtraction. These functions are named D1, D2, D3, D4, G and are centered at ca.  $1350\text{ cm}^{-1}$ , ca.  $1620\text{ cm}^{-1}$ , D3 ca.  $1500\text{ cm}^{-1}$ , ca.  $1250\text{ cm}^{-1}$  and ca.  $1590\text{ cm}^{-1}$ . That is, D1 and D4 describe the composite D-band, while D2, D3 and G describe the G-band. According to Eqs. (3.3.1) and (3.3.2) the RA1 ratio relates the change in integrated intensity of the composite D-band to the total integrated intensity, while the RA2 ratio relates the change in integrated intensity of the composite D-band to the integrated intensity in the G-band. Therefore, these ratios will also work on CM spectra acquired with lasers different to the 514.5 nm laser used by Lahfid et al. (2010). However, the calibration curve of RA1 and RA2 to metamorphic temperature shown in Lahfid et al. (2010) is only valid for the 514.5 nm laser.

$$(3.3.1) \quad RA1 = \frac{D1_{Area} + D4_{Area}}{D1_{Area} + D2_{Area} + D3_{Area} + D4_{Area} + G}$$

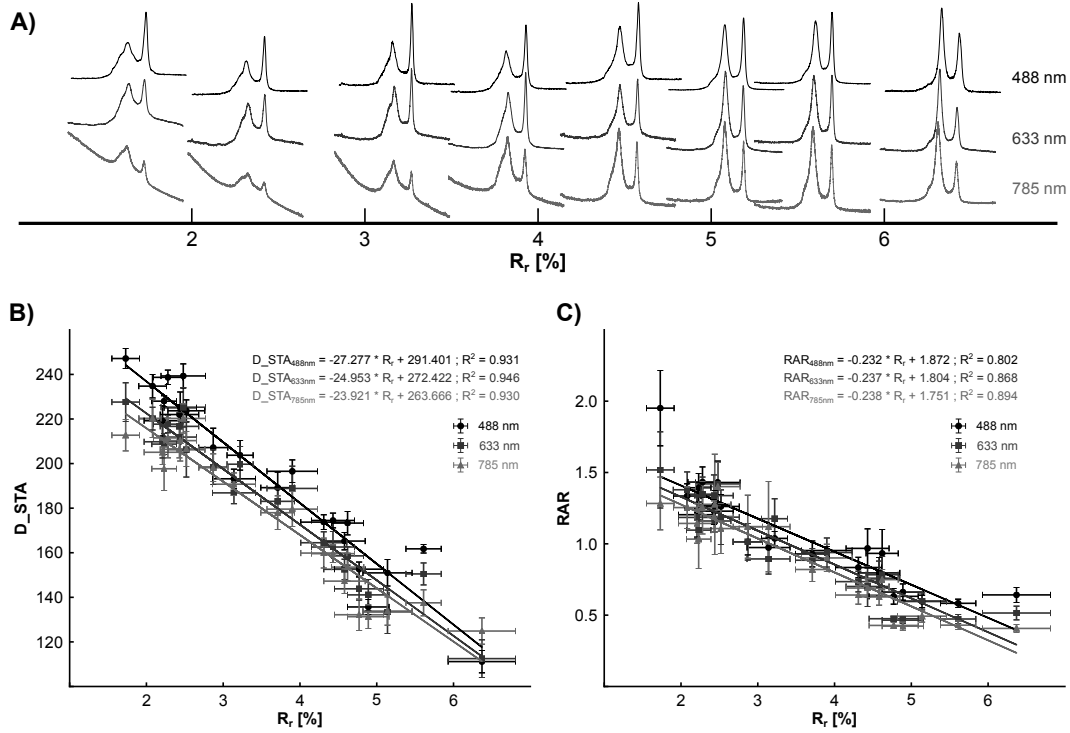


**Figure 3.3.4.** The influence of the excitation wavelength on  $D\_STA$  and the RAR parameter. A) This compilation depicts the change in spectral shape due to the used excitation wavelength with respect to increasing very low grade metamorphic conditions. B) and C) show the correlation between  $R_r$ ,  $D\_STA$  and RAR for the different excitation wavelengths. As expected, there is a systematic offset between the RAR- and  $D\_STA$ -values of the different lasers. However, for each laser RAR and STA decrease linearly with increasing  $R_r$ .

$$(3.3.2) \quad RA2 = \frac{D1_{Area} + D4_{Area}}{D2_{Area} + D3_{Area} + G_{Area}}$$

In order to compare the STA method with the RA1 approach, all spectra have been evaluated according to Lahfid et al. (2010) with the ‘Fityk’ spectral curve-fitting software (Wojdyr, 2010). Figure 3.3.5a allows three observations to be made, (1) RA1 and  $D\_STA$  linearly correlate, (2) RA1 and  $D\_STA$  values of diagenetic to low anchizonal samples increasingly scatter with increasing excitation wavelength and (3) in the case of the 488 nm laser, RA1 shows no variability while  $D\_STA$  is sensitive to changes in epizonal CM spectra and with increasing excitation wavelength the sensitivity of  $D\_STA$  decreases while sensitivity of RA1 increases.

The second observation is readily explained by the fact that the Raman signal in spectra of low matured CM recorded with longer laser wavelengths is stronger affected by luminescent background than in spectra acquired with shorter laser wavelengths (Fig. 3.3.4a; Lünsdorf, 2016). The third observation is explained by different trends in intensity distribution in epizonal CM spectra acquired by different lasers (Fig. 3.3.510b). Figure 3.3.510b shows representative spectra of the five epizonal samples highlighted in Figure 3.3.510a. The presented spectra are baseline corrected and scaled to the maximum value in the D-band. In the case of the 488 nm spectra the total intensity continuously decreases with increasing metamorphism, which is accurately reflected by the corresponding  $D\_STA$  values. This intensity decrease is about equally partitioned between the D- and G-band. Therefore, the RA1 ratio remains constant. The trend in intensity distribution

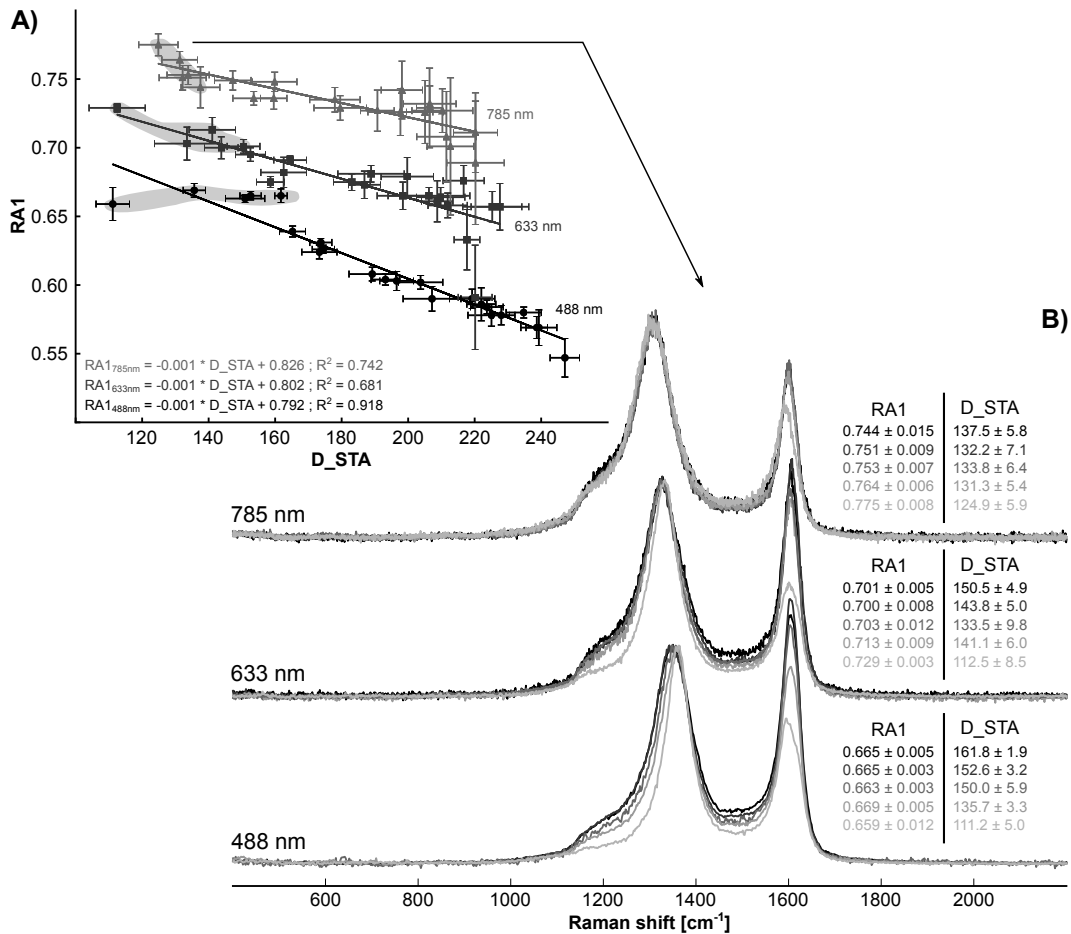


**Figure 3.3.5.** A comparison of the *D\_STA* parameter with the *RA1* ratio of Lahfid et al. (2010). A) *RA1* plotted against *D\_STA* for the complete sample set and each laser. Both parameters correlate linearly and the 488 nm series shows the highest coefficient of correlation. However, *RA1* of epizonal samples (highlighted in gray) in the 488 nm series is constant, while *D\_STA* of the same samples shows significant variation. In the 633 nm and 785 nm series both parameters vary. B) Representative spectra of the five epizonal samples highlighted in A) together with their respective *RA1* and *D\_STA* values. With increasing excitation wavelength the change in intensity distribution in the D-band region decreases until it is virtually constant for the 785 nm laser. For the 488 nm the decrease in intensity in the D-band region is comparable to the intensity decrease in the G-band which results in constant *RA1* values, while the continuous total intensity decrease is accurately represented by the *D\_STA* values.

for the 633 nm spectra is similar, but less pronounced. Finally, the 785 nm spectra show nearly constant intensity values in the D-band and slightly decreasing intensity in the G-band. This results in minor total intensity reduction, indicated by the minor *D\_STA* decrease. Because the intensity reduction is restricted to the G-band the change in intensity distribution is better reflected by a ratio value, for instance *RA1*. These observations allow us to conclude that the STA approach, using a short wavelength laser (488 nm or less), is capable to accurately describe the transformation pathway of carbonaceous matter during very low grade metamorphism. Furthermore, the concept of the Scaled Total Area approach is likely extendable to higher metamorphic degrees which will enable us to formulate a revised RSCM-geothermometer.

### 3.4. Conclusion

The presented software is able to describe Raman spectra of carbonaceous matter without the need for specific user input. Because of this, the subjectivity of curve-fitting in RSCM studies is reduced and the comparability of RSCM results increases, if the STA approach is employed. The proposed STA-RSCM method is able to characterize the structural transformation of CM during very low grade metamorphism and thus correlates with vitrinite reflectance. This implies that STA-RSCM and  $R_r$  are equivalent parameters.

## Raman spectroscopy of dispersed vitrinite - Methodical aspects and correlation with reflectance

Authored by N. K. Lünsdorf and published as: *Raman spectroscopy of dispersed vitrinite - Methodical aspects and correlation with reflectance*. International Journal of Coal Geology, 2016, 153, p. 75-86.

### 4.1. Introduction

Raman spectroscopy of carbonaceous material (RSCM) indicates the degree of metamorphism (Wopenka and Pasteris, 1993; Yui et al., 1996) and is an empiric geothermometer (Beyssac et al., 2002a; Rahl et al., 2005; Aoya et al., 2010; Lahfid et al., 2010) that is used to infer the maximum metamorphic temperature (Beyssac et al., 2007; Wiederkehr et al., 2008, 2011). RSCM is also used to characterize disordered CM (Ferrari and Robertson, 2001) and already Spötl et al. (1998), Kelemen and Fang (2001) and later Liu et al. (2013) noted that maturity trends in kerogen and coal were reflected by their Raman spectra. Recently, Hinrichs et al. (2014) correlated coal rank parameters to RSCM data. However, there are some analytic pitfalls which must be considered, i.e. thermal alteration of CM during measurement, structural defects due to polishing, orientation effects, spectral curve-fitting strategy, wavelength dependent Raman band dispersion, etc. (Wang et al., 1990; Wopenka and Pasteris, 1993; Matthews et al., 1999; Beyssac et al., 2003; Lünsdorf et al., 2014). As outlined above, RSCM has the potential to be used as a maturity parameter. Therefore, a methodical framework for the correlation of dispersed vitrinite reflectance and Raman spectroscopy is established by observing factors that influence the shape of the Raman spectrum on samples that experienced increasing coalification and graphitization. The observed factors are 1) the effect of polishing on the Raman spectrum, 2) the wavelength dependent Raman band dispersion and 3) the effect of fluorescent background signal.

Polishing has a major impact on the Raman spectrum of CM (Beyssac et al., 2003; Ammar and Rouzaud, 2012). This is because organoclasts and graphite usually have a high opacity and thus, the penetration depth of the laser light during Raman measurements is very shallow ( $<1 \mu\text{m}$ ) causing the gained Raman information to be exclusive for the sample surface McCreery (2000). Because grinding and polishing especially affect the graphite lattice at the surface, i.e. by shearing off or crumpling of graphene layers or promotion of dislocations, the Raman spectrum does not reflect the pristine sample signal. To avoid erroneous measurements, usually CM beneath a translucent mineral is analyzed (Beyssac et al., 2003) or chemical separation can be applied (Rantitsch et al., 2004). However, textural information is lost during this process. In the case of dispersed organic matter (DOM), polished surfaces are needed to locate and identify the organoclasts and as the majority of DOM is hosted in (meta-) pelitic rocks (Vandenbroucke and Largeau, 2007) the probability of finding the required geometry is very low. Thus, it is firstly important to know if polishing has an effect on the Raman spectrum of diagenetic CM and secondly at which stage during organic metamorphism or sample preparation it becomes significant. Therefore, dispersed

vitrites of a sample set that spans diagenetic to blueschist facies conditions were analyzed by multi-wavelength Raman spectroscopy and measured for maximum and minimum reflectance. To follow the spectral evolution during the step-wise abrasion and polishing procedure, the location of each vitrinite in each sample was noted and the spectral evaluation was carried out by automated curve-fitting (Lünsdorf and Lünsdorf, 2016) to handle the large data amount and to reduce the spectral analysis bias (Lünsdorf et al., 2014).

The used laser wavelength has prime influence on band positions and band intensity ratios in the Raman spectrum of CM (Vidano et al., 1981; Wang et al., 1990; Pócsik et al., 1998; Ferrari and Robertson, 2001) and further determines the fluorescence response of the sample. In aromatics the energy gap of the highest occupied molecular orbital (HOMO) and the lowest unoccupied molecular orbital (LUMO) decreases with the extend of delocalized electrons and thus decreases with the increasing size of the observed aromatic system (Ruiz-Morales, 2002; Castiglioni et al., 2004). Therefore, resonance and pre-resonance spectra are recorded when the energy gap matches or is close to the laser energy. The multi-wavelength approach revealed a two stage evolution of Raman band dispersion during coalification and graphitization which is related to the size and structure of aromatic compounds in vitrinite and discussed on the basis of molecular models of vitrinite. As the reflectance of vitrinite is also controlled by its aromaticity (Carr and Williamson, 1989) a strong linear correlation between the maximum vitrinite reflectance and the scaled total area (STA) Raman parameter (Lünsdorf and Lünsdorf, 2016) is observed. The characterization of the methodical aspects allows to formulate a methodical approach to the use of STA-RSCM as a rank indicator.

**4.1.1. Molecular evolution during coalification and graphitization.** The primary precursor of kerogen III or vitrinite is lignin (Hatcher, 1990; Hatcher and Clifford, 1997), a polymer of glyceryl methoxyphenol units (Faulon et al., 1994). Thus, in vitrinite and vitrinite rich coals lignin is the major source for aromatic compounds (Hatcher, 1990). Hatcher (1990) suggested that coalification up to the stage of sub-bituminous coal modifies lignin in a series of reactions to form phenols and these react further to diaryl ethers. These reactions are accompanied by a loss of O-bearing groups like -COOH, CO<sub>2</sub> and H<sub>2</sub>O (dehydration stage after Levine, 1993), and depolymerization of the macromolecular organic matter. According to Oberlin and Bonnamy (2013) the depolymerization or 'softening' transforms the organic matter into a more or less viscous suspension in which the heavier molecular fragments or basic structural units (BSU) are dispersed in the lighter molecular units. The concept of BSUs or aromatic 'bricks' (Oberlin et al., 1974) and their evolution during artificial and natural maturation were already proposed by Oberlin et al. (1974, 1975a,b), Rouzaud et al. (1983), Beny-Bassez and Rouzaud (1985) and Oberlin (1989). A more recent definition is given in Oberlin and Bonnamy (2013) which states that BSUs are stacks of 2 – 3 polycyclic aromatic hydrocarbons (PAH) with a size of 0.7 to 1.5 nm. The best model for a BSU is a saturated tri-coronene- or tri-ovalene-like substance (Oberlin and Bonnamy, 2013). It is important to note that a BSU is not equivalent to coronene or ovalene, but can be envisioned as a compound with a hexagonal core saturated at the edges with hydrogen and functional groups (Oberlin and Bonnamy, 2013). Considering this model, the BSUs are probably formed at the rank of subbituminous coal. For this rank and up to low volatile bituminous coal Krüge and Bensley (1994) showed that mono-aromatic units, likely stemming from the lignin, diminish while tri- to tetra-aromatic compounds increase in quantity especially pronounced at about 0.9 % R<sub>max</sub>. Up to this stage, which is equivalent to the bituminization stage after Levine (1993), the BSUs are



randomly oriented. At the point of maximum hydrocarbon generation, the BSUs rearrange to form domains of local molecular orientation (LMO) in which the BSUs form columnar arrangements (Oberlin et al., 1999) with a tilt and twist misorientation of the BSUs inside a LMO of 20 to 40° (Oberlin and Bonnamy, 2013). The size and growth of a LMO depends on the balance of hydrocarbon moieties and cross-linking heteroatoms like oxygen and sulfur in the CM (Oberlin et al., 1999; Oberlin and Bonnamy, 2013). Thus, a high oxygen concentration poses a hindrance on the mobility of a BSU which leads to smaller LMOs (ca. 50 Å for Kerogen III and >1000 Å for Kerogen I). During the debituminization stage (Levine, 1993) the concentration of aromatic CH-groups decreases, manifested as release of light weight hydrocarbons. This leads to “dangling” bonds, i.e. aromatic radicals, which allow the recombination of the BSU columnar stacks to form distorted layers. Further annealing gives rise to rapid ring condensation and the aromatic layers increase in size developing the bi-periodic, turbostratic ordering of anthracites (graphitization stage after Levine, 1993). According to Bonijoly et al. (1982) anthracites are microporous media characterized by a statistical long-range preferred orientation superimposed to the local molecular orientation. The long-range orientation results from the flattened pores with their walls being composed of distorted aromatic layers (see above). Following Bonijoly et al. (1982), Buseck and Huang (1985) and Bustin et al. (1995) natural graphitization of anthracites is a process driven by temperature and pressure, because the activation energy of thermal graphitization is too high to be realized by the natural geothermic gradient. Lithostatic pressure will promote the accumulation of shear stress, and thus strain energy, at the boundaries between two distorted aromatic layer stacks and at the pore-wall boundaries (Bonijoly et al., 1982). The increased strain energy leads to the rupture of pore-walls, which promotes the mechanical reorientation and alignment of the aromatic units and thus will facilitate the reduction of defects by diffusion, elimination of bonding vacancies and annealing of aromatic sheets to form triperiodic graphite (Bustin et al., 1995).

**4.1.2. CM Raman spectra during coalification and graphitization.** Following the discussed molecular evolution of CM to graphite, the ‘graphite-island’ model or molecular approach after Negri et al. (2002), Negri et al. (2004) and Castiglioni et al. (2004) is a reasonable approximation to the above outlined structural evolution through coalification. These authors follow the idea that PAHs are molecularly defined graphite sub-units (Negri et al., 2004), which fits well with the observed BSUs that are supposedly build up of PAHs (Oberlin, 1989; Oberlin et al., 1999; Oberlin and Bonnamy, 2013). In the first order region (up to ca. 2000 cm<sup>-1</sup>) of the Raman spectrum of graphite, two main bands appear at 1582 cm<sup>-1</sup> and at about 1350 cm<sup>-1</sup>. The first one is named G-band, after graphite, and is due to a doubly degenerate phonon mode of E<sub>2g</sub> symmetry (Tuinstra and Koenig, 1970; Reich and Thomsen, 2004; Pimenta et al., 2007) which is the in-plane vibration of the carbon atoms in the graphene sheet. In the case of perfectly crystalline graphite, this is the only Raman active vibration recorded by most Raman systems. The other E<sub>2g</sub> mode at 42 cm<sup>-1</sup>, which is the relative sliding of the graphene sheets (Reich and Thomsen, 2004), is often blocked by the filtersystem. The band at about 1350 cm<sup>-1</sup> is not present in perfect graphite, but is recorded when the graphite becomes disordered, hence it is termed D-band. Its frequency depends on the used excitation wavelength (Vidano et al., 1981; Wang et al., 1990). Currently two models explain the origin and energy dependence of the D-band. In the solid state model (Reich and Thomsen, 2004) a double resonant Raman scattering process (Pócsik et al., 1998; Thomsen and Reich, 2000; Maultzsch et al., 2004; Reich and Thomsen, 2004; Pimenta et al., 2007) gives rise to the D-band and its dispersive behavior. The molecular model (Negri et al., 2002; Castiglioni et al., 2004; Negri

et al., 2004; Di Donato et al., 2004) relates the observed intensity in the D-band region to the collective ring breathing vibration in the graphite sub-units or PAHs and the position of the D-band is then related to the dimensions of the molecule/sub-unit. This vibration resembles the  $A_{1g}$ -mode postulated by Tuinstra and Koenig (1970) for small graphite crystallites and which is inactive in perfect graphite. In addition to the D-band, further bands are detected in the Raman spectrum of disordered graphite or graphitic CM. The D2-band at ca.  $1620\text{ cm}^{-1}$  is disorder induced (Pimenta et al., 2007) and the D3-band roughly at  $1500\text{ cm}^{-1}$  is attributed to out-of-plane tetrahedral carbons (Beny-Bassez and Rouzaud, 1985). In the Raman spectra of semi-graphites to anthracites and to CM of sub-bituminous coal rank the G-band shifts from  $1582\text{ cm}^{-1}$  to ca.  $1610\text{ cm}^{-1}$  and becomes asymmetric (Lahfid et al., 2010), while the D-band becomes a composite band which is centered in the range of  $1330\text{ cm}^{-1}$  to  $1380\text{ cm}^{-1}$ , depending on the laser wavelength and degree of coalification (Liu et al., 2013). These major changes in the Raman spectrum are obviously related to the structural changes in the CM. In this maturity range the poly-aromatic BSUs are the main components and precursors for the distorted aromatic layers in anthracites. The above mentioned molecular model is in good agreement with the actually observed structures and in fact it was shown by quantum chemical density functional theory calculations and measurements on reference material, that the Raman spectra of PAHs always contain strong Raman bands at  $1600 - 1610\text{ cm}^{-1}$  and  $1300 - 1400\text{ cm}^{-1}$  (Colangeli et al., 1992; Castiglioni et al., 2001; Negri et al., 2002; Di Donato et al., 2004). According to these authors, the frequency shift of the bands and the structure (number of normal modes in  $1300 - 1400\text{ cm}^{-1}$ ) of the D-band is due to finite size of the PAHs and the presence of unequal C-C bond lengths, as opposed to the 'infinite' size and equal C-C bond lengths of graphene sheets in graphite.

## 4.2. Methods

**4.2.1. Samples.** A sample set covering the maximum vitrinite reflectance range from about 0.5 to 7 % and extending into the blueschist facies was collected. The samples were taken in the Kainach Gosau Basin (Austria), in the Glarus Alps (Switzerland), in the Valsler Valley (Duvrin/Switzerland) and in the Thuringian Forest (Germany) following the sampling locations of Rantitsch et al. (2005); Rahn et al. (1995); Wiederkehr et al. (2009) and Kunert (1999), respectively. The samples and their corresponding vitrinite reflectance or geothermobarometric information are listed in Table 4.2.1.

**4.2.2. Sample preparation and methods.** Abrasion and polishing was performed with a modified Buehler Metaserv 2000 Grinder/Polisher on 1 inch epoxy mounts of rock chips cut perpendicular to foliation. The weight force exerted on each sample during grinding and polishing was set to 4 N and the number of revolutions per minute was set to 300. Abrasion was carried out in four steps using P400, P800, P1200, P2500 SiC-abrasive paper. Afterwards the samples were polished (4 N, 300 rpm) in four steps using Buehler MetaDi monocrystalline diamond slurry with a grain size of  $9\text{ }\mu\text{m}$ ,  $3\text{ }\mu\text{m}$ ,  $1\text{ }\mu\text{m}$ . Final polishing was performed with a  $0.05\text{ }\mu\text{m}$ , water based alumina slurry. The samples were polished for 5 minutes with the  $9\text{ }\mu\text{m}$  slurry on a Buehler TexMet cloth, for 5 minutes with the  $3\text{ }\mu\text{m}$  slurry on a Struers DP-DAC satin woven acetate cloth, for 10 minutes with  $1\text{ }\mu\text{m}$  slurry on a Struers DP-Dur satin woven natural silk cloth and for 5 minutes with the  $0.05\text{ }\mu\text{m}$  slurry on a Struers DP-NAP short synthetic nap cloth. After each grinding or polishing step the samples were cleaned in an ultrasonic bath.

**Table 4.2.1.** *Sample list giving the lithology, position and maturity. Sampling sites were selected according to coordinates provided in references A to D. All reflectance values were acquired in this study, while the temperature information for sample KL14\_33A1 is given in Wiederkehr et al. (2009). Average maximum and minimum reflectance values are provided for each sample. If the number of measurable vitrinites is less than or equal to three, the spread is shown. The number of particles measured per sample (N) is given for reflectance measurements and for Raman measurements. The number of particles measured for reflectance is often less, because the particle was either of the wrong maceral type (e.g. inertinite, bituminite), too small or the polish quality was insufficient. No reflectance values could be determined for sample KL14\_33A1 due to small particle sizes or insufficient polish quality. Lat. = Latitude, Long. = Longitude, std. = standard deviation, Vr = vitrinite reflectance, Ref. = Reference. A = Rantitsch et al. (2005), B = Rahn et al. (1995), C = Wiederkehr et al. (2009), D = Kunert (1999).*

Sample Code	Lithology	Lat	Long	Avg. R <sub>max</sub> [%] or Temp [°C]	std	Avg. R <sub>min</sub>	std	N (Vr/Raman)	Ref.
KL13_15A	shale	47.1405	15.1737	0.78	0.15	0.48	0.11	4/7	A
KL13_12A	shale	47.1323	15.0996	1.07 – 1.14	na	0.60 – 0.67	na	3/6	A
KL13_21A	slate	47.1214	15.0508	1.73 – 1.99	na	0.67 – 1.18	na	2/7	A
KL5_10A	shale	50.3455	11.3001	2.19	0.15	1.4	0.3	7/8	D
KL13_7C	slate	47.1288	15.0361	2.66	0.16	1.38	0.17	9/10	A
KL14_22A	silty shale	46.9670	9.0323	2.48	0.36	1.37	0.23	8/10	B
KL14_23A	silty shale	46.9532	9.0240	3.25	0.16	1.47	0.21	8/8	B
KL2_4	slate	50.3620	11.4057	3.78	0.32	2.07	0.28	10/10	D
KL2_11	slate	50.2632	11.5218	4.86	0.4	2.77	0.42	9/9	D
KL14_13A	shale	46.9669	9.1710	4.56	0.6	2.32	0.82	9/10	B
KL14_19	fine silt	46.8884	9.0429	5.87	0.43	3.09	1.06	6/10	B
KL14_3	shale	46.8697	9.1228	7.15	0.91	1.12	0.61	4/4	B
KL14_4A	shale	46.8873	9.1271	5.82	0.49	1.48	0.53	5/9	B
KL14_33A1	metapelite	46.7065	9.2270	350 – 400 °C	na	na	na	na/6	C

Between the abrasion/polishing steps the samples were analyzed by Raman spectroscopy. In each sample 10 to 15 organoclasts were selected. Due to the rough surface after abrasion, the maceral type of the organoclasts could not be determined initially. Three spectra were recorded on each organoclast to account for within particle heterogeneity. To verify that the same organoclasts have been measured the coordinates of each clast in a given sample were recorded with respect to three pre-selected reference points. After the next polishing step a coordinate transformation was performed to relocate the original organoclasts. By abiding to this procedure any change in the Raman spectra of the organoclasts during the polishing process should become visible.

After final polishing the minimum and maximum reflectance in linear polarized light of all organoclasts have been measured at 546 nm by a SpectraVision PMT system (A.S. & Co.) consisting of a Zeiss Axio Imager.A2m microscope with attached Zeiss MCS CCD/UV-NIR spectrometer. Whenever possible, three readings were taken on each organoclast.

All Raman measurements were performed with a Horiba Jobin Yvon HR800-UV spectrometer, with attached Olympus BX41 microscope and motorized stage. The measurement configuration used a 488 nm Ar<sup>+</sup>-laser, a 633 nm HeNe-laser and a 785 nm diode laser for excitation, a spectral grating with 600 l/mm, a 100x objective with a numerical aperture of 0.9, and the diameter of the confocal hole was set to 100 µm. The laser light was circular polarized and 3 to 5 accumulations of 10 to 30 s were recorded over the spectral range of 600 to 2200 cm<sup>-1</sup>. The laser power on the sample surface was controlled by density filters to 0.3–0.5 mW to exclude thermal alteration of the sample. The Raman system was calibrated against the 520.4 cm<sup>-1</sup> line of a Si-waver. Unfortunately, the Ar<sup>+</sup>-laser needed to be replaced by a 488 nm diode laser with an output power of 50 mW. Therefore, all spectra of the 0.05 µm step were recorded with the new diode laser.

**4.2.3. Spectral processing.** Because the features of interest are in the spectral range of 800 to 2000  $\text{cm}^{-1}$  the baseline was computed by interpolating a 3rd order polynomial through the data points outside of the indicated spectral range (Fig. 4.2.1).

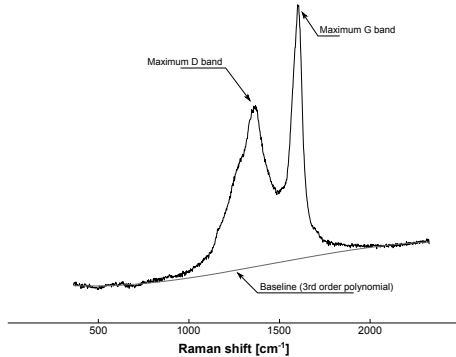


**Figure 4.2.1.** *Determination of the D/G-ratio. The spectral features of interest are in the region of 800  $\text{cm}^{-1}$  to 2000  $\text{cm}^{-1}$ . This region is ignored in the baseline correction and a third order polynomial is interpolated through the data points outside of the region of interest. After baseline subtraction the maximum value in the D-band is divided by the maximum value in the G-band.*

The D/G intensity ratio was calculated by dividing the maximum value of D band by the maximum value of the G band (Fig. 4.2.1). This ratio is sensitive to polishing effects in graphites and graphitic CM which has been shown by Ammar and Rouzaud (2012). It is unknown if the D/G intensity ratio will reflect the polishing effect on the Raman spectrum of less ordered CM, because the molecular structure of CM of diagenetic pressure (P) and temperature (T) conditions is not represented by the graphite lattice. Therefore, an additional indicator for the polishing effect is needed, which is provided by the scaled total area (STA) parameter explained below.

As the Raman spectra of CM of diagenetic P–T conditions exhibit broad overlapping bands, multiple curve-fitting solutions exist, which is described as bias due to spectral evaluation in Lünsdorf et al. (2014). To include this uncertainty, each spectrum has been evaluated three times by curve-fitting based on an iterative, randomized approach (Lünsdorf and Lünsdorf, 2016). In this approach the baseline and signal peaks are modeled by randomly changing the parameters (center, height, width, shape-factor) of Pseudo-Voigt functions, which sum up to a model that describes the spectrum. The Pseudo-Voigt function was chosen because the instrument profile functions adds a Gaussian distributed component to the Lorentzian distributed Raman signal (Rull, 2012; Váczi, 2014). Therefore, the Pseudo-Voigt function, which is a linear combination of a Gaussian and a Lorentzian function, is used as given in Sánchez-Bajo and Cumbreira (1997). Minimization of the difference between the model and spectrum stops when no additional function can be introduced to the model without violating a set of constraints (Lünsdorf and Lünsdorf, 2016). The result is a baseline corrected, smoothed representation of the fitted spectrum (Fig. 4.2.2). The sum of this representation is a measure for the intensity distribution of the Raman signal. These intensity values are scaled to the maximum value in the D-band. This allows us to compare the scaled total area values between different spectra. Any systematic change in STA during polishing reflects the polishing effect, as this parameter incorporates all the spectral features of the first order Raman spectrum of CM.

### 4.3. Results and discussion

**4.3.1. Methodical aspects.** The general change in surface roughness of a given vitrinite is shown in Figure 4.3.1. It was noted that some samples were not polished homogeneously. Therefore, only particles with few or no marks and scratches and an acceptable surface roughness after final polishing were selected to ascertain that the particles experienced polishing.

Most Raman spectra of sample KL14\_33A1, which experienced low blueschist facies metamorphism (Wiederkehr et al., 2008, 2009) show new Raman bands after the 9  $\mu\text{m}$  step. These

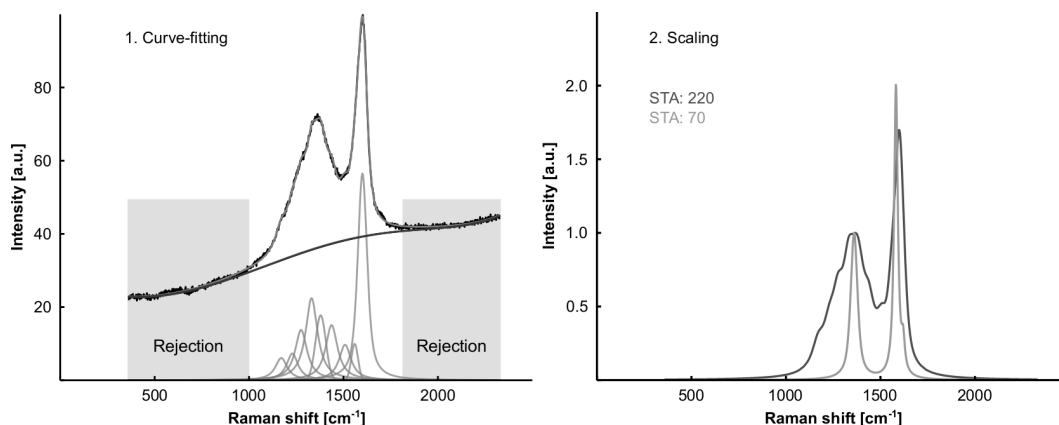


**Figure 4.2.2.** In a first step the spectrum is analyzed by curve-fitting according to Lünsdorf and Lünsdorf (2016). A series of Pseudo-Voigt functions is fitted simultaneously with a polynomial to the spectrum which results in a noise-free and baseline subtracted representation of the spectrum. In a second step this spectral representation is scaled to the maximum value in the D-band. The sum of scaled values provides the total scaled area of the spectrum (STA) which can be compared to STA-values of other CM spectra.

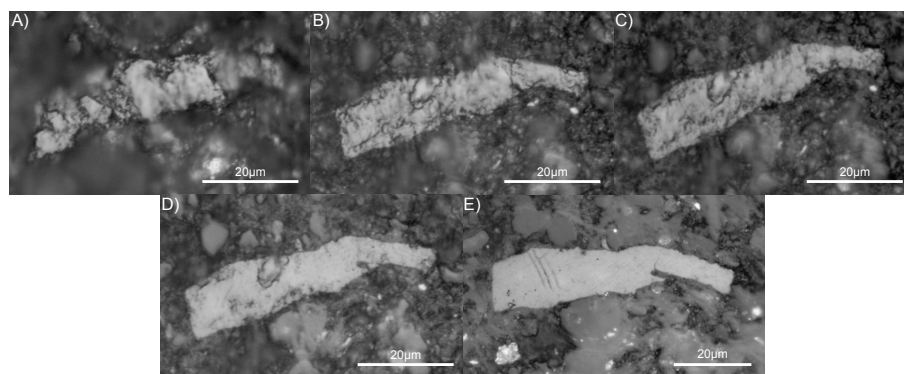


**Figure 4.3.1.** Microphotographs (reflected light, air) of the surface evolution of a vitrinite throughout the sample preparation. A) After P2500 fine abrasion, B) after 9  $\mu\text{m}$  polish, C) after 3  $\mu\text{m}$  polish, D) after 1  $\mu\text{m}$  polish, and E) after 0.05  $\mu\text{m}$  polish.

additional Raman bands remain after the 3  $\mu\text{m}$  and 1  $\mu\text{m}$  polishing steps. Figure 4.3.2 shows that the additional Raman bands occur at the same positions, irrespective of the polishing step. If the band positions are compared to the Raman spectra of the polish slurries it is probable that the 9  $\mu\text{m}$  slurry infiltrated the micro-pores in the CM and blocked those during the 3  $\mu\text{m}$  and 1  $\mu\text{m}$  polishing steps. The final polishing step likely removed the layer with the contaminated pores. Because the 0.05  $\mu\text{m}$  slurry is water based, which shows only weak Raman scattering in the spectral range of interest (Walrafen, 1964), the recorded spectrum is free of the additional Raman bands due to former polish slurry. Crespo et al. (2006) showed that the alteration of the Raman spectrum of graphite due to short periods of grinding (<10 min) is not significant. Because the CM investigated here is far less ordered than graphite and because the P2500 abrasion step was conducted for less than 5 min, the effect of this preparation step on the Raman spectrum is assumed to be negligible. Therefore, only the Raman spectra of the P2500 abrasion step, spectra without additional bands and the final polishing step are used to determine the polishing effect in sample KL14\_33A1. Figure 4.3.3 shows the STA-value, the D/G-intensity ratio and the center value of the G-band for all the samples during the polishing process. With increasing maturation – indicated by vitrinite reflectance – following trends throughout polishing can be observed:

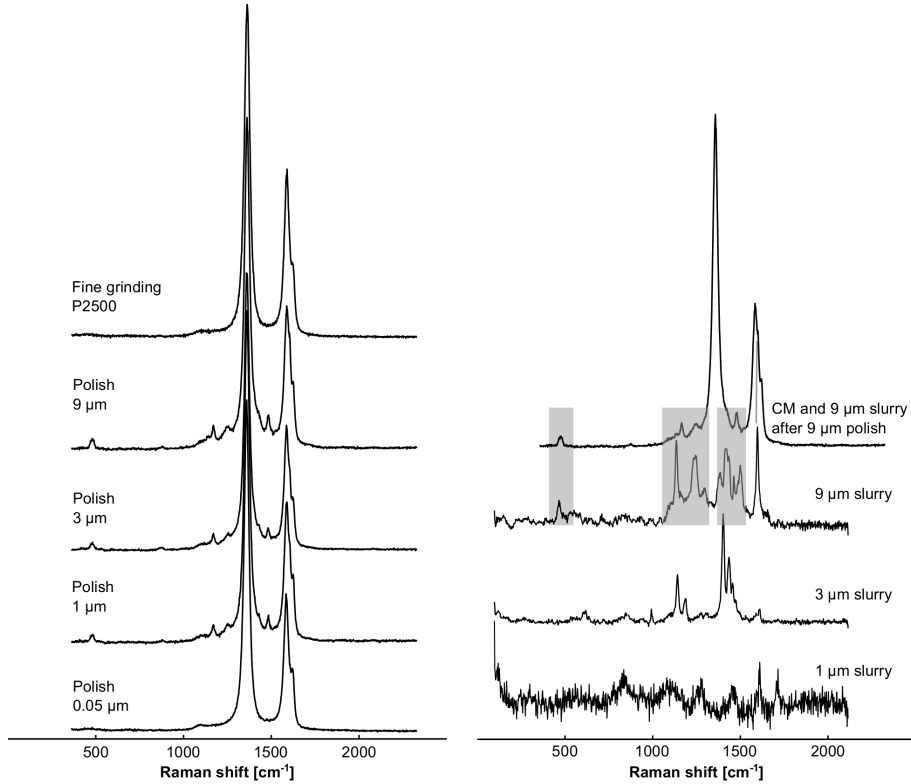
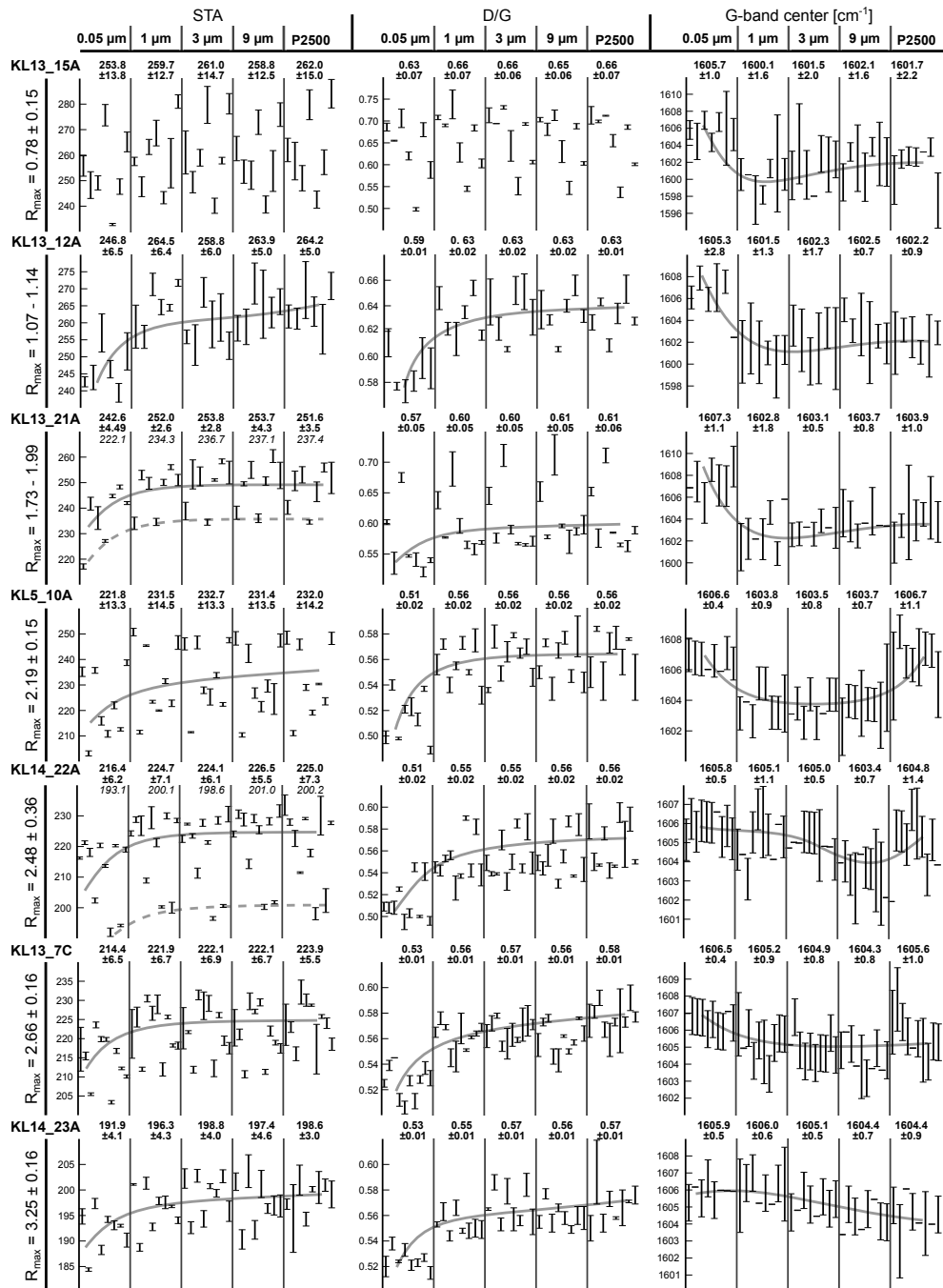


**Figure 4.3.2.** A progression of Raman spectra of graphitic CM (sample KL14\_33A1) influenced by polish slurry. Left: It is evident from the spectrum recorded after P2500 abrasion that the additional Raman bands at  $480\text{ cm}^{-1}$ ,  $1170\text{ cm}^{-1}$ ,  $1250\text{ cm}^{-1}$ ,  $1425\text{ cm}^{-1}$ ,  $1480\text{ cm}^{-1}$  and  $1600\text{ cm}^{-1}$  do not belong to the pristine CM. Also, the additional bands remain at the same positions irrespective of the used polish slurry (except  $0.05\text{ }\mu\text{m}$ ). Right: The spectra of the different polish slurries are plotted. It is obvious that the additional Raman bands in the CM spectrum (top) belong to the  $9\text{ }\mu\text{m}$  slurry.

- STA: From the fine abrasion (P2500) to the  $1\text{ }\mu\text{m}$  polishing step the scaled total area is basically constant. After  $0.05\text{ }\mu\text{m}$  treatment the STA-value systematically decreases, independent of the maturation stage. However, in the least mature sample (sample KL13\_15A of Fig. 4.3.3) this decrease in STA is not very well visible.
- D/G: This parameter is constant up to the  $1\text{ }\mu\text{m}$  polishing step and decreases after  $0.05\text{ }\mu\text{m}$  polishing. However, sample KL14\_3 (semi-graphite) and sample KL14\_33A1 (low blueschist facies) show an increase in the D/G-ratio (Fig. 4.3.3).
- G-band position: The G-band position is constant throughout the preparation steps until  $1\text{ }\mu\text{m}$  polishing (except sample KL5-10A, see Fig. 4.3.3). After  $0.05\text{ }\mu\text{m}$  polishing the G-band position shifts. From  $0.8\%$  to  $2.5\%$   $R_{\text{max}}$  the G-band position tends to be at higher wavenumbers, from  $2.6\%$  to  $4.5\%$   $R_{\text{max}}$  it shows a constant value, from  $4.8\%$  to  $7\%$   $R_{\text{max}}$  it shifts to lower wavenumbers and for sample KL14\_33A1 it stays at  $1584\text{ cm}^{-1}$  which corresponds to the  $E_{2g}$  mode of graphite.

The observed changes are related to the  $0.05\text{ }\mu\text{m}$  polishing step. If the new diode laser would be the source for the changes, an explicit systematic offset would be expected. However, the differently shifted G-band positions show that the diode laser is ruled out. Furthermore, intensity ratios of Raman bands should be unaffected by the minor change of excitation wavelength. Thus, the final  $0.05\text{ }\mu\text{m}$  polish leads to a systematic decrease in STA, that is the total Raman intensity with respect to the maximum intensity in the D-band, and the D-band intensity is decreased with

respect to the G-band. Additionally, the increase in the D/G-ratio of the semi-graphite (KL14\_3) and the low blueschist facies sample (KL14\_33A1) are clearly related to an increasing D-band (Fig. 4.3.4), which is more pronounced in sample KL14\_33A1. In this sample the STA-value and the D/G ratio are already deviating from the abrasion values (P2500) after the 3  $\mu\text{m}$  polish. As the G-band position of 1584  $\text{cm}^{-1}$  demonstrates that the sample contains CM of graphite structure, the D/G-ratio indicates that the sample is affected early in the polishing process. The G-band position in the semi-graphite sample is at ca. 1605  $\text{cm}^{-1}$  showing that  $\text{sp}^2$ -carbon structures are present. Contrary to the graphite bearing sample, the D/G-ratio of the semi-graphite is constant until the 1  $\mu\text{m}$  polish and only slightly changes after 0.05  $\mu\text{m}$  polishing.



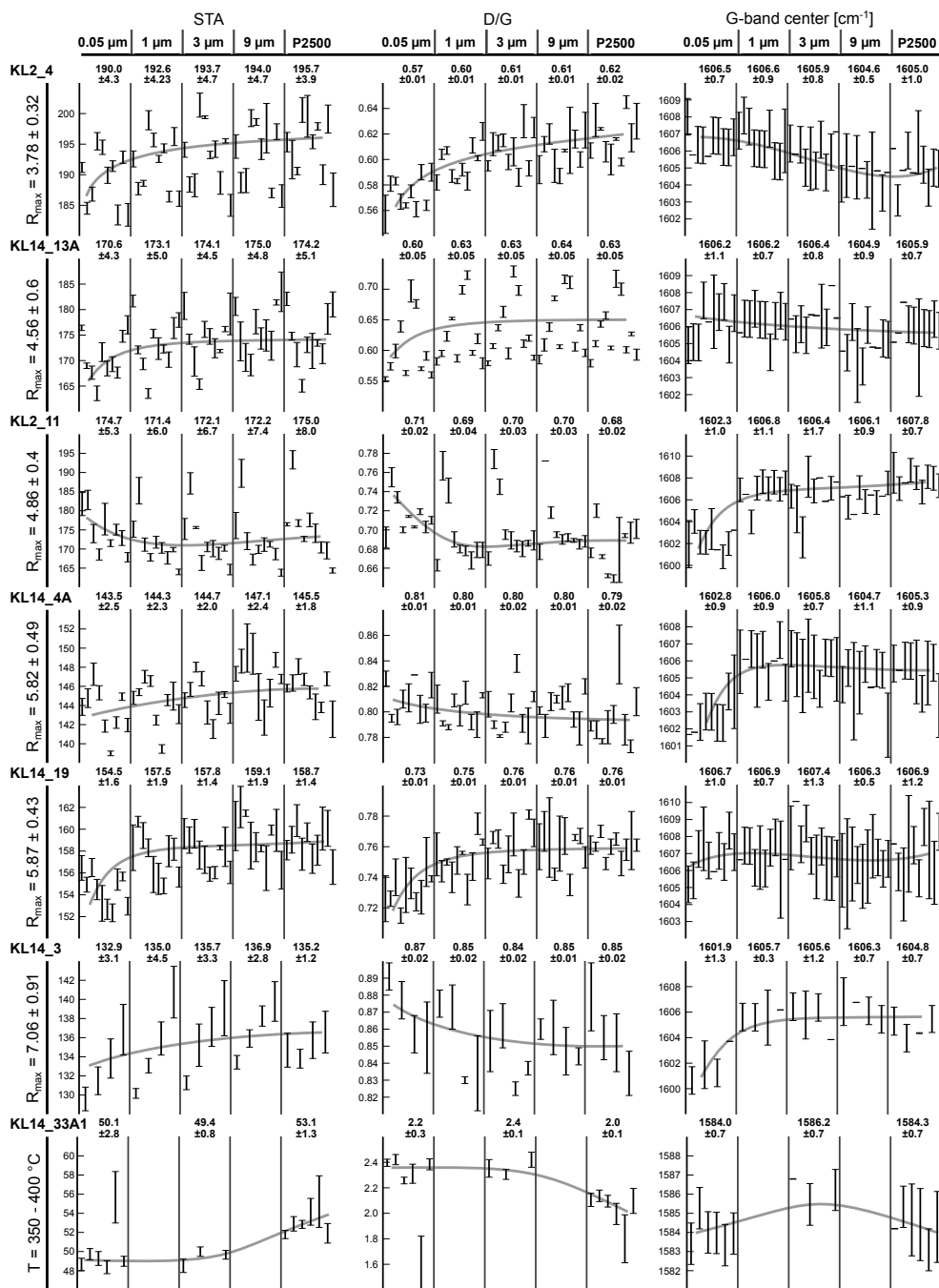


**Figure 4.3.3.** A compilation of the evolution of different Raman parameters throughout sample preparation and coalification. Each row represents one sample ordered from top to bottom by increasing maturity indicated by the average maximum vitrinite reflectance ( $R_{max}$ ). The first column shows the scaled total area (STA) parameter, the second column the D/G intensity ratio and the third column shows the wavenumber value of the maximum intensity in the G-band. Each parameter in each sample is plotted against the sample preparation steps, which are separated by vertical lines. The trend in each parameter and sample during preparation is marked by a gray line, which was manually estimated and serves as a guide for the eyes. For each preparation step the average value and associated standard deviation of all measurements of the preparation step are given above each plot. In samples KL13\_21A and KL14\_22A two separate trends are visible, marked by a solid and a dashed line. The trend with lower STA-values is likely due to a different maceral type (e.g. inertinite or recycled vitrinite). Only the average values (in italics) per preparation step are provided for the trend marked by the dashed line, because only two particles are involved. The bars in each plot show the average value with associated standard deviation for a given particle. Three spectra were recorded per particle and each spectrum has been evaluated three times. The STA and D/G parameter show in almost all samples a distinct change after the 0.05 μm polish step.



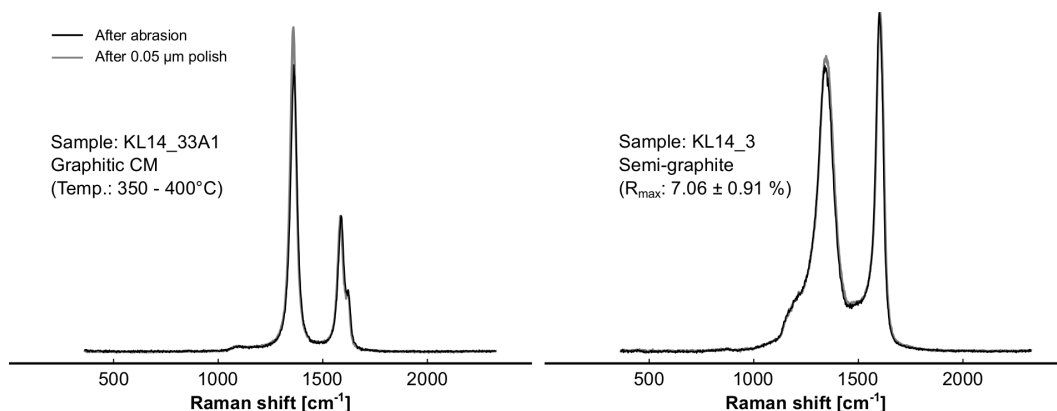


**Figure 4.3.4.** Intensity increase of the D-band due to polishing. On the left the Raman spectra of graphitic CM (sample KL14\_33A1) after abrasion (black line) and after 0.05  $\mu\text{m}$  polish (gray line) are shown. A significant intensity increase of the D-band due to the polishing procedure is evident. On the right the Raman spectra of semi-graphite (sample KL14\_3) after abrasion (black line) and after 0.05  $\mu\text{m}$  polish (gray line) are shown. Only a minor intensity increase in the D-band after 0.05  $\mu\text{m}$  polish is observed.

These observations imply that the Raman spectrum of dispersed vitrinites is virtually unaffected by the polishing process down to the 1  $\mu\text{m}$  step. In contrast, the spectrum of graphite is systematically changed by polishing, regardless of the slurry grain size. Thus, Raman spectroscopy can safely be applied to polished surfaces of CM up to epizonal samples, or  $R_{\text{max}}$  values of at least 7 %. Furthermore, the polish quality does not influence the Raman spectrum.

The STA-Raman method can possibly be extended to very immature vitrinites (ca. 0.5 %  $R_{\text{max}}$ ), which can be deduced from the top part of Figure 4.3.6 in which representative Raman spectra of vitrinites, acquired with 488 nm, 633 nm and 785 nm lasers, are shown. The progression clearly shows that the CM spectra of long wavelengths lasers are sooner affected by fluorescence than short wavelengths lasers. The spectra of the 785 nm laser still show fluorescence at about 3 %  $R_{\text{max}}$ , the spectra of the 633 nm laser are fluorescence free after ca. 2 %  $R_{\text{max}}$  and the 488 nm spectra are affected by fluorescence up to no more than 1 %  $R_{\text{max}}$ . Therefore, if Raman maturity studies are to be conducted on vitrinites, a short wavelength laser is recommended.

**4.3.2. Correlation of STA-RSCM data with vitrinite reflectance.** With the sample set at hand, the average reflectance values of single grains are compared to their average STA-values. Figure 4.3.5 shows the correlation between STA and maximum reflectance after abrasion and after the final polish. On the sample level, three stages of correlation can be determined (Fig. 4.3.5a) and compared to the total correlation. The total correlation is given by the linear regression through all data points, while the within sample correlation is provided by the linear regressions through the data points of each sample, shown by the gray lines in Figure 4.3.5a. Stage A covers samples below ca. 1.5 %  $R_{\text{max}}$  and the within sample correlation is very weak, probably because of evaluation uncertainties due to the increased fluorescence (see Raman spectra in Figure 4.3.6). In Stage B (ca. 1.5 % to ca. 3 %  $R_{\text{max}}$ ) the within sample trend is parallel to sub-parallel to the total trend. In that maturity range the 488 nm laser induces no fluorescence and the bi-reflectance is low. In Stage C (>3 %  $R_{\text{max}}$ )  $R_{\text{max}}$  and STA are correlated linearly in each sample with STA-values remaining constant while  $R_{\text{max}}$  scatters. This is probably due to the increasing bi-reflectance of higher grade samples and slight misorientations of the single grains with respect to the intersecting polished surface. Since the STA-values of the highly bi-reflecting grains are equal (samples KL14\_3, KL14\_4A and KL14\_19 in Figure 4.3.5) it can be deduced that Raman spectra

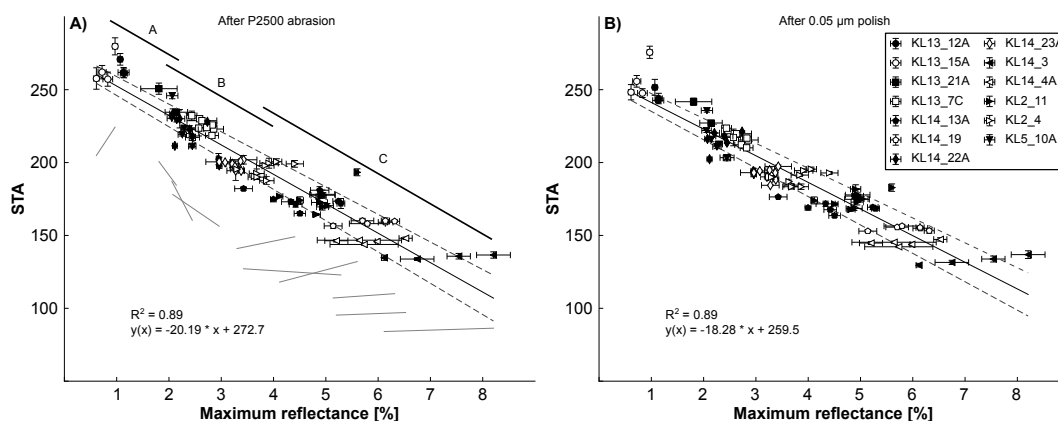


**Figure 4.3.5.** The correlation of STA-RSCM (488 nm) with maximum vitrinite reflectance after the P2500 abrasion step (A) and after the final 0.05  $\mu\text{m}$  polish step (B). A linear model sufficiently describes the correlation of the Raman parameter with the reflectance values. The dashed lines represent the 90 % confidence interval. The labeled black lines in plot A) indicate three different stages of within sample correlation (see Section 4.3.2). The same sample set, consisting out of 84 particles, is shown in both subplots.

recorded with circular polarized laser light are unaffected by slight misorientations of the grains and that the STA values indicate the true maximum reflectance. Thus, an even better correlation between  $R_{\text{max}}$  and STA is expected when the true maximum vitrinite reflectance is plotted against STA.

Similar results have been obtained by Spötl et al. (1998) who analyzed kerogen concentrates of comparable maturity. The good correlation between maximum vitrinite reflectance and STA-values must be related to the amount, size and type of aromatic units in the vitrinite. The reflectivity of a substance depends on its refractive and absorption indices, which both depend on the amount of delocalized electrons (Taylor et al., 1998) and thus correlate with the aromaticity of the substance. Carr and Williamson (1989) showed by nuclear magnetic resonance spectroscopy that vitrinite reflectance increases non-linearly with aromaticity depending on the coal rank. Because the main features of the Raman spectra, namely the G- and D-band, are related to aromatic structures a similar correlation between the Raman spectrum and aromaticity of vitrinites exists. According to Negri et al. (2002) and Di Donato et al. (2004) most of the Raman intensity in the D-band is due to the “collective ring breathing” frequency in confined PAHs. This frequency depends on the size and shape of the given PAH and following the molecular approach of Negri et al. (2002) and Di Donato et al. (2004), CM can be thought of as a mixture of differently sized PAHs. In this view the dispersive behavior of the D-band is explained by selective resonance of certain PAHs with the used laser wavelength. In Figure 4.3.6 the central value of the D-band, excited by three different lasers, is plotted against the maximum reflectance. If we follow the D-band positions from the sub-bituminous coal rank ( $<1\%$   $R_{\text{max}}$ ) through the anthracite (ca.  $4\%$   $R_{\text{max}}$ ) to the semi-graphite rank ( $>6\%$   $R_{\text{max}}$ ), two trends are distinguishable. The first trend in the low-rank samples proposes a parallel downshifting of the D-band center values, while the second trend, after ca.  $3\%$   $R_{\text{max}}$ , clearly shows diverging center values. During the first trend multiple processes and reactions alter the molecular structure and chemical composition of the CM, i.e. softening of the macro-molecular network and BSU formation, expulsion of aliphatic components and rearrangement of BSUs (MOD formation) and beginning aromatic ring condensation followed by solidification. It is therefore very difficult to explain the D-band shift by a certain process. Nevertheless, when the molecular model

is neglected and because the graphite structure can be ruled out for immature samples, the solid state model (Pócsik et al., 1998; Thomsen and Reich, 2000; Maultzsch et al., 2004; Reich and Thomsen, 2004) can also be neglected, then the recorded Raman spectra are the accumulations of all Raman active vibrations in the vitrinite. In that case, the Raman spectra should be similar and independent of the laser wavelength. However, the experimental data (Fig. 4.3.6) show a clear offset in the central value of the D-band between the 488 nm, 633 nm and 785 nm laser in the same vitrinite grain. This implies, that resonance effects must affect the spectra. The resonance Raman effect occurs when the excitation radiation frequency is close to an absorption band of the excited sample, which corresponds to an electronic transition (Rull, 2012). It has been shown (Dabestani and Lvanov, 1999; Dierksen and Grimme, 2004) that PAHs like phenanthrene and tetracene show absorption bands close to the used excitation wavelengths. Furthermore, in a series of computational and experimental studies Ruiz-Morales (2002) and Ruiz-Morales and Mullins (2007) showed that the HOMO-LUMO energy gap decreases with the number of fused aromatic rings for different PAH structures. According to Ruiz-Morales (2002) linear PAHs with 4 to 14 fused aromatic rings show HOMO-LUMO gaps of 2.8 eV to 1.5 eV, which corresponds to the used laser energies (2.54 eV, 1.96 eV, 1.58 eV), and more compact PAHs have a higher energy gap of about 3.6 eV to less than 2.5 eV for higher numbers of fused aromatic rings. Thus, short linear aromatic systems will be in resonance with the 488 nm and 633 nm laser, while larger, more compact PAHs will be in resonance with the 785 nm laser. Additionally, Castiglioni et al. (2004) showed that the dispersion towards lower wavenumbers of Raman bands in poly-conjugated molecules is independent of the excitation frequency and correlates with the degree of conjugation, i.e. the extend of electron delocalization. Structural models for vitrinites at about 0.9 %  $R_{\max}$  after Mathews et al. (2001) indicate that the preferred type of aromatic conjugation is linear and that the number of fused rings is in the range of 2 – 5 with possibly larger systems. Thus, the downshift of the central D-band value is probably related to the increasing degree of aromatic conjugation during coalification and the offset between the used wavelengths is likely due to selective resonance of linear aromatics like tetracene. The selective resonance also explains why the Raman signal of high wavelength lasers is sooner overwhelmed by fluorescence than the signal of low wavelength lasers (see section 4.3.1). As the fraction of small aromatic systems is higher in low mature vitrinites, i.e. a larger HOMO-LUMO gap, the low wavelength lasers will be more readily in pre-resonance or resonance than high wavelength lasers. Thus, the higher concentration of small aromatics and their resonance with low wavelength lasers lead to high Raman intensities which are still visible above the fluorescent background, while the Raman intensities of high wavelength lasers is only poorly or not resonantly enhanced and therefore overwhelmed by the fluorescence.

The second trend begins at the point of divergence, which coincides with the end of solidification at ca. 90 % to 92 % C. At this point the amount of free radicals is at its maximum which favors the recombination of aromatic units (see section 4.1.1). Thus, soon after, many properties of the CM change rapidly, especially the aromaticity, the dimension of aromatic clusters, ring condensation and therefore reflectance (Taylor et al., 1998). Considering these changes, the CM is indeed a mixture of differently sized aromatic units which is supported by structural models of anthracites that suggest warped polycyclic aromatic sheets with ca. 50 to 100 rings (Mathews and Chaffee, 2012). As the size distribution of the aromatic sheets broadens, the divergence of the central D-band values increases (Fig. 4.3.6) which is a strong indication in favor for the selective resonance theory of the molecular model. This divergence is likely related to the structure of the PAHs, because the increased fusing of aromatic units will certainly increase the number of compact PAHs, i.e.

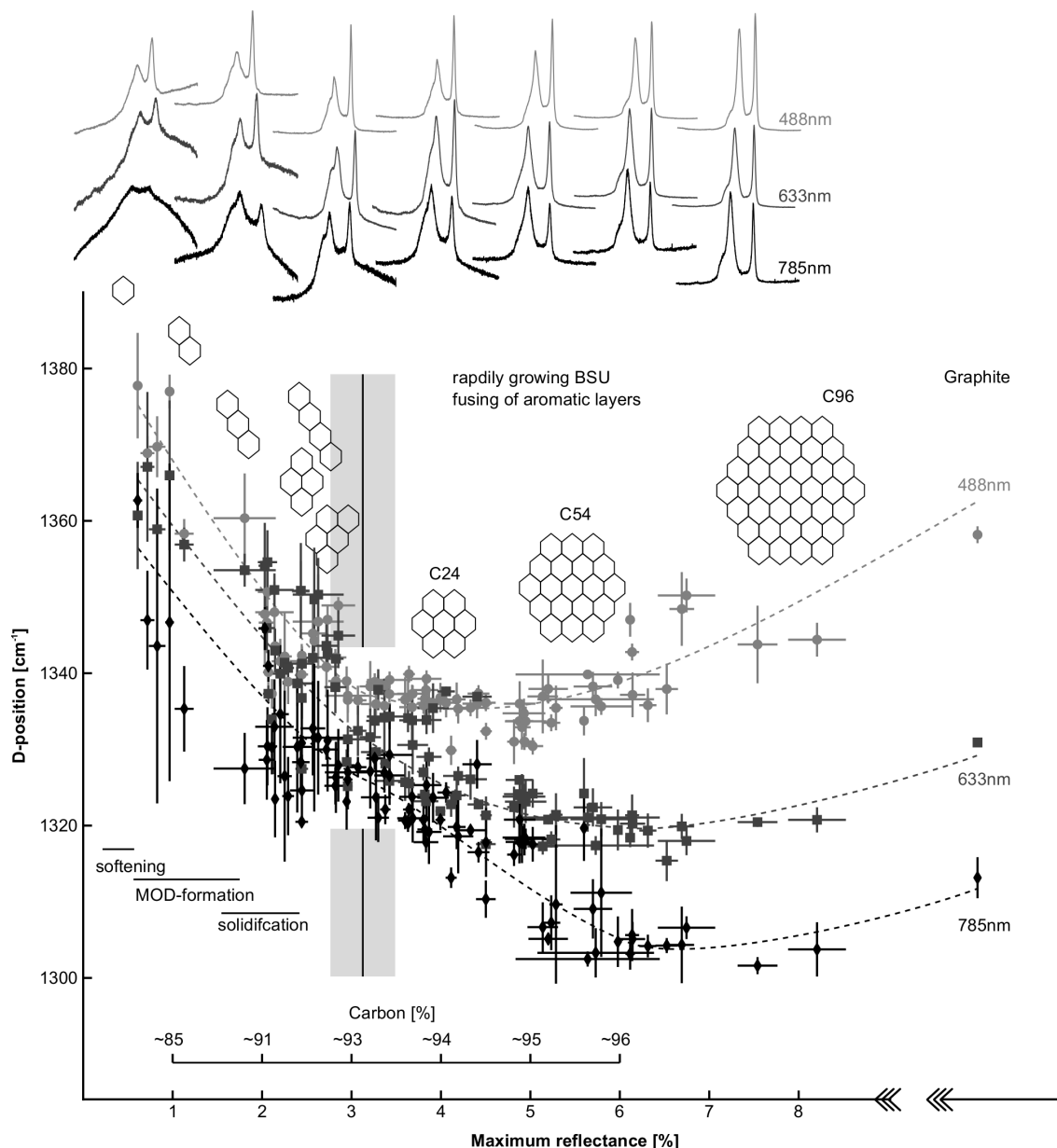


**Figure 4.3.6.** The wavelength dependent shift of the central D-band value throughout maturation. Two stages can be identified and their approximate boundary is marked by the gray bar. In the low maturity stage the D-band positions are offset according to the used laser wavelength, but the positions shift in parallel. In the second stage the D-band positions diverge depending on the used laser wavelength. The evolution of PAHs during the stages is indicated by the hexagon-sketches. In the top part of the figure a progression of representative Raman spectra is shown. The position of the spectra correlates with the maximum reflectance values of the x-axis. It is apparent that the 488 nm laser is less affected by fluorescence than the other two lasers. For more details see Sections 4.3.1 and 4.3.2.

more circular structures like coronene. As stated above the HOMO-LUMO energy gap of small compact PAHs is higher than the energy gap of small linear PAHs (Ruiz-Morales, 2002). However, the energy gap of compact PAHs also decreases with increasing PAH size and depending on their size, the PAHs will be again in resonance with the excitation frequency. That is, in anthracites and semi-graphites small compact PAHs will be in resonance with short wavelengths and larger compact PAHs will be in resonance with longer wavelengths, which explains the strong divergence

of the central D-band value of the 488 nm and 785 nm laser. Additionally, Negri et al. (2002) could show by density functional theory modeling that PAHs which are saturated by hydrogen have a complex Raman intensity distribution in the D-band region. When the hydrogen is replaced by heavier molecules, the models suggest a simpler distribution in which the major proportion of Raman intensity is concentrated in one band. The Raman spectra in the top part of Figure 4.3.6 mimic the computational results. Up to the point of divergence the D-band shows multiple features, which rapidly vanish after the divergence point. At this point, as discussed in section 4.1.1, mostly CH<sub>4</sub> is expelled by demethylation of methyl aromatics (Vandenbroucke and Largeau, 2007) and the aromatic units grow rapidly by fusing. Thus, the hydrogen replacement by heavier molecules in the model of Negri et al. (2002) is in good agreement with the observed reactions and supported by the here observed Raman spectra (Fig. 4.3.6). Additionally, as the PAH size distribution widens and the center values increasingly diverge throughout coalification, a certain PAH size is reached (or a certain size is dominant) at which the wavelength-dependent frequency shift is close to that of micro-crystalline graphite. That is the frequency shift in micro-crystalline graphite is ca. 50 cm<sup>-1</sup>/eV (Matthews et al., 1999; Pócsik et al., 1998; Reich and Thomsen, 2004; Wang et al., 1990) and after 3.5 % R<sub>max</sub> it increases from ca. 10 cm<sup>-1</sup>/eV to ca. 48 cm<sup>-1</sup>/eV at about 8 % R<sub>max</sub>. Consequently, if the size-dependent resonance frequencies of the PAHs are known, multi-wavelength Raman experiments could possibly estimate the size distribution of aromatic sheets in CM.

#### 4.4. Conclusions

From the discussion it follows that STA-RSCM works best on polished samples, avoiding the final polish step to exclude spectral alteration. For high signal to noise ratios and to reduce fluorescence and to increase signal intensity, the usage of a low wavelength visible light laser (405 – 488 nm) is recommended. High wavelength lasers can not be used for low matured vitrinites. For calculation of STA and to reduce the curve-fitting bias it is further recommended to use the curve-fitting approach after Lünsdorf and Lünsdorf (2016).

It is shown that the final 0.05 µm polish step influences the Raman spectra, while all preparation steps before do not. As a result, vitrinites are unaffected by polishing up to maximum reflectance values of 7 %. This allows us to safely analyze vitrinites in fine grained lithologies. It can further be concluded that the STA-RSCM method will increase the inter-laboratory comparability because it is independent of the polish quality and less affected by structural anisotropy, as STA-values are constant in strongly bi-reflecting samples. The STA-RSCM method is in good agreement with maximum vitrinite reflectance and thus represents a linear maturity index over a very large maturity range. Additionally, there are strong indications that STA-RSCM is correlated to the true maximum vitrinite reflectance. Finally, it might be possible to infer the size distribution of aromatic units within anthracites and semi-graphites by multi-wavelength excitation.



## Towards a higher comparability of geothermometric data obtained by Raman spectroscopy of carbonaceous material.

### Part 2: A revised geothermometer

Authored by N. K. Lünsdorf, I. Dunkl, B. C. Schmidt, G. Rantitsch and H. v. Eynatten and submitted as: *Towards a higher comparability of geothermometric data obtained by Raman spectroscopy of carbonaceous material. Part 2: A revised geothermometer.* Journal of Metamorphic Geology.

#### 5.1. Introduction

Raman spectroscopy of carbonaceous matter (RSCM) characterizes the transformation of immature organic matter to crystalline graphite, which mainly depends on temperature. Because this transformation is irreversible, RSCM is used to derive the peak metamorphic temperature of metasediments containing organic matter (e.g. Rahl et al., 2005; Beyssac et al., 2007; Wiederkehr et al., 2011; Scharf et al., 2013). The most widely used temperature range is about 330 to 650 °C (Beyssac et al., 2002a) but attempts have been made to expand this range to diagenetic temperatures (e.g. Rahl et al., 2005; Lahfid et al., 2010; Kouketsu et al., 2014). Furthermore, the RSCM method is easily applicable, non-destructive, requires little preparation, and thus is frequently applied in organic petrology studies, in which it is commonly correlated with organic maturity (Liu et al., 2013; Hinrichs et al., 2014; Wilkins et al., 2014; Rantitsch et al., 2016). Different empiric calibrations exist to relate RSCM spectra to peak temperature (e.g. Beyssac et al., 2002a; Rantitsch et al., 2004; Rahl et al., 2005; Aoya et al., 2010; Lahfid et al., 2010; Kouketsu et al., 2014). Usually, the calibration curves of RSCM-geothermometers or the correlation of RSCM data to reflectance values depend on a specific evaluation scheme of the acquired Raman spectra and therefore many protocols for spectral evaluation exist. These often consist of a baseline subtraction, followed by curve-fitting, using varying numbers (2 to 9) of Gauss, Lorentz, Voigt, pseudo-Voigt or Breit-Wigner-Fano functions to describe the intensity distribution in the recorded spectrum (Kelemen and Fang, 2001; Beyssac et al., 2002a; Sadezky et al., 2005; Li et al., 2006; Quirico et al., 2009; Lahfid et al., 2010; Liu et al., 2013; Hinrichs et al., 2014; Kouketsu et al., 2014; Wilkins et al., 2014). The results of these procedures are often parameter ratios, like the R1, R2, RA1 and RA2 ratios after Beyssac et al. (2002a) and Lahfid et al. (2010), that compare intensity, width or area values of the fitted functions. Many of these protocols require manual intervention during baseline estimation. All function parameters derived during curve-fitting depend on this estimation and thus, subjectivity is introduced during the spectral processing. According to Lünsdorf et al. (2014) the personal fitting strategy (operator bias) belongs to the spectral processing bias which represents one of three bias sources in RSCM studies. The operator bias can lead to significant differences in estimated temperatures, with respect to the used curve-fitting protocol. Lünsdorf et al. (2014) showed that the operator bias can be as high as 60 °C for the RA1 ratio

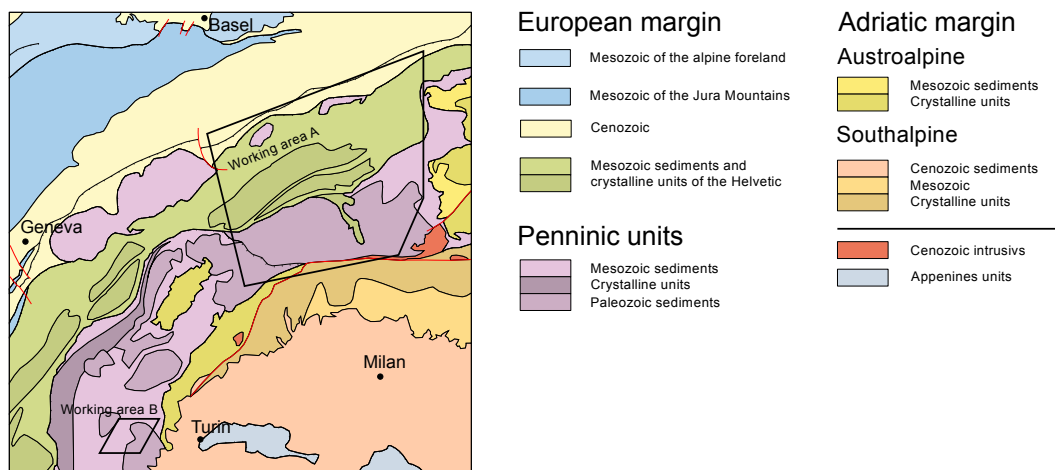


**Figure 5.1.1.** *Simplified geological overview of the sampling regions (after Pfiffner, 2010).*

after Lahfid et al. (2010) and up to 12 °C for the R2 ratio after Beyssac et al. (2002a), when the same spectral data is evaluated by different operators. The other two sources of error are due to sample heterogeneity and due to different analytical conditions, including the used Raman devices, in which the excitation wavelength is of prime importance. Lünsdorf et al. (2014) concluded that a standardized, automatic curve-fitting routine would rule out the operator bias and that a reference sample series would allow each laboratory to create their own calibration curve, which decreases bias due to different analytical setups and therefore the overall comparability of RSCM temperature information increases. This study aims at initiating a reference series which is then combined with the automated curve-fitting routine 'IFORS', presented in Lünsdorf and Lünsdorf (2016), to provide a standardized approach to a revised RSCM-geothermometer. Therefore, samples were collected in the Central and Western Alps focusing on locations with well-established metamorphic conditions. The proposed reference series covers a peak temperature range of ca. 160 °C to ca. 600 °C, i.e. from deep burial to lower amphibolite facies conditions. In this temperature range the evolution of CM Raman spectra is complex and none of the published evaluation approaches is capable to describe this evolution continuously or without user guidance. Hence, an automated, operator independent approach is presented that is based on the STA-RSCM method of Lünsdorf (2016) and Lünsdorf and Lünsdorf (2016).

## 5.2. Samples

In order to compile a reference series, sample locations were selected which adhere to the following rules with decreasing priority, (1) independent and well constrained peak metamorphic temperature, (2) fresh character (3), uniform Raman spectra of CM particles, (4) accessibility of the sampling location. The samples were collected across the Central and Western Alps (Fig. 5.1.1) and are categorized in three groups. The first group represents the low temperature branch of the sample series and was collected in the Northern Helvetic Flysch units of the Glarus Alps and in the Helvetic units along the pyrophyllite-in (Prl-in) reaction isograd (Fig. 5.2.1, Frey, 1987b). The second group was taken along a profile in the Schistes Lustrés units in the Western Alps (Fig. 5.2.2, Agard et al., 2001a). The third group was gathered in the Bündnerschiefer (meta-) sediments of the Central Alps (Switzerland) and was extended by samples from the central Lepontine Alps (Fig. 5.2.1). The second and third group represent the high temperature branch of the sample series.



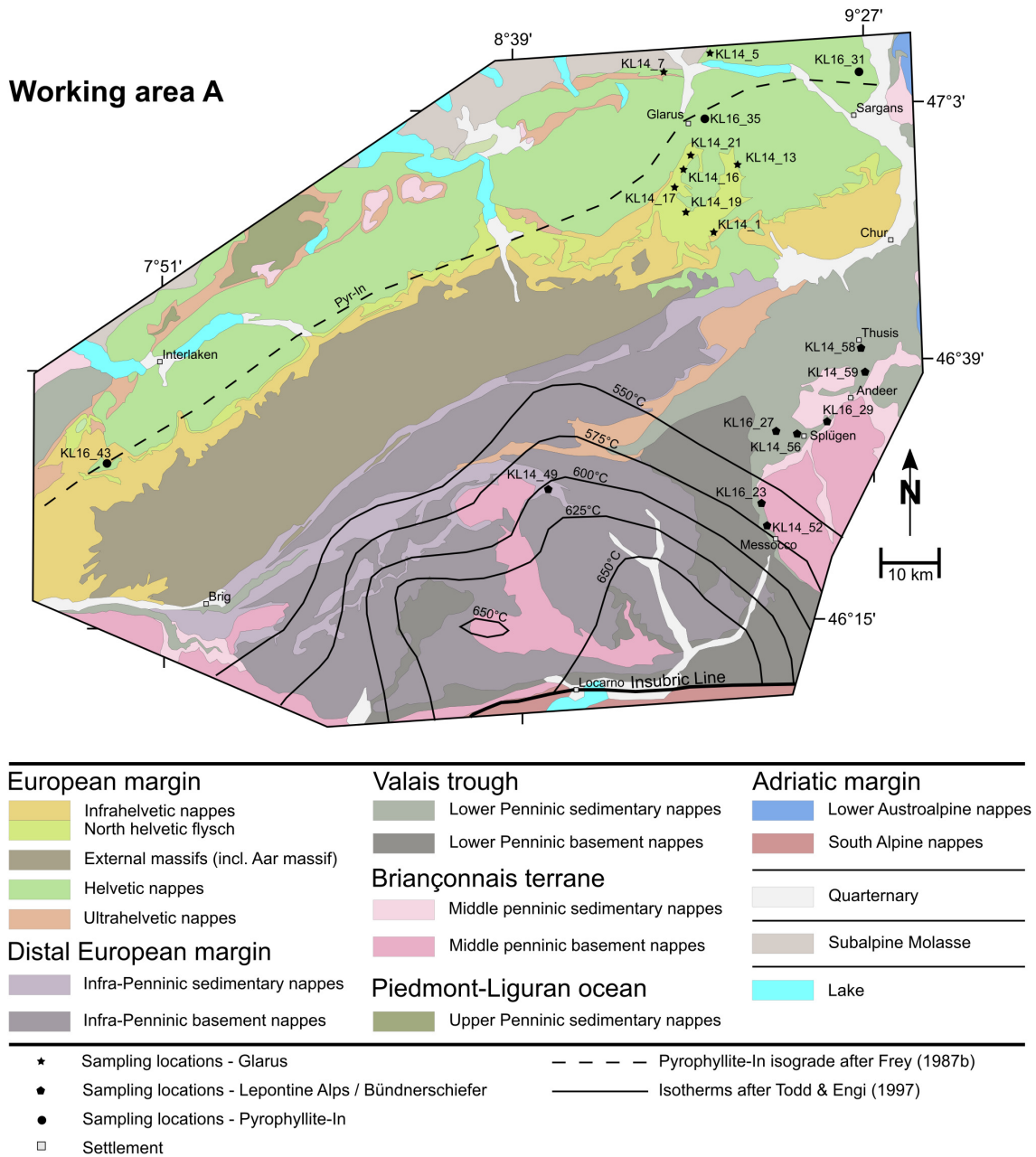


**Figure 5.2.1.** Simplified map of tectonic units in the working area A (Fig. 5.1.1). The sample locations are shown together with the Prl-in isograd (Frey, 1987b) and the isotherms in the Lepontine dome (Todd and Engi (1997); map-base after Swisstopo, 2005)

Samples of the first group are organic rich black slates and metapelites which cover very low grade to lower greenschist facies conditions (Frey, 1987b; Rahn, 1996; Ebert et al., 2007). The peak metamorphic temperatures in the Glarus Alps are well constrained by fluid inclusion thermobarometry, chlorite thermometry and calcite-dolomite thermometry (Rahn, 1996; Ebert et al., 2007) covering a temperature range of about 160 °C to 320 °C. The reaction kaolinite + quartz → pyrophyllite + water was mapped by Frey (1987b) and the P-T conditions along this isograd were determined by fluid inclusion thermobarometry to 240 °C – 260 °C at about 1.5 kbar to 2 kbar (Frey, 1987b). For the reference series eight samples were selected in the Glarus Alps and three samples along the Prl-in isograd (Fig. 5.2.1).

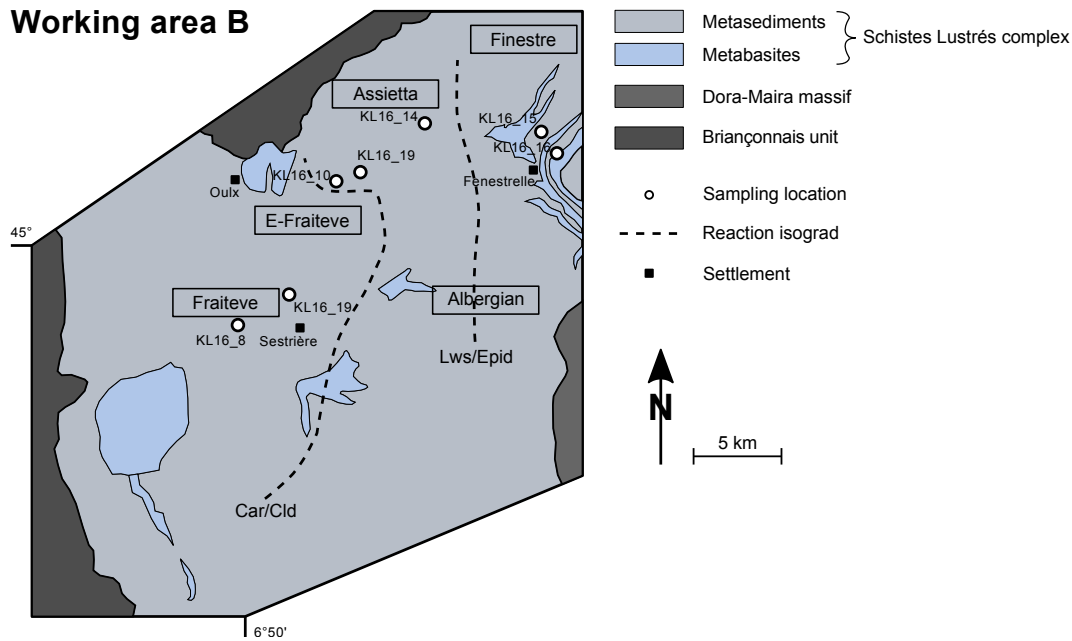


**Figure 5.2.2.** Simplified geologic overview map of the working area B (Fig. 5.1.1) with sampling locations, see Table 5.2.1 for accurate coordinates. (after Agard et al., 2001a).

Calcareous black schists and marbles of the Schistes Lustrés, also sampled by Beyssac et al. (2002a), assemble the second group. The sediments of the Schistes Lustrés were deposited during Early Jurassic to Middle Cretaceous times in the Piemont-Ligurian trough (Lemoine et al., 1986; Deville et al., 1992) and experienced prograde blueschist to eclogite facies metamorphism followed by exhumation under greenschist facies conditions (Agard et al., 2001a). Agard et al., 2001a,b, 2002 provide P-T conditions from 300 – 350 °C at 12 – 13 kbar to 450 – 530 °C at 20 – 21 kbar continuously increasing from W to E in the Schistes Lustrés units. A profile consisting of seven samples was collected along this P-T gradient (Fig. 5.2.2). Samples of the third group were selected along a profile from Messocco to Thusis (Fig. 5.2.1). They belong to the Bündnerschiefer in the Central Alps and consist of metamorphosed, mostly Cretaceous, hemipelagic-turbiditic pelites, marls and sandy limestones deposited in the northern Penninic Valaisan trough (Steinmann, 1994). Peak metamorphic conditions in the Bündnerschiefer reached 350 – 400 °C and 1.2 to 1.4 GPa during a subduction related HP-LT event (Bousquet et al., 2002; Wiederkehr et al., 2008) and were followed by rapid isothermal decompression under lower greenschist facies conditions. Wiederkehr et al. (2009) dated the HP-LT event to ca. 41 Ma. Metamorphic conditions decrease in the Bündnerschiefer towards the NE. In the SW of the Bündnerschiefer profile, the HP-LT event has been overprinted by a Barrovian-type thermal event, reaching amphibolite facies conditions that lead to the present-day distribution of isotherms in the Lepontine Alps (Todd and Engi, 1997; Wiederkehr et al., 2009). In general, peak metamorphic temperatures in the Lepontine area increase from ca. 500 °C in the peripheral parts to ca. 675 °C in the central parts near the Insubric Line (Fig. 5.2.1, Todd and Engi, 1997; Frey and Mählmann, 1999). Wiederkehr et al. (2009) dated the Barrovian-type overprint to ca. 19-18 Ma. To complete the high temperature branch of the reference series, an additional sample (KL14\_49) was collected in the central Lepontine Alps in the Lebendun Nappe at Lake Tremorgio where a peak metamorphic temperature of about 600 °C has been determined. All sample locations are listed in Table 5.2.1 together with their associated temperature and the used geothermometers.

**Table 5.2.1.** A list of the reference sample set with associated coordinates, peak metamorphic temperature, used method to obtain the temperature information and the references for the temperature information. In the case of fluid inclusion homogenization temperatures marked by a star, only the analytical error was provided in literature and thus a geological uncertainty of  $\pm 30^\circ\text{C}$  is assumed, which is in the same order of magnitude as the other thermometers, i.e. chlorite-thermometry (Rahn, 1996), calcite-dolomite thermometry (Ebert et al., 2007). Lat. = Latitude; Long. = Longitude; 1 = Chlorite-thermometry; 2 = Fluid inclusion homogenization temperature; 3 = Calcite-dolomite thermometry; 4 = Pressure-temperature estimation by multi-equilibrium calculation; A = Rahn (1996); B = Frey (1987b); C = this study; D = Todd and Engi (1997); E = Agard et al. (2001a).

Sample code	Sample group	Lat	Long	Peak Temperature [ $^\circ\text{C}$ ]	Method	Reference
KL14_1	1	46.85627	9.10359	295 $\pm$ 20	1	A
KL14_5	1	47.1405	9.10165	162 $\pm$ 30*	2	A
KL14_7	1	47.11788	9.00371	178 $\pm$ 30*	2	A
KL14_13	1	46.9669	9.171	267 $\pm$ 30*	2	A
KL14_16	1	46.97697	9.05716	236 $\pm$ 30*	2	A
KL14_17	1	46.94665	9.03288	256 $\pm$ 30*	2	A
KL14_19	1	46.88838	9.04286	299 $\pm$ 23	1	A
KL14_21	1	46.9617	9.09306	228 $\pm$ 30*	2	A
KL16_31	1	47.11033	9.44794	236 $\pm$ 30*	2	B
KL16_35	1	47.0344	9.09412	240 $\pm$ 30*	2	B
KL16_43	1	46.51734	7.7493	260 $\pm$ 30*	2	B
KL14_49	3	46.477916	8.724217	610 $\pm$ 50	3,4	C/D
KL14_52	3	46.40111	9.228	520 $\pm$ 25	3,4	C/D
KL16_23	3	46.43464	9.21321	480 $\pm$ 40	3,4	C/D
KL14_56	3	46.546089	9.279393	450 $\pm$ 30	3	C
KL14_58	3	46.646578	9.448071	370 $\pm$ 50	3	C
KL14_59	3	46.67832	9.44969	420 $\pm$ 50	3	C
KL16_27	3	46.55367	9.23969	440 $\pm$ 30	3	C
KL16_29	3	46.56221	9.35223	420 $\pm$ 30	3	C
KL16_8	2	44.97242	6.85448	325 $\pm$ 25	4	E
KL16_10	2	45.02926	6.89736	370 $\pm$ 35	4	E
KL16_11	2	45.0331	6.91046	370 $\pm$ 35	4	E
KL16_14	2	45.06127	6.96675	415 $\pm$ 35	4	E
KL16_15	2	45.06413	7.0562	490 $\pm$ 40	4	E
KL16_16	2	45.052905	7.063419	490 $\pm$ 40	4	E
KL16_19	2	44.98675	6.87342	350 $\pm$ 325	4	E

### 5.3. Methodical background

**5.3.1. Methods.** Samples of group one were prepared as polished blocks. The polished surface is needed to identify CM grains (i.e. vitrinite, inertinite and bituminite), which is important for diagenetic to very low grade samples. The molecular structure of metamorphic CM alters during polishing (Wopenka and Pasteris, 1993; Beyssac et al., 2003; Crespo et al., 2006; Ammar and Rouzaud, 2012), which leads to increasing D-band intensities and ultimately to false temperature information. However, Lünsdorf (2016) showed that Raman spectra of CM in samples from very low to low grade conditions are unaffected by polishing if the process is stopped after using a 1  $\mu\text{m}$  diamond suspension. Therefore, samples of group one were prepared as blocks, cut perpendicular to foliation. Afterwards, the blocks were ground and polished by 9, 3 and 1  $\mu\text{m}$  diamond suspension. The samples of group two and three were prepared as thin sections, cut perpendicular to foliation. CM in these samples is partly graphitized or composed of micro-crystalline graphite and

to avoid alteration due to polishing, the CM grains were measured beneath a translucent mineral, as suggested by Beyssac et al. (2003).

Raman spectra were acquired with the 488 nm laser line of a Horiba Jobin Yvon HR800-UV system with an attached Olympus BX-41 microscope. The instrumental setup included a 100x objective with 0.9 numerical aperture, the confocal hole diameter was set to 100  $\mu\text{m}$ , a grating with 600 l/mm and the recorded spectrum was centered at 1399.81  $\text{cm}^{-1}$ . Each spectrum represents 3 to 5 accumulations of 10 to 30 s. The on-sample laser power was controlled by density filters to less than 0.5 mW and immature samples were checked for burn marks or photo-bleaching after each measurement. The system was calibrated against the 520.4  $\text{cm}^{-1}$  line of silicon. In the case of metamorphic samples (sample groups two and three) care was taken to measure CM grains in parts of the sample which show an isotropic fabric. Obviously strained parts, showing elongated grains, were excluded. This was done because Bustin et al. (1995) showed that strain energy promotes graphitization and Barzoi (2015) proved that even on the thin section scale strain leads to differential graphitization and ultimately to temperature differences of up to 150  $^{\circ}\text{C}$  when the RSCM thermometer after Beyssac et al. (2002a) is applied. Depending on the abundance of grains, 20 to 50 CM grains were measured in samples of group one, and in group two and three 10 to 30 grains were analyzed.

Calcite-dolomite thermometry was performed on selected samples (see Table 5.2.1). Metamorphic temperatures were calculated according to the Fe-corrected calibration given by equation 31 in Anovitz and Essene (1987) as most calcites contain iron. Analyses were carried out with a JEOL JXA-8900RL electron microprobe. The beam diameter was set to 20  $\mu\text{m}$  at 15 nA with an acceleration voltage of 15 kV. Samples across the Pr1-in isograd were analyzed by X-ray powder diffractometry to verify the co-existence of pyrophyllite and kaolinite. XRD spectra were acquired using a Panalytical XPERT-MPD spectrometer with Cu-K $\alpha$  radiation at 40 kV and 30 mA. A spectral range of 2 to 40  $^{\circ}2\theta$  with a stepsize of 0.02  $^{\circ}2\theta$  was recorded for 4 s per step.

**5.3.2. Evaluation of Raman spectra.** The Raman spectrum of CM is composed of two major intensity accumulations in the regions of 1000 to 1500  $\text{cm}^{-1}$  and 1500 to 1700  $\text{cm}^{-1}$ , named here the D- and G-band-region (Fig. 5.3.1). The intensity distribution in these regions depends on the maturity stage or degree of graphitization and used excitation wavelength (Vidano et al., 1981; Wang et al., 1990; Wopenka and Pasteris, 1993; Yui et al., 1996; Pócsik et al., 1998; Matthews et al., 1999; Ferrari and Robertson, 2001; Castiglioni et al., 2004; Reich and Thomsen, 2004; Pimenta et al., 2007). In none graphitized CM, the spectrum is made up of two strong bands centered at 1330 to 1370  $\text{cm}^{-1}$  and 1590 to 1610  $\text{cm}^{-1}$ , depending on maturity stage and used excitation wavelength. The band centered at 1330 to 1370  $\text{cm}^{-1}$  shows additional shoulders on both sides (Fig. 5.3.1a). Thus, the CM spectra of none graphitized CM are usually curve-fitted by five Lorentz functions (Lahfid et al., 2010) or a mixture of four Lorentz and one Gauss function (Sadezky et al., 2005), i.e. several functions are needed to describe the intensity distribution in the D-band- and G-band-region (Fig. 5.3.1a). In the case of graphitic CM the intensity distribution in the D-band- and G-band-region reduces to three distinct bands, the D-band (s.s.), the G-band (s.s.) and the D'-band (Fig. 5.3.1b), and each band is commonly described by one Voigt function, namely the D1-, D2-, G-, and if present the D3-function (Beyssac et al., 2002a; Rantitsch et al., 2016). Instead of these 'classic' instructions (e.g. Beyssac et al., 2002a; Sadezky et al., 2005; Lahfid et al., 2010), a different curve-fitting approach is chosen here because the classical ones are prone to operator bias (Lünsdorf et al., 2014). Therefore, the user input independent

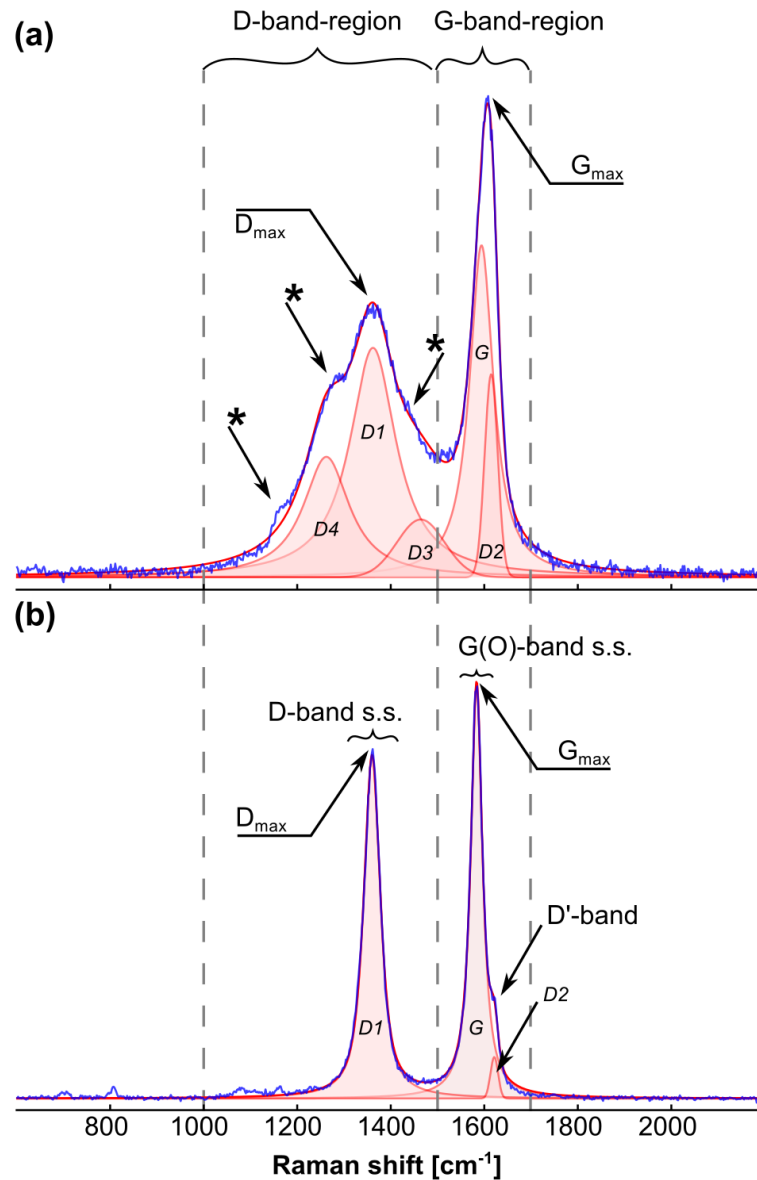


**Figure 5.3.1.** Nomenclature of CM Raman spectra. (a) A Raman spectrum of CM from very low grade metamorphic conditions. The intensity is distributed in the D-band- and G-band-region, from 1000 – 1500  $\text{cm}^{-1}$  and from 1500 – 1700  $\text{cm}^{-1}$ , respectively.  $D_{\text{max}}$  and  $G_{\text{max}}$  refer to the maximum intensity value in D-band- and G-band-region. The D-band-region is characterized by a central Raman band containing  $D_{\text{max}}$ . This band is often decorated by additional shoulders on the low- and high-wavenumber side (indicated by the asterisks). Due to the additional shoulders, the D-band-region is generally curve-fitted by 3 functions, commonly labeled D1, D3, and D4 (Sadezky et al., 2005; Lahfid et al., 2010). The G-band-region consists of one broad Raman band containing  $G_{\text{max}}$ . This Raman band is frequently curve-fitted by two functions, commonly labeled D2 and G (Beysac et al., 2002a; Sadezky et al., 2005; Lahfid et al., 2010). (b) A Raman spectrum of graphitic CM. The intensity is also distributed in the D-band- and G-band-region, but here the D1-function suffices to describe the single Raman band in the D-band-region. This band is the D-band sensu strictu, meaning that it is induced by defects or disorder in the graphite lattice. In the G-band-region the intensity is distributed between G(O)- and D¹-band, with G referring to graphite and O to ‘ordered’. The G- and D¹-band are sufficiently described by the G- and D2-functions.

software suite of Lünsdorf and Lünsdorf (2016), is used, that facilitates iterative, random based curve-fitting. The software simultaneously models the background and the Raman signal, approached by a 5th order polynomial and pseudo-Voigt functions (PV), respectively. The model is given by the sum of the PV functions and the polynomial which are fitted to the spectrum by randomly changing a single function parameter (center, height, half width at half maximum (HWHM), Gauss/Lorentz factor). This optimization process is partly guided, as the function parameters adhere to a set of constraints, i.e. HWHM must stay below a maximum value and negative function values are not allowed (see Lünsdorf and Lünsdorf, 2016 for details). The optimization continues until a threshold value is reached and the model will be extended by another PV function. This iterative process repeats itself until no more PV functions can be added to the model. The sum of the optimized PV functions yields a curve which is a smoothed, accurate, baseline corrected representation of the spectrum from which the D\_STA and G\_STA parameters are computed, with STA being the abbreviation for scaled total area (Lünsdorf and Lünsdorf, 2016).

**Table 5.3.1.** Raman shift intervals of Raman bands of typical, rock-forming translucent minerals.

Raman band interval [cm <sup>-1</sup> ]	Mineral
1083 - 1095	Carbonate
1070 - 1083	Carbonate
1432 - 1445	Carbonate
1744 - 1760	Carbonate
1095 - 1105	Plagioclase
1110 - 1118	Plagioclase
1155 - 1165	Quartz
1060 - 1070	Quartz

These parameters represent the sum of all intensity values in the interval from 1000 to 1800 cm<sup>-1</sup> of the spectral representation, with D\_STA being scaled to the maximum value in the D-band-region ( $D_{\max}$  in Fig. 5.3.1a) and G\_STA being scaled to the maximum value in the G-band-region ( $G_{\max}$  in Fig. 5.3.1a). D\_STA reliably describes the evolution of dispersed organic matter Raman spectra during coalification and graphitization (Lünsdorf, 2016; Lünsdorf and Lünsdorf, 2016).

Additional Raman bands will be present in the spectrum when measuring through a translucent mineral. To exclude these bands

during the computation of D\_STA or G\_STA they need to be removed from the model. This is achieved by defining Raman shift intervals for the additional mineral Raman bands in the STA interval (1000 – 1800 cm<sup>-1</sup>) and by removing any PV function with a center value that coincides with mentioned intervals (Table 5.3.1). The list of intervals can be adjusted and extended by the user if other phases than the ones shown in Table 5.3.1 occur in the sample.

## 5.4. Results

**5.4.1. Glarus Alps.** In the Glarus samples (Fig. 5.4.1), D\_STA decreases linearly with increasing temperature, while G\_STA decreases and above ca. 270 °C increases again. The position of the maximum value in the D-band-region shifts significantly from 1350 cm<sup>-1</sup> at ca. 180 °C to 1335 cm<sup>-1</sup> at about 270 °C and seems to increase again at ca. 300 °C. The position of the maximum value in the G-band-region continuously decreases from ca. 1607 cm<sup>-1</sup> to 1602 cm<sup>-1</sup>. The shift in the  $D_{\max}$  position is related to selective resonance Raman spectra of differently sized polyaromatic layers in the turbostratic structure of the CM. This effect is discussed in more detail in Lünsdorf (2016) and essentially shows that the growth of aromatic layers due to increasing temperature is reflected by the  $D_{\max}$ -position shift. The  $D_{\max}/G_{\max}$  intensity ratio is constant at ca. 0.6 for temperatures below 300 °C. Above 300 °C this ratio increases to 0.8 – 1.0.

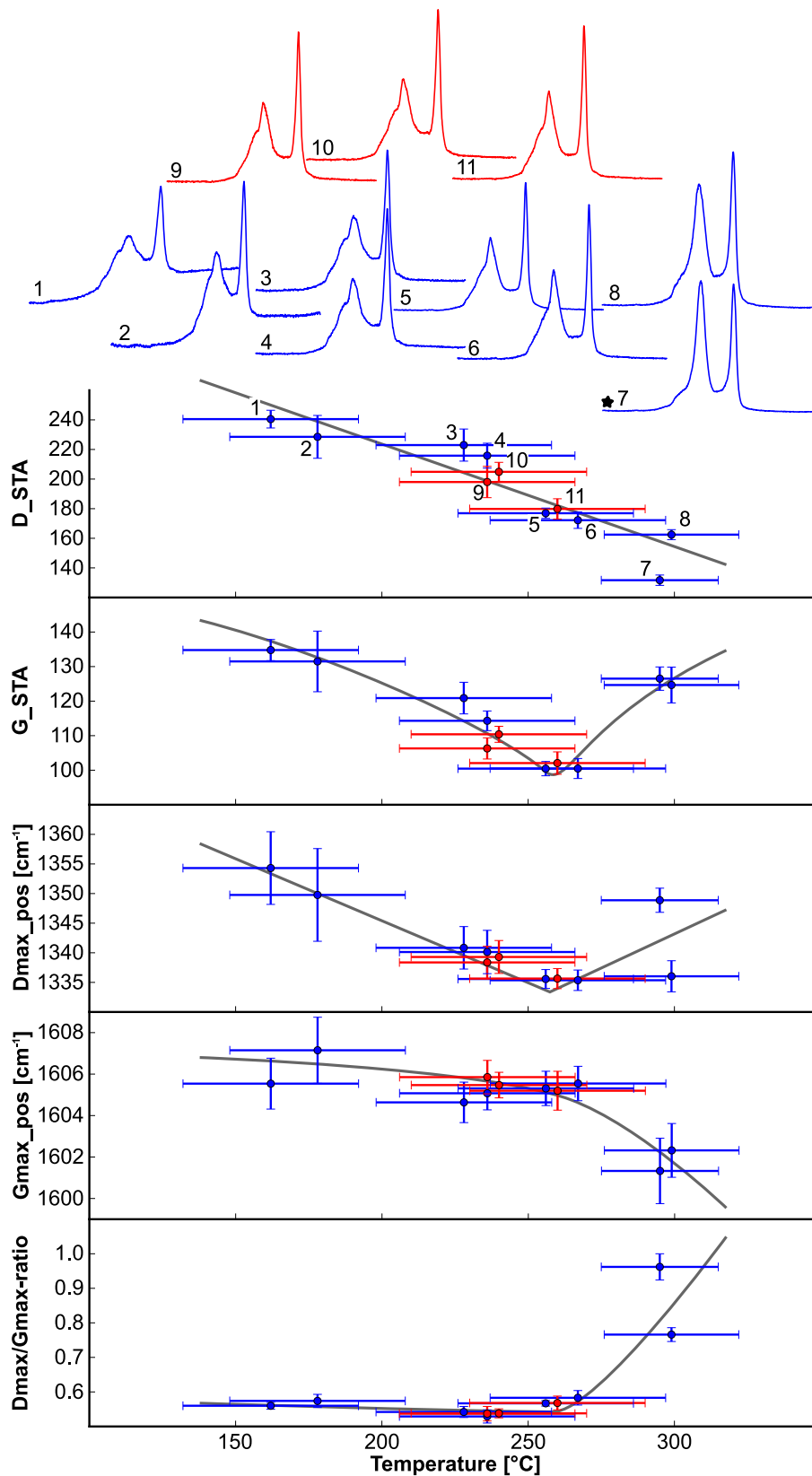


**Figure 5.4.1.** A compilation of the most indicative Raman parameters obtained on the samples from the Glarus Alps and across the pyrophyllite-in isograd. Representative spectra for each data point are shown on the top. Spectra of the Glarus profile are presented in blue and spectra of the pyrophyllite-in isograd in red. The numbers indicate which parameters are associated with each spectrum and the star marks a spectrum that shows large deviation in the Raman parameter  $D\_STA$  and the associated temperature information. The grey lines indicate the trends.

Frey (1987b) mapped the Prl-in isograd within the Helvetic Nappes by coexisting kaolinite and pyrophyllite. Three samples (KL16\_31, KL16\_35, KL16\_43) were collected along the Prl-in isograd from NE to SW (Fig. 5.2.1, samples 51, 53, 54 in Frey, 1987b). To verify the proximity to the isograd, all three samples were analyzed for pyrophyllite and kaolinite by XRD. Only sample KL16\_35 contained both minerals while in the other two neither pyrophyllite nor kaolinite was detected. However, these samples were used due to their proximity to the sampling locations of Frey (1987b). KL16\_31 north of Sargans and KL16\_35 east of Glarus show similar Raman parameters ( $D\_STA$  ca.  $200 \pm 8$ ) and Frey (1987b) reported a fluid inclusion homogenization temperature of  $236 \text{ }^\circ\text{C}$  for KL16\_31, i.e. sample 51 in Frey (1987b), while KL16\_43 shows lower  $D\_STA$  values (ca.  $180 \pm 7$ ) and a higher homogenization temperature of  $262 \text{ }^\circ\text{C}$ . The linear correlation of  $D\_STA$  and temperature of the Prl-in samples parallels the linear correlation of the Glarus samples. The Prl-in samples demonstrate that the STA approach is able to resolve relative temperature differences of at least  $20 \text{ }^\circ\text{C}$  for CM that underwent low temperature metamorphism in the sense of Frey (1987a). The temperature information linked to sample KL14\_1A (spectrum 7 in Fig. 5.4.1) was estimated to  $295 \pm 20 \text{ }^\circ\text{C}$  by Rahn (1996) using chlorite-thermometry and the empirical calibration after Cathelineau (1988). The  $D\_STA$  value suggests a higher temperature which is supported by temperature estimates after Ebert et al. (2007). Furthermore,  $D_{\text{max}}$  is more intense than  $G_{\text{max}}$ , which indicates temperatures well above  $300 \text{ }^\circ\text{C}$ .

**5.4.2. Schistes Lustrés in the Western Alps.** A profile in the Schistes Lustrés of the Cottian Alps (Fig. 5.2.2) covers metamorphic conditions of low blueschist facies,  $300$  to  $350 \text{ }^\circ\text{C}$  at  $12$  to  $13$  kbar at Fraiteve in the west, to beginning eclogite facies in the east at Finestre ( $450$  to  $530 \text{ }^\circ\text{C}$  at  $20$  to  $21$  kbar, Agard et al., 2001a,b, 2002). Agard et al. (2001a; 2002) provide average metamorphic conditions for five regions in the sampling area, i.e. Fraiteve, E-Fraiteve, Assietta, Albergian and Finestre (Fig. 5.2.2). The pressure and temperature conditions increase continuously from west to east (Agard et al., 2001a) and the carpholite/chloritoide as well as the lawsonite/epidote isograds cross the profile in the eastern parts (Fig. 5.2.2). The selected samples cover the regions of Fraiteve, E-Fraiteve, Assietta and Finestre and the central values of the P-T ellipses in Agard et al. (2001a) provide the temperature estimation with associated uncertainty. The sequence of CM Raman spectra shown in Figure 5.4.2 indicates strong spectral variability along the profile, which is especially true for the Assietta. Thus, it is unreasonable to assume a single, averaged temperature for the Assietta. Samples KL16\_10 and KL16\_11 are situated in the western part of the Assietta and close to the Car/Cld isograd, while KL16\_14 is situated in the eastern part of the Assietta closer to the Lws/Ep isograd. Due to the Fe-Mg composition of carpholite and chloritoide Agard et al. (2001b) deduced the reaction  $\text{Car} = \text{Qz} + \text{Cld} + \text{water}$  in a temperature range of  $350$  to  $400 \text{ }^\circ\text{C}$ . Therefore, samples KL16\_10 and KL16\_11 are associated with  $375 \text{ }^\circ\text{C}$  and an uncertainty of  $\pm 35 \text{ }^\circ\text{C}$  which is the temperature uncertainty provided for the Assietta-Albergian region in Agard et al. (2001a). For sample KL16\_14 the average temperature and its associated uncertainty ( $415 \pm 35 \text{ }^\circ\text{C}$ ) of the Assietta-Albergian region of Agard et al. (2001a) is assumed, as this sample is situated to the west of the Lws/Ep isograd, which marks a temperature of  $400$  to  $450 \text{ }^\circ\text{C}$  at  $14 \pm 2$  kbar (Agard et al., 2001a).

Figure 5.4.2 shows that  $D\_STA$  linearly decreases from  $325$  to ca.  $400 \text{ }^\circ\text{C}$  and linearly increases above.  $G\_STA$  values remain constant at ca.  $145$  from  $325$  to  $375 \text{ }^\circ\text{C}$ , rapidly drop to ca.  $65$  at  $415 \text{ }^\circ\text{C}$  and continue to decrease to ca.  $35$  at  $490 \text{ }^\circ\text{C}$ . The maximum value in the D-band-region linearly shifts from  $1356 \text{ cm}^{-1}$  at  $325 \text{ }^\circ\text{C}$  to  $1364 \text{ cm}^{-1}$  at  $490 \text{ }^\circ\text{C}$ , while the maximum value in the



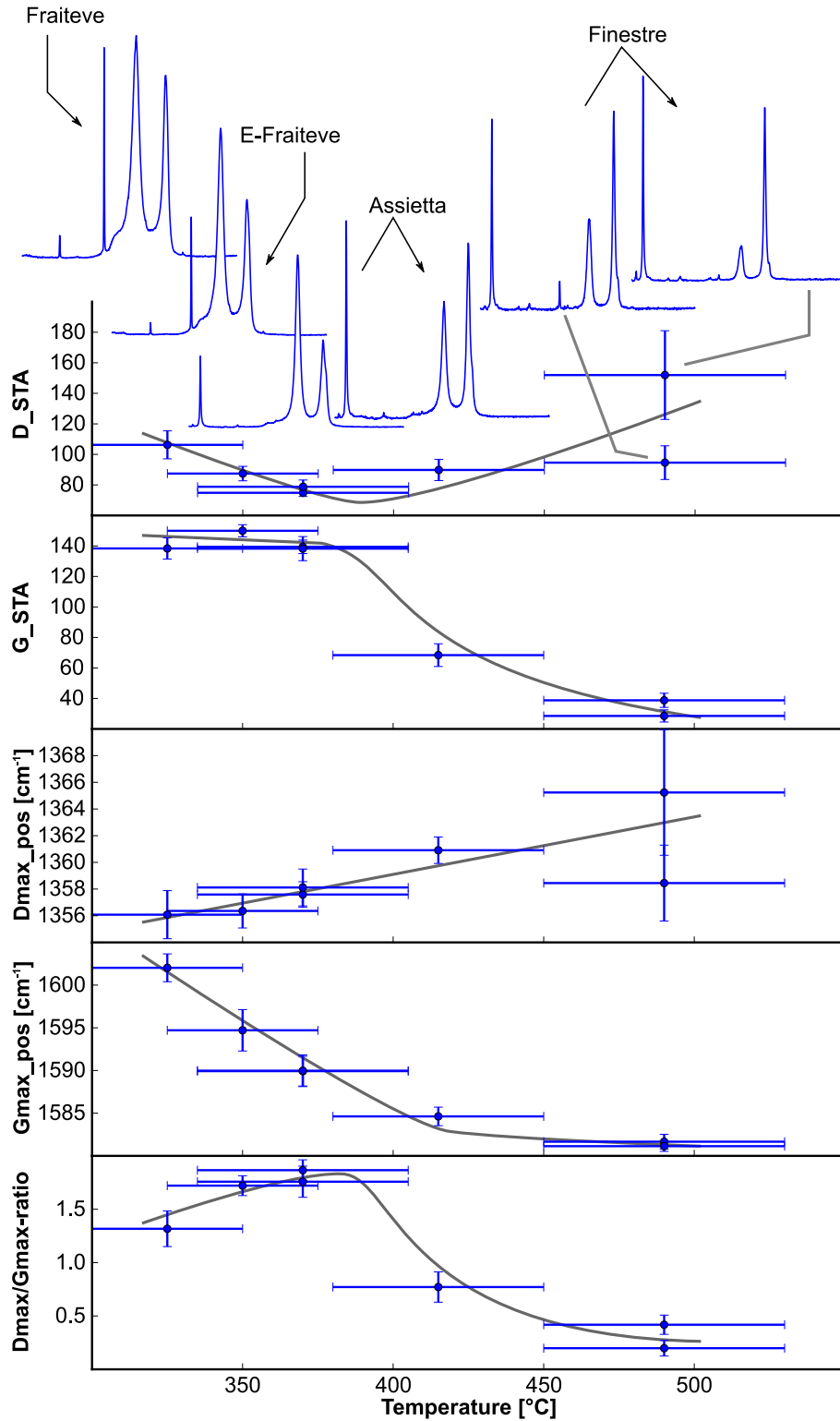


**Figure 5.4.2.** A compilation of the most indicative Raman parameters obtained on the Schistes Lustrés metasediments. Representative spectra for each data point are shown on the top. The additional sharp Raman bands in the spectra belong to calcite (ca. 1080 cm<sup>-1</sup>) and quartz (ca. 464 cm<sup>-1</sup>). The gray lines indicate the data trends.

G-band-region shifts from 1602 cm<sup>-1</sup> at 325 °C to 1585 cm<sup>-1</sup> at 415 °C and continuous to decrease

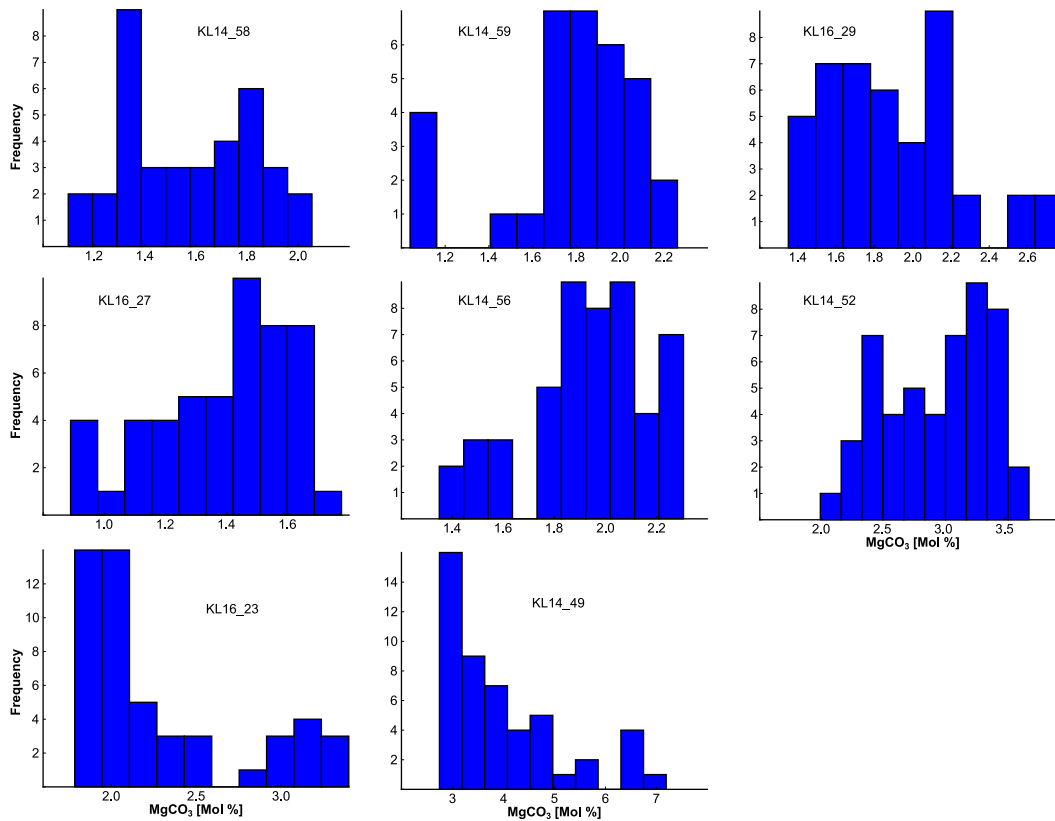


**Figure 5.4.3.** Histograms showing the distribution of  $MgCO_3$ -content in the calcites of the Bündnerschiefer and Lepontine Dome schists. The distributions are either bi-modal or skewed, indicating the impact of retrograde overprint that resulted in partial re-equilibration of carbonates.

to  $1582\text{ cm}^{-1}$  at  $490\text{ }^\circ\text{C}$ . The  $D_{\text{max}}/G_{\text{max}}$ -ratio increases from ca. 1.3 at  $325\text{ }^\circ\text{C}$  to ca. 1.8 at  $375\text{ }^\circ\text{C}$ , rapidly decreases to ca. 0.8 at  $415\text{ }^\circ\text{C}$  and continues to decrease to ca. 0.3 at  $490\text{ }^\circ\text{C}$ .

**5.4.3. Lepontine Alps and Bündnerschiefer.** In total 8 samples were collected of which seven compose a profile in the Bündnerschiefer series from Mesocco to Thusis (Fig. 5.2.1). Sample KL14\_49 was collected in the central Lepontine Alps and provides the highest peak metamorphic temperature of the sample set. Although, it does not belong to the Bündnerschiefer profile, it is included since KL14\_52 and KL16\_23 mark the transition from the Lepontine into the Bündnerschiefer units, at which the HP-LT metamorphic event was overprinted by Early Miocene Barrovian-type metamorphism (Wiederkehr et al., 2009). Thus, samples KL14\_49, KL14\_52 and KL16\_23 represent the amphibolite facies conditions of the Barrovian event and the other samples indicate high to low blueschist facies conditions of the subduction related HP-LT event. From the bimodal distributions of the Mg-content in calcite (Fig. 5.4.3) it is evident that most samples experienced a retrograde overprint during exhumation (Dachs, 1990). Consequently, average Cc-Dol temperatures underestimate any temperature estimates. However, the maximum Cc-Dol temperatures are in good agreement with the temperature gradient of Todd and Engi (1997). Thus,  $Cc\text{-Dol}_{\text{max}}$  is used as a minimum peak metamorphic temperature estimate (Essene, 1983). The certainty of the maximum value is conservatively estimated by the sample standard deviation. From  $370$  to  $610\text{ }^\circ\text{C}$   $D_{\text{STA}}$  linearly increases while  $G_{\text{STA}}$  exponentially decreases (Fig. 5.4.4). In the same temperature interval the maximum value in the D-band-region also increases linearly from  $1358\text{ cm}^{-1}$  to  $1366\text{ cm}^{-1}$ , which is related to an increasing asymmetry of the D-band (s.s.).

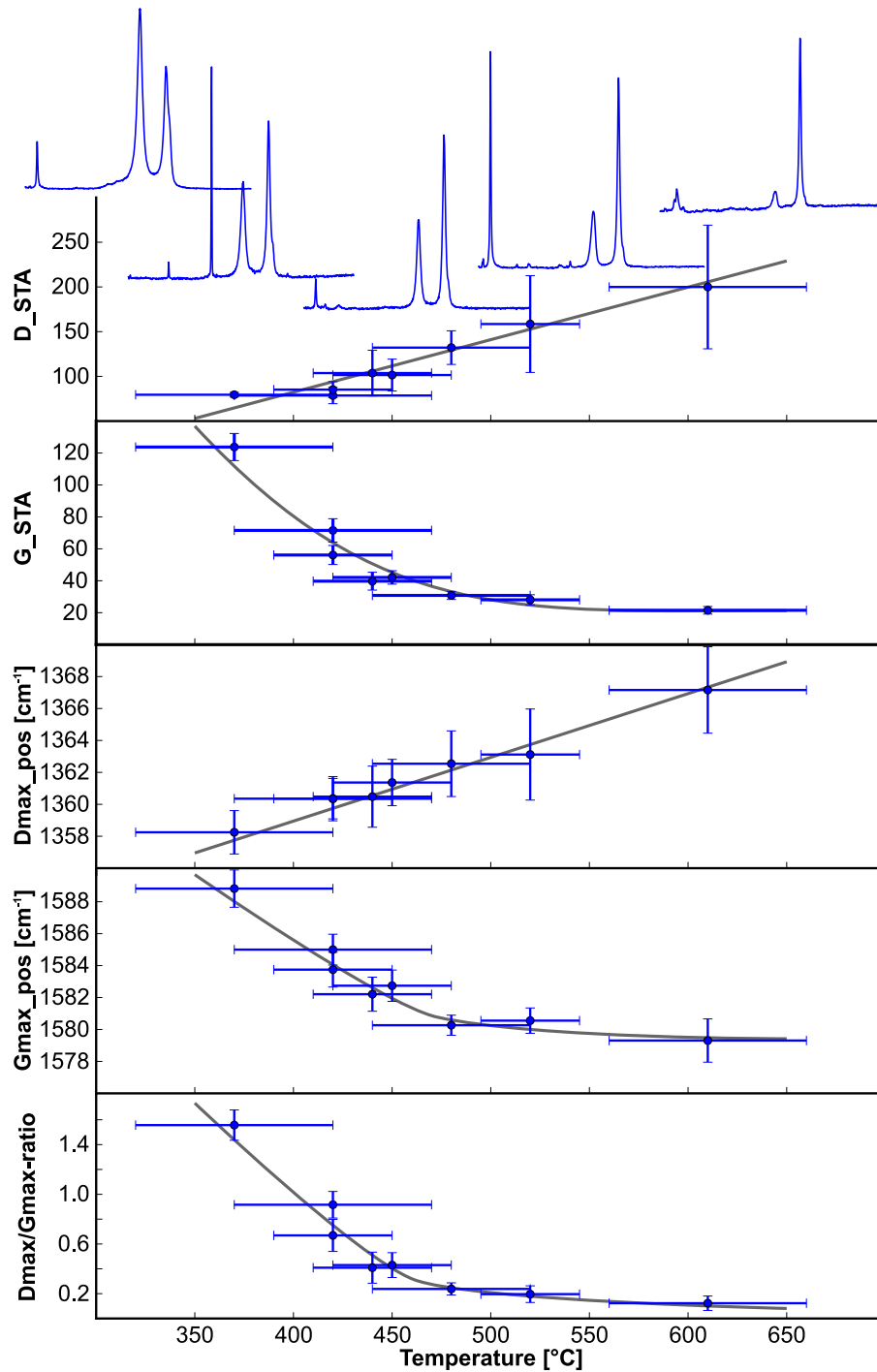


**Figure 5.4.4.** A compilation of the most indicative Raman parameters obtained on the Bündnerschiefer and Lepontine Alps samples. Representative spectra for each data point are shown on the top. The additional sharp Raman bands in the spectra belong to calcite (ca.  $1080\text{ cm}^{-1}$ ) and quartz (ca.  $464\text{ cm}^{-1}$ ). The gray lines indicate the data trends.

The maximum value in the G-band-region shifts from  $1590\text{ cm}^{-1}$  at  $370\text{ °C}$  to ca.  $1580\text{ cm}^{-1}$  at ca.  $450\text{ °C}$ . The  $D_{\text{max}}/G_{\text{max}}$ -ratio shows a similar trend as  $G\_STA$  (Fig. 5.4.4).

**5.4.4. A revised geo-thermometer.** The presented sample series covers deep burial to metamorphic temperatures from about  $160\text{ °C}$  to ca.  $600\text{ °C}$ . Figure 5.4.5 shows the composite

trends in  $D\_STA$ ,  $G\_STA$ ,  $D_{max\_pos}$ ,  $G_{max\_pos}$  and the  $D_{max}/G_{max}$ -ratio across the whole temperature range. They are separated into a low temperature zone, a transition zone and a high temperature zone. All parameters change significantly in the transition zone between ca. 300 °C and ca. 400 °C. This zone is marked by significant changes in the intensity distribution and positions of the maximum values in the G- and D-band-regions. Up to ca. 270 °C  $D_{max}$  is always lower than  $G_{max}$  ( $D_{max}/G_{max}$  ca. 0.6) and the G-band-region is centered at ca. 1605  $cm^{-1}$ . Between 300 °C and 375 °C  $D_{max}$  increases and surpasses the value of  $G_{max}$ . This first intensity inversion, when the  $D_{max}/G_{max}$ -ratio increases from values less than 1 to values greater than 1, is correlated with a temperature of ca. 300 °C to 320 °C.  $D_{max}$  reaches its maximum intensity at ca. 375 °C ( $D_{max}/G_{max}$  ca. 1.8) and decreases to a  $D_{max}/G_{max}$ -ratio of ca. 0.8 at 415 °C while passing through a second inversion point at about 400 °C, at which  $D_{max}$  becomes lower than  $G_{max}$  again. In the same temperature interval the position of  $G_{max}$  shifts from ca. 1602  $cm^{-1}$  to ca. 1585  $cm^{-1}$ , the D'-band develops as a distinguishable shoulder on the G-band (s.s.) at ca. 1620  $cm^{-1}$  and the D-band (s.s.) shifts to ca. 1360  $cm^{-1}$ . All these characteristics are typical for Raman spectra of micro-crystalline graphite recorded with an excitation wavelength of 488 nm (Tuinstra and Koenig, 1970). Thus, after the transition zone, most of the CM has changed into micro-crystalline graphite. The  $G\_STA$  parameter passes through a maximum in the transition zone and decreases afterwards while the  $D\_STA$  parameter continuously decreases linearly to the end of the transition zone and linearly increases again after the transition zone. Therefore, the thermometer can solely rely on the  $D\_STA$  parameter. However, after the second  $D_{max}/G_{max}$ -inversion point, the spread of  $D\_STA$  values for a given sample increases. This is because the intensity values are scaled to  $D_{max}$  and thus, small intensity differences in  $D_{max}$  within a sample lead to over-amplification of the strong, relative intensity increase in the G-band-region. This over-amplification can be compensated for if the intensity values are scaled to  $G_{max}$ , i.e. using the  $G\_STA$  parameter. Up to the second  $D_{max}/G_{max}$ -inversion point this parameter does not produce a consistent correlation with temperature, while after the second  $D_{max}/G_{max}$ -inversion point a negative, exponential correlation becomes evident (Fig. 5.4.5).

A reliable method is needed to decide which STA parameter to apply. This method is given by the G-shape-factor. It is the ratio of the average intensity value in the Raman shift interval from 1575  $cm^{-1}$  to 1590  $cm^{-1}$  (G-band position *sensu stricto*) divided by the average intensity value in the Raman shift interval from 1610  $cm^{-1}$  to 1630  $cm^{-1}$  (D'-band) and describes the characteristic progression of intensity distribution in the G-band-region from ca. 160 °C to ca. 600 °C (Fig. 5.4.6). From ca. 160 to ca. 300 °C the intensity distribution is roughly symmetric with  $G_{max}$  situated at 1600  $cm^{-1}$  to 1610  $cm^{-1}$ , resulting in a G-shape-factor of about 1. Neither the G-band (s.s.), nor the D'-band can be resolved properly in the G-band-region in this temperature interval. At about 350 °C the maximum intensity in the G-band-region shifts towards lower wavenumbers and the D'-band becomes visible, which is marked by increasing G-shape-factor values. After the second  $D_{max}/G_{max}$ -inversion point is reached at about 400 °C, the maximum intensity value in the G-band region stays at the G-band (s.s.) position (i.e. 1582  $cm^{-1}$ ). With increasing temperature the intensity distribution in the G-band-region becomes narrower and the average intensity value in the D'-band interval decreases which results in increasing G-shape-factor values (Fig. 5.4.6).

In Figure 5.4.7 the G-shape-factor, the natural logarithm of  $D\_STA$  and  $G\_STA$  are plotted against the metamorphic temperature. The natural logarithm of  $D\_STA$  and  $G\_STA$  is used because especially  $G\_STA$  shows an exponential trend after the transition zone. Up to temperatures of about 350 °C the G-shape-factor remains constant at ca. 1. Above 350 °C the G-shape-factor

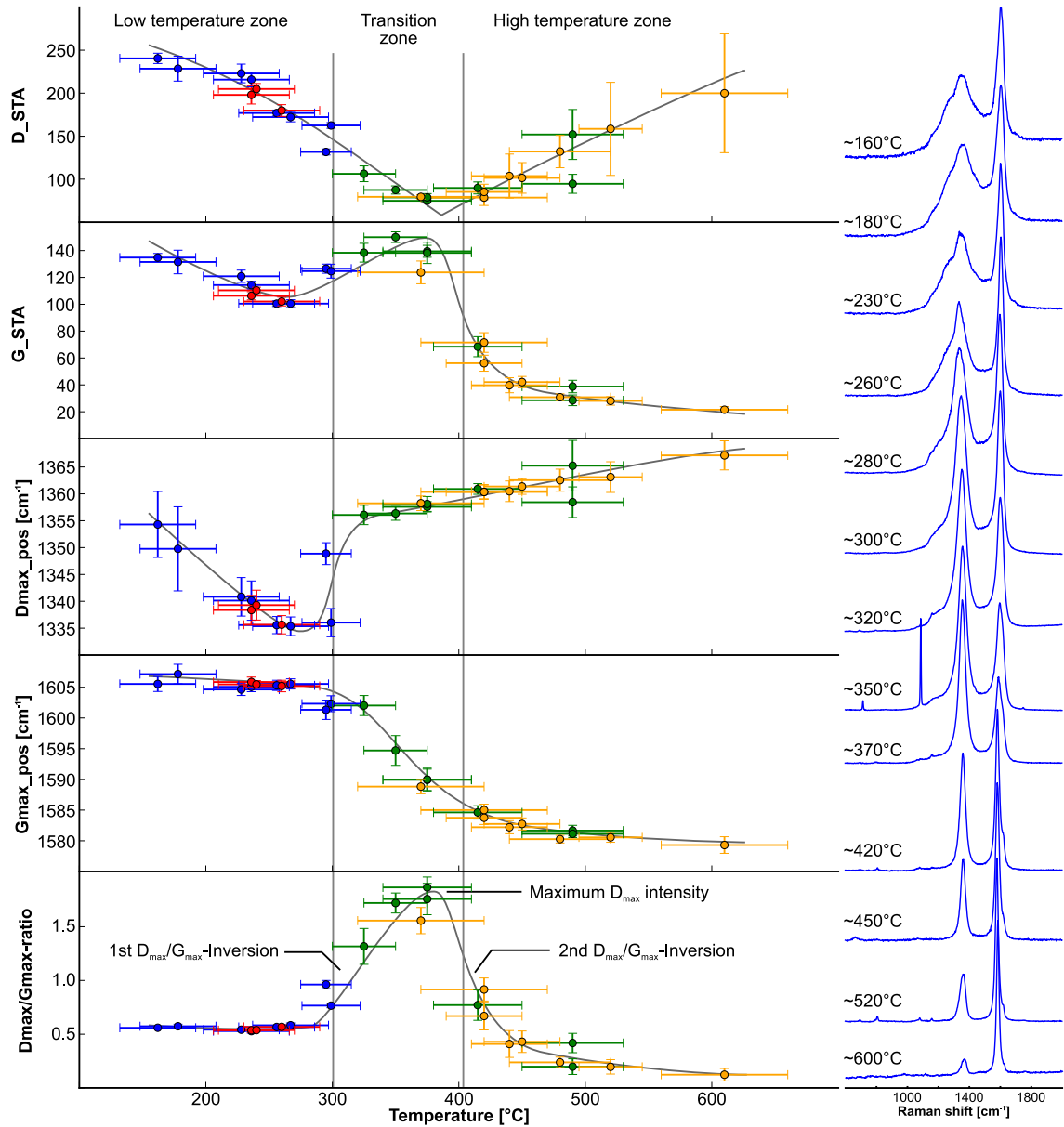


**Figure 5.4.5.** A compilation of the results of the complete reference sample series. Representative spectra of the temperature intervals are shown on the right. Every parameter plotted, changes in the transition zone except  $D\_STA$ . Blue: Glarus Alps samples, red: Prl-in samples, green: Schistes Lustrés samples, yellow: Lepontine Alps and Bündnerschiefer samples. The gray lines indicate the data trend.

rapidly increases and the slope maximizes in the temperature interval between ca. 370 °C and 450 °C. From 450 to 600 °C the slope decreases and remains constant. Close before the second  $D_{max}/G_{max}$ -inversion (ca. 380 °C),  $\ln(D\_STA)$  is at its minimum (ca. 4.2),  $\ln(G\_STA)$  is at its maximum (ca. 5.1) and the slope of the G-shape-factor begins to increase. After this interval at about 420 °C the slope of the G-shape-factor rapidly increases,  $\ln(G\_STA)$  drops to ca. 4.2 and  $\ln(D\_STA)$  rises to ca. 4.5. These significant changes in parameters are related to the second  $D_{max}/G_{max}$ -inversion. It is also evident that  $G\_STA$  and  $D\_STA$  give similar values at the second  $D_{max}/G_{max}$ -inversion and because the intensity in the D-band-region gradually decreases after this inversion point,  $G\_STA$  also gives decreasing values while  $D\_STA$  gives increasing values (Fig. 5.4.7a). By using the G-shape-factor, spectra that have crossed the second  $D_{max}/G_{max}$ -inversion

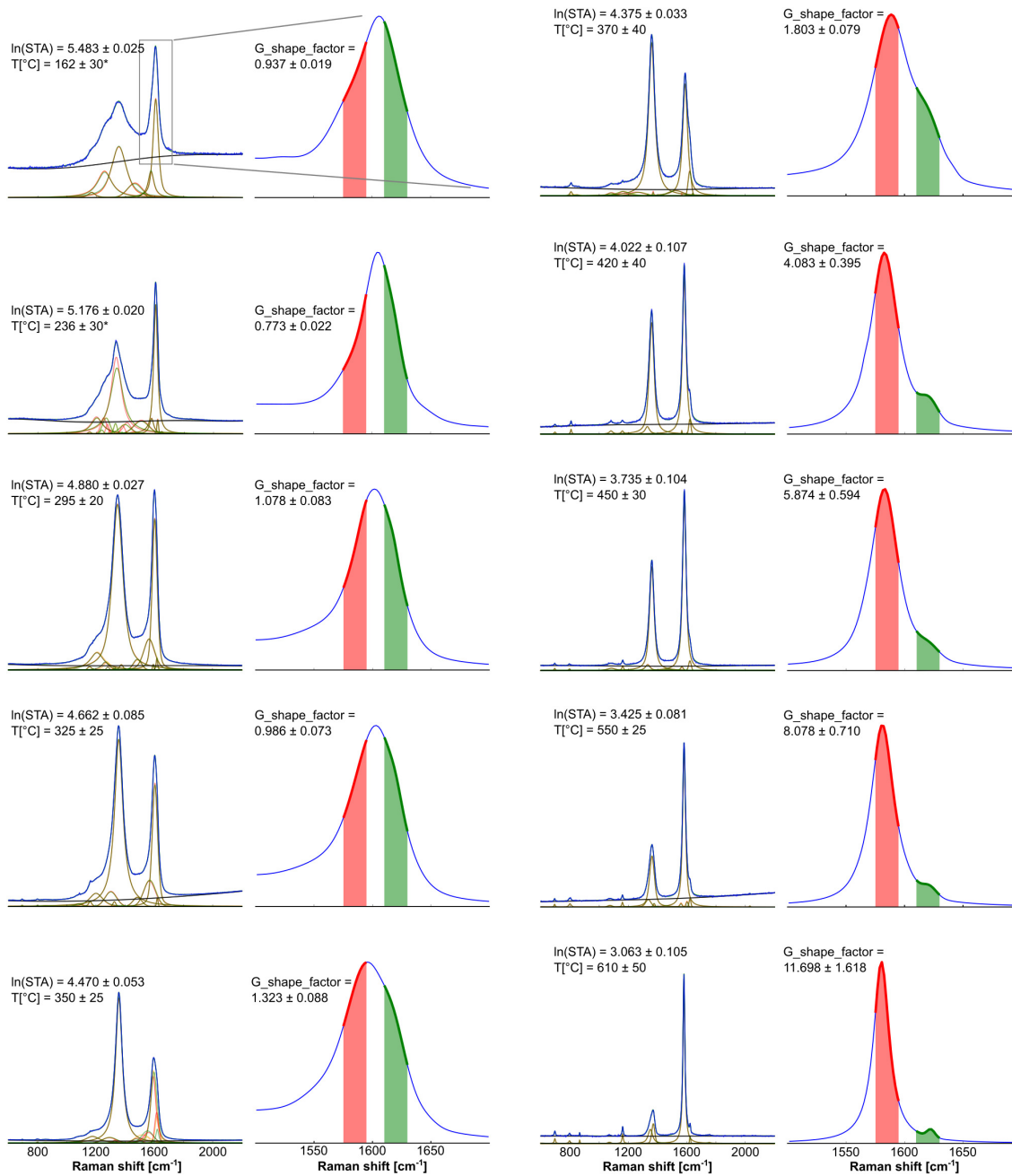


**Figure 5.4.6.** Selected examples that demonstrate the intensity distribution in the G-band-region of the CM Raman spectrum during maturation and graphitization, i.e. the evolution of the G-shape-factor.

are identified. Spectra at the second inversion point, with a  $D_{\max}/G_{\max}$ -ratio of about 1, a distinguishable D'-band and a  $G_{\max}$  situated at ca.  $1585 \text{ cm}^{-1}$  show G-shape-factors of 2.7 to 3.2. Hence, the critical G-shape-factor is set to 2.5 (Fig. 5.4.7a). This allows connecting the linear  $\ln(D\_STA)$  values of the low temperature and transition zones with the linear  $\ln(G\_STA)$  values of the high temperature zone, which results in linearly decreasing  $\ln(STA)$  values from ca.  $160 \text{ }^\circ\text{C}$  to ca.  $600 \text{ }^\circ\text{C}$  (Fig. 5.4.7b). Weighted orthogonal distance regression (Boggs et al., 1988, 1992) was used to determine the coefficients of the linear model (eq. 5.4.1) and to account for the uncertainties in both variables, i.e. temperature and  $\ln(STA)$ , see Table 5.2.1.

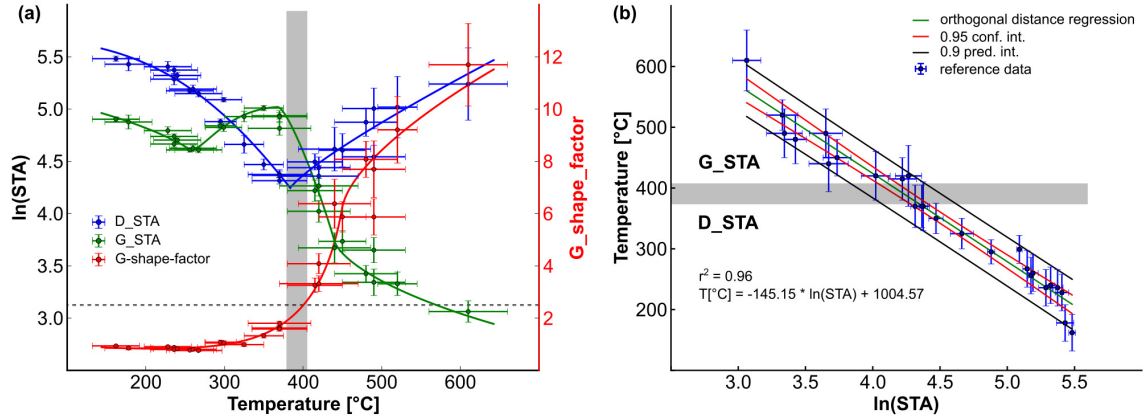


**Figure 5.4.7.** (a) A plot of  $\ln(D\_STA)$ ,  $\ln(G\_STA)$  and the  $G$ -shape-factor. Until the end of the transition zone (marked by gray bar), the  $\ln(D\_STA)$  decreases linearly and  $\ln(G\_STA)$  shows varying values. After the transition zone  $\ln(D\_STA)$  increases, showing increasing spread of values, while  $\ln(G\_STA)$  decreases linearly with less scattered values. The  $G$ -shape-factor rapidly increases after the transition zone and values greater than 2.5 (stippled line) mark the end of the transition zone. (b) Because the  $G$ -shape-factor identifies the end of the transition zone it allows to connect  $\ln(G\_STA)$  to  $\ln(D\_STA)$ . The combined  $\ln(STA)$  data set shows a linear correlation with peak metamorphic temperature from ca. 160 to ca. 600 °C.

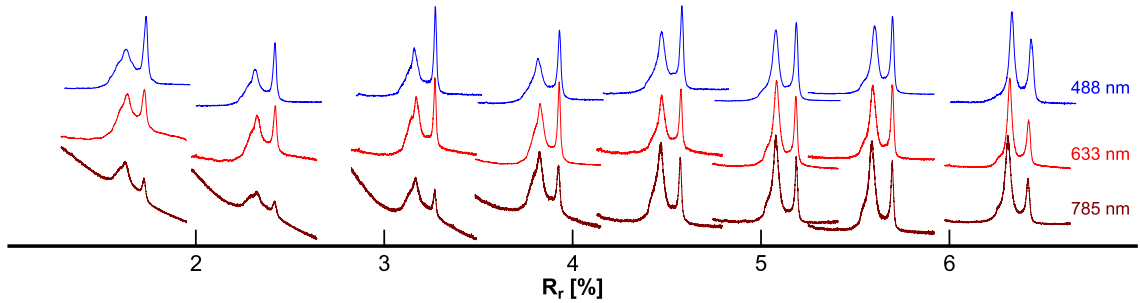


**Figure 5.4.8.** Raman spectra of CM, acquired with different excitation wavelengths, from very low grade metamorphic to lower greenschist facies conditions. Although the spectra are of different shape, the general evolution with increasing metamorphism is comparable. (after Lünsdorf and Lünsdorf, 2016). Note the pronounced baseline increase with increasing excitation wavelength for the very low grade metamorphic samples.

$$(5.4.1) \quad T[°C] = -145.15 \cdot \ln(STA) + 1004.57$$

where STA refers to scaled total area. The reference to the value used for scaling ( $D_{\max}$  or  $G_{\max}$ ) has been omitted since both parameters ( $G\_STA$ ,  $D\_STA$ ) were used during regression. Based on a 90 % confidence level, an uncertainty of ca.  $\pm 40$  °C is assigned to temperature values predicted from eq. 5.4.1 (Fig. 5.4.7b). This uncertainty is in agreement with values reported in Beyssac et al. (2002a) and Aoya et al. (2010).

The proposed STA-RSCM method can be used as a geothermometer when a 488 nm laser is used, and will also work with different wavelengths, because the general spectral evolution is similar when other lasers are used (Fig. 5.4.8). However, the  $G$ -shape-factor will probably need adjustment according to the used wavelength, because the position of the  $D'$ -band is wavelength dependent and shows a dispersion of ca.  $10 \text{ cm}^{-1}/\text{eV}$  (Pimenta et al., 2007). Thus, if a 532 nm laser is used, the excitation energy is decreased by 0.21 eV, compared to 488 nm, and the  $D'$ -band would down-shift by ca.  $2 \text{ cm}^{-1}$  which results in a  $D'$ -band interval of ca. 1608 to ca. 1628  $\text{cm}^{-1}$ .

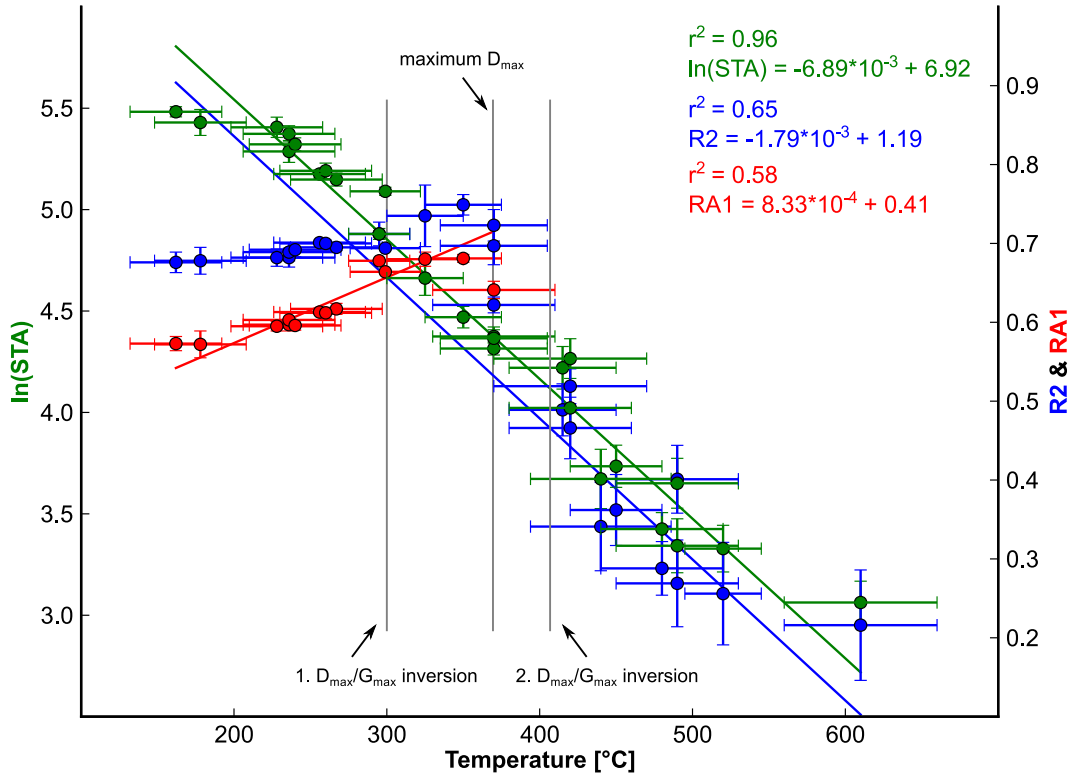


**Figure 5.4.9.** Comparison of the R2 and RA1 ratio with the STA parameter. The RA1 ratio is applicable until the point of maximum  $D_{max}$  intensity, and the R2 ratio shows no variation until the first  $D_{max}/G_{max}$ -inversion, a slight increase to the maximum  $D_{max}$  value and linear decrease afterwards. The STA parameter shows a linear correlation to metamorphic temperature across the whole temperature range. The plotted regression lines are derived from orthogonal distance regression.

The advantage of the STA-RSCM method compared to the other geothermometers of Beyssac et al. (2002a), Aoya et al. (2010) and Lahfid et al. (2010) is its consistency over a large temperature range (160 °C to 600 °C), while the others are only valid for either higher temperatures, i.e. more than 320 °C (Beyssac et al., 2002a; Aoya et al., 2010), or lower temperatures, i.e. less than 300 °C (Lahfid et al., 2010). A comparison of the geothermometers, e.g. calculated against known temperature, was not possible, because the spectra were acquired with a 488 nm laser. The calibration lines given in Beyssac et al. (2002a) and Lahfid et al. (2010) are only valid for spectra recorded with a 514.5 nm laser. Using 488 nm or any other excitation wavelength, the R2- or RA1-ratios of the obtained CM Raman spectra cannot be used to calculate temperature values according to the calibration lines of Beyssac et al. (2002a) or Lahfid et al. (2010). Nevertheless, the parameters or ratios that describe the spectra can be compared (Fig. 5.4.9). The RA1-ratio linearly increases until  $D_{max}$  reaches its maximum value at ca. 350 to 370 °C, after which a D4-function can no longer be used during curve-fitting, because the additional shoulders in the D-band-region are no longer resolvable (Fig. 5.3.1a and Fig. 5.4.5). Thus, the RA1-ratio is not usable beyond this point. The R2-ratio describes spectra from the low temperature and transition zone, because the intensity distribution in the D-band-region is fitted by only one Voigt function in the approach of Beyssac et al. (2002a). This ratio is basically constant (ca. 0.69) in the low temperature zone and increases to 0.75 from the first  $D_{max}/G_{max}$ -inversion to the maximum value of  $D_{max}$ , after which it linearly decreases to ca. 0.2 at ca. 600 °C.



Kouketsu et al. (2014) proposed a scheme that is valid over a temperature range of 165 °C to 655 °C. However, their method requires seven different curve-fitting approaches and it is up to the user to decide which spectrum has to be evaluated with any of these approaches. This procedure will be prone to subjectivity and slow due to the constant manual intervention. To increase comparability of temperature values derived from RSCM we propose in the following a methodical protocol (STA-RSCM) for a more objective evaluation of CM spectra for geothermometric purposes.

#### 5.4.4.1. *Proposed Protocol.*

- Preparation of polished rock fragments from samples that experienced very-low to low grade metamorphism:
  - Cut the rock samples perpendicular to foliation and embed them in the usual resin mount.
  - Grind the samples using emery paper and polish them in several steps with diamond suspension on a hard polishing cloth to avoid relief. The finest diamond suspension cannot be finer than 1  $\mu\text{m}$  (see Lünsdorf (2016) for details).
- Preparation of polished thin sections from samples of greenschist/blueschist and higher metamorphic overprint:
  - Prepare the samples by multi-step polishing for Raman analysis of CM below transparent, rock-forming minerals (follow the instructions given in e.g. Beyssac et al., 2002a).
- Measurement:
  - It is advised to use a blue or near UV excitation wavelength in order to reduce the fluorescence and increase the Raman signal of low mature CM.
  - When analyzing polished rock fragments of low-grade samples, consider the maceral type and measure the Raman signal of vitrinite particles (Taylor et al., 1998) whenever possible.
  - When analyzing thin sections, avoid sheared/strained zones.
  - Try to analyze 30 particles, 50 if possible.
  - Avoid photo-bleaching or thermal destruction of the CM by attenuating the laser power.
  - For proper baseline modeling, make sure that enough baseline is present in the spectrum, for CM a spectral range from 400 to 2200  $\text{cm}^{-1}$  is sufficient. If this range does not fit into one spectral window, use the extended acquisition mode.
- Evaluation:
  - To exclude operator bias and to apply the proposed geothermometer, use the IFORS software (Lünsdorf and Lünsdorf, 2016) to curve-fit CM Raman spectra. IFORS is available upon request from the first author or can be downloaded from: <http://www.sediment.uni-goettingen.de/download/>
  - If any parameters are changed in IFORS for a customized curve-fitting, report the changed parameters.
  - If Raman bands of additional phases are present in the spectrum, exclude these bands before computing the results by indicating their Raman shift intervals.
- Calibration:

- Measure and evaluate CM Raman spectra from reference samples, following the above protocol. The described reference series is available upon request from the first author.
- Use the orthogonal distance regression script of the IFORS software on your  $\ln(\text{STA})$  and temperature values to generate a calibration line specific to your laboratory.

Opposed to the current practice to reuse a published calibration line, the STA-RSCM method, following the proposed protocol and using the presented reference series, allows any laboratory to create their own specific calibration curve for RSCM-geothermometry. In this way effects of the measuring conditions bias (Lünsdorf et al., 2014), especially the effect of different excitation wavelengths, on the RSCM-temperatures is omitted and the spectral processing bias (Lünsdorf et al., 2014), including the operator bias is excluded. To advance the method further and to increase the quality of the reference series the scientific community is encouraged to extend the series with additional samples.

### 5.5. Conclusions

This study introduces a reference series of CM-bearing rock fragments that experienced a maximum thermal overprint between 160 and 600 °C determined by independent methods. This sample series is available from the first author on request and is supposed to be extended and refined by the scientific community. On the basis of this sample series a methodological protocol has been established that will help to increase the overall comparability of temperature information derived from RSCM analysis. Using the automated curve-fitting software (Lünsdorf and Lünsdorf, 2016) the spectral processing bias (Lünsdorf et al., 2014) can be reduced significantly and the measuring conditions bias, which is primarily due to the usage of different excitation wavelengths (Lünsdorf et al., 2014), can also be reduced by using the reference sample series to calibrate the STA-RSCM geothermometer for each laboratory individually.

## Discussion and summary

### 6.1. Discussion

Assessing the peak metamorphic temperature is of great interest in geodynamic modeling and interpretation of prograde metamorphism. Common techniques to infer the P-T conditions of metamorphism require the identification of equilibrium phase transitions and often involve exchange and net transfer reactions (Bucher and Grapes, 2011). These methods rely on the correct identification of equilibrium textures, an adequate mineral assemblage, correct thermodynamic data and can be altered by retrograde re-equilibration of the mineral assemblage. Additionally, the determination of mineral composition requires electron microprobe analysis, which is an accurate method, but time and cost intensive when compared to Raman spectroscopy. Considering this, the RSCM-geothermometer of Beyssac et al. (2002a) is an attractive method. It is an empirical geothermometer calibrated against temperature information derived by the classic methods mentioned above and thus, incorporates their analytical as well as their 'geological' error, which is estimated by Beyssac et al. (2002a) to  $\pm 50$  °C. Hence, the accuracy of the RSCM-geothermometer is comparable with the common geothermobarometers. The relative ease of applicability, theoretically no sample preparation is needed, and the availability of organic matter in nearly every sedimentary or metasedimentary rock, rapidly advanced the use of this method.

Nevertheless, there are methodical aspects that need to be considered and have already been recognized by several authors (Wopenka and Pasteris, 1993; Beyssac et al., 2003; Aoya et al., 2010), but no standardized protocol has been presented. Therefore it has been evaluated in this thesis which of the methodical aspects has the strongest impact on the comparability of the RSCM-data and the automated STA-RSCM method has been introduced and a reference sample series initialized. Combination of the STA-RSCM method with the reference series results in a generalized methodical framework and the revised STA-RSCM-geothermometer. The proposed methodical framework will help to increase the comparability of RSCM-geothermometric data and because the reference series will be available to the scientific community, additional working groups will be able to safely apply the method by calibrating their own STA-RSCM-geothermometer to the reference series. However, sample heterogeneity of the reference samples will still introduce variability to the calibrations and it is therefore important to extend the reference series and to select the least heterogeneous samples. In addition, further investigation is required considering the effect of shear stress on graphitization and the resulting implications for RSCM-thermometry (Barzoi, 2015) and the effect of different types of metamorphism need to be analyzed further, most importantly contact metamorphism.

In chapter 5 and in Lünsdorf and Lünsdorf (2016) it has been shown that the STA-RSCM method is also valid for low temperature metamorphism, with a lower temperature limit of approximately 160 °C. Furthermore, a distinct correlation between the random and maximum vitrinite reflectance values and the D\_STA Raman parameter has been documented (Lünsdorf, 2016) and the obvious question is: "Can the STA-RSCM-geothermometer be calibrated to temperatures lower

than 160 °C?” Due to the mentioned correlation, which is valid from ca. 0.5 % to ca. 8 %  $R_{\max}$ , Lünsdorf (2016) suggested that D\_STA and vitrinite reflectance are analogue methods. However, more research is needed to determine the resolution of the STA-RSCM method, in terms of maturity, i.e. is the D\_STA parameter able to resolve reflectance differences of, for instance, ca. 0.1 % in the range of 0.5 % to 2.5 %  $R_r$ ? At the moment the STA-RSCM method is capable of discriminating different maturity stages, i.e. is the maturity of the sample lower than the 'oil-window' stage, between the 'oil-window' and the 'gas-window', or higher than the 'gas-window' stage? Since a certain amount of time is needed for vitrinite reflectance to equilibrate with a given formation temperature, the heating rate and therefore rate of subsidence and geothermal gradient are important factors in the interpretation of vitrinite reflectance data and usually in fast subsiding basins the reflectance values lag behind temperature (Taylor et al., 1998). Thus, temperature estimations based solely on vitrinite reflectance data are always debatable. It is likely that STA-RSCM will behave similar and that a 'peak-diagenesis' temperature can not be derived directly by the method. On the other hand, if both methods are analogue to each other, it should be possible to introduce the STA-RSCM method to basin modeling software, similar to the Easy-Ro approach after Sweeney and Burnham (1990). However, experimental studies are needed for verification and it would be advisable to further elucidate the analogy of both methods, because Raman microspectroscopy has several advantages when compared to classic reflectance measurement.

According to Borrego et al. (2006) reflectance measurements of vitrinites dispersed in sedimentary rocks are limited by 1) particles being too small 2) minerals surrounding the vitrinite particle 3) poor polishing and 4) the reflectance of vitrinite particles can be suppressed. Point one and two are of no concern for STA-RSCM method, due to the high spatial and axial resolution of the confocal system, which allows to analyze very small sample volumes, particles of less than 10  $\mu\text{m}$  diameter can be measured safely. Any additional mineral phase will be recognized in the Raman spectrum and the measurement can either be repeated on a mineral free location or the spectrum can be corrected for the additional mineral Raman bands as shown in chapter 5. Lünsdorf (2016) demonstrated that point 3 is also irrelevant for the STA-RSCM method because the polish quality of the sample surface has virtually no effect on the Raman spectrum of diagenetic organoclasts. The fourth point needs more research to evaluate if the Raman spectra of suppressed and unsuppressed vitrinites give similar STA values. Since the suppression of vitrinite reflectance is often related to the presence of abundant liptinite and impregnation of the vitrinite by aliphatic species (Carr, 2000), it is likely that fluorescence of the aliphatic species will become an issue. Besides all these apparent advantages of the Raman method, the most important factor in dispersed organic matter reflectance studies is the correct identification of the primary vitrinite. This requires a microscopical system that allows the usage of immersion objectives to increase contrast and resolution. Also, the fluorescence image of the sample must be made available. Thus, a combination of a typical vitrinite reflectance microscope with a Raman spectrometer system would be a logic solution.

As argued in Lünsdorf (2016) Raman spectra of CM are resonance Raman spectra and therefore subgroups of the macro-molecular CM are selectively analyzed; in the case of vitrinite these subgroups are most likely linear aromatic compounds and polycyclic aromatic hydrocarbons. These aromatic compounds are also found in Kerogen 1 and asphaltenes/bitumen (Ruiz-Morales, 2002) and should give similar Raman spectra as vitrinite. This has strong implications for the maturity assessment in gas shale exploration, because marine gas shales often lack vitrinites while solid bitumen is abundant. Thus, the effect of the organic precursor on the Raman spectrum needs further

investigation. To this end artificial maturation experiments have been conducted and first preliminary results indicate that larger polycyclic aromatic hydrocarbons are generated faster in kerogen type I than in type III. This implies that the Raman spectra of type I and type III kerogen will probably evolve differently during early maturation. Additional research is needed to depict the Raman spectroscopic maturation pathways of the different kerogen types. If the 'Raman maturation pathway' of kerogen type I is known, maturity studies in pre-Silurian (vitrinite free) sediments should be possible.

## 6.2. Summary

The general aim of the thesis to provide means to increase the comparability of the RSCM geothermometer was laid out in Lünsdorf et al. (2014). Nine tests were conducted by the authors to elucidate three groups of biasing factors in finding RSCM parameter ratios. These groups compile (1) biasing factors intrinsic to the spectral curve-fitting, (2) biasing factors intrinsic to the CM and (3) biasing factors intrinsic to the experimental design and specific Raman system used. The results of the tests indicated that the curve-fitting procedure has a major impact on the RSCM results, followed by the operator dependent subjectivity, which is heavily influenced by subjective baseline correction. Due to the wavelength dispersive nature of the CM Raman spectrum, the experimental design is of prime importance and the sample heterogeneity also provides a potential source of variability. The final conclusions drawn by Lünsdorf et al. (2014) are that the comparability of RSCM data between different laboratories needs to be increased and it was suggested that this will be achieved by a combination of an user-independent curve-fitting approach to reduce personal bias and by generating a laboratory specific temperature calibration based on a reference series with independent temperature information.

The basis for developing a more comparable RSCM geothermometer is thus the user independent curve-fitting approach. This was realized by the 'Iterative Fitting Of Raman Spectra' (IFORS) software presented in Lünsdorf and Lünsdorf (2016). The IFORS software tries to reduce the residuals as far as possible by iteratively introducing pseudo-Voigt functions during modeling and by random variation of a single pseudo-Voigt function parameter by a random value. This random approach allows to estimate the variability due to curve-fitting by repetitive evaluation, which is usually not assessed by manual evaluation, and thus provides information on the quality of each curve-fit. The applicability of IFORS was tested on mineral Raman spectra and on very low grade metamorphic CM. The results given in Lünsdorf and Lünsdorf (2016) show that the IFORS software is able to curve-fit various mineral spectra and to provide information on the Raman bands (center, width, intensity, area). More importantly, two new parameters were found, that accurately describe the transformation of CM Raman spectra during very low grade metamorphism. The Raman Area Ratio (RAR), which is prone to variability during modeling, and the Scaled Total Area (STA), which provides a more robust measure of the structural state of CM. In terms of precision the STA parameter outperforms the RA1 and RA2 ratios of Lahfid et al. (2010). Because of their linear correlation, it was proposed that the STA-RSCM method and vitrinite reflectance can be regarded as analogue methods.

Lünsdorf (2016) further investigated the relationship between the two methods, focusing on three aspects, (1) the effect of polishing on Raman spectra of dispersed vitrinites, (2) the wavelength dependent Raman band dispersion and (3) the effect of fluorescence on evaluation. It has been shown that the STA-RSCM method is unaffected by polishing down to the 1  $\mu\text{m}$  polish step, while the final 0.05  $\mu\text{m}$  polish step leads to significant changes in the Raman spectrum of vitrinite. This

result is important, because it is known that the Raman spectrum of micro-crystalline graphite is very sensitive to polishing and must be measured through translucent phases (Beyssac et al., 2003). This is, however, not practicable for RSCM studies on DOM due to the fact that the majority of DOM is hosted in (meta-)pelitic rocks. Furthermore, it has been shown that the effect of polishing on the vitrinite Raman spectrum has to be considered for samples of higher metamorphic conditions than the transition from the epizone to low greenschist facies. The second aspect was analyzed by multi-wavelength resonance Raman spectroscopy of the same vitrinite grains. This approach revealed a two stage molecular evolution during organic metamorphism. The first stage is marked by a parallel shift of the D-band position towards lower wavenumbers. After a maturity range that corresponds to the gas-window, the D-band positions diverge. The stages are explained by the selective nature of resonance Raman spectroscopy. In the first stage the growth of linear aromatic compounds is documented by the D-band positions and in the second stage by the growth of condensed, polycyclic aromatic hydrocarbons. The multi-wavelength approach also revealed that blue to near ultraviolet lasers (488 to 405 nm) are best suited to analyze low mature vitrinites. This is very likely related to the (pre-)resonance of these lasers with the linear aromatic structures present in the vitrinite which leads to a strong amplification of the Raman signal, while red to near infrared lasers (633 to 785 nm) are off-resonance and the Raman signal is overwhelmed by fluorescence. Finally, a strong linear correlation between STA-RSCM and the maximum vitrinite reflectance has been demonstrated and a methodical framework for the Raman analysis of dispersed vitrinites was established.

This methodical framework has been modified and extended to metamorphic conditions in chapter 5. Samples were collected across the Central and Western Alps, focusing on the Glarus Alps, the trace of the pyrophyllite-In reaction isograd in the Helvetic nappes, the Bündnerschiefer units, the Lepontine Alps and the Schistes Lustrés in the Franco-Italian Alps. Out of these samples 26 were chosen to compile a reference series that covers a temperature range of 160 °C to 600 °C. It was realized that the evolution of CM Raman spectra through this temperature interval is three-parted, with a transition zone separating the low temperature zone from the high temperature zone and the framework of the STA-RSCM method needed to be modified to properly describe the complete spectral evolution. The linear correlation of the peak metamorphic temperature and STA-RSCM through the low temperature and transition zone is described by the  $\ln(D\_STA)$  parameter, while the  $\ln(G\_STA)$  parameter linearly correlates with the peak metamorphic temperature in the high temperature zone. To automatically decide if a given spectrum is described by its  $D\_$  or  $G\_STA$  parameter the G-shape-factor has been developed, which is based on the redistribution of intensity values in the G-band region during organic metamorphism. This allows to connect both STA parameters and provides a linear correlation between the STA-RSCM method and peak metamorphic temperature from 160 °C to 600 °C. Thus, it has been demonstrated that the STA-RSCM method provides a revised, user independent and automatic geothermometer, which reduces the variability due to the first and third group of biasing factors. The second group of biasing factors, namely the sample heterogeneity, can be reduced by expanding the reference series and selecting samples with least heterogeneity. Therefore, the reference series needs to be publicly available and contributions from the scientific community are required.

## Bibliography

- Agard, P., Jolivet, L., and Goffé, B. (2001a). Tectonometamorphic evolution of the Schistes Lustrés Complex; implications for the exhumation of HP and UHP rocks in the Western Alps. *Bulletin de la Société Géologique de France*, 172(5):617–636.
- Agard, P., Monié, P., Jolivet, L., and Goffé, B. (2002). Exhumation of the Schistes Lustrés complex: In situ laser probe  $^{40}\text{Ar}/^{39}\text{Ar}$  constraints and implications for the Western Alps. *Journal of Metamorphic Geology*, 20(6):599–618.
- Agard, P., Vidal, O., and Goffé, B. (2001b). Interlayer and Si content of phengite in HP-LT carpholite-bearing metapelites. *Journal of Metamorphic Geology*, 19:479–495.
- Ahn, J. H., Cho, M., and Buseck, P. R. (1999). Interstratification of carbonaceous material within illite. *American Mineralogist*, 84(11-12):1967–1970.
- Ammar, M. R. and Rouzaud, J.-N. (2012). How to obtain a reliable structural characterization of polished graphitized carbons by Raman microspectroscopy. *Journal of Raman Spectroscopy*, 43(2):207–211.
- Anovitz, L. M. and Essene, E. J. (1987). Phase Equilibria in the System  $\text{CaCO}_3\text{-MgCO}_3\text{-FeCO}_3$ . *Journal of Petrology*, 28(2):389–414.
- Aoya, M., Kouketsu, Y., Endo, S., Shimizu, H., Mizukami, T., Nakamura, D., and Wallis, S. (2010). Extending the applicability of the Raman carbonaceous-material geothermometer using data from contact metamorphic rocks. *Journal of Metamorphic Geology*, 28(9):895–914.
- Ascher, D., Dubois, P. F., Hinsien, K., Hugunin, J., and Oliphant, T. (2001). "Numerical Python", tech. report UCRL-MA-128569. Technical report, Lawrence Livermore National Laboratory.
- Auzende, A. L., Daniel, I., Reynard, B., Lemaire, C., and Guyot, F. (2004). High-pressure behaviour of serpentine minerals: A Raman spectroscopic study. *Physics and Chemistry of Minerals*, 31(5):269–277.
- Baek, S.-J., Park, A., Shen, A., and Hu, J. (2011). A background elimination method based on linear programming for Raman spectra. *Journal of Raman Spectroscopy*, 42(11):1987–1993.
- Bartholomew, P. R. (2013). Comparing the Success Rate of Raman Spectroscopy and Powder XRD for Routine Mineral Identification. *Geostandards and Geoanalytical Research*, 37(3):353–359.
- Barzoi, S. C. (2015). Shear stress in the graphitization of carbonaceous matter during the low-grade metamorphism from the northern Parang Mountains (South Carpathians) - Implications to graphite geothermometry. *International Journal of Coal Geology*, 146:179–187.
- Baziotis, I., Mposkos, E., and Skarpelis, N. (2006). Raman micro-spectroscopy of carbonaceous material using the 633nm line of a He-Ne laser: application to the metamorphic rocks of Attica. *Geophysical Research Abstracts*, 8:2.
- Beny-Bassez, C. and Rouzaud, J.-N. (1985). Characterization of carbonaceous materials by correlated electron and optical microscopy and Raman microspectroscopy. *Scanning electron microscopy*, 1:119–132.

- Beyssac, O., Goffé, B., Chopin, C., and Rouzaud, J. N. (2002a). Raman spectra of carbonaceous material in metasediments: a new geothermometer. *Journal of Metamorphic Geology*, 20(9):859–871.
- Beyssac, O., Goffé, B., Petitet, J.-P., Froigneux, E., Moreau, M., and Rouzaud, J.-N. (2003). On the characterization of disordered and heterogeneous carbonaceous materials by Raman spectroscopy. *Spectrochimica Acta Part A: Molecular and Biomolecular Spectroscopy*, 59(10):2267–2276.
- Beyssac, O. and Lazzeri, M. (2012). Application of Raman spectroscopy to the study of graphitic carbons in Earth Sciences. In Dubessy, J., Caumon, M.-C., and Rull, F., editors, *EMU Notes in Mineralogy - volume 12 Raman spectroscopy applied to Earth Sciences and Cultural Heritage*, chapter 12, pages 415–454. European Mineralogical Union & Mineralogical Society of Great Britain & Ireland, London.
- Beyssac, O., Rouzaud, J. N., Goffé, B., Brunet, F., and Chopin, C. (2002b). Graphitization in a high-pressure, low-temperature metamorphic gradient: a Raman microspectroscopy and HRTEM study. *Contributions to Mineralogy and Petrology*, 143(1):19–31.
- Beyssac, O., Simoes, M., Avouac, J. P., Farley, K. a., Chen, Y.-G., Chan, Y.-C., and Goffé, B. (2007). Late Cenozoic metamorphic evolution and exhumation of Taiwan. *Tectonics*, 26(6):1–32.
- Bishop, J. L., Murad, E., Lane, M. D., and Mancinelli, R. L. (2004). Multiple techniques for mineral identification on Mars: a study of hydrothermal rocks as potential analogues for astrobiology sites on Mars. *Icarus*, 169(2):311–323.
- Boggs, P. T., Byrd, R. H., Rogers, J. E., and Schnabel, R. B. (1992). User’s reference guide for ODRPACK version 2.01 software for weighted orthogonal distance regression. Technical report, Center for Computing and Applied Mathematics, US Department of Commerce, Gaithersburg, MD.
- Boggs, P. T., Spiegelman, C. H., Donaldson, J. R., and Schnabel, R. B. (1988). A computational examination of orthogonal distance regression. *Journal of Econometrics*, 38(1-2):169–201.
- Bonijoly, M., Oberlin, M., and Oberlin, A. (1982). A possible mechanism for natural graphite formation. *International Journal of Coal Geology*, 1:283–312.
- Borrego, A., Araujo, C., Balke, A., Cardott, B., Cook, A., David, P., Flores, D., Hámor-Vidó, M., Hiltmann, W., Kalkreuth, W., Koch, J., Kommeren, C., Kus, J., Ligouis, B., Marques, M., Mendonça Filho, J., Misz, M., Oliveira, L., Pickel, W., Reimer, K., Ranasinghe, P., Suárez-Ruiz, I., and Vieth, A. (2006). Influence of particle and surface quality on the vitrinite reflectance of dispersed organic matter: Comparative exercise using data from the qualifying system for reflectance analysis working group of ICCP. *International Journal of Coal Geology*, 68(3-4):151–170.
- Bousquet, R., Goffé, B., Vidal, O., Oberhänsli, R., and Patriat, M. (2002). The tectono-metamorphic history of the Valaisan domain from the Western to the Central Alps: New constraints on the evolution of the Alps. *Geological Society of America Bulletin*, 114(2):207–225.
- Bradley, M. (2007). Curve Fitting in Raman and IR Spectroscopy : Basic Theory of Line Shapes and Applications. Technical report, Thermo Fisher Scientific, Madison, USA.
- Bridges, W. B. (1964). Laser oscillation in singly ionized argon in the visible spectrum. *Applied Physics Letters*, 4(7):128–130.
- Bridges, W. B. and Chester, A. N. (1965). Visible and uv Laser Oscillation at 118 Wavelengths in Ionized Neon, Argon, Krypton, Xenon, Oxygen, and Other Gases. *Applied Optics*, 4(5):573–580.



- Bucher, K. and Grapes, R. (2011). *Petrogenesis of Metamorphic Rocks*. Springer, Berlin, Heidelberg, 8th edition.
- Burke, E. A. J. (2001). Raman microspectrometry of fluid inclusions. *Lithos*, 55(1-4):139–158.
- Buseck, P. R. and Huang, B. J. (1985). Conversion of Carbonaceous Material To Graphite During Metamorphism. *Geochimica Et Cosmochimica Acta*, 49(10):2003–2016.
- Bustin, R. M., Ross, J. V., and Rouzaud, J. N. (1995). Mechanisms of Graphite Formation From Kerogen - Experimental-evidence. *International Journal of Coal Geology*, 28(1):1–36.
- Cao, A., Pandya, A. K., Serhatkulu, G. K., Weber, R. E., Dai, H., Thakur, J. S., Naik, V. M., Naik, R., Auner, G. W., Rabah, R., and Freeman, D. C. (2007). A robust method for automated background subtraction of tissue fluorescence. *Journal of Raman Spectroscopy*, 38(9):1199–1205.
- Carr, A. D. (2000). Suppression and retardation of vitrinite reflectance, part 1. formation and significance for hydrocarbon generation. 23(July):313–343.
- Carr, A. D. and Williamson, J. E. (1989). The relationship between aromaticity, vitrinite reflectance and maceral composition of coals: Implications for the use of vitrinite reflectance as a maturation parameter. *Organic Geochemistry*, 16(1-3):313–323.
- Castiglioni, C., Mapelli, C., Negri, F., and Zerbi, G. (2001). Origin of the D line in the Raman spectrum of graphite: A study based on Raman frequencies and intensities of polycyclic aromatic hydrocarbon molecules. *The Journal of Chemical Physics*, 114(2):963.
- Castiglioni, C., Tommasini, M., and Zerbi, G. (2004). Raman spectroscopy of polyconjugated molecules and materials: confinement effect in one and two dimensions. *Philosophical transactions. Series A, Mathematical, physical, and engineering sciences*, 362(1824):2425–59.
- Cathelineau, M. (1988). Cation site occupancy in chlorites and illites as a function of temperature. *Clay Minerals*, 23:471–485.
- Colangeli, L., Mennella, V., Baratta, G. A., Bussoletti, E., and Strazzulla, G. (1992). Raman and infrared spectra of polycyclic aromatic hydrocarbon molecules of possible astrophysical interest. *The Astrophysical Journal*, 396:369–377.
- Compagnini, G., Puglisi, O., and Foti, G. (1997). Raman spectra of virgin and damaged graphite edge planes. *Carbon*, 35(12):1793–1797.
- Compston, W., Williams, I. S., and Meyer, C. (1984). U-Pb Geochronology of Zircons From Lunar Breccia 73217 Using a Sensitive High Mass-Resolution Ion Microprobe. *Journal of Geophysical Research*, 89:B525—B534.
- Crespo, E., Luque, F. J., Barrenechea, J. F., and Rodas, M. (2006). Influence of grinding on graphite crystallinity from experimental and natural data: implications for graphite thermometry and sample preparation. *Mineralogical Magazine*, 70(6):697–707.
- Dabestani, R. and Lvanov, I. N. (1999). A Compilation of Physical, Spectroscopic and Photo-physical Properties of Polycyclic Aromatic Hydrocarbons. *Photochemistry and photobiology*, 70(1):10–34.
- Dachs, E. (1990). Geothermobarometry in metasediments of the southern Grossvenediger area (Tauern Window, Austria). *Journal of Metamorphic Geology*, 8(2):217–230.
- Daniel, I., Gillet, P., and Ghose, S. (1995). A new high-pressure phase transition in anorthite (CaAl<sub>2</sub>Si<sub>2</sub>O<sub>8</sub>) revealed by Raman spectroscopy. *American Mineralogist*, 80:645–648.
- Das, S. and Hendry, M. J. (2011). Application of Raman spectroscopy to identify iron minerals commonly found in mine wastes. *Chemical Geology*, 290(3-4):101–108.
- de Rooij, J. J. and Eilers, P. H. (2012). Mixture models for baseline estimation. *Chemometrics and Intelligent Laboratory Systems*, 117:56–60.

- Deville, E., Fudral, S., Lagabrielle, Y., Marthaler, M., and Sartori, M. (1992). From oceanic closure to continental collision: A synthesis of the Schistes lustrés metamorphic complex of the Western Alps. *Geological Society of America Bulletin*, 104:127–139.
- Di Donato, E., Tommasini, M., Fustella, G., Brambilla, L., Castiglioni, C., Zerbi, G., Simpson, C. D., Müllen, K., and Negri, F. (2004). Wavelength-dependent Raman activity of D<sub>2h</sub> symmetry polycyclic aromatic hydrocarbons in the D-band and acoustic phonon regions. *Chemical Physics*, 301(1):81–93.
- Dierksen, M. and Grimme, S. (2004). The Vibronic Structure of Electronic Absorption Spectra of Large Molecules: A Time-Dependent Density Functional Study on the Influence of Exact HartreeFock Exchange. *The Journal of Physical Chemistry A*, 108(46):10225–10237.
- Dietzek, B., Cialla, D., Schmitt, M., and Popp, J. (2011). High-Resolution Optical and Confocal Microscopy. In Dieing, T., Hollricher, O., and Toporski, J., editors, *Confocal Raman Microscopy*, volume 158 of *Springer Series in Optical Sciences*, pages 21–42. Springer Berlin Heidelberg, Berlin, Heidelberg.
- Dubessy, J., M-C, C., Rull, F., and Sharma, S. (2012). Instrumentation in Raman spectroscopy: elementary theory and practice. In Dubessy, J., Caumon, M.-C., and Rull, F., editors, *EMU Notes in Mineralogy - volume 12 Applications of Raman spectroscopy to Earth sciences and cultural heritage*, chapter 3, pages 83–172. European Mineralogical Union & Mineralogical Society of Great Britain & Ireland, London.
- Dunkl, I., Antolín, B., Wemmer, K., Rantitsch, G., Kienast, M., Montomoli, C., Ding, L., Carosi, R., Appel, E., El Bay, R., Xu, Q., and Von Eynatten, H. (2011). Metamorphic evolution of the Tethyan Himalayan flysch in SE Tibet. *Geological Society, London, Special Publications*, 353(1):45–69.
- Ebert, A., Herwegh, M., and Pfiffner, A. (2007). Cooling induced strain localization in carbonate mylonites within a large-scale shear zone (Glarus thrust, Switzerland). *Journal of Structural Geology*, 29(7):1164–1184.
- Eilers, P. H. C. (2003). A perfect smoother. *Analytical chemistry*, 75(14):3631–6.
- Enami, M., Nishiyama, T., and Mouri, T. (2007). Laser Raman microspectrometry of metamorphic quartz: A simple method for comparison of metamorphic pressures. *American Mineralogist*, 92(8-9):1303–1315.
- Endo, S., Wallis, S. R., Tsuboi, M., Torres De León, R., and Solari, L. a. (2012). Metamorphic evolution of lawsonite eclogites from the southern Motagua fault zone, Guatemala: insights from phase equilibria and Raman spectroscopy. *Journal of Metamorphic Geology*, 30(2):143–164.
- Essene, E. J. (1983). Solid solution and solvi among metamorphic carbonates with applications to geologic thermobarometry. *Reviews in Mineralogy and Geochemistry*, 11:77–96.
- Faulon, J. L., Carlson, G. A., and Hatcher, P. G. (1994). A three-dimensional model for lignocellulose from gymnospermous wood. *Organic Geochemistry*, 21(12):1169–1179.
- Ferrari, A. C. and Robertson, J. (2001). Resonant Raman spectroscopy of disordered, amorphous, and diamondlike carbon. *Physical Review B*, 64(7):1–13.
- Ferraro, J. R., Nakamoto, K., and Brown, C. W., editors (2003). *Introductory Raman Spectroscopy*. Academic Press, 2nd edition.
- Forer, U., Kaindl, R., Tropper, P., and Mair, V. (2009). Mikro-Raman-Spektroskopische Thermometrie an graphithaltigen Bündnerschiefern am Tauern Südrand im Ahrntal (S-Tirol, Italien). *Mitteilungen der Österreichischen Mineralogischen Gesellschaft*, 155:183–188.

- Frei, D. and Gerdes, A. (2009). Precise and accurate in situ UPb dating of zircon with high sample throughput by automated LA-SF-ICP-MS. *Chemical Geology*, 261(3-4):261–270.
- Frey, M. (1987a). *Low Temperature Metamorphism*. Blackie & Son Limited, Glasgow, London.
- Frey, M. (1987b). The reaction-isograd kaolinite + quartz = pyrophyllite + H<sub>2</sub>O, Helvetic Alps, Switzerland. *Schweizerische Mineralogische und Petrographische Mitteilungen*, 67:1–11.
- Frey, M. and Mählmann, R. F. (1999). Alpine metamorphism of the Central Alps. *Schweizerische Mineralogische und Petrographische Mitteilungen*, 79:135–154.
- Frezzotti, M. L., Tecce, F., and Casagli, A. (2012). Raman spectroscopy for fluid inclusion analysis. *Journal of Geochemical Exploration*, 112:1–20.
- Gillet, P. (1996). Raman spectroscopy at high pressure and high temperature. Phase transitions and thermodynamic properties of minerals. *Physics and Chemistry of Minerals*, 23(4-5):263–275.
- Gonfiantini, R. (1978). Standards for stable isotope measurements in natural compounds. *Nature*, 273:534–536.
- Groppo, C., Rinaudo, C., Cairo, S., Gastaldi, D., and Compagnoni, R. (2006). Micro-Raman spectroscopy for a quick and reliable identification of serpentine minerals from ultramafics. *European Journal of Mineralogy*, 18(3):319–329.
- Guedes, A., Noronha, F., and Prieto, a. C. (2005). Characterisation of dispersed organic matter from lower Palaeozoic metasedimentary rocks by organic petrography, X-ray diffraction and micro-Raman spectroscopy analyses. *International Journal of Coal Geology*, 62(4):237–249.
- Guedes, A., Valentim, B., Prieto, A. C., Rodrigues, S., and Noronha, F. (2010). Micro-Raman spectroscopy of collotelinite, fusinite and macrinite. *International Journal of Coal Geology*, 83:415–422.
- Guillaume, D., Teinturier, S., Dubessy, J., and Pironon, J. (2003). Calibration of methane analysis by Raman spectroscopy in H<sub>2</sub>O-NaCl-CH<sub>4</sub> fluid inclusions. *Chemical Geology*, 194(13):41–49.
- Gunasekaran, S. and Anbalagan, G. (2007). Spectroscopic study of phase transitions in dolomite mineral. *Journal of Raman Spectroscopy*, 38(7):846–852.
- Haskin, L. a., Wang, A., Rockow, K. M., Jolliff, B. L., Korotev, R. L., and Viskupic, K. M. (1997). Raman spectroscopy for mineral identification and quantification for in situ planetary surface analysis: A point count method. *Journal of Geophysical Research: Planets*, 102(E8):19293–19306.
- Hatcher, P. G. (1990). Chemical structural models for coalified wood (vitrinite) in low rank coal. *Organic Geochemistry*, 16(1987):959–968.
- Hatcher, P. G. and Clifford, D. J. (1997). The organic geochemistry of coal: from plant materials to coal. *Organic Geochemistry*, 27(5-6):251–274.
- Hinrichs, R., Brown, M. T., Vasconcellos, M. A. Z., Abrashev, M. V., and Kalkreuth, W. (2014). Simple procedure for an estimation of the coal rank using micro-Raman spectroscopy. *International Journal of Coal Geology*, 136:52–58.
- Hollricher, O. (2011). Raman Instrumentation for Confocal Raman Microscopy. In Dieing, T., Hollricher, O., and Toporski, J., editors, *Springer Series in Optical Sciences*, volume 158 of *Springer Series in Optical Sciences*, pages 43–60. Springer Berlin Heidelberg, Berlin, Heidelberg.
- Hope, G., Woods, R., and Munce, C. (2001). Raman microprobe mineral identification. *Minerals Engineering*, 14(12):1565–1577.
- Huang, E.-P., Huang, E., Yu, S.-C., Chen, Y.-H., Lee, J.-S., and Fang, J.-N. (2010). In situ Raman spectroscopy on kerogen at high temperatures and high pressures. *Physics and Chemistry of Minerals*, 37(9):593–600.

- Hurford, A. J. and Green, P. F. (1983). The zeta age calibration of fission-track dating. *Chemical Geology*, 41:285–317.
- Hutton, A., Bharati, S., and Robl, T. (1994). Chemical and Petrographic Classification of Kerogen/Macerals. *Energy & Fuels*, 8:1478–1488.
- ICCP (1998). The new vitrinite classification (ICCP System 1994). *Fuel*, 77(5):349–358.
- Jehlička, J. and Bény, C. (1992). Application of Raman microspectrometry in the study of structural changes in Precambrian kerogens during regional metamorphism. *Organic Geochemistry*, 18(2):211–213.
- Jehlička, J., Víttek, P., Edwards, H., Heagraves, M., and Čapoun, T. (2009). Application of portable Raman instruments for fast and non-destructive detection of minerals on outcrops. *Spectrochimica Acta Part A: Molecular and Biomolecular Spectroscopy*, 73(3):410–419.
- Katagiri, G., Ishida, H., and Ishitani, A. (1988). Raman spectra of graphite edge planes. *Carbon*, 26(4):565–571.
- Kelemen, S. R. and Fang, H. L. (2001). Maturity trends in Raman spectra from kerogen and coal. *Energy & Fuels*, 15(3):653–658.
- Kisch, H., Árkai, P., and Brime, C. (2004). On the calibration of the illite Kübler index (illite "crystallinity"). *Schweizerische Mineralogische und Petrographische Mitteilungen*, 84(3):323–331.
- Kisch, H. J. (1990). Calibration of the anchizone: a critical comparison of illite crystallinity scales used for definition. *Journal of Metamorphic Geology*, 8(1):31–46.
- Kouketsu, Y., Mizukami, T., Mori, H., Endo, S., Aoya, M., Hara, H., Nakamura, D., and Wallis, S. (2014). A new approach to develop the Raman carbonaceous material geothermometer for low-grade metamorphism using peak width. *Island Arc*, 23(1):33–50.
- Kribek, B., Hrabal, J., Landais, P., and Hladikova, J. (1994). The Association of Poorly Ordered Graphite, Coke and Bitumens In Greenschist Facies Rocks of the Ponikla Group, Lugicum, Czech-republic - the Result of Graphitization of Various Types of Carbonaceous Matter. *Journal of Metamorphic Geology*, 12(4):493–503.
- Kruger, M. A. and Bensley, D. F. (1994). Flash Pyrolysis - Gas Chromatography - Mass Spectrometry of Lower Kittanning Vitrinites: Changes in Distributions of Polyaromatic Hydrocarbons as a Function of Coal Rank. In Mukhopadhyay, P. K. and Dow, W. G., editors, *ACS Symposium Series 570*, chapter 9, pages 136–148. American Chemical Society, Washington.
- Kunert, V. (1999). *Die Frankenwälder Querzone: Entwicklung einer thermischen Anomalie im Saxothuringikum*. PhD thesis, Justus-Liebig-Universität Gießen.
- Lahfid, A., Beyssac, O., Deville, E., Negro, F., Chopin, C., and Goffé, B. (2010). Evolution of the Raman spectrum of carbonaceous material in low-grade metasediments of the Glarus Alps (Switzerland). *Terra Nova*, 22(5):354–360.
- Lemoine, M., Bas, T., Arnaud-Vanneau, A., Arnaud, H., Dumont, T., Gidon, M., Bourbon, M., de Graciansky, P.-C., Rudkiewicz, J.-L., Megard-Galli, J., and Tricart, P. (1986). The continental margin of the Mesozoic Tethys in the Western Alps. *Marine and Petroleum Geology*, 3(3):179–199.
- Levine, J. R. (1993). Coalification: The Evolution of Coal as Source Rock and Reservoir. In Law, B. E. and Rice, D. D., editors, *Hydrocarbons from Coal*, chapter 3, pages 39–77. The American Association of Petroleum Geologists, Tulsa, USA.
- Li, X., Hayashi, J., and Li, C. (2006). FT-Raman spectroscopic study of the evolution of char structure during the pyrolysis of a Victorian brown coal. *Fuel*, 85(12-13):1700–1707.

- Lin, C.-C. (2003). Pressure-induced metastable phase transition in orthoenstatite (MgSiO<sub>3</sub>) at room temperature: a Raman spectroscopic study. *Journal of Solid State Chemistry*, 174(2):403–411.
- Liu, D. H., Xiao, X. M., Tian, H., Min, Y. S., Zhou, Q., Cheng, P., and Shen, J. G. (2013). Sample maturation calculated using Raman spectroscopic parameters for solid organics: Methodology and geological applications. *Chinese Science Bulletin*, 58(11):1285–1298.
- Ludwig, K. R. (2003). User’s manual for Isoplot 3.00 - A geochronological toolkit for Microsoft Excel. *Berkeley Geochronology Center Special Publication*, 4:71.
- Lünsdorf, N. K. (2016). Raman spectroscopy of dispersed vitrinite Methodical aspects and correlation with reflectance. *International Journal of Coal Geology*, 153:75–86.
- Lünsdorf, N. K., Dunkl, I., Schmidt, B. C., Rantitsch, G., and von Eynatten, H. (2014). Towards a Higher Comparability of Geothermometric Data obtained by Raman Spectroscopy of Carbonaceous Material. Part I: Evaluation of Biasing Factors. *Geostandards and Geoanalytical Research*, 38(1):73–94.
- Lünsdorf, N. K. and Lünsdorf, J. O. (2016). Evaluating Raman spectra of carbonaceous matter by automated, iterative curve-fitting. *International Journal of Coal Geology*, 160-161:51–62.
- Marshall, C. P., Edwards, H. G. M., and Jehlicka, J. (2010). Understanding the application of Raman spectroscopy to the detection of traces of life. *Astrobiology*, 10(2):229–43.
- Mathews, J. P. and Chaffee, A. L. (2012). The molecular representations of coal A review. *Fuel*, 96:1–14.
- Mathews, J. P., Hatcher, P. G., and Scaroni, A. W. (2001). Proposed Model Structures for Upper Freeport and Lewiston-Stockton Vitrinites. (17):863–873.
- Matthews, M., Pimenta, M., Dresselhaus, G., Dresselhaus, M., and Endo, M. (1999). Origin of dispersive effects of the Raman D band in carbon materials. *Physical Review B*, 59(10):R6585–R6588.
- Maultzsch, J., Reich, S., Thomsen, C., Requardt, H., and Ordejón, P. (2004). Phonon Dispersion in Graphite. *Physical Review Letters*, 92(7):075501.
- McCreery, R. L. (2000). Raman Spectroscopy for Chemical Analysis. In Winefordner, J. D., editor, *Volume 157 in Chemical Analysis - A Series of Monographs on Analytical Chemistry and Its Applications*. Wiley-Interscience.
- Moré, J. J. (1978). The Levenberg-Marquardt algorithm: Implementation and theory. In *Numerical Analysis*, pages 105–116. Springer, Berlin, Heidelberg.
- Morga, R. (2011). Micro-Raman spectroscopy of carbonized semifusinite and fusinite. *International Journal of Coal Geology*, 87(3-4):253–267.
- Morga, R., Jelonek, I., Kruszewska, K., and Szulik, W. (2015). Relationships between quality of coals, resulting cokes, and micro-Raman spectral characteristics of these cokes. *International Journal of Coal Geology*, 144-145(April):130–137.
- Negri, F., Castiglioni, C., Tommasini, M., and Zerbi, G. (2002). A Computational Study of the Raman Spectra of Large Polycyclic Aromatic Hydrocarbons: Toward Molecularly Defined Subunits of Graphite. *The Journal of Physical Chemistry A*, 106(14):3306–3317.
- Negri, F., di Donato, E., Tommasini, M., Castiglioni, C., Zerbi, G., and Müllen, K. (2004). Resonance Raman contribution to the D band of carbon materials: modeling defects with quantum chemistry. *The Journal of chemical physics*, 120(24):11889–900.
- Nzoussi-Mbassani, P., Copard, Y., and Disnar, J. (2005). Vitrinite recycling: diagnostic criteria and reflectance changes during weathering and reburial. *International Journal of Coal Geology*,

- 61(3-4):223–239.
- Oberlin, A. (1989). High-Resolution TEM studies of carbonization and graphitization. In Throver, P. A., editor, *Chemistry and Physics of Carbon: Volume 22*, chapter 1, pages 1–144. CRC Press, London, New York.
- Oberlin, A. and Bonnamy, S. (2013). A Realistic Approach to Disordered Carbons. In Radovic, L. R., editor, *Chemistry and Physics of Carbon*, chapter 1, page 297. CRC Press.
- Oberlin, A., Bonnamy, S., and Rouxhet, P. G. (1999). Colloidal and Supramolecular Aspects of Carbon. In Throver, P. A. and Radovic, L. R., editors, *Chemistry and Physics of Carbon: Volume 26*, chapter 1, page 424. Marcel Dekker, Inc.
- Oberlin, A., Boulmier, J. L., and Durnand, B. (1974). Electron microscope investigation of the structure of naturally and artificially metamorphosed kerogen. *Geochimica et Cosmochimica Acta*, 38(4):647–650.
- Oberlin, A., Terriere, G., and Boulmier, J. L. (1975a). Carbonification, Carbonization and Graphitization as Studied by High Resolution Electron Microscopy. *TANSO*, 1975(80):29–42.
- Oberlin, A., Terrière, G., and Boulmier, J. L. (1975b). Carbonification, Carbonization and Graphitization as Studied by High Resolution Electron Microscopy (Part II). *TANSO*, 1975(83):153–171.
- Oliphant, T. E. (2007). Python for Scientific Computing. *Computing in Science & Engineering*, 9(3):10–20.
- Palmer, D., Hemley, R., and Prewitt, C. (1994). Raman spectroscopic study of high-pressure phase transitions in cristobalite. *Physics and Chemistry of Minerals*, 21(8):481–488.
- Pasteris, J. D. and Wopenka, B. (1991). Raman Spectra of Graphite as Indicators of Degree of Metamorphism. *Canadian Mineralogist*, 29:1–9.
- Pasteris, J. D., Wopenka, B., and Seitz, J. C. (1988). Practical aspects of quantitative laser Raman microprobe spectroscopy for the study of fluid inclusions\*. *Geochimica et Cosmochimica Acta*, 52(1):979–988.
- Pfiffner, O. A. (2010). *Geologie der Alpen*. Haupt, Bern, Stuttgart, Wien, 2te edition.
- Pilgrim, M. (2004). *Dive Into Python*. Apress, Berkeley, CA.
- Pimenta, M. A., Dresselhaus, G., Dresselhaus, M. S., Cançado, L. G., Jorio, A., and Saito, R. (2007). Studying disorder in graphite-based systems by Raman spectroscopy. *Physical chemistry chemical physics : PCCP*, 9(11):1276–91.
- Pócsik, I., Hundhausen, M., Koos, M., Ley, L., Pócsik, I., Hundhausen, M., Koós, M., and Ley, L. (1998). Origin of the D peak in the Raman spectrum of microcrystalline graphite. *Journal of Non-Crystalline Solids*, 227-230:1083–1086.
- Powell, R., Hergt, J., and Woodhead, J. (2002). Improving isochron calculations with robust statistics and the bootstrap. *Chemical Geology*, 185(3-4):191–204.
- Quirico, E., Bonal, L., and Montagnac, G. (2005). Maturation grade of coals as revealed by Raman spectroscopy: Progress and problems. 61:2368–2377.
- Quirico, E., Montagnac, G., Rouzaud, J. N., Bonal, L., Bourot-denise, M., Duber, S., and Reynard, B. (2009). Precursor and metamorphic condition effects on Raman spectra of poorly ordered carbonaceous matter in chondrites and coals. *Earth and Planetary Science Letters*, 287(1-2):185–193.
- Quirico, E., Raynal, P.-I., and Bourot-Denise, M. (2003). Metamorphic grade of organic matter in six unequilibrated ordinary chondrites. *Meteoritics and Planetary Science*, 38(5):795–811.

- Rahl, J. M., Anderson, K. M., Brandon, M. T., and Fassoulas, C. (2005). Raman spectroscopic carbonaceous material thermometry of low-grade metamorphic rocks: Calibration and application to tectonic exhumation in Crete, Greece. *Earth and Planetary Science Letters*, 240(2):339–354.
- Rahn, M. (1996). *Incipient Metamorphism of the Glarus Alps: Petrology of the Tavayanne Greywacke and Fission Track Dating*. PhD thesis, Albert-Ludwigs-Universität Freiburg.
- Rahn, M., Mullis, J., Erdelbrock, K., and Frey, M. (1995). Alpine metamorphism in the North Helvetic flysch of the Glarus Alps, Switzerland. *Eclogae Geologicae Helveticae*, 88(1):157–178.
- Raman, C. V. and Krishnan, K. S. (1928). A New Type of Secondary Radiation. *Nature*, 121:501–502.
- Rantitsch, G., Bhattacharyya, A., Schenk, J., and Lünsdorf, N. K. (2014). Assessing the quality of metallurgical coke by Raman spectroscopy. *International Journal of Coal Geology*, 130:1–7.
- Rantitsch, G., Grogger, W., Teichert, C., Ebner, F., Hofer, C., Maurer, E.-M., Schaffer, B., and Toth, M. (2004). Conversion of carbonaceous material to graphite within the Greywacke Zone of the Eastern Alps. *International Journal of Earth Sciences*, 93(6):959–973.
- Rantitsch, G., Lämmerer, W., Fisslthaler, E., Mitsche, S., and Kaltenböck, H. (2016). On the discrimination of semi-graphite and graphite by Raman spectroscopy. *International Journal of Coal Geology*, 159:48–56.
- Rantitsch, G., Sachsenhofer, R. F., Hasenhüttl, C., Russegger, B., and Rainer, T. (2005). Thermal evolution of an extensional detachment as constrained by organic metamorphic data and thermal modeling: Graz Paleozoic Nappe Complex (Eastern Alps). *Tectonophysics*, 411(1-4):57–72.
- Reich, S. and Thomsen, C. (2004). Raman spectroscopy of graphite. *Philosophical Transactions of the Royal Society A: Mathematical, Physical and Engineering Sciences*, 362(1824):2271–2288.
- Rosasco, G. J. and Roedder, E. (1979). Application of a new Raman microprobe spectrometer to nondestructive analysis of sulfate and other ions in individual phases in fluid inclusions in minerals. *Geochimica et Cosmochimica Acta*, 43(12):1907–1915.
- Rosso, K. M. and Bodnar, R. J. (1995). Microthermometric and Raman Spectroscopic Detection Limits of CO<sub>2</sub> in Fluid Inclusions and the Raman Spectroscopic Characterization of CO<sub>2</sub>. *Geochimica et Cosmochimica Acta*, 59(19):3961–3975.
- Rouzaud, J., Oberlin, A., and Beny-Bassez, C. (1983). Carbon films: Structure and microtexture (optical and electron microscopy, Raman spectroscopy). *Thin Solid Films*, 105(1):75–96.
- Rowlands, C. and Elliott, S. (2011). Automated algorithm for baseline subtraction in spectra. *Journal of Raman Spectroscopy*, 42(3):363–369.
- Ruiz-Morales, Y. (2002). HOMO-LUMO gap as an index of molecular size and structure for polycyclic aromatic hydrocarbons (PAHs) and asphaltenes: A theoretical study. I. *Journal of Physical Chemistry A*, 106(46):11283–11308.
- Ruiz-Morales, Y. and Mullins, O. C. (2007). Polycyclic Aromatic Hydrocarbons of Asphaltenes Analyzed by Molecular Orbital Calculations with Optical Spectroscopy. *Energy & Fuels*, 21(1):256–265.
- Rull, F. (2012). The Raman effect and the vibrational dynamics of molecules and crystalline solids. In Dubessy, J., Caumon, M.-C., and Rull, F., editors, *EMU Notes in Mineralogy - volume 12 Raman spectroscopy applied to Earth Sciences and Cultural Heritage*, chapter 1, pages 1–60. European Mineralogical Union & Mineralogical Society of Great Britain & Ireland, London.
- Sadezky, A., Muckenhuber, H., Grothe, H., Niesser, R., and Poeschl, U. (2005). Raman microspectroscopy of soot and related carbonaceous materials: Spectral analysis and structural information. *Carbon*, 43:1731–1742.

- Saito, R., Jorio, A., Souza Filho, A., Dresselhaus, G., Dresselhaus, M., and Pimenta, M. (2001). Probing Phonon Dispersion Relations of Graphite by Double Resonance Raman Scattering. *Physical Review Letters*, 88(2):027401.
- Salje, E., Schmidt, C., and Bismayer, U. (1993). Structural phase transition in titanite, CaTiSiO<sub>5</sub>: A ramanspectroscopic study. *Physics and Chemistry of Minerals*, 19(7):502–506.
- Sánchez-Bajo, F. and Cumbreira, F. L. (1997). The use of the pseudo-Voigt function in the variance method of X-ray line-broadening analysis. *Journal of Applied Crystallography*, 30:427–430.
- Sato, K., Saito, R., Oyama, Y., Jiang, J., Caçado, L. G., Pimenta, M. A., Jorio, A., Samsonidze, G. G., Dresselhaus, G., and Dresselhaus, M. S. (2006). D-band Raman intensity of graphitic materials as a function of laser energy and crystallite size. *Chemical Physics Letters*, 427(1-3):117–121.
- Scharf, A., Handy, M. R., Ziemann, M. A., and Schmid, S. M. (2013). Peak-temperature patterns of polyphase metamorphism resulting from accretion, subduction and collision (eastern tauern window, european alps) - a study with raman microspectroscopy on carbonaceous material (RSCM). *Journal of Metamorphic Geology*, 31(8):863–880.
- Schulze, G., Jirasek, A., Yu, M. M. L., Lim, A., Turner, R. F. B., and Blades, M. W. (2005). Investigation of selected baseline removal techniques as candidates for automated implementation. *Applied Spectroscopy*, 59(5):545–574.
- Spötl, C., Houseknecht, D. W., and Jaques, R. C. (1998). Kerogen maturation and incipient graphitization of hydrocarbon source rocks in the Arkoma Basin, Oklahoma and Arkansas: a combined petrographic and Raman spectrometric study. *Organic Geochemistry*, 28(9-10):535–542.
- Steinmann, M. (1994). Ein Beckenmodell für das Nordpenninikum der Ostschweiz. *Jahrbuch der geologischen Bundesanstalt*, 137(4):675–721.
- Sweeney, J. J. and Burnham, A. K. (1990). Evaluation of a simple model of vitrinite reflectance based on chemical kinetics. *The American Association of Petroleum Geologists Bulletin*, 74(10):1559–1570.
- Swisstopo (2005). *Tektonische Karte der Schweiz, 1:500000*. Bundesamt für Landestopografie, Schweiz.
- Taylor, G. H., Teichmüller, M., Davis, A., Diessel, C. F. K., Littke, R., and Robert, P., editors (1998). *Organic Petrology*. Schweizerbart Science Publishers, Stuttgart, Germany.
- Thomsen, C. and Reich, S. (2000). Double resonant raman scattering in graphite. *Physical review letters*, 85(24):5214–7.
- Todd, C. S. and Engi, M. (1997). Metamorphic field gradients in the Central Alps. *Journal of Metamorphic Geology*, 15(4):513–530.
- Tuinstra, F. and Koenig, J. L. (1970). Raman Spectrum of Graphite. *Journal of Chemical Physics*, 53(3):1126–1130.
- Vácz, T. (2014). A new, simple approximation for the deconvolution of instrumental broadening in spectroscopic band profiles. *Applied Spectroscopy*, 68(11):1274–1278.
- Valentim, B., Guedes, A., Prieto, A. C., and de Sousa, M. J. (2004). Characterization of Coal Maceral Groups by Micro-Raman Spectroscopy. *Revista da Faculdade de Ciências*, (1):318–325.
- van den Kerkhof, A. M. and Olsen, S. N. (1990). A natural example of superdense CO<sub>2</sub> inclusions: Microthermometry and Raman analysis. *Geochimica et Cosmochimica Acta*, 54(3):895–901.
- Vandenbroucke, M. and Largeau, C. (2007). Kerogen origin, evolution and structure. *Organic Geochemistry*, 38(5):719–833.



- Vermeesch, P. (2010). HelioPlot, and the treatment of overdispersed (U-Th-Sm)/He data. *Chemical Geology*, 271(3-4):108–111.
- Vidano, R. P., Fischbach, D. B., Willis, L. J., and Loehr, T. M. (1981). Observation of Raman Band Shifting With Excitation Wavelength For Carbons and Graphites. *Solid State Communications*, 39(2):341–344.
- Villanueva, U., Raposo, J. C., Castro, K., de Diego, A., Arana, G., and Madariaga, J. M. (2008). Raman spectroscopy speciation of natural and anthropogenic solid phases in river and estuarine sediments with appreciable amount of clay and organic matter. *Journal of Raman Spectroscopy*, 39(9):1195–1203.
- Walrafen, G. E. (1964). Raman Spectral Studies of Water Structure. *The Journal of Chemical Physics*, 40(11):3249.
- Wang, A., Dhamelinourt, P., Dubessy, D., Guerard, D., Landais, P., and Lelaurain, M. (1989). Characterization of graphite alteration in an uranium deposit by micro-Raman spectroscopy, X-ray diffraction, transmission electron microscopy and scanning electron microscopy. *Carbon*, 27(2):209–218.
- Wang, Y., Alsmeyer, D. C., and McCreery, R. L. (1990). Raman-spectroscopy of Carbon Materials - Structural Basis of Observed Spectra. *Chemistry of Materials*, 2(5):557–563.
- White, A. D. and Gordon, E. I. (1963). Excitation mechanisms and current dependence of population inversion in He-Ne Lasers. *Applied Physics Letters*, 3(11):197–199.
- White, S. N. (2009). Laser Raman spectroscopy as a technique for identification of seafloor hydrothermal and cold seep minerals. *Chemical Geology*, 259(3-4):240–252.
- Wiederkehr, M., Bousquet, R., Schmid, S. M., and Berger, A. (2008). From subduction to collision: Thermal overprint of HP/LT meta-sediments in the north-eastern Lepontine Dome (Swiss Alps) and consequences regarding the tectono-metamorphic evolution of the Alpine orogenic wedge. *Swiss Journal of Geosciences*, 101(S1):127–155.
- Wiederkehr, M., Bousquet, R., Ziemann, M. a., Berger, A., and Schmid, S. M. (2011). 3-D assessment of peak-metamorphic conditions by Raman spectroscopy of carbonaceous material: an example from the margin of the Lepontine dome (Swiss Central Alps). *International Journal of Earth Sciences*, 100(5):1029–1063.
- Wiederkehr, M., Sudo, M., Bousquet, R., Berger, A., and Schmid, S. M. (2009). Alpine orogenic evolution from subduction to collisional thermal overprint: The  $^{40}\text{Ar}/^{39}\text{Ar}$  age constraints from the Valaisan Ocean, central Alps. *Tectonics*, 28(6):1–28.
- Wilkins, R. W. T., Boudou, R., Sherwood, N., and Xiao, X. (2014). Thermal maturity evaluation from inertinites by Raman spectroscopy: The 'RaMM' technique. *International Journal of Coal Geology*, 128-129:143–152.
- Wojdyr, M. (2010). Fityk : a general-purpose peak fitting program. *Journal of Applied Crystallography*, 43(5):1126–1128.
- Wopenka, B. and Pasteris, J. D. (1993). Structural Characterization of Kerogens To Granulite-facies Graphite - Applicability of Raman Microprobe Spectroscopy. *American Mineralogist*, 78(5-6):533–557.
- Yui, T. F., Huang, E., and Yu, J. (1996). Raman spectrum of carbonaceous material: A possible metamorphic grade indicator for low-grade metamorphic rocks. *Journal of Metamorphic Geology*, 14:115–124.



## Appendix

### 7.1. Supplements to chapter 2

Measuring and evaluation protocol:

- When the evaluation is performed with Fityk (Wojdyr, 2010) set the standard deviation of  $y$  to 1 for all spectra. (Data > Transformations > Std.dev.=1)
  - Use the Levenberg-Marquardt Method. (In Fityk: Fit > Method > Levenberg-Marquardt)
  - In general, only evaluate spectra with none or very low fluorescence.
  - When a spectrum shows obvious curvature in fluorescence (i.e. baseline) reject the spectrum and try to record one with a more linear baseline.
- (1) Determination of the 'crystallinity' level:
- (a) 'crystallinity' level 1:
    - (i) Five components are needed: D1 (ca. 1360  $\text{cm}^{-1}$ ), D2 (ca. 1620  $\text{cm}^{-1}$ ), D3 (ca. 1540  $\text{cm}^{-1}$ ), D4 (ca. 1250  $\text{cm}^{-1}$ ) and G (ca. 1580  $\text{cm}^{-1}$ )
    - (ii) The D1-component is usually broad and more intense than the G-component.
    - (iii) The G- and D2-component are not separable or hard to separate.
    - (iv) The D3-component is broad and intense.
  - (b) 'crystallinity' level 2:
    - (i) 3 to 4 components are needed: D1 (ca. 1360  $\text{cm}^{-1}$ ), D2 (ca. 1620  $\text{cm}^{-1}$ ), D3 (ca. 1540  $\text{cm}^{-1}$ ) and G (ca. 1580  $\text{cm}^{-1}$ )
    - (ii) Sometimes a weak band at ca. 1080  $\text{cm}^{-1}$  is present.
    - (iii) The D1- and D3-component decrease in intensity relatively to the G-component.
    - (iv) The D2-component appears as a distinct shoulder on the high wavenumber side of the G-component.
    - (v) The D4-component is absent.
  - (c) 'crystallinity' level 3:
    - (i) The D2-, D3- and D4-components are absent.
    - (ii) The G-component is very intense and sharp.
    - (iii) The D1-component is of very low intensity and broad.
- (2) Baseline correction:
- (a) If needed, cut the spectrum to the first order spectral range (700  $\text{cm}^{-1}$  to 2000  $\text{cm}^{-1}$ ).
  - (b) Determine the 'crystallinity' level by optical evaluation.
  - (c) Perform a linear baseline correction with the baseline control points located at ca. 800  $\text{cm}^{-1}$  – 900  $\text{cm}^{-1}$  and ca. 1850  $\text{cm}^{-1}$  – 1950  $\text{cm}^{-1}$ .
  - (d) Subtract the baseline function from the data.
- (3) Component placement and fitting:
- (a) Generally, all components are Lorentz functions and all component parameters are unrestrained.
  - (b) For 'crystallinity' level 1:

- (i) Automatic component detection of D1 and G by the software.
  - (ii) Fit D1 and G once.
  - (iii) Place D2 (about half as intense as fitted G, at ca. 1610 cm<sup>-1</sup>, sharp) and D3 (ca. 1500 cm<sup>-1</sup>, broad) by hand.
  - (iv) Run one fit (the combined G-, D2-, D3-component should now be modeled properly).
  - (v) Place D4 by hand (sharp at ca. 1200 cm<sup>-1</sup>).
  - (vi) Fit the model.
- (c) For 'crystallinity' level 2:
- (i) Automatic component detection of D1 and G by the software.
  - (ii) Fit D1 and G once.
  - (iii) Automatic detection of D2.
  - (iv) Fit once.
  - (v) When D3 is present, automatic detection of D3 (if D3 is not detected, place component by hand at ca. 1500 cm<sup>-1</sup> as a broad component).
  - (vi) If the weak band at ca. 1080 cm<sup>-1</sup> is present, place a component at that location and fit.
  - (vii) Fit the model.
- (d) For 'crystallinity' level 3:
- (i) Automatic detection of G.
  - (ii) Fit G once.
  - (iii) Automatic detection of D1.
  - (iv) Fit the model.

Basic Fityk-scripts of steps 3b, 3c and 3d of the fitting protocol are given below. The scripts were tested with Fityk 0.9.8 running on Ubuntu 12.04 LTS and Windows 7. Copy the lines into a file and save it with the extension ".fit". Then load your spectra into Fityk perform the baseline correction, select all your spectra, choose "Execute script" in Fityk (Session > Execute script) and navigate to the script.

Script of step 3b:

```
@*: S=1 # set the standard deviation of every data point to 1
@*: guess Lorentzian[1580:1620]
@*: guess Lorentzian[1320:1360]
@*: fit
@*: guess Lorentzian(hwhm=~5)[1610:1630]
@*: guess Lorentzian(center=~1500,hwhm=~50)
@*: fit @*: guess Lorentzian(center=~1200,hwhm=~5)
@*: fit
@*: fit
# give the export path for the peak parameters
@*: info peaks >> '/your/path/to/your/files/Cryst_LvL1_protocol.peaks'
```

Script of step 3c:

```
@*: S=1 # set the standard deviation of every data point to 1
@*: guess Lorentzian
```

```

@*: guess Lorentzian
@*: fit
@*: guess Lorentzian
@*: guess Lorentzian(center=~1500,hwhm=~50)
@*: fit
@*: guess Lorentzian(center=~1080)
@*: fit
@*: fit
# give the export path for the peak parameters
@*: info peaks >> '/your/path/to/your/files/Cryst_LvL2_protocol.peaks'

```

Script of step 3d:

```

@*: S=1
@*: guess Lorentzian
@*: fit
@*: guess Lorentzian
@*: fit
@*: fit
# give the export path for the peak parameters
@*: info peaks >> '/your/path/to/your/files/Cryst_LvL3_protocol.peaks'

```

Note that the last line in the scripts is valid for linux systems and needs to be edited according to your local path. When a Windows system is used, change the last line to @\*: info peaks >> 'C:\your\path\to\your\files\Cryst\_LvL1\_protocol.peaks'. The peak-parameters in the “.peaks” files are sorted according to the order of your spectra in Fityk. Also note that the “.peaks” files will be overwritten by each script execution.

## 7.2. Supplements to chapter 3

**7.2.1. The IFORS-software.** The IFORS-software can be downloaded as a zip-archive from:  
<http://www.sediment.uni-goettingen.de/download/>

The archive contains the following files:

- ifors\_canvas.py
- ifors\_cli.py
- ifors\_estimate\_temperature.py
- ifors\_gui.py
- ifors\_ifors.py
- ifors\_manual.pdf
- ifors\_optimize\_python.py
- ifors\_readout.py
- ifors\_start\_curve-fit.py
- test\_spectra\Almandine.txt
- test\_spectra\KL2-8HS\_1\_ics.txt
- test\_spectra\KL2-19\_2.txt
- reference\_series\_data.xls

User instructions are given in the 'ifors\_manual.pdf'. Please write questions or suggestions to:  
kluensd@gwdg.de

### 7.2.2. The IFORS user manual (Iterative Fitting of Raman Spectra).

#### 7.2.2.1. Installation - Windows.

- The software was tested under Windows 7 64bit, but it is very likely that it will also work under Windows 8 and 10. Download Winpython from <http://winpython.sourceforge.net/> and download a Winpython version that contains Python3. All required software packages for IFORS are contained in Winpython.
- Install Winpython to a folder of your choice. To keep the path length short, it is advised to **not** install in your Windows user folder. Instead, 'C:\WinPython' is suggested in this manual.
- All needed files for the IFORS-software are contained in the IFORS.zip archive. Extract the IFORS-files in a directory of your choice, for this manual 'C:\Python\_scripts\ifors' is chosen.

##### NB! #####

You will have to edit some of the IFORS-files during usage and you will need a text-editor for this. Notepad++ (<https://notepad-plus-plus.org/>) is suggested for this purpose, but you can use any other text-editor. **When editing the script files, make sure that you set the 'Tab-settings' in your editor to: Tab-size = 4 and replace tab by space. You can do this in Notepad++ in 'Settings → Preferences → Tab Settings'. '.' (dot) is used as decimal separator in the '.fit' files (section 7.2.4.3).**

#### 7.2.2.2. Installation - Linux.

- Install the following packages: PyQt4 or PyQt5, Numpy, Scipy, Matplotlib; Python3 should be implemented in most Linux distributions.
- Extract the IFORS-files in a directory of your choice.

**7.2.3. Usage (Windows/Linux).** The usage of the software is command line driven, but only very few commands are needed to invoke the required python scripts. Command line input is written in **this font**. A [...] in the command line input indicates that the following line break is due to text formatting and that the actual command line input has no line break. Make use of the tabulator-key and the arrow-keys when writing in the command line. Hitting the tabulator-key triggers the auto-completion, i.e. file- or folder-names will be completed. The up and down arrow-keys let you cycle through already submitted commands. This avoids repetitive typing.

The software works with Raman spectra that have been saved in txt-files. These files are from now on referred to as ‘spectrum-files’. A spectrum-file contains two columns and the first column lists the Raman-shift values (relative wavenumbers) and the second column lists the associated intensity.

7.2.3.1. *Curve-fitting with IFORS.* To start a curve-fit with ifors you have to use the Winpython-command-prompt, which has been installed along with Winpython. Before you start to evaluate your spectra, it suggested to keep your folder structure clearly arranged. Therefore, copy or move your spectra into a specific folder or follow the suggestions of this manual (see below):

- In Windows Explorer create a ‘Raman\_data’ folder with two sub-folders ‘spectra’ and ‘results\_curve-fitting’. In this example the following paths are used:
  - C:\Raman\_data\spectra
  - C:\Raman\_data\results\_curve-fitting
- Of course you can use other folders, but it is advised to use a consistent folder structure.
- When you start a new project, create a sub-folder in the ‘spectra’ and ‘results\_curve-fitting’ folders. Here, we will use ‘project\_1’:
  - C:\Raman\_data\spectra\project\_1
  - C:\Raman\_data\results\_curve-fitting\project\_1
- Copy your spectrum-files in the ‘Raman\_data\spectra\project\_1’ folder (in this example the spectrum-files (KL2-8\_HS\_1\_ics.txt, KL2-19\_2.txt) in the test\_spectra folder from the IFORS.zip archive)
- In Windows Explorer start the “WinPython Command Prompt.exe” (Fig. 7.2.1).
- In the command prompt navigate to the folder in which you want to save the results of the curve-fit, in this example C:\Raman\_data\results\_curve-fitting\project\_1. By default, the command prompt is active in the installation folder of Winpython, in this case C:\WinPython\scripts. To navigate to the results\_curve-fitting\project\_1 folder type in the command prompt:
  - cd .. (hit enter)
  - cd ..

\* now the command prompt is active in the root of drive C (Fig. 7.2.2):

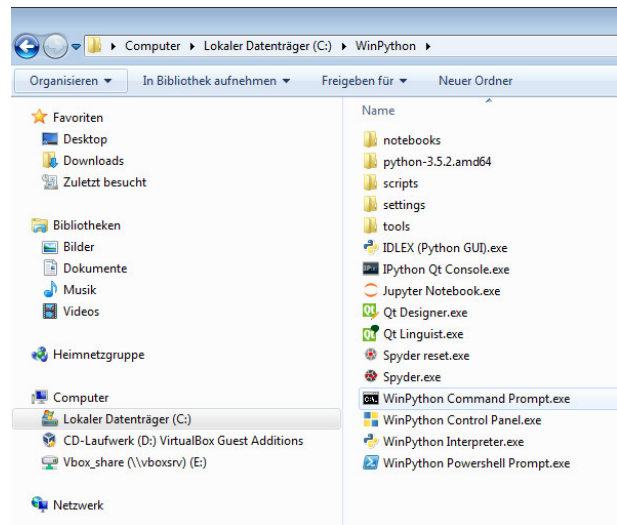


**Figure 7.2.1.** Starting the Winpython command prompt.

```

C:\Windows\system32\cmd.exe - cmd.bat
C:\Winpython\scripts>cd ..
C:\Winpython>cd ..
C:\>cd Raman_data\results_curve-fitting\project_1
C:\Raman_data\results_curve-fitting\project_1>

```

Figure 7.2.2. Changing the directory in the command prompt.

```

C:\Windows\system32\cmd.exe - cmd.bat
C:\Winpython\scripts>cd ..
C:\Winpython>cd ..
C:\>cd Raman_data\results_curve-fitting\project_1
C:\Raman_data\results_curve-fitting\project_1>python c:\Python_scripts\ifors\ifors_start_curve-fit.py -Gui c:\Raman_data\spectra\project_1\KL2-19_2.txt

```

Figure 7.2.3. Starting the 'ifors\_start\_curve-fit.py' script using the command prompt.

- cd Raman\_data\results\_curve-fitting\project\_1
  - \* Now the command prompt is active in the chosen director, e.g.
 

```
C:\Raman_data\results_curve-fitting\project_1.
```
- Now you have to start the 'ifors\_start\_curve-fit.py' script file with python and indicate on which spectrum-file the script should work (Fig. 7.2.3). To do this, type the following in your command prompt (continuing from the example above):
  - python c:\Python\_scripts\ifors\ifors\_start\_curve-fit.py -Gui [...]
 

```
c:\Raman_data\spectra\project_1\KL2-19_2.txt
```
  - This command consists of four parts:
    - \* The first part 'python' starts python.
    - \* The second part 'c:\Python\_scripts\ifors\ifors\_start\_curve-fit.py' points to the script file python is to execute.
    - \* The third part '-Gui' is an option of the 'ifors\_start\_curve-fit.py' script that will show a live preview of the curve-fitting.
    - \* The fourth part 'c:\Raman\_data\spectra\project\_1\KL2-19\_2.txt' points to the spectrum-file that the 'ifors\_start\_curve-fit.py' script should work on.
  - When you hit enter, a new window will open, showing the live progress of curve-fitting, from now on named live-view (Fig. 7.2.4), and some output about the progress of the curve-fitting is printed in the command prompt (Fig. 7.2.5).
  - The curve-fit will continue until optimization with the current constraints is reached, or if you close the live-view window.

7.2.3.2. *Generating Output.* When you have found a satisfying set of constraints, you will have to start the 'ifors\_start\_curve-fit.py' with the '-Cli' option:

- In the command prompt navigate to the folder in which you want to save the results of the curve-fit, in this example `C:\Raman_data\results_curve-fitting\project_1`. (Follow the steps in section 7.2.3.1)
- Once you are in the correct folder, type in the Winpython command prompt and press enter (Fig. 7.2.6):



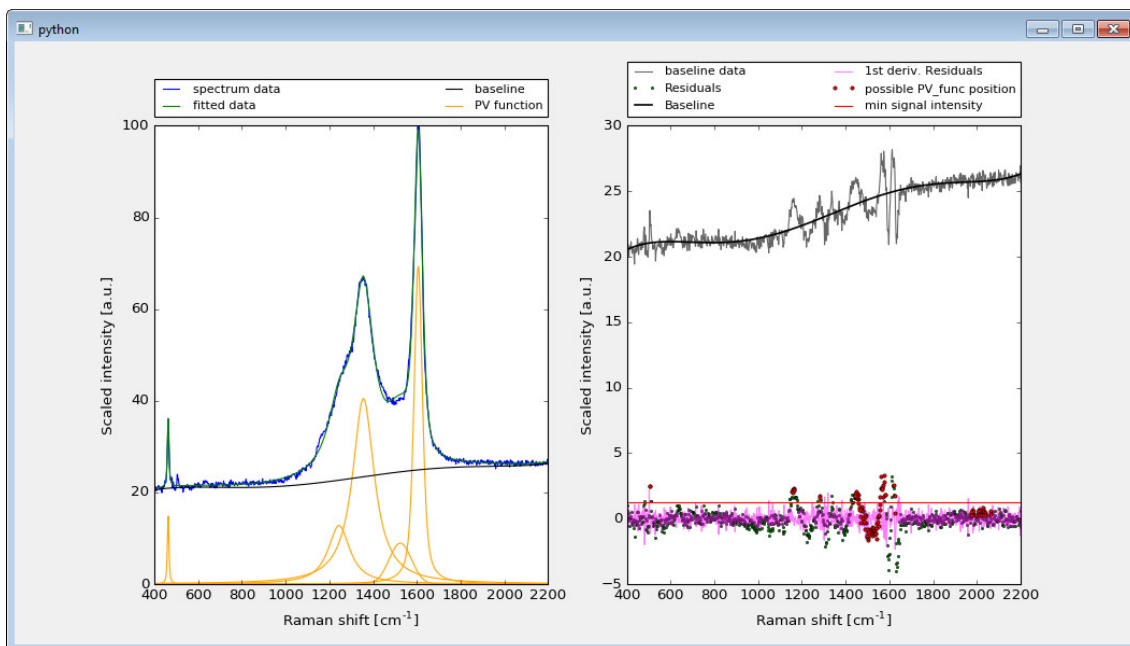


Figure 7.2.4. The live-view window showing a curve-fit in progress.

```

C:\Windows\system32\cmd.exe - cmd.bat
Testing position: 4.3991416309 best_rating 177.118130578 rating 173.126311288
peak position 4.3991416309
model rating 173.126311288 177.118130578
Improve
rating after improve 171.008039032
## model ##
[[ 6.24939243e+01 3.16770089e+00 6.71819699e+01 1.01880604e+00]
 [ 4.00766636e+01 9.32530151e+02 5.31593025e+01 3.17032589e+00]
 [ 1.46558506e+01 9.18281733e-01 3.52334497e+00 2.46521349e-01]
 [ 1.25297939e+01 -1.46386673e+00 4.72252105e+01 3.11249970e+00]
 [ 1.92785014e+01 -5.73507429e+02 6.58469289e+01 1.49961009e+00]
 [ 2.57134329e+00 1.66629867e-05 5.91277661e+00 1.95349925e-01]
 [ 7.28175811e+00 4.02307079e-05 6.06282333e+01 3.3332486e+00]
 [ 3.65689191e+00 -2.95946141e+02 4.24814032e+01 1.58528636e+00]
 [ 2.66393566e+00 4.73710170e+01 5.19624587e+01 5.73622975e-01]
 [ 1.80749893e+00 5.39518664e-01 4.90088297e+01 6.55462264e-01]
 [ 4.00920076e+00 1.06952654e-05 6.79455006e+01 2.27687024e-01]
 [ 1.80139466e+00 0.00000000e+00 4.37769037e+00 1.37806196e-01]]
adding peak 171.008039032
model rating inf 171.008039032
found no improvement
--- duration 381.140625
--- Final Rating --- 171.008039032
C:\Raman_data\results_curve-fitting\project_1>

```

Figure 7.2.5. The command prompt output when the curve-fit is finished.

```

- python c:\Python_scripts\ifors\ifors_start_curve-fit.py -Cli [...]
c:\Raman_data\spectra\project_1\KL2-19_2.txt

```

- When the curve-fitting process is completed, the duration is reported and you can again execute commands in command prompt window (Fig. 7.2.7).
- When finished, three files are saved in the 'results\_curve\_fitting\project\_1' folder which have the name of the spectrum-file added with the prefix 'fit\_'. In this case the three files are 'fit\_KL2-19\_2.npz', 'fit\_KL2-19\_2.pdf' and 'fit\_KL2-19\_2.png'.
- The npz-file contains all curve-fitting results, i.e. optimized pseudo-Voigt function parameters, baseline values, and the spectrum itself.

```

C:\Windows\system32\cmd.exe - cmd.bat
C:\Winpython\scripts>cd ..
C:\Winpython>cd ..
C:\>cd Raman_data\results_curve-fitting\project_1
C:\Raman_data\results_curve-fitting\project_1>python c:\Python_scripts\ifors\ifors_start_curve-fit.py -Cli c:\Raman_data\spectra\project_1\KL2-19_2.txt

```

Figure 7.2.6. Starting the 'ifors\_start\_curve-fit.py' script with the -Cli option. The results will be saved in a '.npz' file.

```

C:\Windows\system32\cmd.exe - cmd.bat
adding peak 221.365777576
min_signal_intensity 1.15891888905
Testing position: 48.9270386266 best_rating 221.365777576 rating 217.647172485
peak position 48.9270386266
model rating 217.647172485 221.365777576
Improve
rating after improve 207.407103716
## model ##
[[ 6.46691941e+01 -1.76375067e+00 6.71815172e+01 1.06614562e+00]
 [ 4.09977478e+01 -5.69448499e+02 5.30267332e+01 3.19206559e+00]
 [ 1.48816410e+01 -2.25640670e+00 3.52429457e+00 2.38663304e-01]
 [ 1.19966737e+01 -6.78529389e+00 4.70472259e+01 2.84207798e+00]
 [ 7.07031883e+00 2.97171284e-06 6.06184643e+01 3.3330632e+00]
 [ 1.70903167e+01 -1.82008122e+02 6.56576156e+01 1.48895977e+00]
 [ 2.54774474e+00 -7.74343969e-05 5.91249118e+00 1.92513906e-01]
 [ 3.40231396e+00 -8.35674043e-01 4.26823706e+01 1.66143309e+00]
 [ 2.38269002e+00 3.26656596e+01 4.89429118e+01 5.75982493e-01]]
adding peak 207.407103716
model rating inf 207.407103716
found no improvement
duration 46.70
Done
C:\Raman_data\results_curve-fitting\project_1>

```

Figure 7.2.7. The command prompt window after curve-fitting finished with -Cli option.

- The pdf-file shows the plot of the spectrum with the optimized pseudo-Voigt functions, the baseline, etc. and can be modified in any vector-graphic program (e.g. InkScape or Adobe Illustrator).
- The png-file shows the same as the pdf but can be modified in any pixel-graphic program (e.g. Gimp or Adobe Photoshop).

7.2.3.3. *Fitting multiple spectra.* If you want to apply curve-fitting for several spectra, you have to move all your spectrum-files into the same folder (here *Raman data\spectra\project\_1*) and proceed as outlined in section 7.2.3.2:

- Once you are in the folder where you want your results to be stored (here *Raman data\results\_curve-fitting\project\_1*), type in the Winpython command prompt and press enter:
  - `python c:\Python_scripts\ifors\ifors_start_curve-fit.py -Cli [...]`
  - `c:\Raman_data\spectra\project_1\*.txt`
  - `*.txt` passes a list of all txt-files present in the indicated directory to the `'ifors_start_curve-fitting.py'` script.
- For each spectrum-file a pdf-, npz- and png-file is created (see section 7.2.3.2)
- You can quickly evaluate the quality of your curve-fits by browsing through the curve-fit plots in the png files.

```

ca: C:\Windows\system32\cmd.exe - cmd.bat
C:\Winpython\scripts>cd ..
C:\Winpython>cd ..
C:\>cd Raman_data\results_curve-fitting\project_1
C:\Raman_data\results_curve-fitting\project_1>

```

Figure 7.2.8. Navigate to your project folder.

**7.2.4. Working with the curve-fit results.** The results of a curve-fit done by IFORS are stored in the npz-file generated by the *ifors\_start\_curve-fit.py* script using the *-Cli* option (see section 7.2.3.2 & 7.2.3.3). The following steps concern the results of Raman spectra of carbonaceous material (CM).

7.2.4.1. *Structuring your output.* To keep your *'project'* folders clearly arranged it is suggested:

- Inside the *'project\_1'* folder create a folder for the npz-files and a folder for the plots, i.e. *'\results\_curve-fitting\project\_1\npzs'* and *'\results\_curve-fitting\project\_1\plots'*
- Move the npz-, pdf- and png-files in their respective folder.

7.2.4.2. *Extracting the results from the npz-files.*

- In the command prompt window, navigate to the *'project\_1'* folder (Fig. 7.2.8).
- In the Winpython command prompt window type and press enter:
  - `python c:\Python_scripts\ifors\ifors_readout.py -Cm_readout [...] npzs\fit_KL2-19_2.npz`
- This command will start the *ifors\_readout.py* script with the *'-Cm\_readout'* option. In this mode the *ifors\_readout.py*-script will generate three files in the *'project\_1'* folder, i.e. *ifors\_peaks.fit*, *ifors\_all\_data.fit* and *ifors\_averaged\_data.fit*. These files are **space-delimited txt-files** and can be imported into LibreOffice 5 Calc, Microsoft Excel or any other spreadsheet calculator.

In the following section we will examine the contents and structure of the generated *'fit'* files.

7.2.4.3. *Contents of the 'ifors\_peaks.fit' file.* To open any of the *'fit'* files in Excel, set Excel to show all files in the open-file-dialog and select the *'fit'* file, in this case *ifors\_peaks.fit*. In the *'Textconverter-wizard'* select the delimited option, hit next and in the following step select space as delimiter and hit *'done'*.

Figure 7.2.9 shows the content of the *ifors\_peaks.fit* file after successfully importing into Excel. Each line below the header contains the parameters of a pseudo-Voigt function, i.e. the scaled intensity, shape (Gauss/Lorentz ratio), area, half width at half maximum in  $\text{cm}^{-1}$  and the center value, also in  $\text{cm}^{-1}$ . In this case on spectrum-file (KL2-19\_2) has been evaluated three times (*'repetition'* parameter is set to be 3 by default (section 7.2.3.2)). Thus, all functions with the same eval-number (Figure 7.2.9) belong to the same evaluation. Within each evaluation-block the functions are sorted by ascending center-value.

7.2.4.4. *Contents of the 'ifors\_all\_data.fit' file.* To open the *ifors\_all\_data.fit* file with Excel proceed in the same way as in section 7.2.4.2. Figure 7.2.10 shows the contents of *ifors\_all\_data.fit* after opening it in Excel.

In this file the results, in terms of *D\_STA*, *G\_STA*,  $\ln(D\_STA)$ ,  $\ln(G\_STA)$ , *G\_shape\_factor*, *center\_D\_band*, *center\_G\_band* and the D/G intensity ratio, are shown for each evaluation (i.e.

	A	B	C	D	E	F
1	sample	scaled_intensity	shape	area	hwhm_[cm-1]	center_[cm-1]
2	fit_KL2-19_2_eval_1_func_1	14.882	0.693	92.114	4.296	463.734
3	fit_KL2-19_2_eval_1_func_2	2.548	0	9.732	3.465	506.223
4	fit_KL2-19_2_eval_1_func_3	3.402	0.455	134.82	29.906	1168.67
5	fit_KL2-19_2_eval_1_func_4	11.997	0.872	925.444	51.157	1245.923
6	fit_KL2-19_2_eval_1_func_5	2.383	0.97	39.513	10.368	1280.687
7	fit_KL2-19_2_eval_1_func_6	40.998	0.998	3673.94	57.457	1354.077
8	fit_KL2-19_2_eval_1_func_7	7.07	0	467.62	60	1491.202
9	fit_KL2-19_2_eval_1_func_8	17.09	0.995	728.213	26.801	1581.974
10	fit_KL2-19_2_eval_1_func_9	64.669	0.638	1763.492	19.191	1609.013
11						
12	fit_KL2-19_2_eval_2_func_1	14.657	0.479	86.85	4.436	463.734
13	fit_KL2-19_2_eval_2_func_2	1.803	0	4.918	2.475	479.185
14	fit_KL2-19_2_eval_2_func_3	2.566	0	9.986	3.53	506.223
15	fit_KL2-19_2_eval_2_func_4	3.525	0.362	141.413	31.37	1170.601
16	fit_KL2-19_2_eval_2_func_5	11.873	0.952	883.905	48.071	1245.923
17	fit_KL2-19_2_eval_2_func_6	2.491	0	37.054	13.494	1280.687
18	fit_KL2-19_2_eval_2_func_7	41.423	0.999	3765.75	58.316	1354.077
19	fit_KL2-19_2_eval_2_func_8	7.11	0	470.282	60	1491.202
20	fit_KL2-19_2_eval_2_func_9	18.602	0.997	793.087	26.797	1583.906
21	fit_KL2-19_2_eval_2_func_10	63.079	0.747	1721.837	18.492	1609.013
22	fit_KL2-19_2_eval_2_func_11	3.854	0	16.911	3.98	1622.532
23						
24	fit_KL2-19_2_eval_3_func_1	14.876	0.691	92.101	4.3	463.734
25	fit_KL2-19_2_eval_3_func_2	2.547	0	9.734	3.467	506.223
26	fit_KL2-19_2_eval_3_func_3	3.137	0.106	107.853	29.786	1168.67
27	fit_KL2-19_2_eval_3_func_4	12.292	0.981	994.475	51.928	1247.854
28	fit_KL2-19_2_eval_3_func_5	2.407	0.986	39.739	10.269	1280.687
29	fit_KL2-19_2_eval_3_func_6	40.763	0.998	3642.424	57.284	1354.077
30	fit_KL2-19_2_eval_3_func_7	7.06	0	466.943	60	1491.202
31	fit_KL2-19_2_eval_3_func_8	17.376	0.994	745.298	26.985	1581.974
32	fit_KL2-19_2_eval_3_func_9	64.371	0.639	1749.215	19.118	1609.013
33						

Figure 7.2.9. The content of the 'ifors\_peaks.fit' file after importing into Excel.

	A	B	C	D	E	F	G	H	I
1	sample	D_STA	G_STA	ln(D_STA)	ln(G_STA)	G_shape_factor	center_D_band	center_G_band	D_G_ratio
2	fit_KL2-19_2_eval_1	209.95	121.216	5.347	4.798	0.788	1354.077	1607.082	0.578
3	fit_KL2-19_2_eval_2	211.161	122.169	5.353	4.805	0.788	1354.077	1607.082	0.579
4	fit_KL2-19_2_eval_3	210	121.301	5.347	4.798	0.787	1354.077	1607.082	0.578

Figure 7.2.10. Contents of the 'ifors\_all\_data.fit' file.

one line equals one evaluation). For details on the STA- values and the G\_shape\_factor see Lünsdorf (2016), Lünsdorf and Lünsdorf (2016) and Lünsdorf et al. (in subm.).

7.2.4.5. Contents of the 'ifors\_averaged\_data.fit' file. This file is used later for the temperature estimation, see section 7.2.5. To open the 'ifors\_averaged\_data.fit' file proceed in the same way as in section 7.2.4.2. Figure 7.2.11 shows the contents of the 'ifors\_averaged\_data.fit' after opening it in Excel. The 'ifors\_averaged\_data.fit' contains essentially the same data as the 'ifors\_all\_data.fit' file, but here the data of each evaluation, which is given in 'ifors\_all\_data.fit', is averaged in the 'ifors\_averaged\_data.fit' file and the mean values with their associated standard

	A	B	C	D	E	F	G	H	I	J	K	L	M	N	O	P	Q
1	sample	D_STA(mesa)	std	G_STA(mesa)	std	ln(D_STA)(mesa)	std	ln(G_STA)(mesa)	std	G_shape_factor(mesa)	std	center_D_band(mesa)	std	center_G_band(mesa)	std	D_G_ratio(mesa)	std
2	fit_KL2-19_2	210.37	0.56	121562	0.43	5.349	0.003	4.8	0.004	0.788	0	1354.077	0	1607.082	0	0.578	0

Figure 7.2.11. Contents of the 'ifors\_averaged\_data.fit' file after opening it in Excel.

```
C:\Raman_data\results_curve-fitting\project_1>python c:\Python_scripts\ifors\ifors_readout.py -Peak_parameters npzs\*.npz
fit_KL2-19_2
fit_KL2-8HS_1_ics
C:\Raman_data\results_curve-fitting\project_1>
```

Figure 7.2.12. Starting the 'ifors\_readout.py', using the '-Peak\_parameters' option, for multiple npz-files.

deviation are reported. Thus, each line in this file represents the averaged evaluation results of one spectrum-file.

7.2.4.6. *Extracting results from non-CM samples.* If you recorded, for instance, a mineral Raman spectrum and you are only interested in the pseudo-Voigt function parameters, you have to proceed as in section 7.2.3.1.

- In the command prompt window, navigate to the 'project\_1' folder and type:
  - python c:\Python\_scripts\ifors\ifors\_readout.py -Peak\_parameters [...] npzs\fit\_KL2-19\_2.npz
- This will start the 'ifors\_readout.py' script with the '-Peak\_parameters' option and only the 'ifors\_peaks.fit' file will be generated.

7.2.4.7. *Extracting the results from multiple curve-fits.* If you have curve-fits (i.e. npz-files) of multiple spectrum-files, you can extract the results of each curve-fit from the respective npz-file (in this case we are only interested in the function parameters).

- In the command prompt window, navigate to the 'project\_1' folder and type:
  - python c:\Python\_scripts\ifors\ifors\_readout.py [...] -Peak\_parameters npzs\\*.npz
- In the Winpython command prompt the name of each npz-file, that the 'ifors\_readout.py' script is working on, is displayed; here KL2-19\_2 and KL2-8\_HS\_1\_ics (Fig. 7.2.12).
- Open the saved 'ifors\_peaks.fit' file in Excel and each pseudo-Voigt function parameter of each evaluation for the KL2-19\_2 and KL2-8HS\_1\_ics spectrum-files is presented (Fig. 7.2.13).
- The same procedure is valid for the '-Cm\_readout' option of the 'ifors\_readout.py' script.

7.2.4.8. *Extracting the spectrum data, fitted function values and baseline values.* If you want to work with the values of the fitted pseudo-Voigt functions, baseline values or Raman intensity values (for instance plotting in Excel or alike), you can extract these values from the npz-file. To do this, you will have to start the 'ifors\_readout.py' script with the '-Fitted\_values' option.

- In the command prompt window, navigate to the 'project\_1' folder and type:
  - python c:\Python\_scripts\ifors\ifors\_readout.py -Fitted\_values [...] npzs\fit\_KL2-19\_2.npz
- This will generate a new file named 'ifors\_fitted\_values\_fit\_KL2-19\_2.fit'
- The first column in this file contains the Raman shift values of the spectrum, followed by the scaled Raman intensity, baseline values of the first evaluation (eval\_1\_bl), values

	A	B	C	D	E	F
1	sample	scaled_intensity	shape	area	hwhm_[cm-1]	center_[cm-1]
2	fit_KL2-19_2_eval_1_func_1	14.882	0.693	92.114	4.296	463.734
3	fit_KL2-19_2_eval_1_func_2	2.548	0	9.732	3.465	506.223
4	fit_KL2-19_2_eval_1_func_3	3.402	0.455	134.82	29.906	1168.67
5	fit_KL2-19_2_eval_1_func_4	11.997	0.872	925.444	51.157	1245.923
6	fit_KL2-19_2_eval_1_func_5	2.383	0.97	39.513	10.368	1280.687
7	fit_KL2-19_2_eval_1_func_6	40.998	0.998	3673.94	57.457	1354.077
8	fit_KL2-19_2_eval_1_func_7	7.07	0	467.62	60	1491.202
9	fit_KL2-19_2_eval_1_func_8	17.09	0.995	728.213	26.801	1581.974
10	fit_KL2-19_2_eval_1_func_9	64.669	0.638	1763.492	19.191	1609.013
11						
12	fit_KL2-8HS_1_ics_eval_1_func_1	0.956	0	31.004	38.905	423.287
13	fit_KL2-8HS_1_ics_eval_1_func_2	1.118	0.996	68.24	40.297	628.988
14	fit_KL2-8HS_1_ics_eval_1_func_3	1.165	0	16.952	13.26	1156.824
15	fit_KL2-8HS_1_ics_eval_1_func_4	6.793	0.995	630.055	60	1203.397
16	fit_KL2-8HS_1_ics_eval_1_func_5	13.721	0.887	1232.62	59.999	1315.951
17	fit_KL2-8HS_1_ics_eval_1_func_6	79.774	0.999	4246.876	33.734	1358.643
18	fit_KL2-8HS_1_ics_eval_1_func_7	8.46	0.719	653.924	54.315	1494.483
19	fit_KL2-8HS_1_ics_eval_1_func_8	14.165	0.166	681.067	40.934	1574.047
20	fit_KL2-8HS_1_ics_eval_1_func_9	1.671	0	7.546	4.116	1593.453
21	fit_KL2-8HS_1_ics_eval_1_func_10	69.401	0.475	2081.097	22.546	1605.096
22	fit_KL2-8HS_1_ics_eval_1_func_11	6.315	0	46.649	6.733	1620.621

**Figure 7.2.13.** Content of the 'ifors\_peaks.fit' file generated from multiple npz-files. Only one evaluation was performed for this example.

of function one of evaluation one (eval\_1\_f1), values of function two of evaluation one (eval\_1\_f2), and so forth (Fig. 7.2.14).

- To extract these data from multiple npz-files type in the command prompt window:
  - python c:\Python\_scripts\ifors\ifors\_readout.py [...]
  - Fitted\_values npzs\\*.npz
- For each npz-file present in the 'project\_1\npzs' folder a 'ifors\_fitted\_values\_filename.fit' file will be created for further use.

**7.2.5. Estimating peak-metamorphic temperature from computed STA-values.** To estimate the peak-metamorphic temperature from the STA-value of a sample with unknown temperature, you have to prepare first a calibration line. In order to this you will need to measure the reference samples described in Lünsdorf et al. (in subm.). The samples are available (email to: kluensd@gwdg.de) and of course, you can extend this reference sample set with your own samples of known temperature.

As an example, the data of the reference sample series described in Lünsdorf et al. (in subm.), is provided in the 'reference\_series\_data.xls' file (Fig. 7.2.15).

#### 7.2.5.1. Creating the calibration line .

- Measure the reference samples and evaluate the recorded spectrum-files using the 'ifors\_start\_curve-fit.py' script with the '-Cli' option and extract the results from the generated npz-files with the 'ifors\_readout.py' script using the '-Cm\_readout' option (section 7.2.3.3, 7.2.4.2 & 7.2.4.5).
- Open the 'reference\_series\_data.xls' file in Excel or LibreOffice Calc and insert your  $\ln(D\_STA)$ ,  $\ln(G\_STA)$  and  $G\_shape\_factor$  (Fig. 7.2.15).

	A	B	C	D	E	F	G	H	I	J	K	L	M	N
1	Raman_shift [cm-1]	Intensity [a.u.]	eval_1_bl	eval_1_f1	eval_1_f2	eval_1_f3	eval_1_f4	eval_1_f5	eval_1_f6	eval_1_f7	eval_1_f8	eval_1_f9	eval_2_bl	eval_2_f1
2	400	21.7799	21.1461	0.0471	0	0.0023	0.038	0.0003	0.1478	0	0.0087	0.0104	21.1473	0.0342
3	401.9313	21.3883	21.1435	0.0501	0	0.0024	0.0382	0.0003	0.1484	0	0.0088	0.0104	21.1445	0.0363
4	403.8627	21.2159	21.1409	0.0533	0	0.0024	0.0384	0.0003	0.149	0	0.0088	0.0105	21.1418	0.0387
5	405.794	21.2597	21.1383	0.057	0	0.0024	0.0385	0.0003	0.1496	0	0.0088	0.0105	21.139	0.0414
6	407.7253	20.7286	21.1357	0.061	0	0.0024	0.0387	0.0003	0.1502	0	0.0089	0.0105	21.1363	0.0443
7	409.6567	20.3438	21.1332	0.0654	0	0.0024	0.0389	0.0003	0.1508	0	0.0089	0.0106	21.1337	0.0475
8	411.588	21.0614	21.1307	0.0703	0	0.0024	0.0391	0.0003	0.1514	0	0.0089	0.0106	21.131	0.051
9	413.5193	21.0689	21.1283	0.0758	0	0.0024	0.0393	0.0003	0.152	0	0.0089	0.0106	21.1284	0.055
10	415.4506	21.1424	21.1258	0.082	0	0.0024	0.0394	0.0003	0.1527	0	0.009	0.0107	21.1258	0.0595
11	417.382	21.0438	21.1234	0.0889	0	0.0025	0.0396	0.0003	0.1533	0	0.009	0.0107	21.1233	0.0646
12	419.3133	21.4987	21.1211	0.0968	0	0.0025	0.0398	0.0003	0.1539	0	0.009	0.0107	21.1207	0.0703
13	421.2446	20.9718	21.1188	0.1058	0	0.0025	0.04	0.0003	0.1545	0	0.0091	0.0108	21.1183	0.0768
14	423.176	20.7931	21.1165	0.1161	0	0.0025	0.0402	0.0003	0.1552	0	0.0091	0.0108	21.1158	0.0843
15	425.1073	20.621	21.1142	0.1279	0	0.0025	0.0404	0.0003	0.1558	0	0.0091	0.0108	21.1134	0.0929
16	427.0386	20.8376	21.112	0.1417	0	0.0025	0.0406	0.0003	0.1565	0	0.0092	0.0109	21.111	0.1028
17	428.97	21.102	21.1098	0.1577	0	0.0025	0.0407	0.0003	0.1571	0	0.0092	0.0109	21.1087	0.1145
18	430.9013	20.9518	21.1077	0.1767	0	0.0025	0.0409	0.0003	0.1578	0	0.0092	0.0109	21.1064	0.1283
19	432.8326	20.5048	21.1056	0.1992	0	0.0026	0.0411	0.0003	0.1584	0	0.0092	0.011	21.1042	0.1446
20	434.7639	19.922	21.1036	0.2264	0	0.0026	0.0413	0.0003	0.1591	0	0.0093	0.011	21.102	0.1643
21	436.6953	21.0608	21.1016	0.2594	0	0.0026	0.0415	0.0003	0.1598	0	0.0093	0.0111	21.0998	0.1882
22	438.6266	21.2115	21.0996	0.3002	0	0.0026	0.0417	0.0004	0.1604	0	0.0093	0.0111	21.0977	0.2178
23	440.5579	20.9198	21.0977	0.3512	0	0.0026	0.0419	0.0004	0.1611	0	0.0094	0.0111	21.0957	0.2547
24	442.4893	21.3679	21.0958	0.4162	0	0.0026	0.0421	0.0004	0.1618	0	0.0094	0.0112	21.0936	0.3018
25	444.4206	21.2084	21.094	0.5007	0	0.0026	0.0423	0.0004	0.1625	0	0.0094	0.0112	21.0917	0.363
26	446.3519	21.5351	21.0922	0.6132	0	0.0027	0.0425	0.0004	0.1632	0	0.0095	0.0112	21.0897	0.4446
27	448.2833	22.4671	21.0905	0.7679	0	0.0027	0.0427	0.0004	0.1639	0	0.0095	0.0113	21.0878	0.5578
28	450.2146	22.6415	21.0888	0.9909	0	0.0027	0.0429	0.0004	0.1646	0	0.0095	0.0113	21.086	0.7286
29	452.1459	22.0768	21.0872	1.3419	0	0.0027	0.0431	0.0004	0.1653	0	0.0096	0.0113	21.0842	1.0286
30	454.0773	22.4703	21.0856	1.9644	0	0.0027	0.0434	0.0004	0.166	0	0.0096	0.0114	21.0825	1.646
31	456.0086	24.2821	21.084	3.1593	0	0.0027	0.0436	0.0004	0.1667	0	0.0096	0.0114	21.0808	2.9584
32	457.9399	26.746	21.0825	5.3783	0	0.0027	0.0438	0.0004	0.1674	0	0.0097	0.0115	21.0791	5.437

Figure 7.2.14. Contents of the 'ifors\_fitted\_values\_fit\_KL2-19\_2.fit' file.

	A	B	C	D	E	F	G	H	I	J
1	Reference sample	Peak temperature [°C]	uncertainty	ln(D_STA)	std	ln(G_STA)	std	G_shape factor	std	n
2	KL14_5	162	30	5.482	0.025	4.903	0.023	0.937	0.019	32
3	KL14_7	178	30	5.430	0.064	4.877	0.068	0.852	0.071	30
4	KL14_21	228	30	5.406	0.050	4.794	0.038	0.907	0.035	20
5	KL14_16	236	30	5.374	0.040	4.739	0.025	0.880	0.027	50
6	KL16_31	236	30	5.287	0.054	4.666	0.029	0.798	0.024	37
7	KL16_35	240	30	5.322	0.032	4.704	0.021	0.829	0.023	50
8	KL14_17	256	30	5.176	0.020	4.609	0.021	0.773	0.022	50
9	KL14_43	260	30	5.191	0.038	4.625	0.031	0.804	0.034	50
10	KL14_13	267	30	5.148	0.032	4.610	0.029	0.761	0.029	38
11	KL14_1	295	20	4.880	0.027	4.840	0.026	1.078	0.083	50
12	KL14_19	299	23	5.090	0.020	4.825	0.040	1.050	0.083	50
13	KL16_8	325	25	4.662	0.085	4.929	0.051	0.986	0.073	20
14	KL16_19	350	25	4.470	0.053	5.010	0.027	1.323	0.088	15
15	KL14_58	370	40	4.375	0.033	4.816	0.068	1.803	0.079	15
16	KL16_10	370	35	4.315	0.032	4.937	0.032	1.621	0.073	20
17	KL16_11	370	35	4.365	0.056	4.928	0.059	1.584	0.087	20
18	KL16_14	415	35	4.495	0.079	4.220	0.105	3.257	0.283	21
19	KL16_29	420	40	4.440	0.106	4.022	0.107	4.083	0.395	15
20	KL14_59	420	50	4.359	0.104	4.265	0.098	3.318	0.307	20
21	KL14_27	440	46	4.617	0.212	3.672	0.146	6.379	0.951	30
22	KL14_56	450	30	4.607	0.162	3.735	0.104	5.874	0.594	20
23	KL16_23	480	40	4.875	0.138	3.425	0.081	8.078	0.710	20
24	KL16_15	490	40	4.543	0.114	3.651	0.123	5.872	0.711	19
25	KL16_16	490	40	5.006	0.205	3.343	0.133	7.696	1.144	10
26	KL14_52	520	25	5.019	0.301	3.328	0.115	9.208	1.308	20
27	KL14_49	610	50	5.240	0.354	3.063	0.105	11.698	1.618	20

Figure 7.2.15. Temperature values and the associated STA-values of the reference series samples.

- In your 'Raman\_data\' folder create a 'reference\_data' sub-folder (Fig. 7.2.16)
- Save the updated 'reference\_series\_data.xls' file and save it also as a 'tab-delimited.txt' file in the 'Raman\_data\reference\_data' folder.
- In the Winpython command prompt navigate to your 'Raman\_data\results\_curve-fitting\project\_1' folder.
- To create only the calibration line from the reference data, type in the Winpython command prompt and press enter:

```

- python c:\Python_scripts\ifors\ifors_estimate_temperature.py [...]
  c:\Raman_data\reference_data\reference_series_data.txt

```

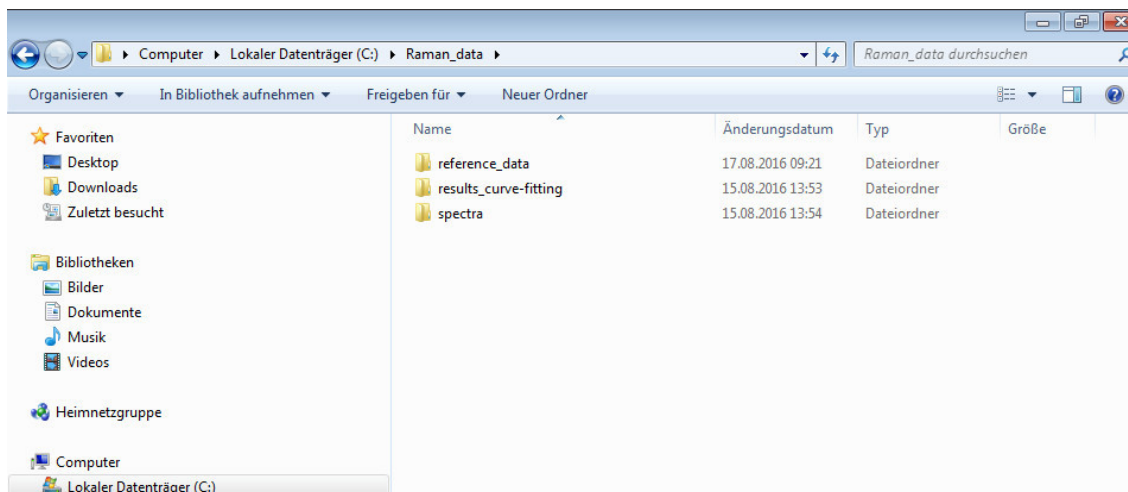


**Figure 7.2.16.** Contents of the 'Raman\_data' folder.

- Provide the confidence level for the confidence interval.
  - Provide the confidence level for the prediction interval.
  - Plot the calibration line together with the reference data (*optional*).
  - If you answer the last question with yes, a window will open, showing the plot (Fig. 7.2.17). For the script to continue close the plot-window.
  - Perform a temperature point estimate (*optional*).
  - If you answer with no, the script will stop, if answer with yes, you must enter a  $\ln(\text{STA})$  value (the range of possible  $\ln(\text{STA})$  values can be seen in the plot-window) and the estimated temperature will be printed in the command prompt window (Fig. 7.2.18).
  - A txt-file 'calib\_curve\_coefs.txt' will be stored in your 'results\_curve-fitting\project\_1' folder which contains the slope and intercept of the regression line and their respective standard errors (Fig. 7.2.19).
- If you change/extend your reference data, the 'ifors\_estimate\_temperature.py' script will automatically compute a new calibration line.

7.2.5.2. *Estimating the temperature of unknown samples.* You can use the 'ifors\_estimate\_temperature.py' script to estimate the temperature for multiple samples. If you evaluated multiple spectrum-files and extracted the results with the 'ifors\_readout.py' script using the '-Cm\_readout' option, you can then use the 'ifors\_averaged\_data.fit' file with the 'ifors\_estimate\_temperature.py' script.

- In the Winpython command prompt navigate to your 'Raman\_data\results\_curve-fitting\project\_1' folder.
- To estimate the temperature from multiple samples, type in the Winpython command prompt:
  - `python c:\Python_scripts\ifors\ifors_estimate_temperature.py [...]`
  - `c:\Raman_data\reference_data\reference_series_data.txt [...]`
  - `ifors_averaged_data.fit`
  - Provide the confidence level for the confidence interval.
  - Provide the confidence level for the prediction interval.



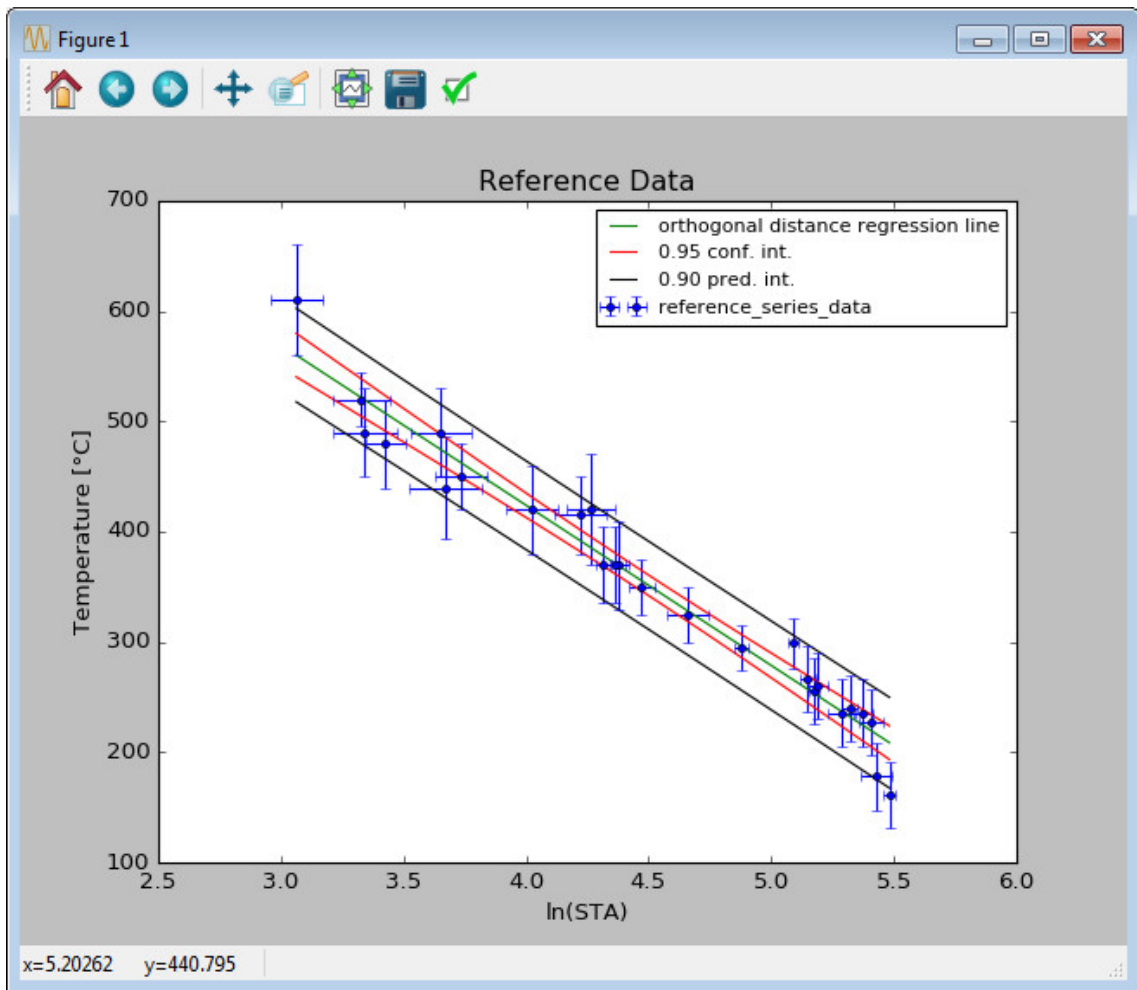


Figure 7.2.17. The calibration line (orthogonal distance regression line), reference data, confidence and prediction interval.

```

C:\Windows\system32\cmd.exe - cmd.bat

C:\Raman_data\results_curve-fitting\project_1>python c:\Python_scripts\ifors\ifors_estimate_temperature.py c:\Raman_data\reference_data\reference_series_data.txt
Give the level of confidence for the confidence interval(e.g. 0.95): 0.95
Give the level of confidence for the prediction interval(e.g. 0.9): 0.9
Do you want to plot the calibration curve and reference data? (y/n): y

regression coefficients: -145.1544 (slope), 1004.5668 (intercept)
                        5.9269 (SE slope), 28.0858 (SE intercept)
unweighted r2: 0.962
Do you want a temperature point estimate? (y/n): y
Type your ln(STA) value here: 4
Estimated temperature: 423.9 +- 40 (based on 0.90 pred. int.)

C:\Raman_data\results_curve-fitting\project_1>

```

Figure 7.2.18. Output of the 'ifors\_estimate\_temperature.py' script.

- Plot the calibration line together with the reference data (optional).
- Once the script is finished, a txt-file 'temperature\_estimates.txt' is stored in the 'results\_curve-fitting\project\_1' folder. In this file the estimated temperatures are stored for each sample (Fig. 7.2.20).

	A	B	C	D	E
1	Slope	SE	Intercept	SE	
2	-145.15	5.93	1004.57	28.09	
3					

Figure 7.2.19. Contents of the 'calib\_curve\_coefs.txt' file.

	A	B	C	D	E	F
1	sample	est_Temp.[°C]	uncertainty	conf_int_lvl:0.95	pred_int_lvl:0.90	
2	fit_KL2-19_2	228	40			
3	fit_KL2-8HS_1_ics	301	40			

Figure 7.2.20. Contents of the 'temperature\_estimates.txt' file.

```

54
55     #####apply use_filter function to smooth the spectrum. NB win_size must be
56     #####odd
57     #####y = use_filter(y,3)
58
59     #####Set here the range to fit with start_wn and stop_wn
60     #####dat = norm_and_cut(x,y,start_wn=400, stop_wn=2200)
61     #####constraints = Constraints()
62
63     #####set here the constraints for the curve-fit
64     #####min_width, max_width, min_dist = 1, 60, 5
65     #####constraints.min_signal_width = dat['dist_n'] * min_width
66     #####constraints.max_signal_width = dat['dist_n'] * max_width/dat['dist_e']
67     #####constraints.min_signal_distance = dat['dist_n'] * min_dist
68     #####constraints.baseline_mode = 'window_filter'##'polynom'
69     #####constraints.polynom_order = 5
70     #####constraints.window_size = 301
71     #####constraints.alpha = 0.985
72     #####constraints.sigma_threshold = 0.01
73     #####constraints.noise_intensity = 2.5
74     #####constraints.max_peak_number = 100
75
76     #####seed = 0
77     #####repetitions = 3
78
Python f length: 2942 lines: 87 Ln: 74 Col: 42 Sel: 0 | 0 UNIX UTF-8 INS

```

Figure 7.2.21. The constraints section in 'ifors\_start\_curve-fit.py'. Line numbers are provided in the left column.

## 7.2.6. Options.

7.2.6.1. *Changing constraints.* The 'ifors\_start\_curve-fit.py' script will not save any results if you start it with '-Gui' option. This mode of operation is used to control the curve-fit when constraints are changed. To change constraints open the 'ifors\_start\_curve-fit.py' script with Notepad++ (or another editor of your choice). Figure 7.2.21 shows the section in the script where constraints are controlled.

- The function `'norm_and_cut()'` (line 60 in Fig. 7.2.21) allows to clip the spectrum to a specific wavenumber interval by setting the `'start_wn'` and `'stop_wn'` parameters. If you set these parameters to `'None'`, the whole spectrum will be fitted, e.g. `'start_wn=None'` and `'stop_wn=None'`.
- The parameters `'min_width'`, `'max_width'` and `'min_dist'` (line 64 in Fig. 7.2.21) control the minimum and maximum width of and the minimum distance between the fitted pseudo-Voigt functions. The maximum width, in wavenumbers (default is 60), refers to the half width at half maximum of the pseudo-Voigt functions. The minimum width and distance are given in integer multiples of the spectral resolution (e.g. distance between two data-points).
- The parameter `'baseline_mode'` (line 68 in Fig. 7.2.21) lets you choose the style of baseline approximation. If set to `'window_filter'`, the baseline is approximated by a convolution of the baseline-data with a moving Hanning-window. The size of the Hanning-window is set with the `'window_size'` parameter (line 70 in Fig. 7.2.21) and must be an odd integer. If `'baseline_mode'` is set to `'polynom'`, the baseline is approximated by a polynomial of the order set with the `'polynom_order'` parameter (default is 5, line 69 in Fig. 7.2.21). If `'baseline_mode'` is set to `'off'` no baseline will be used during curve-fitting.
- The parameter `'alpha'` (line 71 in Fig. 7.2.21) controls the width of the normal distribution from which the value is chosen that is added or subtracted from a randomly chosen pseudo-Voigt function parameter. An `'alpha'` close to 1 results in small value and thus, chances are higher to find a valid change in parameters, e.g. the time spent in the mutation-loop increases (see Lünsdorf and Lünsdorf, 2016 for details). An `'alpha'` close to zero leads to a larger value added or subtracted from a randomly chosen pseudo-Voigt function parameter and thus, the duration in the mutation-loop is shorter.
- The parameter `'sigma_threshold'` (line 72 in Fig. 7.2.21) controls the duration of the mutation-loop more directly. Legit values for `'sigma_threshold'` are from the interval `'2 > sigma_threshold > 0'`. Values close to 2 result in short and values close to 0 in long mutation-loop duration.
- The parameter `'noise_intensity'` (line 73 in Fig. 7.2.21) is a multiple of the standard deviation of the estimated noise distribution.
- The parameter `'max_peak_number'` (line 74 in Fig. 7.2.21) sets the maximum number of pseudo-Voigt functions allowed during curve-fitting, e.g. if this number is reached the program stops.
- The parameter `'seed'` (line 76 in Fig. 7.2.21) controls the seed for the random number generator.
- The parameter `'repetitions'` (line 77 in Fig. 7.2.21) is only valid when the `-Cli` option is invoked with the `'ifors_start_curve-fit.py'` script and controls how often a spectrum is evaluated (each time with a different seed for the random number generator). The default value of this parameter is 3.

If you change any of these parameters, you have to save the script file before executing the script again. In the live-view window you can then observe the curve-fit with your changed set of parameters.

7.2.6.2. *Excluding pV-functions from STA-computation.* Frequently, the Raman spectrum of neighboring mineral phases are recorded together with the CM Raman spectrum. In the case of the STA-values, the additional mineral Raman bands need to be excluded from the STA-computation.

```

262     ...f4.write('\n')
263
264 def main():
265     """If Raman bands of minerals are present in the carbonaceous material
266     spectrum and you are only interested in the CM signal, set 'mineral_phases'
267     to True. Then select in the 'remove_mineral_peaks'-function the Raman shift
268     intervals of the mineral Raman bands you want to exclude from the
269     STA-computation."""
270
271     mineral_phases = False
272     plot_results = False
273
274     if platform.system() == 'Windows':
275         from glob import glob
276         file_list = glob(sys.argv[2])
277     else:
278         file_list = sys.argv[2:]
279
280     if sys.argv[1] == '-Cm_readout':
281         f1 = open('ifors_peaks.fit', 'w')
282         f2 = open('ifors_all_data.fit', 'w')
283         f3 = open('ifors_averaged_data.fit', 'w')
284
285         f1.write('sample scaled_intensity shape area hwhm [cm-1] center [cm-1]')
286         f1.write('\n')

```

**Figure 7.2.22.** Part of the 'ifors\_readout.py' script in Notepad++, showing the 'mineral\_phases' and 'plotting' option.

- Open the 'ifors\_readout.py' with Notepad++
- Set 'mineral\_phases' to 'True' (line 271 in Fig. 7.2.22).
- Set 'plotting' to 'True' if you want to see if your selected functions were excluded.
- With Notepad++ open, scroll to the top of the script file and locate the 'remove\_mineral\_peaks' function (line 30 in Fig. 7.2.23).
- In the 'remove\_mineral\_peaks' function you can declare the Raman shift intervals of specific mineral Raman bands.
- Any pV-function that has its central value within one of the declared intervals is excluded from the STA computation.

```
C:\Python_scripts\ifors\ifors_readout.py - Notepad++
File Edit Search View Encoding Language Settings Macro Run Plugins Window ?
ifors_readout.py ifors_estimate_temperature.py ifors_start_curve-fit.py
29
30 def remove_mineral_peaks(signal):
31     """Add here positions of Raman bands that are to be excluded
32     from the evaluation"""
33     cc_idx = np.where((1083 < signal[:,6]) & (signal[:,6] < 1093))[0]
34     cc_idx2 = np.where((1071 < signal[:,6]) & (signal[:,6] < 1083))[0]
35     cc_idx3 = np.where((1435 < signal[:,6]) & (signal[:,6] < 1445))[0]
36     cc_idx4 = np.where((1744 < signal[:,6]) & (signal[:,6] < 1760))[0]
37     dol_idx = np.where((1093 < signal[:,6]) & (signal[:,6] < 1100))[0]
38     plag_idx = np.where((1095 < signal[:,6]) & (signal[:,6] < 1105))[0]
39     plag_idx2 = np.where((1110 < signal[:,6]) & (signal[:,6] < 1118))[0]
40     qz_idx = np.where((1158 < signal[:,6]) & (signal[:,6] < 1164))[0]
41     qz_idx2 = np.where((1060 < signal[:,6]) & (signal[:,6] < 1066))[0]
42     misc_idx = np.where((1325 < signal[:,6]) & (signal[:,6] < 1335))[0]
43     misc_idx2 = np.where((1370 < signal[:,6]) & (signal[:,6] < 1375))[0]
44
45     """add the mineral indices (cc_idx, etc.) to the concatenate function to
46     exclude these Raman bands from the computation"""
47     mineral_peaks = np.concatenate((cc_idx, cc_idx2, cc_idx3, cc_idx4, qz_idx,
48     qz_idx2, dol_idx, plag_idx, plag_idx2, misc_idx, misc_idx2))
49     mineral_peaks = np.unique(mineral_peaks)
50     signal = np.delete(signal, mineral_peaks, 0)
51     return signal
52
53 def check_G_band(fit, orig wn):
Python f length: 13592 lines: 333 Ln: 275 Col: 30 Sel: 0 | 0 UNIX UTF-8 INS
```

Figure 7.2.23. Part of the 'ifors\_readout.py' script in Notepad++, showing the 'remove\_mineral\_peaks' function.

# Curriculum Vitae

## NILS KENO LÜNSDORF

### PERSONAL INFORMATION

*Born in Germany, 05.05.1984*  
*email* keno.luensdorf@geo.uni-goettingen.de  
*phone* (W) 0049-551-3919455 · (M) 0049-178-8017124

### EDUCATION

*04/2011–recent* Georg-August-Universität, Göttingen  
*Phd candidate* Thesis: *Geothermometry by Raman spectroscopy of dispersed organic matter*  
Advisors: Prof. Hilmar VON EYNATTEN & Prof. Volker THIEL

*10/2008–04/2011* Georg-August-Universität, Göttingen  
*Master of Science Studies* Thesis: *The Comparability of Raman Data of Carbonaceous Material – A Systematical Approach to Uncertainties in Measurement and Evaluation*  
Advisors: Prof. Hilmar VON EYNATTEN & Dr. Burkhard SCHMIDT

*10/2004–03/2008* Georg-August-Universität, Göttingen  
*Bachelor of Science Studies* Thesis: *Joint systems in the lower Muschelkalk of the northern Kraichgau – Fracture controlled fluid transport in a deep geothermal reservoir horizon of the Upper Rhine graben*  
Advisor: Prof. Sonja PHILIPP

### TEACHING

*2012–2014*  
*Fieldtrip, undergraduate* Winter-semester:  
Basic geological field techniques and characterization of rocks  
Summer-Semester:  
Basic geological field techniques and characterization of rocks  
Sedimentary rocks and facies

*2014*  
*Bachelor Thesis* Supervision of a Bachelor Thesis:  
Topic: Anwendung von Raman-Spektroskopie in der Schwermineralanalyse

### PUBLICATIONS

*2011* Geothermiekongress 2011 Bochum Proceedings  
*Reyer et al.* *Heterogenitäten bohrungsrelevanter Gesteinseigenschaften im Norddeutschen Becken: Geländestudien und Laboranalysen*  
Authors: D. REYER, N. K. LÜNSDORF, P. SIECK, S. L. PHILIPP

*2012* Austrian Journal of Earth Sciences  
*Lünsdorf et al.* *The thermal history of the Steinach nappe (Eastern Alps) during extension along the Brenner normal fault system indicated by organic maturation and zircon (U-Th)/He thermochronology*  
Authors: N. K. LÜNSDORF, I. DUNKL, B. C. SCHMIDT, G. RANTITSCH, H. VON EYNATTEN

*2013* Berg- und Hüttenännische Monatshefte  
*Rantitsch et al.* *Structural characterization of metallurgical coke by Raman spectroscopy*

Authors: G. RANTITSCH, J. SCHENK, N. K. LÜNSDORF, A. BHATTACHARYYA, M. HANEL, D. WALLNER, H. KALTENBÖCK

- 2014 Geostandards and Geoanalytical Research  
*Lünsdorf et al.* Towards a higher comparability of geothermometric data obtained by Raman spectroscopy of carbonaceous material. Part 1: Evaluation of biasing factors  
Authors: N. K. LÜNSDORF, I. DUNKL, B. C. SCHMIDT, G. RANTITSCH, H. VON EYNATTEN
- 2014 International Journal of Coal Geology  
*Rantitsch et al.* Assessing the quality of metallurgical coke by Raman spectroscopy  
Authors: G. RANTITSCH, A. BHATTACHARYYA, J. SCHENK, N. K. LÜNSDORF

#### CONFERENCES

- 2012 European Geoscience Union, Vienna (Austria)  
*EGU2012* LÜNSDORF N. K., DUNKL I., SCHMIDT B. C., RANTITSCH G. and VON EYNATTEN H. - 'Cautionary notes on the comparability of geothermometric data gained by Raman spectroscopy of carbonaceous material' (Poster presentation)
- 2012 Geohannover, Hannover (Germany)  
*GeoHannover* LÜNSDORF N. K., DUNKL I., SCHMIDT B. C. and VON EYNATTEN H. - 'Temperature assesment of the dry gas zone by Raman spectroscopy and (U-Th)/He thermochronometry: Call for co-operation' (Poster presentation)
- 2013 Conference On Raman And Luminescence Spectroscopy, Vienna (Austria)  
*CORALS* LÜNSDORF N. K., LÜNSDORF J. O. - 'Iterative, randomized fitting of Raman spectra of carbonaceous material based on genetic algorithms' (Poster presentation)
- 2014 GeoRaman2014, St. Louis (USA)  
*GeoRaman2014* LÜNSDORF N. K., LÜNSDORF J. O. - 'Automated curve-fitting of Raman spectra by an iterative, randomized approach applied to carbonaceous matter and minerals' (Poster presentation)  
LÜNSDORF N. K. - 'The influence of polishing on the Raman spectrum of diagenetic carbonaceous matter' (Oral presentation)
- 2014 GeoFrankfurt2014, Frankfurt (Germany)  
*GeoFrankfurt2014* LÜNSDORF N. K., DUNKL I., SCHMIDT B. C. and VON EYNATTEN H. - 'Evolution of Raman maturity parameters in Kerogen Type I and III - an experimental study' (Oral presentation)
- 2015 67th Annual meeting of the International Committee for Coal and Organic Petrology, Potsdam (Germany)  
*ICCP Meeting* LÜNSDORF N. K. - 'Methodical aspects and interpretation of dispersed vitrinite Raman spectroscopy and its correlation with vitrinite reflectance' (Poster presentation)

#### COMPUTER SKILLS

- Basic* MATLAB, R, OCTAVE
- Intermediate* PYTHON, L<sup>A</sup>T<sub>E</sub>X

#### ADDITIONAL SKILLS AND QUALIFICATIONS

- Further Education* Short Course · Matlab Recipes for Earth Sciences, Potsdam, March 26 – 30, 2012 – Supervisor: Prof. Dr. M. H. Trauth

Short Course · ICCP Course in Organic Petrology, Helmholtz Centre Potsdam, June 10 – 14, 2013 – Supervisor: Prof. C. Diessel and Dr. W. Pickel

Short Course · Geochemistry in oil and gas exploration, Göttingen, March 3 – 7, 2014 – Supervisor: Dr. J. Rückheim and Dr. T. Schwarzkopf

Short Course · 2014 ICCP Course in Dispersed Organic Matter, Helmholtz Centre Potsdam, June 23 – 27, 2014 – Supervisor: Prof. Dr. J. G. Mendonça Filho and Dr. A. G. Borrego

*Languages*

GERMAN · native speaker

ENGLISH · fluent in text and speech

September 30, 2015